# Meteorological Applications of Satellite Indirect Soundings II

Department of Meteorology
University of Wisconsin–Madison
1225 W. Dayton Street
Madison, Wisconsin 53706


Contributions by

L. H. Horn
R. A. Hyde
T. L. Koehler
R. A. Petersen
L. W. Uccellini

L. H. Horn, Principal Investigator

PROJECT REPORT

The research in this report has been supported
by the National Environmental Satellite Service of the
National Oceanic and Atmospheric Administration under Grant 04-4-158-2

December 1977

# Meteorological Applications of Satellite Indirect Soundings II

Department of Meteorology
University of Wisconsin–Madison
1225 W. Dayton Street
Madison, Wisconsin 53706


Contributions by

L. H. Horn
R. A. Hyde
T. L. Koehler
R. A. Petersen
L. W. Uccellini

L. H. Horn, Principal Investigator

PROJECT REPORT

The research in this report has been supported
by the National Environmental Satellite Service of the
National Oceanic and Atmospheric Administration under Grant 04-4-158-2

December 1977

Table of Contents

# INTRODUCTION

This Project Report contains research done with the full or partial support of the National Oceanic and Atmospheric Administration Grant 04-4-158-2 during the period August, 1975 through December, 1977. The fundamental goal of the research has been to apply temperature profiles derived from infrared and microwave radiances measured from polar orbiting satellites to various meteorological problems.

Although the major thrust of the research has been toward the meteorological application of the satellite sounding data, a considerable amount of the project work has necessarily involved the development of analysis methods which are applicable to this very new data set. This is reflected in the variety of papers contained in the report. The article by Petersen and Horn, which has already been published in the Bulletin of the American Meteorological Society, represents a successful application of Nimbus-6 soundings to a description of the 500mb height and geostrophic wind over a large portion of northeastern North America. The following paper by Petersen describes a three-dimensional analysis method, which represents an extension of the objective cross section analysis procedure described by Whittaker and Petersen in our previous project report and subsequently in Monthly Weather Review. This three-dimensional analysis technique may become a significant tool in evaluating the quality of consistency of satellite soundings. Since data problems such as those which arise from cloud contaminated satellite soundings can seriously degrade the data sets, methods like this which have the potential of easily identifying the poor soundings are needed.

The article by Koehler, which evaluates seven methods of grid to observation interpolations, is part of a larger research effort designed to seek the most effective method in employing satellite soundings in numerical models. However, the evaluations, which employ analytic functions for comparisons, have more general implications to the entire subject of operational objective analyses. The initial incentive of the study by Hyde was to provide a follow-up to the comparison of isentropic cross sections based on radiosonde, Nimbus-5 satellite soundings and initial hour data from the Limited Fine Mesh (LFM) model of the National Meteorological Center described in our 1975 report. However, the paper which deals with the effects of post-processing of operational model data, has implications far beyond our basic research efforts.

The final article by Petersen and Uccellini, which involves the computation of isentropic trajectories using a discrete model formulation, follows quite naturally from the emphasis that we have placed on isentropic analyses. Again, its implication extends well beyond the narrower research goals of this project.

Lyle H. Horn
Principal Investigator
December, 1977

[Reprinted from BULLETIN OF THE AMERICAN METEOROLOGICAL SOCIETY, Vol. 58, No. 11, November 1977]
Printed in U. S. A.

# An Evaluation of 500 mb Height and Geostrophic Wind Fields Derived from Nimbus-6 Soundings

Ralph A. Petersen [1] and Lyle H. Horn

*Department of Meteorology, University of Wisconsin–Madison*
*Madison, Wis. 53706*

## Abstract

**Temperature profiles obtained from Nimbus-6 radiance measurements and sea level pressures are used to construct 500 mb height and geostrophic wind fields over northeastern North America for the 3-day period 18–20 August 1975. These satellite-derived fields, obtained at about 1600 GMT daily, are compared with bracketing 1200 and 0000 GMT analyses prepared by the National Meteorological Center. The results indicate that carefully screened satellite soundings are very capable of delineating the location and intensity of a closed 500 mb low. The implications of this study to the First GARP Global Experiment are briefly considered.**

## 1. Introduction

An important component of the basic observing system for the First GARP Global Experiment (FGGE) is the polar-orbiting satellite, which is capable of providing vertical temperature profiles on a global scale. In a recent experiment, Phillips (1976) has found that if satellite soundings are to be of value in improving forecasts during FGGE, care must be taken to reduce the spatially variable error in the temperature profiles. He suggests that efforts be made to assign probable error magnitudes to individual satellite temperature retrievals to enhance their contribution as numerical model input. The lack of impact shown in most previous numerical forecast experiments based on combinations of satellite soundings and conventional data supports this suggestion (see Bengtsson and Morel, 1974; Atkinson, 1975; Halem, 1976). Phillips, however, qualifies his conclusions regarding the impact of satellite data during FGGE by noting that his results may be overly pessimistic if the temperature retrievals are capable of closely delineating the principal baroclinic zones and closed upper-level lows over the oceans.

Some recent work at the University of Wisconsin indicates that the satellite soundings are indeed capable of closely delineating baroclinic zones and upper-level lows provided care is taken to screen poor data. Horn *et al.* (1976) have shown that Nimbus-5 soundings were of sufficient quality to accurately define the thermal structure through an intense baroclinic zone. In a second study, which is presented here, we go on to demonstrate that the Nimbus-6 satellite temperature retrievals are capable of monitoring a closed 500 mb low during a 3-day period (18–20 August 1975). Both studies were conducted primarily over continental North America, where radiosonde coverage provides verification data. Because the satellite soundings offer a very new data set, it is important that it first be evaluated in regions that are rich in conventional sounding data. In both studies, special care was taken to eliminate poor data. Although the clear column retrieval schemes are intended to minimize cloud contamination, our past studies using satellite soundings indicate that poor data are occasionally included.

Nimbus-6, launched in June 1975, contained a 17-channel High Resolution Infrared Sounder (HIRS) and a 5-channel Scanning Microwave Spectrometer (SCAMS), both of which scan ~700 km left and right of the orbital path. The configuration of scanning instruments aboard Nimbus-6 makes it possible to describe *fields* of atmospheric temperature and humidity. Nearly all previous

[1] Now at the Department of Geography, Northern Illinois University, DeKalb, Ill. 60115.

studies based on Nimbus series satellite soundings used only nadir data. In this case study we evaluate 500 mb height and geostrophic wind fields obtained from Nimbus-6 soundings processed in April and May 1976.

## 2. Data and case selection

The Nimbus-6 temperature sounding retrieval system uses HIRS radiance measurements from two portions of the infrared spectrum (near 15 $\mu$m and 4.3 $\mu$m) and SCAMS measurements made in the 0.5 cm region of the microwave spectrum (see NASA (1975) for details of the instrumentation). Temperature profiles were retrieved from the combined HIRS and SCAMS radiance data by the National Environmental Satellite Service (NESS) using a procedure that employs eigenvectors of covariance matrices determined from observed radiance, climatalogical atmospheric temperature, and water vapor mixing ratio profiles (see Smith and Woolf, 1976). After spatial averaging and local consistency checks, soundings were produced with an average spacing of 250 km at 40° latitude. If soundings from successive passes (~107 min apart) are combined, overlapping coverage is provided poleward of ~56° latitude. Between 48° and 56° the spacing between observations from adjacent scans is at most 400 km, which is a typical spacing between radiosonde stations in the United States. The time separation between any two passes is not critical since it is only slightly greater than the time required for a radiosonde to ascend to 100 mb.

Although the retrieval procedure used by NESS attempts to flag questionable soundings, our experience has shown that some poor data pass the checking procedure. Consequently, in this study, we have applied additional subjective screening by examining horizontal gradients of the thermal (thickness) fields. Through this procedure we found it necessary to reject fewer than 5% of the ~400 soundings. The relatively good quality of this data set is probably due to the fact that the region studied had only limited areas of solid overcast. (See Fig. 1 (g–i) for nephanalyses.)

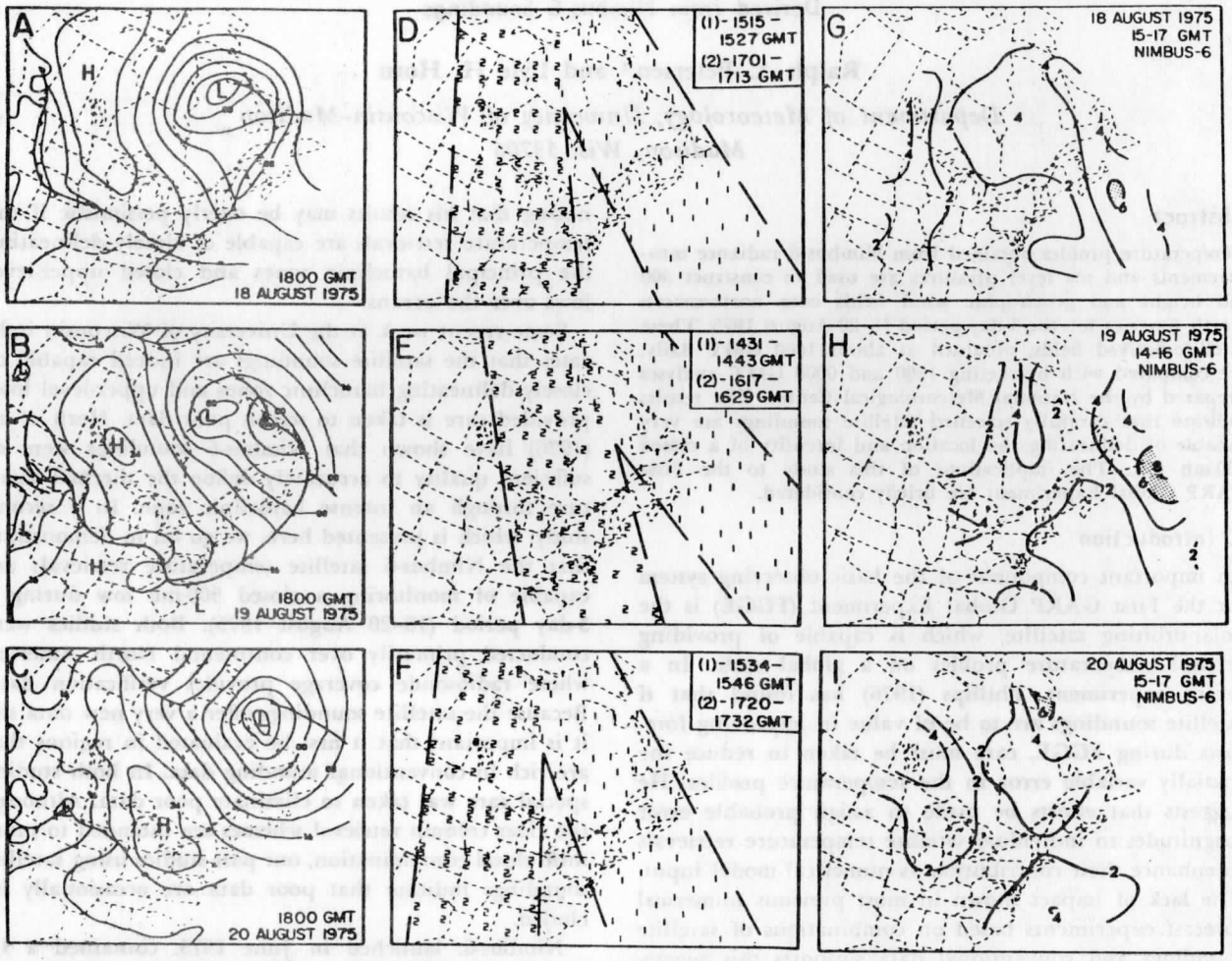


FIG. 1. (a–c) Sea level pressure analyses for continental North America for the 3 days studied. (d–f) Locations of satellite soundings used from two consecutive ascending Nimbus-6 passes. The 1s indicate locations for earlier pass, and the 2s refer to later pass. Times of passes are given in upper right corners. Note that within each pass, soundings tend to be clustered in groups of 12, separated by swaths containing no soundings. (g–i) Percent of total cloud cover derived from Nimbus-6 radiances.

Temperature soundings retrieved from successive ascending orbits made between 1400 and 1700 GMT on three successive days were used to obtain 500 mb height and geostrophic wind fields in a region of relatively strong baroclinity over eastern Canada and the northeastern United States. Data obtained from the descending orbits (about 0400 GMT) were not incorporated, because large data gaps were present due to readout scheduling. Comparisons were made between the satellite data and the bracketing 1200 and 0000 GMT operational radiosonde analyses prepared by the National Meteorological Center (NMC) and transmitted by facsimile.

The situation studied, covering the period from 18 to 20 August 1975, was advantageous in two respects. As shown in Fig. 1 (a–c), the synoptic situation was relatively unchanging during the 3-day period, with a large, nearly stationary cold-core low positioned east of Hudson Bay. In addition, since the temperature gradients during this summer situation were greater than usual, the case provided a reasonable test of the sounder's capability to resolve thermal gradients. It should also be noted that this was a period during which all of the Nimbus-6 radiation sensors were functioning well. (In early September 1975, the HIRS 15 $\mu$m channel sensor became very noisy.)

## 3. Procedure

The satellite temperature profiles for 1400–1700 GMT and the 1800 GMT sea level pressures obtained from the NMC surface analyses were used to estimate the 500 mb height fields. The satellite soundings were used to compute the 1000–500 mb thickness by using the hypsometric equation for dry air. The 1000 mb heights were calculated by using sea level pressures at the locations of the satellite soundings and the 1000 mb satellite-derived temperatures, which were assumed to be representative of the column of air between 1000 mb and sea level. Since the surface elevations in the area studied were relatively low, the sea level pressure–1000 mb height conversion could be done quite accurately. In all calculations, only retrieved satellite temperatures, processed to the nearest whole degree, were used.

An objective procedure was employed to analyze the 500 mb heights. The calculated heights within individual satellite passes were interpolated onto a 2° × 2° latitude-longitude grid extending from 100°W, 64°N to 50°W, 34°N. To avoid contamination from other data sources, the analysis technique did not use a first guess field. Instead, data were interpolated directly from the sounding locations to each grid point. Weights for the one-pass interpolation were assigned according to a modified Cressman (1959) formula:

$$W_n = (R^2 - D_n^2)/(R^2 + D_n^2),$$

where $W_n$ is the weight applied to the $n$th closest sounding, $D_n$ is the distance from that sounding location to the grid point, and $R$ was chosen as the mean of the distances from the grid point to the seventh and eighth closest soundings (Whittaker, 1976). It should be noted that within individual satellite passes the Nimbus-6 soundings are clustered in groups, separated by regions that lack data due to periodic HIRS instrument calibra-

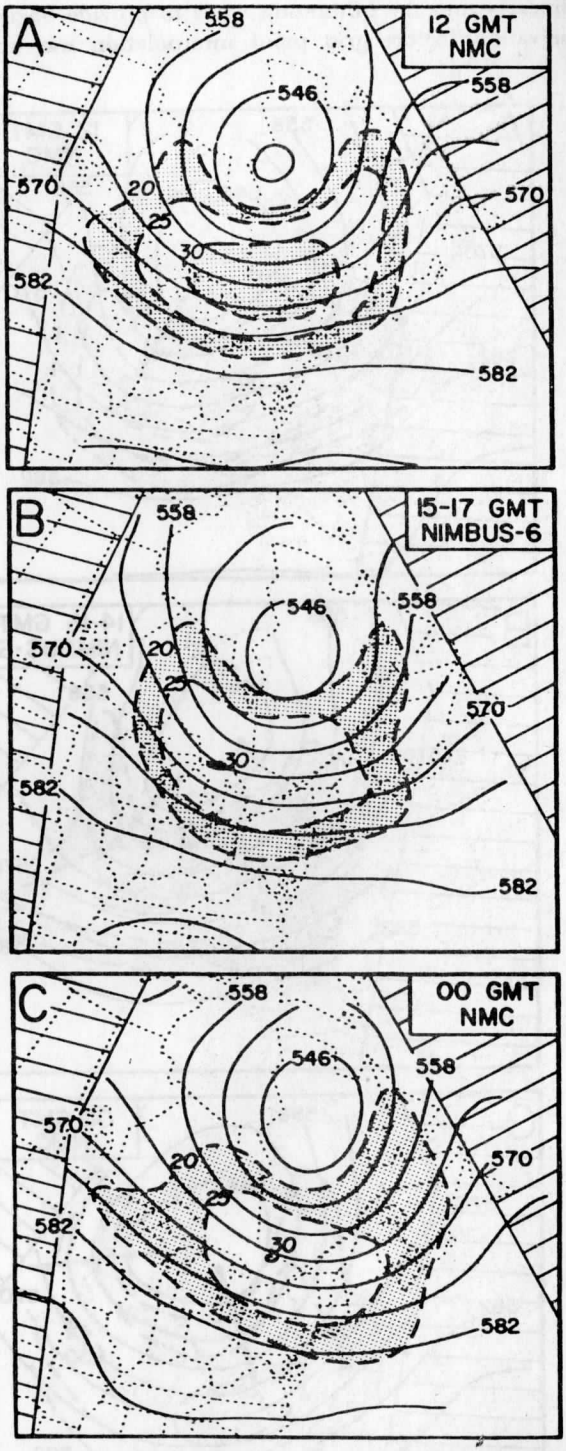


FIG. 2. 500 mb heights in decameters (solid lines) and corresponding geostrophic wind speed in meters per second (dashed lines) for (a) 18 August 1975, (b) 18 August 1975, and (c) 19 August 1975. The time and source (NMC or Nimbus-6) are indicated in the upper right corners. Alternating 5 m s$^{-1}$ bands (stipled areas) and areas that lacked satellite observations or were outside the grid (hatched areas) are also indicated.

tion (see Fig. 1 (d–f)). Because no first guess field was used, special treatment was necessary to avoid the development of anomalous gradients in the data void regions. To prevent this, satellite data were interpolated linearly into the calibration voids to provide bogus observations before grid point interpolation was accomplished. These analyses were then extended equatorward of 56°N into the small gaps between passes. The gridded data were then slightly smoothed using one pass of a five-point binomial filter.

For comparison purposes, 500 mb height values from NMC analyses were visually transcribed onto the 2° × 2°

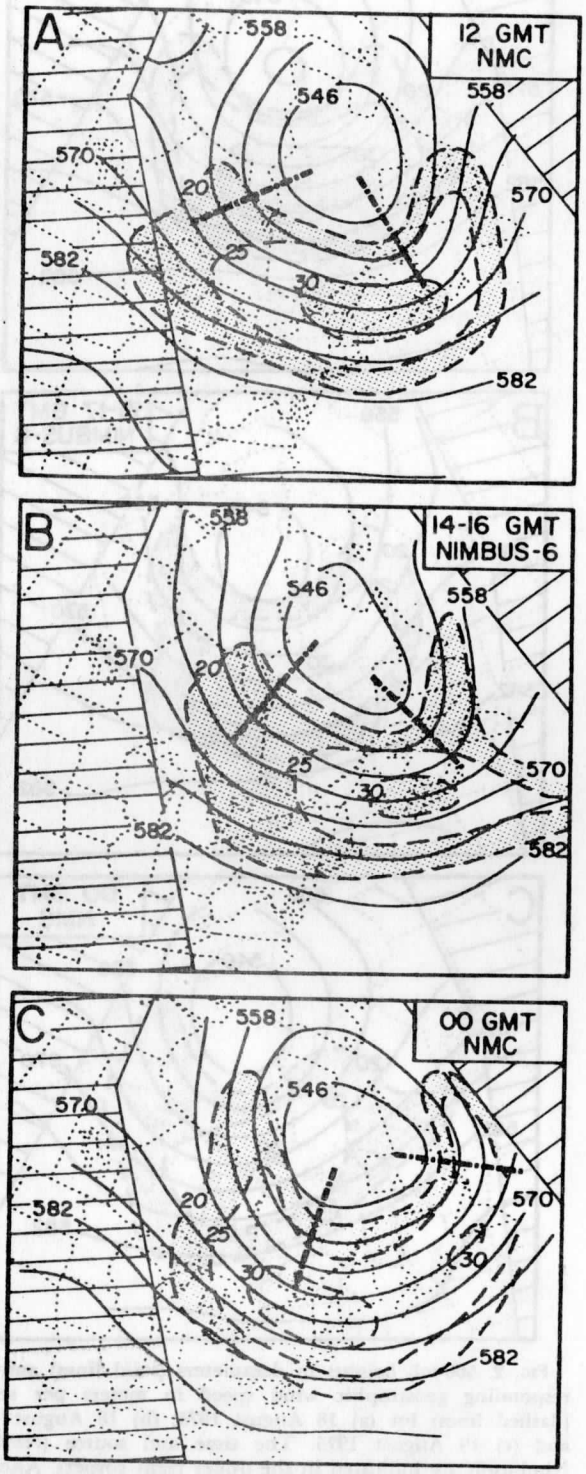


FIG. 3. Same as Fig. 2 except for (a) 19 August 1975, (b) 19 August 1975, and (c) 20 August 1975. The positions of 500 mb short waves (heavy dash-dot lines) are also indicated.

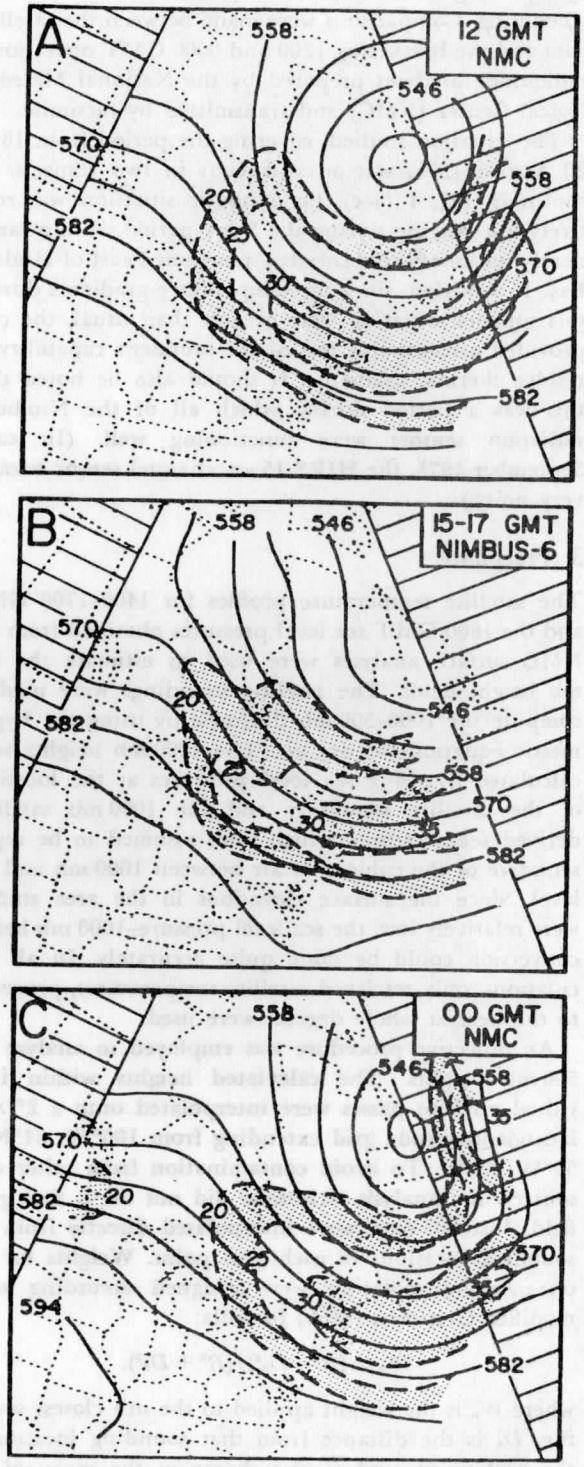


FIG. 4. Same as Fig. 2 except for (a) 20 August 1975, (b) 20 August 1975, and (c) 21 August 1975.

TABLE 1. Positions and central heights of 500 mb low as indicated by NMC and Nimbus-6 analyses.

| August 1975 | NMC (1200 GMT) | | Nimbus-6 (1400–1700 GMT) | | NMC (0000 GMT) | |
|---|---|---|---|---|---|---|
| | Position | Height, m | Position | Height, m | Position | Height, m |
| 18–19 | 54°N, 78°W | 5397 | 54°N, 76°W | 5419 | 56°N, 74°W | 5415 |
| 19–20 | 56°N, 72°W | 5415 | 56°N, 72°W | 5420 | 54°N, 69°W | 5407 |
| 20–21 | 56°N, 64°W | 5386 | 56°N, 64°W* | 5402 | 56°N, 62°W | 5381 |

* Since no closed center was analyzed within the region covered by the satellite passes on 20 August, values shown are for a point at the edge of the grid that had the lowest height.

array of grid points. The same binomial filter was applied to this gridded data to reduce the effects of any human transcription errors. Finally, the 500 mb geostrophic winds were calculated from the 2° × 2° grid for both the satellite and the NMC data. The geostrophic wind fields provide a convenient way of evaluating the gradients obtained from the satellite data.

## 4. Results

The 500 mb height and geostrophic wind fields obtained from the NMC analyses and Nimbus-6 soundings are shown in Figs. 2–4. The hatched areas lacked satellite observations or, in the case of the northwest corner, were outside the grid. For all time periods the 500 mb height fields, including the positions of the closed low, calculated from the satellite soundings (panels b) compare favorably with the bracketing NMC analyses (panels a and c). By assuming a linear translation of the low center between 1200 GMT and 0000 GMT each day, the largest deviation of the center obtained from the Nimbus-6 analyses was 100 km, which is less than one grid unit (Table 1). The Nimbus-6 analysis for 20 August (Fig. 4b) does not show a closed contour since the satellite coverage terminated (hatched area) at the approximate position of the center of the closed low. Data from the previous orbit (to the east) were not available. However, the Nimbus analysis reveals the lowest height at the boundary and, in general, is consistent with the NMC analyses.

To further examine the temporal continuity, fields of height differences were calculated between the 1200 and the 0000 GMT NMC analyses and also between the Nimbus-6 analyses and the bracketing NMC analyses for each day. Although not shown here, the difference fields substantiated the slow eastward progression of the 500 mb features. Furthermore, the positions of the two short waves revolving about the closed low on 19 August maintained temporal continuity between successive NMC analyses. (See the heavy dash-dot trough lines on the three successive 500 mb analyses of Fig. 3.)

The subjective evaluations discussed above are supported by objective computations of height bias and rms differences. A total of between 313 and 336 grid points were used to represent the data area for which calculations were made. Within each day the bias figures in the right column of Table 2 represent the mean 500 mb height tendency between the 1200 and the 0000 GMT NMC analyses. These values are in accordance with ridging observed in the western portion of the grid and the gradual progression of the 500 mb low toward the eastern grid boundary. The bias differences between the satellite analyses and bracketing NMC analyses (left and center columns) were always within 6 m of the values that would have been expected from linear variation between NMC analyses. For example, on 18 August the mean 500 mb height over the grid rose by 9.1 m between 1200 and 0000 GMT. A linear variation would imply a height tendency of ~3 m between 1200 and 1600 GMT (the approximate time of the Nimbus analysis). The computed value was −2.8 m, yielding a discrepancy of 5.8 m. This was the largest discrepancy for the three periods studied and is equivalent to a mean 1000–500 mb temperature bias of ~0.3°C.

The rms differences between successive NMC analyses, averaging ~32 m, represent local deviations inherent in the slowly changing synoptic pattern. The rms differences

TABLE 2. Intercomparisons of 500 mb height bias and rms differences (in meters) between Nimbus-6 and NMC analyses.

| August 1975 | No. of Grid Points | Nimbus-6 (≃1600 GMT) minus NMC (1200 GMT) | | NMC (0000 GMT) minus Nimbus-6 (≃1600 GMT) | | NMC (0000 GMT) minus NMC (1200 GMT) | |
|---|---|---|---|---|---|---|---|
| | | Bias | rms | Bias | rms | Bias | rms |
| 18–19 | 336 | −2.8 | 24.5 (1.2°C) | +11.9 | 22.4 (1.1°C) | +9.1 | 29.7 (1.4°C) |
| 19–20 | 324 | −2.1 | 26.3 (1.3°C) | +14.0 | 28.0 (1.4°C) | +11.8 | 33.9 (1.7°C) |
| 20–21 | 313 | +8.8 | 24.8 (1.2°C) | +15.2 | 30.1 (1.5°C) | +23.9 | 33.5 (1.7°C) |

Numbers in parentheses are equivalent 1000–500 mb layer mean temperature differences.

TABLE 3. Intercomparisons of 500 mb geostrophic wind speed bias and rms differences (in meters per second) between Nimbus-6 and NMC analyses.

| August 1975 | No. of Grid Points | Nimbus-6 (≃1600 GMT) minus NMC (1200 GMT) | | NMC (0000 GMT) minus Nimbus-6 (≃1600 GMT) | | NMC (0000 GMT) minus NMC (1200 GMT) | |
|---|---|---|---|---|---|---|---|
| | | Bias | rms | Bias | rms | Bias | rms |
| 18–19 | 270 | −1.0 | 3.5 (0.4°C) | +0.7 | 3.8 (0.4°C) | −0.3 | 3.9 (0.4°C) |
| 19–20 | 259 | −0.4 | 3.5 (0.4°C) | +2.2 | 5.0 (0.6°C) | +1.8 | 4.7 (0.5°C) |
| 20–21 | 250 | −0.4 | 3.7 (0.4°C) | +0.1 | 3.9 (0.4°C) | −0.3 | 3.5 (0.4°C) |

Numbers in parentheses are equivalent 1000–500 mb mean temperature gradient differences per 222 km.

between the satellite-derived height fields and the bracketing NMC analyses were consistently less than the rms values between successive NMC analyses. These satellite-radiosonde rms differences are equivalent to a mean temperature difference in the 1000–500 mb layer of 1.3°C, a value well within the range expected from simultaneous radiosonde ascents (Bengtsson and Morel, 1974). Of course, since the time interval between the satellite data and the bracketing NMC data is roughly one-half of that used in comparing successive NMC analyses, the rms differences should be less. Nevertheless, the results are particularly encouraging since the satellite-derived temperatures used to obtain the 1000–500 mb thickness were available only to the nearest whole degree, and the sea level pressures employed were estimated to the nearest whole millibar (equivalent to 8 m).

The derived geostrophic wind fields offer a means of comparing the gradients obtained from the various height fields. A visual comparison of geostrophic isotach fields (Figs. 2–4) shows good continuity between the satellite and the bracketing NMC analyses. Although the Nimbus-6 derived values were generally a few meters per second less than those obtained from the radiosonde analyses, as indicated by the bias statistics shown in Table 3, the locations of the 500 mb velocity maximums (30–35 m $s^{-1}$) were reasonably consistent in the two data sets.

As was the case for the height field comparisons, the rms differences between the satellite and the NMC geostrophic wind fields (Table 3) showed values compatible with the slow evolution of the synoptic system. These differences, ranging from 3.5 to 5.0 m $s^{-1}$, were comparable to the differences observed between successive NMC analyses. The satellite-radiosonde differences are equivalent to a mean temperature gradient discrepancy of between 0.4°C and 0.6°C per 222 km (8–12 m per 222 km) for the region of the atmosphere below 500 mb. These values are well within normal observation and analysis tolerances (see Bengtsson and Morel, 1974).

## 5. Summary and conclusions

The case studied here strongly suggests that satellite-derived temperature profiles of the quality of Nimbus-6 are very capable of providing the data needed to locate the principal 500 mb features during periods of moderate baroclinity. For the 3 days studied, the fields of 500 mb height and corresponding geostrophic velocity derived from Nimbus-6 temperature soundings and sea level pressures compared favorably with bracketing NMC analyses. The gradients derived from the satellite data were slightly less than those in the NMC analyses, as is expected from the areal average nature of the individual satellite retrievals. Nevertheless, the variability observed between the satellite analyses and the bracketing NMC analyses was comparable to that observed between successive radiosonde-derived fields.

In this study, data obtained over a portion of North America were employed to allow verification. There is every reason to expect equally good satellite results over oceanic areas; however, the scarcity of sea level pressure observations over the oceans could cause an increase in 500 mb height errors. Where shipping lanes exist, the problem of obtaining sea level pressures should be no greater than the problem of obtaining data in northeastern Canada. During FGGE the deployment of buoys should further reduce the problem of obtaining the sea level pressure field.

Horn *et al.* (1976) have illustrated the usefulness of satellite soundings in obtaining the gradients of thickness needed to locate and define the intensity of strong wintertime jet maximums. The results achieved in this study showed that satellite soundings are also capable of delineating closed upper-level circulations. However, in both of these studies, special care was taken to eliminate poor data. Until automated methods are perfected, the screening of the satellite data by trained meteorologists appears essential if the full impact of this new data source is to be achieved. It is important to remember that radiosonde information was used for many years before automated analysis techniques were available. Others have recognized this and have initiated investigations that carefully merge satellite sounding data with radiosonde observations to improve the quality and resolution of meteorological analyses (see Fritz (1977) and Hillger and Vonder Haar (1977) who have employed Vertical Temperature Profile Radiometer (VTPR) data).

As mentioned in the introduction, Phillips notes that his conclusions regarding the prospects for improved 1-

to 5-day forecasts for North America during FGGE may be too pessimistic since his experiments did not consider the possibility that satellites may be able to delineate the principal baroclinic zones and closed upper-level lows over mid-oceans. The results of this study and of Horn *et al.* suggest that satellite sounders of the quality of those on Nimbus-5 and Nimbus-6 are currently capable of locating and describing such features. We recognize that two such positive studies do not conclusively confirm the quality of the satellite soundings. On the other hand, it should be noted that neither have we simply chosen two favorable studies to present.

*Acknowledgments.* We thank Drs. William L. Smith and Christopher M. Hayden of NESS for providing the Nimbus-6 data and Amy Alexander and Thomas Koehler for assistance in preparing the data. We also thank Prof. Verner E. Suomi for his comments concerning the manuscript. This study was supported by the Meteorological Satellite Laboratory of NESS under NOAA Grant 04-40158-2.

## References

Atkins, M. J., 1975: The value of satellite Vertical Temperature Profile Radiometer (VTPR) data in numerical weather prediction. Paper presented at the 16th General Assembly of IUGG, Grenoble, France.

Bengtsson, L., and P. Morel, 1974: The performance of space observing systems for the First GARP Global Experiment. Rept. 6, GARP Working Group on Numerical Experimentation, Washington, D.C., 31 pp.

Cressman, G. P., 1959: An operational objective analysis system. *Mon. Wea. Rev.*, 6(4), 309–318.

Fritz, S., 1977: Temperature retrievals from satellite radiance measurements—An empirical method. *J. Appl. Meteor.*, 16(2), 172–176.

Halem, M., 1976: Report on a four-dimensional DST temperature sounding impact test. Paper presented at the Symposium on Meteorological Observations from Space: Their Contribution to the First GARP Global Experiment, Philadelphia, COSPAR.

Hillger, D. W., and T. Vonder Haar, 1977: Deriving mesoscale temperature and moisture fields from satellite radiance measurements over the United States. *J. Appl. Meteor.*, 16(7), 715–726.

Horn, L. H., R. A. Petersen, and T. M. Whittaker, 1976: Intercomparisons of data derived from Nimbus-5 temperature profiles, rawinsonde observations, and initialized LFM model fields. *Mon. Wea. Rev.*, 104(11), 1361–1371.

NASA, 1975: *Nimbus-6 User's Guide*. Goddard Space Flight Center, Greenbelt, Md.

Phillips, N. A., 1976: The impact of synoptic observing and analysis systems on flow pattern forecasts. *Bull. Amer. Meteor. Soc.*, 57(10), 1225–1240.

Smith, W. L., and H. M. Woolf, 1976: The use of eigenvectors of statistical covariance matrices for interpreting satellite sounding radiometer observations. *J. Atmos. Sci.*, 33(7), 1127–1140.

Whittaker, T. M., 1976: A simplified grid interpolation scheme for use in atmospheric budget studies. M.S. thesis, Dept. of Meteor., Univ. of Wisconsin, Madison, 42 pp.

# Three-Dimensional Objective Analysis Based on Isentropic Cross-Sectional Techniques

Ralph A. Petersen

Department of Geography, Northern Illinois University, De Kalb, ILL 60115

## Abstract

Recent advances in meteorological objective analysis have been directed toward the problem of improved numerical model initialization; often however at the expense of representing detail in data rich regions. An objective scheme is presented here which gives detailed, yet efficient and economical analyses over data rich regions which are independent of any numerical model bias, and are particularly suited to diagnostic studies and satellite sounding applications. Three-dimensional grid point analyses are obtained by first constructing a series of nearly parallel, north-to-south isentropic cross sections over an area of interest and then filling in the space between adjacent vertical analyses using a second set of nearly orthogonal cross-sections. Thermal information obtained from these analyses is then combined with observed wind data to obtain a thermally consistent observed wind analysis. Examination of preliminary results indicates the detail and continuity inherent in the technique. A discussion of future modifications and possible applications is also included.

## I. Introduction

Objective analysis was first introduced to the meteorological community in 1949, when Panofsky proposed objectively relating meteorological variables to space coordinates as a means of eliminating subjectivity and hastening the process of manual analysis. In 1959, Cressman defined objective analysis as "the procedure of transforming data observations at irregularly spaced points onto... points of a regularly spaced grid." Since that time, further development of objective analysis techniques has followed a course closely associated with that of numerical weather prediction. Emphasis has evolved from simple data fitting techniques to sophisticated statistical/dynamical assimilation methods. For example, in a recent discussion of multivariate statistical analysis, Schlatter, et. al. (1976) noted that "objective analysis is a programmable method for estimating grid point values compatible with a particular numerical prediction model." (Emphasis added.) The development in numerical weather prediction has necessitated this change of emphasis in the approach to objective meteorological analysis; often, however at the expense of representing detail in data rich regions (Otto-Bliesner, et al., 1977). To better appreciate this change of direction of objective analysis toward numerical model initialization, a short chronology of some early objective analysis techniques follows. (For another review, including more recent techniques, see Schlatter, et al., 1976.) This discussion is followed by the introduction of a new analysis model which has been designed to emphasize the "detail" available from observations while still enforcing dynamic consistency.

The Panofsky (1949) technique fit third-order polynomial surfaces to observed data over fairly large areas. While the use of a least-squares fitting method showed potential, the resulting analyses were characteristically

quite smooth. Certain discrepancies and difficulties revealed by Panofsky lead Gilchrist and Cressman (1954) to investigate modifications which could give a more accurate representation of the data and incorporate more detail in the analyses. Successive fits of second-order polynomials were applied to data in a limited area around each grid point. In effect, a series of modifications are made to a "first guess" field, using the difference between each station's observations and the values from the previous analysis cycle as the interpolation parameter. In order to make the analysis more adaptable to numerical prediction, a variable degree of geostrophic constraint was included. Similar work by Johnson (1957) corroborated that in a close network of observations, a reasonably accurate objective interpolation of contour height and wind can be made using such an analysis scheme.

To alleviate the difficulties incurred using these techniques over areas of widely scattered observations, Cressman (1959) proposed an alternative approach to objective analysis appropriate for global analysis and forecast applications. This successive correction technique, patterned after the method of Bergthorssen and Döös (1955), used empirical weighting of data within a "radius of influence" about each grid point to make modifications to a forecast-based first guess field. This "radius of influence" was reduced during successive passes over the grid to increase the contributions of smaller scale features. Used operationally, this method became the first model update technique (McPherson, 1975).

Recently, both eigenfunction expansions (Flattery, 1970) and statistical interpolation techniques (Gandin, 1963; Schlatter, 1975; Schlatter, et al., 1976) have been applied to the hemispheric analysis problem. These techniques are tailored to large scale numerical model application and often prove inappropriate for detailed investigations of the atmosphere. Also

these techniques can be prohibitively expensive. The need for a detailed, yet efficient and economical objective analysis technique, which is independent of any numerical model bias and applicable to limited region of abundant data, has been underscored by diagnostic studies of the extratropical cyclone and certain aspects of severe weather development being conducted at the University of Wisconsin-Madison, and elsewhere. Such a detailed scheme could prove beneficial not only in synoptic research but also in such a diverse application as nested grid modeling, and could provide another mode of comparison for statistically based analysis schemes. Studies using the rich horizontal array of satellite soundings that is expected to be achieved from the VISSR (Visible Infrared Spin-Scan Radiometer) Atmospheric Sounder will likewise benefit from such an objective analysis technique. An attempt to provide such a tool is described below.

## II. Analysis Technique

While the concept of deriving grid point values of observed parameters through least-squares polynomial surface fitting has had a long history in objective analysis, it was not until 1973 that Shapiro and Hastings first proposed the use of Hermite polynomial interpolation between radiosonde stations to objectively analyze the detailed thermal structure revealed in isentropic cross sections. In independent work, Whittaker and Petersen (1977) constructed cross sectional analyses using overlapping second-order Lagrangian polynomials. The resulting third-order representation not only fit the data exactly at the observations, but also included thermal gradient information obtained from higher order derivative approximations made at the stations. Additionally, thermal gradients were integrated with wind observations to obtain an enhanced representation of the vertical wind structure consistent with the thermal wind relationship. Cross sections, which use the relatively

rich vertical arrays of data available in a given set of radiosonde or satellite derived temperature observations, have provided a much more detailed view of atmospheric thermal and velocity fields and their inter-relationship. In addition, the subjective synthesis of several cross sections with conventional map analyses has often provided a degree of vertical continuity which otherwise might not have been achieved.

A method is now presented for economically obtaining 3-dimensional analyses of the atmosphere using extensions of these proven cross-sectional analysis techniques. This cross-sectional synthesis incorporates both the horizontal and vertical structures of the atmosphere, and provides a degree of consistency between analyses of the thermal and observed wind fields. This method is also independent of any "first guess" field bias such as climatology or a previous forecast.

As with objective cross-sectional analysis, several analysis requirements must be prescribed. The original data values should be maintained as closely as possible at each station. The analyses must maintain hydrostatic balance and, in isentropic coordinates, not violate the stability criterion that $\Delta P/\Delta\theta<0$, where P is pressure and $\theta$ potential temperature. Finally, the analyses must maintain a smooth, continuous character, over the entire field. The key to continuity on the quasi-horizontal analysis technique presented here lies in the method of interpolating values between sets of adjacent observations. During cross-section analysis the interpolation is accomplished by using overlapping polynomials which connect successive data points exactly forming cubic functions and which meet quadratic transition constraints at the observation points [see Figure 1 which has been taken from Whittaker and Petersen (1977)]. Quasi-horizontal analyses are, in effect, produced by applying this same procedure repeatedly, first to obtain a set of nearly

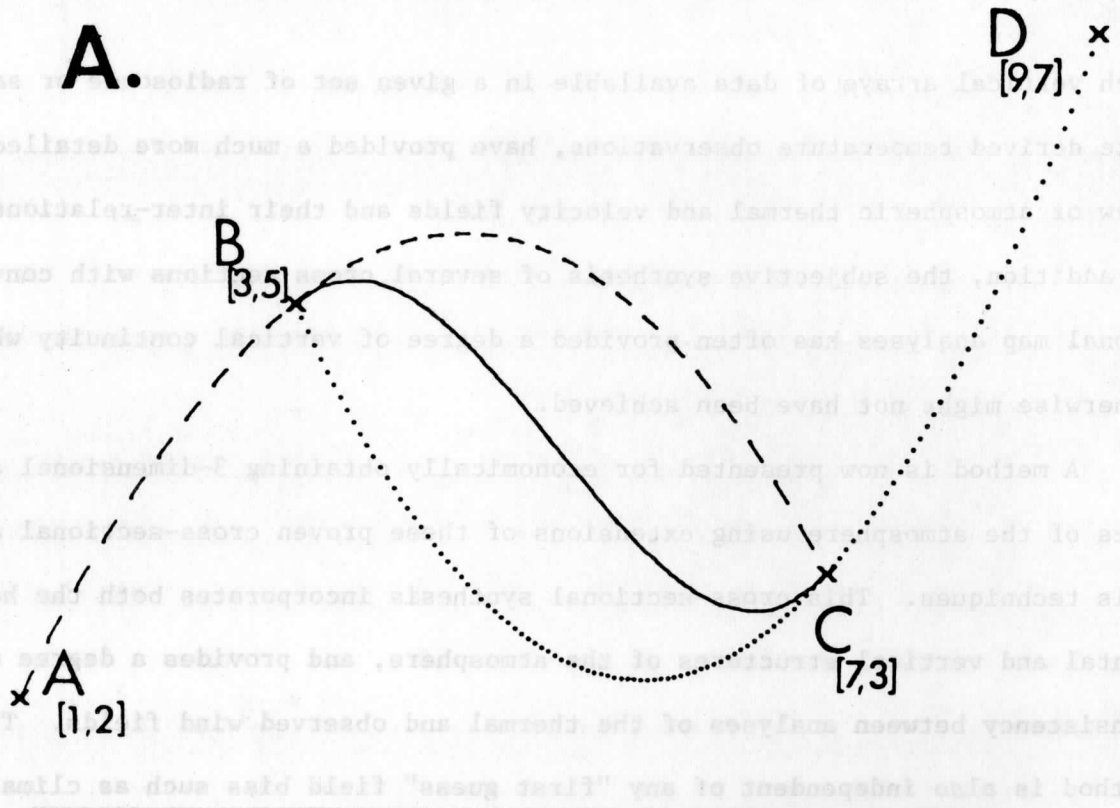


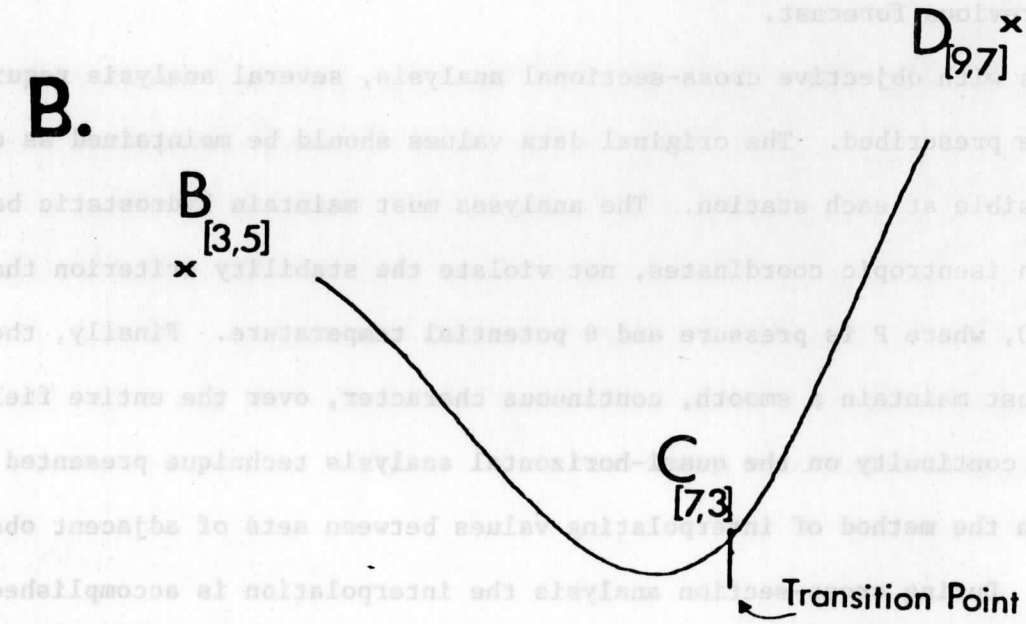


Fig. 1. Illustration of overlapping polynomials. (a) Two quadratic Lagrangian polynomials connecting points A,B and C (dashed) and points B,C and D (dotted). The x,y coordinates of the points are shown in brackets. Linear merger of the two polynomials between B and C shown by solid line. (b) Illustration of the smooth transition, at data point C between two overlapping quadratic Lagrangian polynomials.

parallel cross sections and then to fill in the space between adjacent sections. In doing so, observed gradients are maintained to a higher degree in the analysis than if empirical areal weights had been applied.

To better describe the analysis procedure, two examples are given. The first shows the procedure for obtaining an analysis of a strictly two-dimensional scalar field, while the second represents the full three-dimensional analysis procedure. In both examples, a latitude-longitude grid has been used.

The analysis of a hypothetical field of scalar observations (located in Fig. 2a with the data values in brackets), proceeds as follows. Various nearly north-to-south paths are first selected to connect all observations (heavy dashed lines in Fig. 2b). The overlapping quadratic polynomial method shown in Fig. 1 is then used to obtain curves connecting the data values along each path (e.g. between points B, C, D and E (easternmost path on Panel B) as shown in Panel C). The overlapping technique dictates smooth transitions between adjacent cubics, providing the continuous data fit. Values computed at regularly spaced latitudinal intersection (crosses) are stored along with their longitudinal location for each of the north-to-south data sets (parenthetical values in Panels B and D). Finally, a regularly spaced grid array is achieved by cubic interpolation of the unevenly spaced data along each latitude line to specified longitudinal intervals. The final grid point values for this example are shown in Panel D.

The three-dimensionality of the analysis procedure can be illustrated by a conceptual <u>isentropic</u> example that emphasizes the dependence of this scheme on the principles of objective cross section analysis. In Panel A of figure 3, a hypothetical isentropic cross section, made along the set of observations indicated by circles, has been analyzed using the overlapping polynomial technique. The intersections of the cross section with each grid

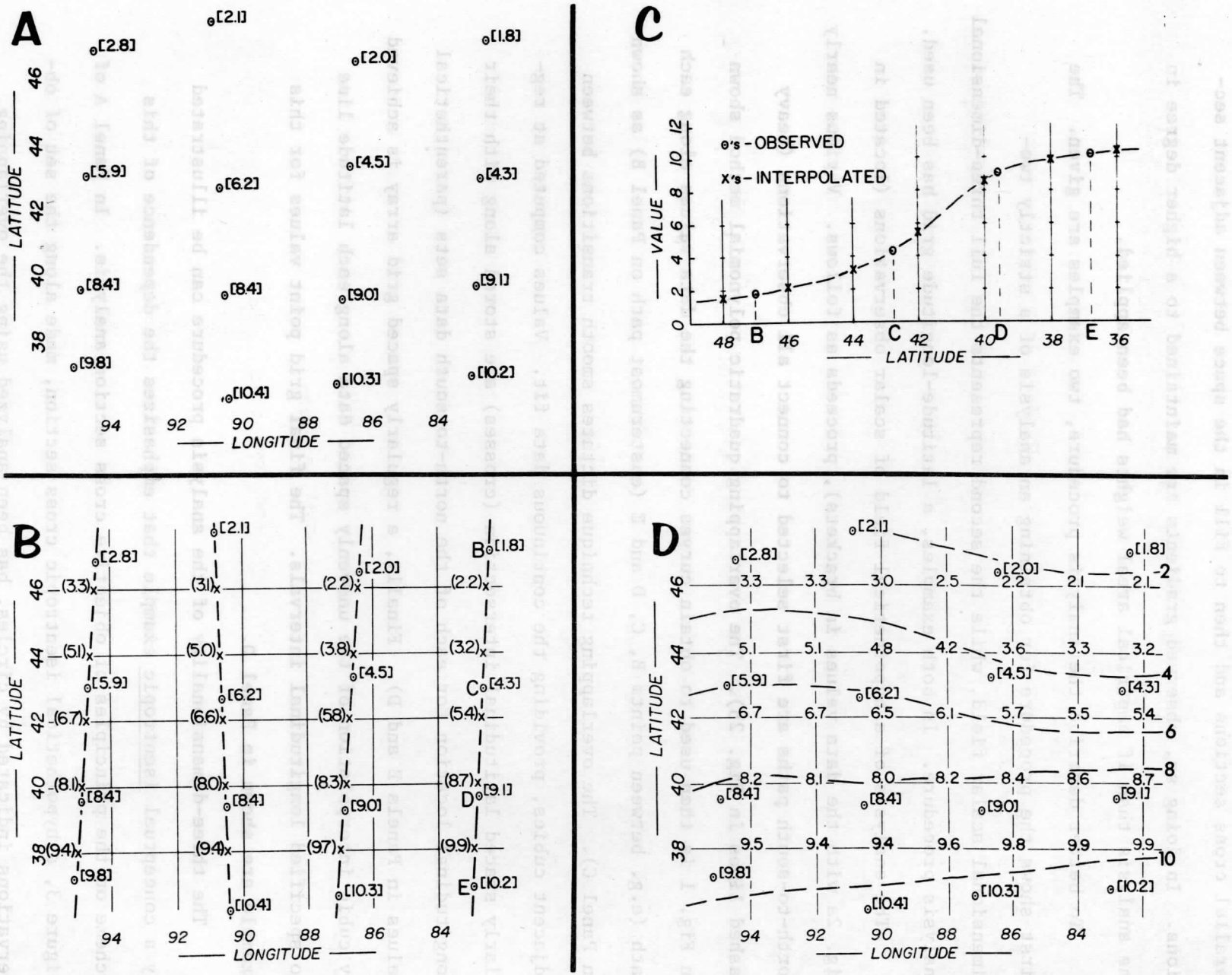


Fig. 2. Illustration of the 2-dimensional analysis procedure. (a) Set of randomly spaced data points to be analyzed with data values in brackets. (b) Set of cross-sectional paths used for analysis. (c) Evaluation of polynomial connecting eastmost points B,C,D and E. (d) Analysis of final grid point values obtained by interpolating between the 4 north/south paths.

row have been projected onto the cross section with thin-dashed vertical lines. (In practice, the cross section paths are defined as a "curtain" containing each of the stations.) To accomodate all available data points in this example, a total of four cross-sectional analyses were used (Panel B). At each point where the vertical analyses intersect a grid row, the location of the grid row intersection and the values of pressure at each isentropic level (indicated by arrows) are calculated and stored. Once the full set of nearly columnar cross sections has been analyzed, transverse cross sections are analyzed along each grid row using the previously derived intersection data (Panel C). Grid point values of isentropic pressure are then obtained from the analyses at each row-column intersection (heavy crosses on short-dashed vertical projections).

In practice, the three-dimensional analysis is constructed starting at the earth's surface, continuing upward using a large number of individual isentropic surfaces spaced at 5K intervals, or isobaric surfaces spaced at 100 mb intervals. The method described earlier for simple horizontal analyses is employed in making analyses of surface parameters [pressure (P), temperature (T), potential temperature ($\theta$), height (Z), derived Montgomery stream function ($\psi_m = c_p T + gZ$), dew-point temperature ($T_d$), derived mixing ratio (q), wind direction and speed]. The same procedure is used to analyze pressure and mixing ratio on each isentropic surface or temperature and dew point on each isobaric surface.

In the 3-dimensional thermal analysis, several modifications must be made similar to those applied in 2-dimensional cross section analysis. In regions where a station's surface potential temperature is greater than that of the isentropic surface being analyzed (i.e., the isentropic surface is underground), vertical extrapolation is necessary. A hypothetical value of

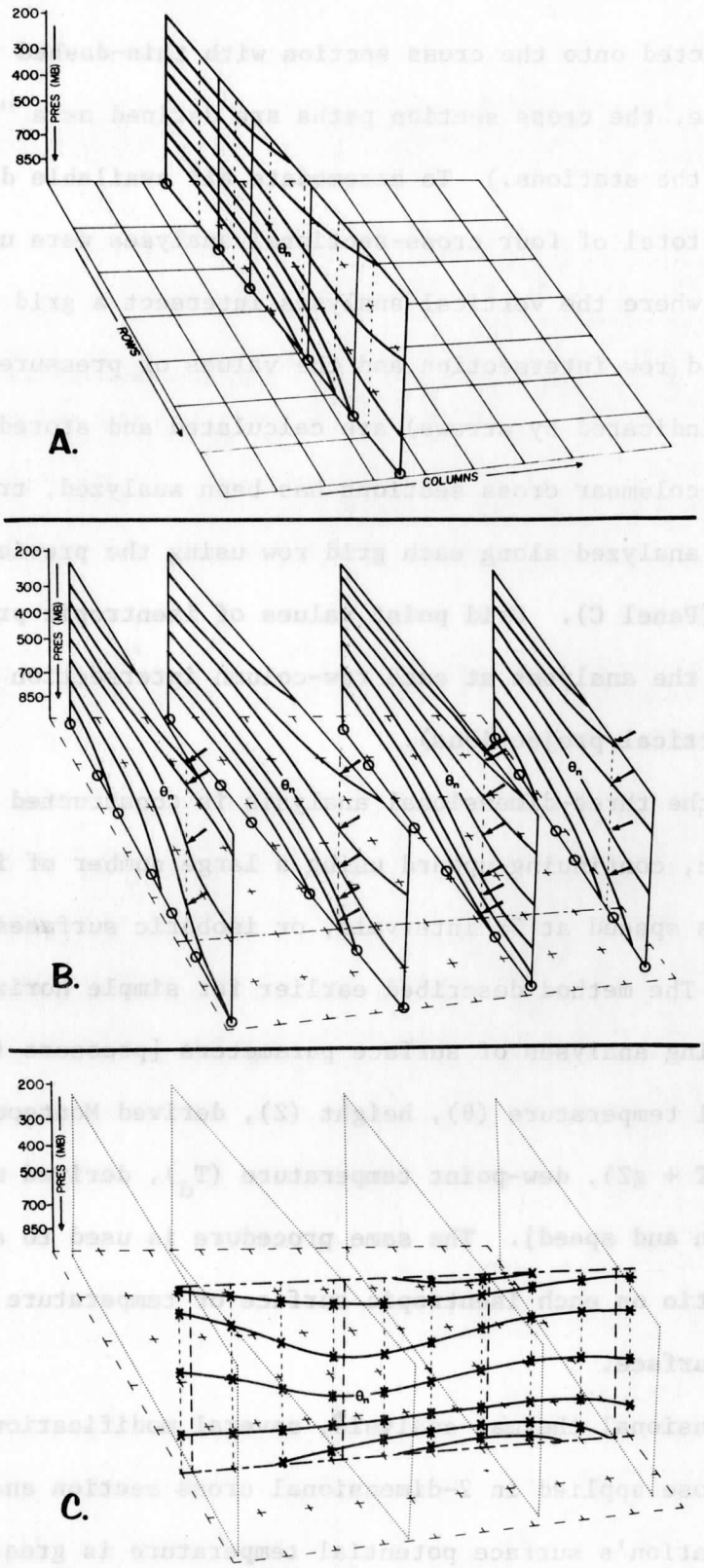


Fig. 3. Illustration of the 3-dimensionality of the isentropic analysis procedure. See text for detailed explanation.

isentropic pressure for that level ($P_{\theta_L}$) is defined by

$$P_{\theta_L} = P_{\theta_K} - [(\theta_K - \theta_L)\ (P_{\theta_K} - P_{\theta_S})/(\theta_K - \theta_S)]$$

where $\theta_S$ is the surface potential temperature and $\theta_K$ is the potential temperature of the first isentropic analysis level above ground. Further, the hypothetical static stability ($\Delta P/\Delta\theta$) in the layer extending underground is constrained within the range -4 to -40 mb $°K^{-1}$, and $P_{\theta_L} - P_{\theta_S}$ is limited to 200 mb. These conditions allow isentropic surfaces to enter the ground and preserve surface frontal structure, while limiting the influences of local low-level diurnal effects. (Equivalent extrapolations are made for isobaric analyses, where 100 mb increments are normally used in the vertical.) Finally, to insure that the area covered by the gridded analysis includes the stations at the ends of each cross section, bogus observations, obtained by linear extrapolation of data from the first-two and last-two cross section stations, are positioned 1.05 grid units beyond the normal limits of the individual sections. This modification is necessary if the wind observations made at the cross section termini are to be used in the final wind analysis procedure.

Once gridded values of isentropic pressure are available for a level, checks are made to reinstate the surface pressure in regions where the isentropic surface is underground. To make sure that superadiabatic conditions do not occur, i.e., that $\Delta P/\Delta\theta < 0$ mb $°K^{-1}$, gridded pressure values for the isentropic level are compared with those for the level immediately below. If either the upper surface is above ground and $\Delta P/\Delta\theta \geq 0$ mb $°K^{-1}$, or if both surfaces are above ground and $\Delta P/\Delta\theta \geq -1$ mb $°K^{-1}$, the pressure of the upper surface is assigned a value 5 mb less than that of the lower surface. A very light filter (coefficients 1.0, 1.5, 1.0) is then applied to obtain the final gridded fields.

The next step is to compute hydrostatically, non-surface grid point values of Montgomery stream function, $\psi_m$ , for isentropic analyses, or geopotential height for isobaric analyses, using surface fields and the appropriate thermal fields. The Montgomery stream function is found using,

$$\psi_{m_{L+1}} = \psi_{m_L} + c_p * \Delta\theta * \overline{P_\theta^\kappa} \, /1000^\kappa$$

where $c_p$ is the specific heat for dry air at constant pressure, $\overline{P_\theta}$ is the mean pressure between isentropic levels L and L+1, $\kappa = R_d/c_p$ and $\Delta\theta$ is the potential temperature difference between this isentropic surface and the one immediately below it (5K, or less if the next lowest surface is the ground). Although the effects of moisture on the constant $c_p$ were not included in the figures shown here, the computations of $\psi_m$ should provide such a modification. The present isobaric analyses procedure performs the vertical integration using

$$Z_{L+1} = Z_L + \frac{R_d \bar{T}^*}{g} \ln (P_L/P_{L+1})$$

where $\bar{T}^*$ represents the mean virtual temperature in the layer between $P_{L+1}$ and $P_L$ .

Geostrophic wind estimates are then obtained using 3-point central differences on the interior of the grid and 2-point forward/backward differences along the grid limits. The geostrophic components are then interpolated bilinearly back to the location of each observation. Estimates of the ageostrophic speed departure, $\vec{V}_{ag} = |\vec{V}| - |\vec{V}_g|$, and the normalized ageostrophic components, $u^*_{ag} = (u-ug)/|\vec{V}_g|$ and $V^*_{ag} = (\vec{V}-\vec{V}_g)/|\vec{V}_g|$, are calculated and interpolated back to the grid using the same cubic polynomial scheme described previously. (If a wind measurement terminated prematurely, the ageostrophic estimates from the last observed level are used.) These gridded values of

$\vec{V}_{ag}$ are then added to the geostrophic speed computations to obtain the final isotach analysis, while the unnormalized ageostrophic components provide the necessary corrections to the gridded wind direction values.

## III. Preliminary Results

The sample analyses shown in this section were obtained using a total of 21 cross sections, connecting all North American radiosonde stations between approximately 20°N and 75°N latitude (Fig. 4). Since data are often missing from some radiosonde stations, accomodations were made wherever possible to include alternate stations along the cross sections. In all cases, a 2° x 2° latitude-longitude grid was used, extending from 130°W to 60°W and from 62°N to 20°N.

The case chosen used radiosonde data obtained at 1200 GMT 3 April 1974 and 0000 GMT 4 April 1974. Since analyses of this case have been discussed by other authors, no detailed synoptic description is given here. Rather, a few of the salient features of various analyses will be noted. The reader is urged to compare the analyses shown here with analyses available from various other sources such as Hoxit & Chappel (1975).

To aid in evaluating the analyses shown for the 1200 GMT time period, the vertical isentropic cross sections which form the basis for the various quasi-horizontal analyses are shown in Figs. 5 through 11. (Each cross-section is labelled according to Fig. 4, and the last three digits of each station identifier are given.) The horizontal analyses obtained at the surface and at selected isobaric and isentropic levels are shown in Figs. 12 through 21.

Rather than examining in detail all of the many analyses shown, only two sets will be discussed here. Consider for example the analyses for the

500 mb and 315 K surfaces (Figs. 15 & 19). The amount of spatial consistency inherent in this one pass technique is immediately apparent in the analyses, especially considering that only one pass of a very light filter was applied at each level. At the same time, the degree of detail and strength of gradients observed in the analyses, particularly in the baroclinic zone indicated in the 500 mb temperature field over the Southwest United States, equals that found in most subjective analyses. The quality of the height and Montgomery stream function analyses is further evidenced by the continuity present in both the derived geostrophic wind field (speeds and streamlines), as well as the thermally enhanced observed wind analyses. Not only do these analyses maintain the "elongated" nature of the jet streak, but the degree of horizontal shear observed between individual stations is preserved to an extremely high degree. Note for example, the observed wind analyses in the vicinity of Monet, Missouri (72349). The extreme horizontal shear observed between stations in this region is also evident in the cross section analysis shown in Fig. 17R.

Further study of the remaining figures for this time period and for 0000 GMT 4 April 1974 (Figs. 22-31) verify the degree of detail and amount of continuity present among the various analyses. Of additional importance to future applications of the technique, however, are the computer requirements needed for the execution of the analysis programs. For one time period, a full set of 172 analyses, both isentropic (23 levels) and isobaric (10 levels), were generated for a 792 point grid at a cost of less than $6.00 on the Univac 1110, using less than 36K words of core storage. Figures such as these support the utility of this system to problems where detailed, yet efficient and inexpensive, analyses are desired.

## IV. Future Considerations

While the examples shown in the previous section indicate the potential of this cross-section approach to 3-dimensional objective analysis in regions of abundant data, further studies and modifications must be made to verify its full merit. Cursory computations of divergence and vorticity obtained from the analyses shown were within reason. Computations of the isentropic mass budget statistics (Johnson and Downey, 1976), also showed improvement over results obtained from a one-pass empirical method. However, several modifications are planned. For example, an improved final wind field analysis might be achieved with a more realistic approximation to the wind/mass balance (e.g., gradient balance or N.M.C. balance [Schuman, 1957]). Some degree of filtering may be necessary in the interpolated wind corrections. In addition, since many features of atmospheric flow are represented more continuously in the isentropic framework, improvements in the isobaric analyses are anticipated once modifications have been implemented which extract pressure level data by vertical interpolation between a full set of isentropic analyses.

Before any final evaluation of the analysis technique can be made, however, the scheme must be tested on a large number of cases to isolate areas needing further improvement. These analyses must be subjected to quantitative comparisons with other subjective and objective analyses. Only after more experience is gained using the technique and statistical and practical evaluations have been made, will the full merit of this cross-sectionally based method be known.

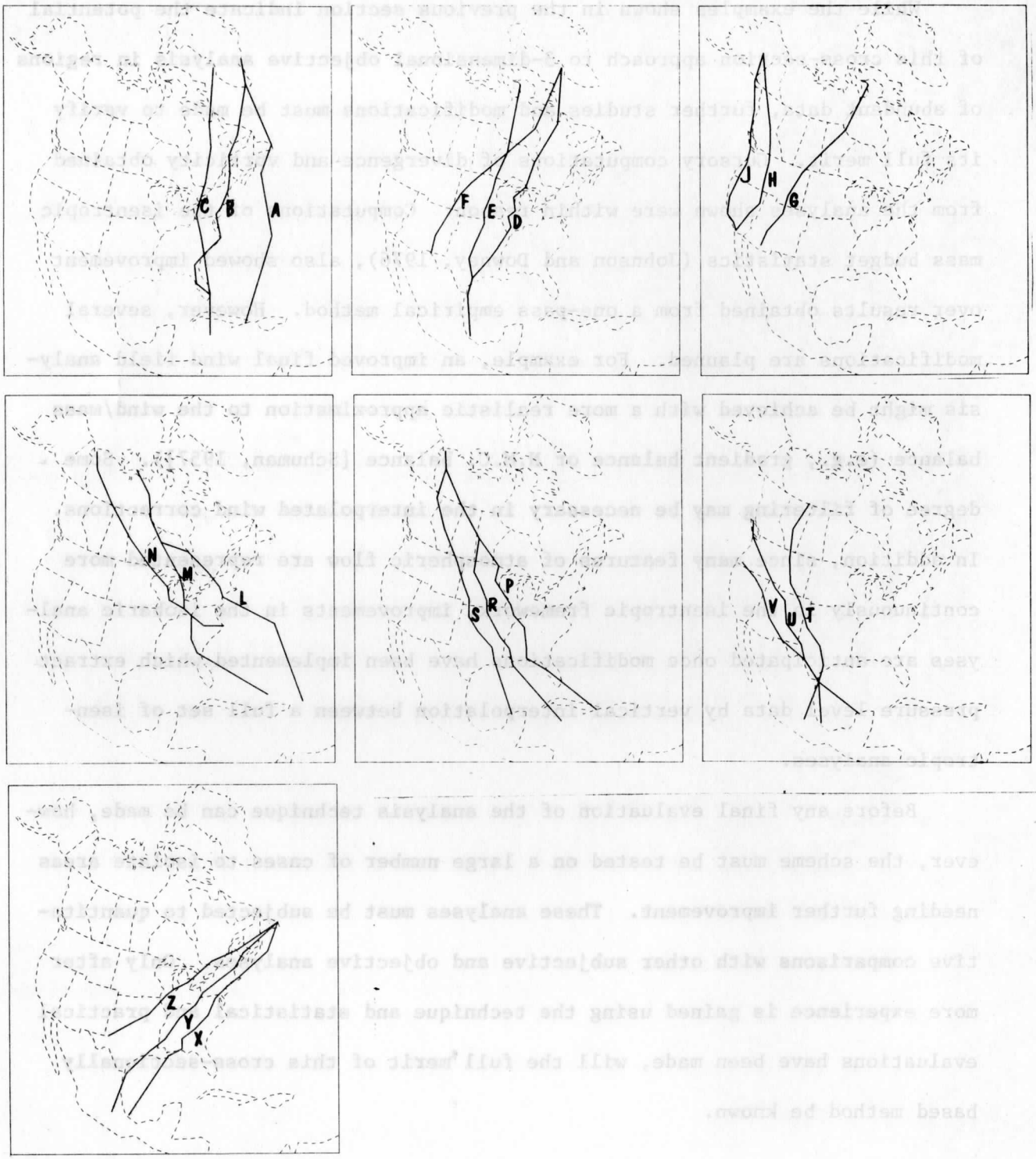


Fig. 4. Paths of 21 cross-sections used to obtain quasi-horizontal analyses from North American radiosonde stations.

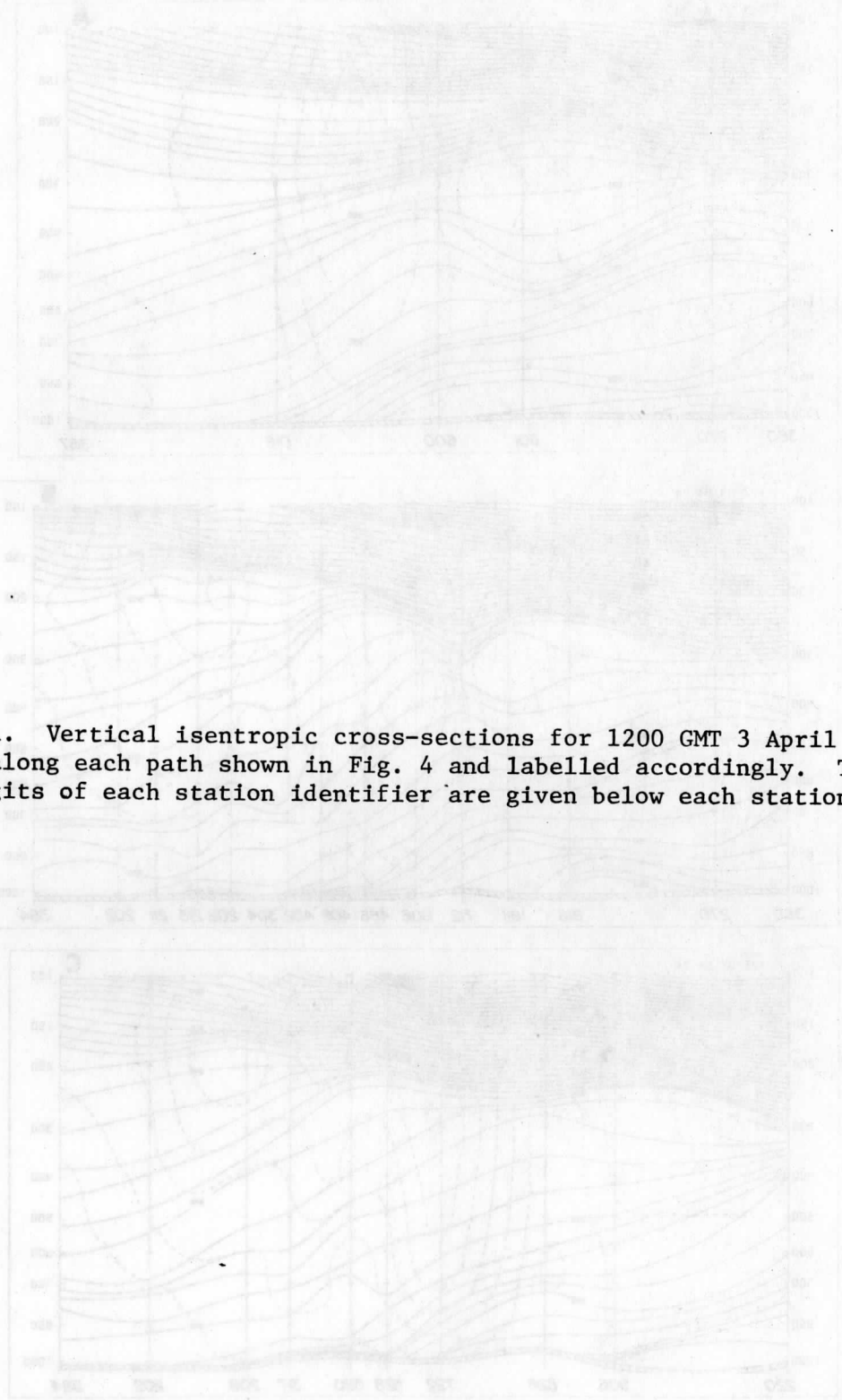

Figs. 5-11. Vertical isentropic cross-sections for 1200 GMT 3 April 1974 obtained along each path shown in Fig. 4 and labelled accordingly. The last 3 digits of each station identifier are given below each station.

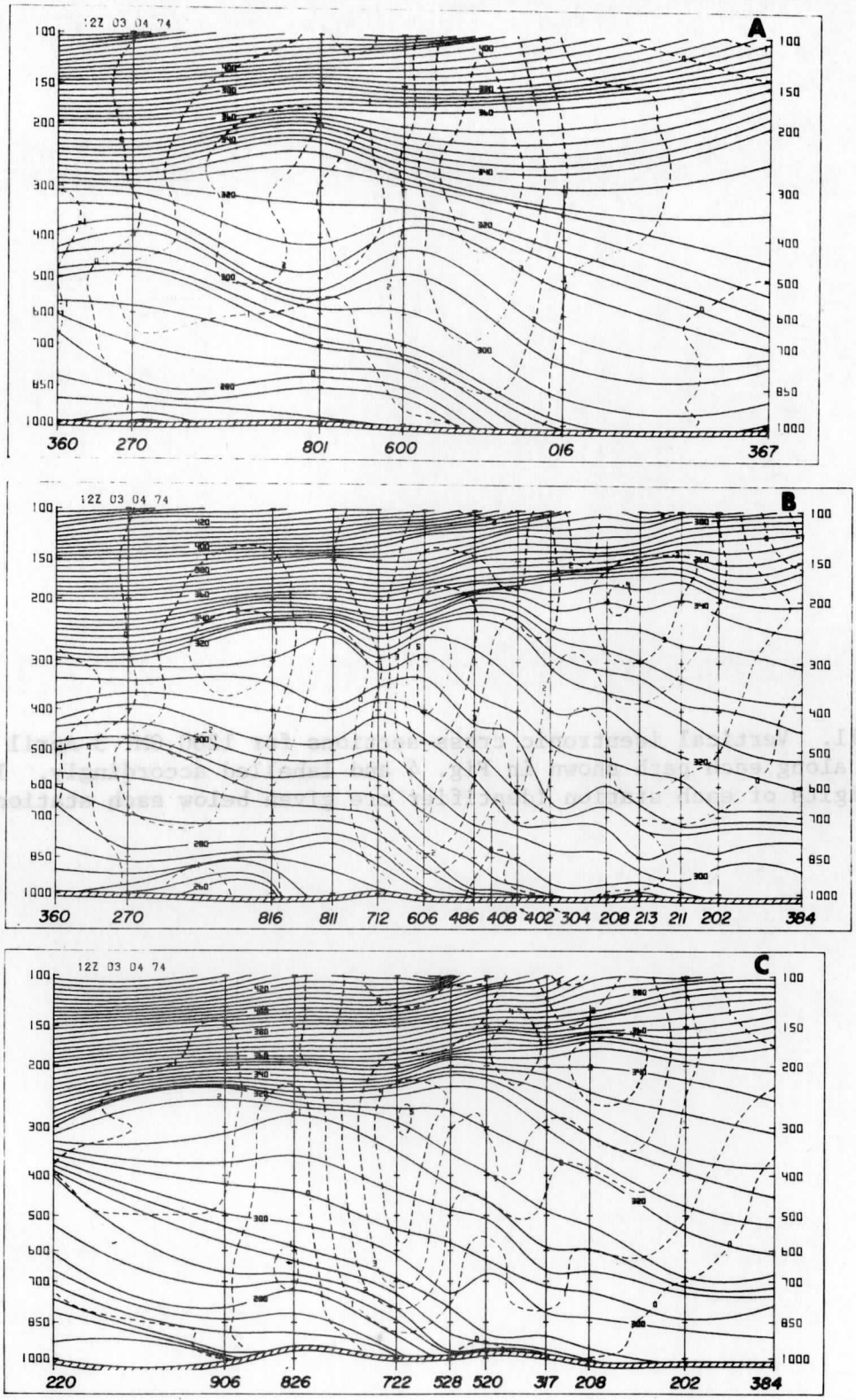
12Z 03 04 74
A
100
150
200
300
400
500
600
700
850
1000
360 270 801 600 016 367
12Z 03 04 74
B
360 270 816 811 712 606 486 408 402 304 208 213 211 202 384
12Z 03 04 74
C
220 906 826 722 528 520 317 208 202 384

FIG. 5

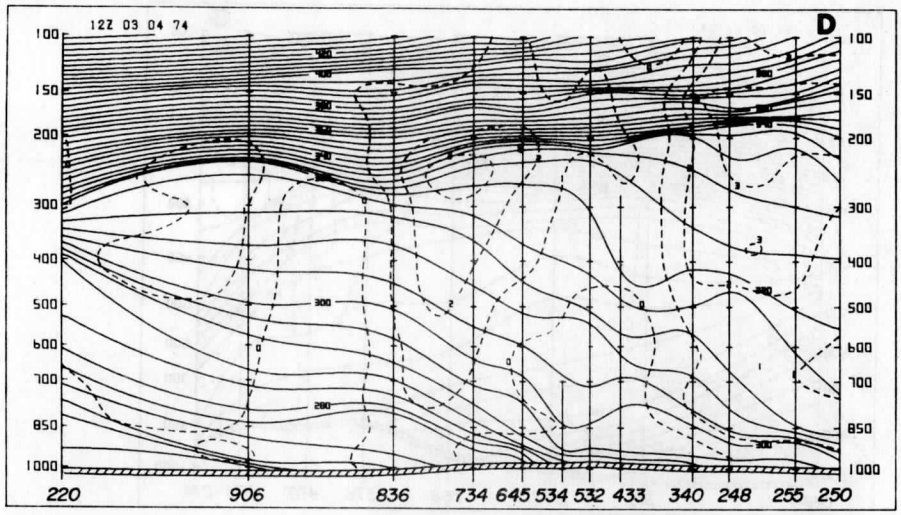
12Z 03 04 74
D
100
150
200
300
400
500
600
700
850
1000
220
906
836
734 645 534 532 433
340 248 255 250

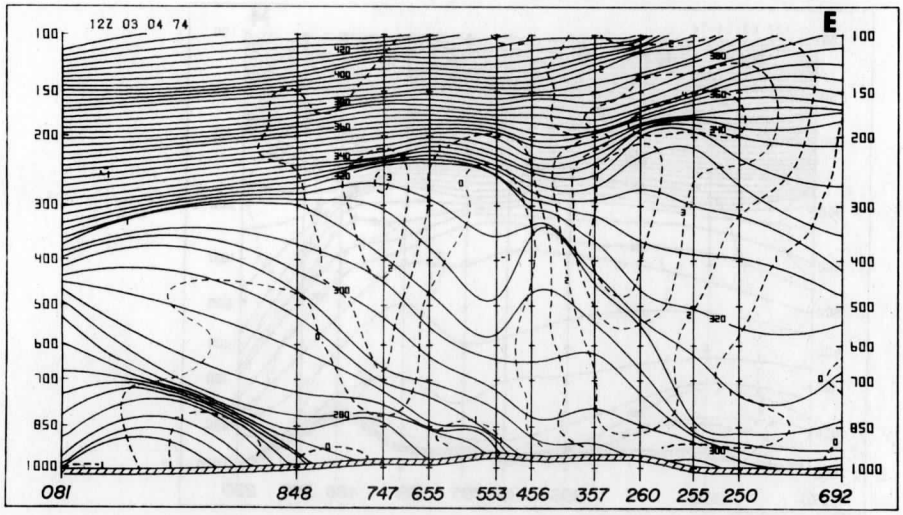
12Z 03 04 74
E
100
150
200
300
400
500
600
700
850
1000
081
848
747 655
553 456
357 260 255 250
692

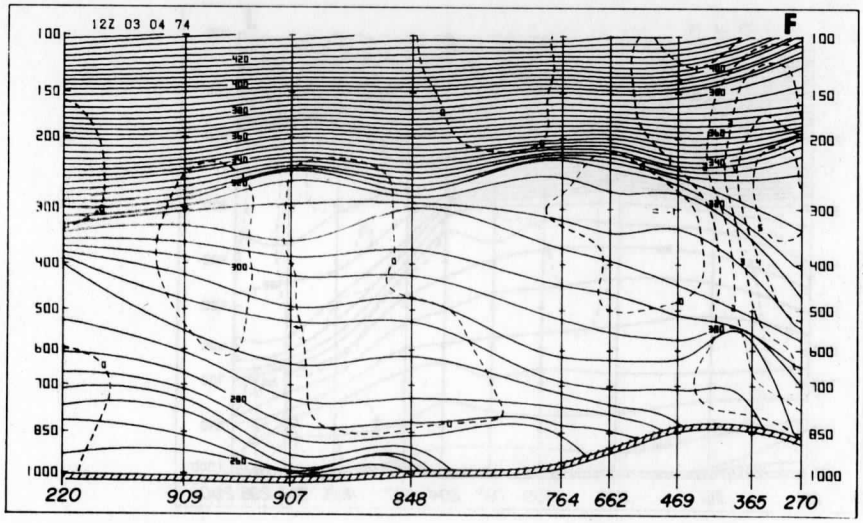
12Z 03 04 74
F
100
150
200
300
400
500
600
700
850
1000
220
909
907
848
764 662
469
365 270

FIG. 6

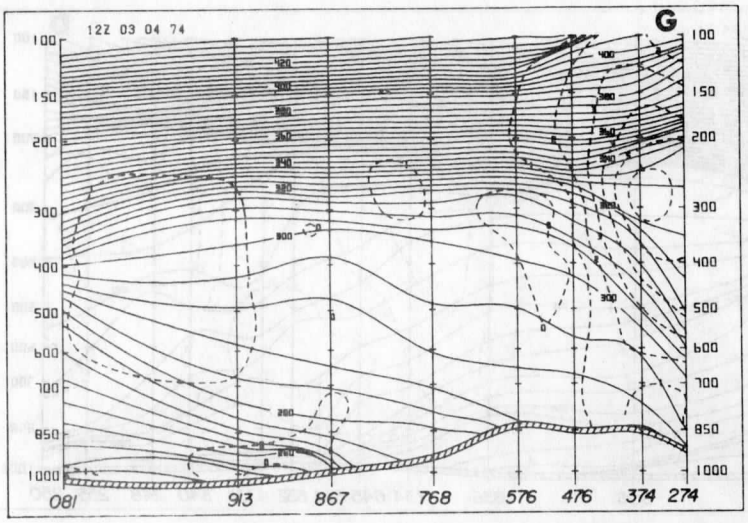
12Z 03 04 74
G
100
150
200
300
400
500
600
700
850
1000
081
913
867
768
576
476
374
274

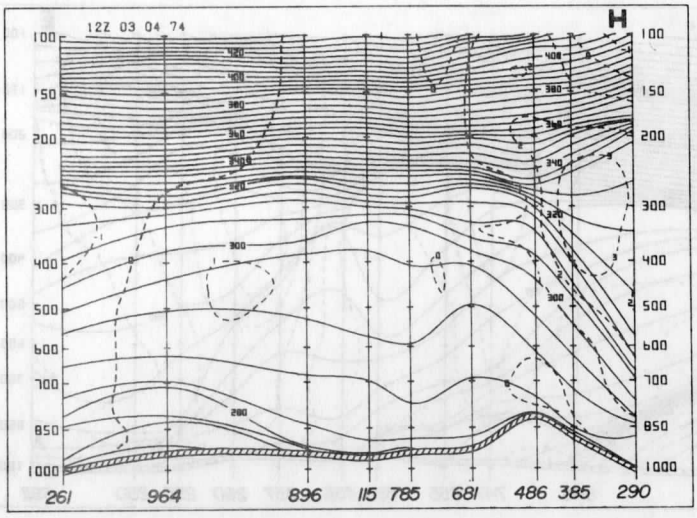
12Z 03 04 74
H
100
150
200
300
400
500
600
700
850
1000
261
964
896
115
785
681
486
385
290

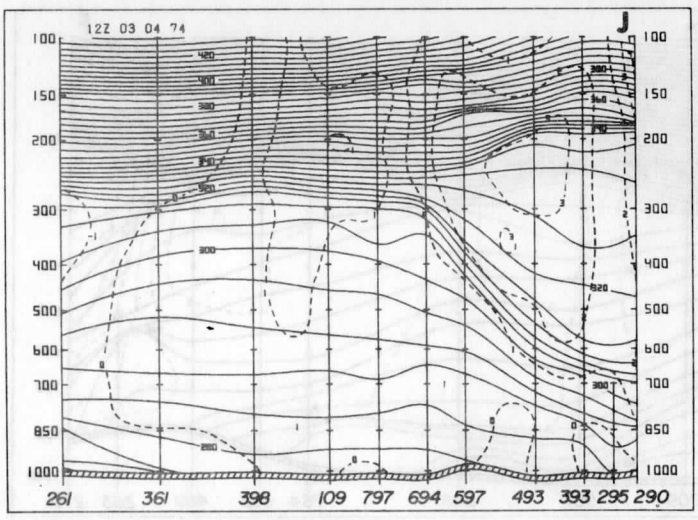
12Z 03 04 74
J
100
150
200
300
400
500
600
700
850
1000
261
361
398
109
797
694
597
493
393
295
290

FIG. 7

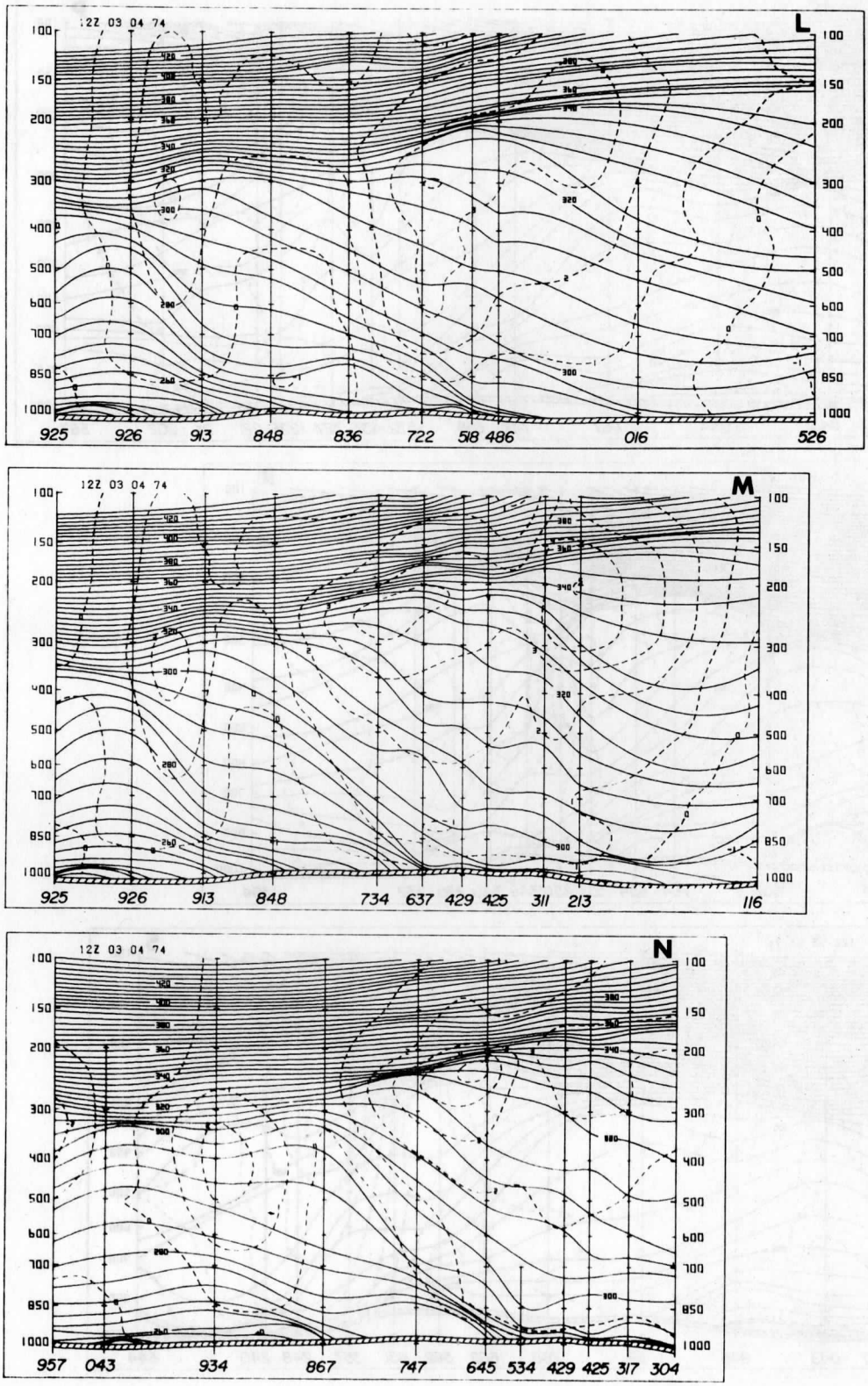
12Z 03 04 74
L
925 926 913 848 836 722 518 486 016 526
12Z 03 04 74
M
925 926 913 848 734 637 429 425 311 213 116
12Z 03 04 74
N
957 043 934 867 747 645 534 429 425 317 304

FIG. 8

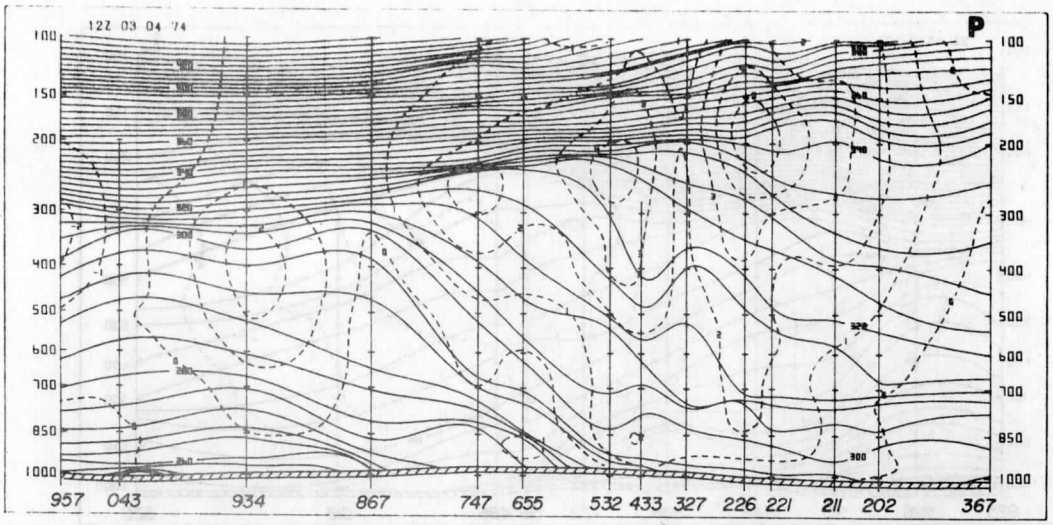
12Z 03 04 74
P
100
150
200
300
400
500
600
700
850
1000
957 043 934 867 747 655 532 433 327 226 221 211 202 367

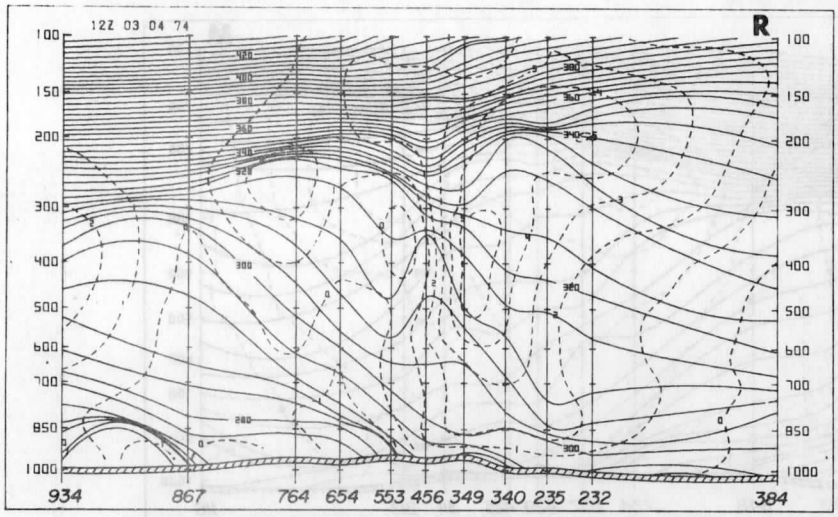
12Z 03 04 74
R
100
150
200
300
400
500
600
700
850
1000
934 867 764 654 553 456 349 340 235 232 384

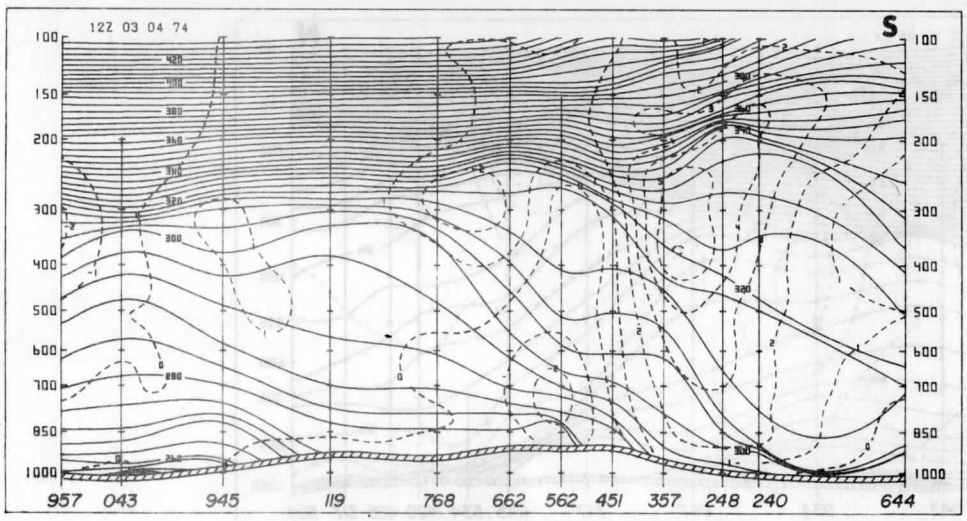
12Z 03 04 74
S
100
150
200
300
400
500
600
700
850
1000
957 043 945 119 768 662 562 451 357 248 240 644

FIG. 9

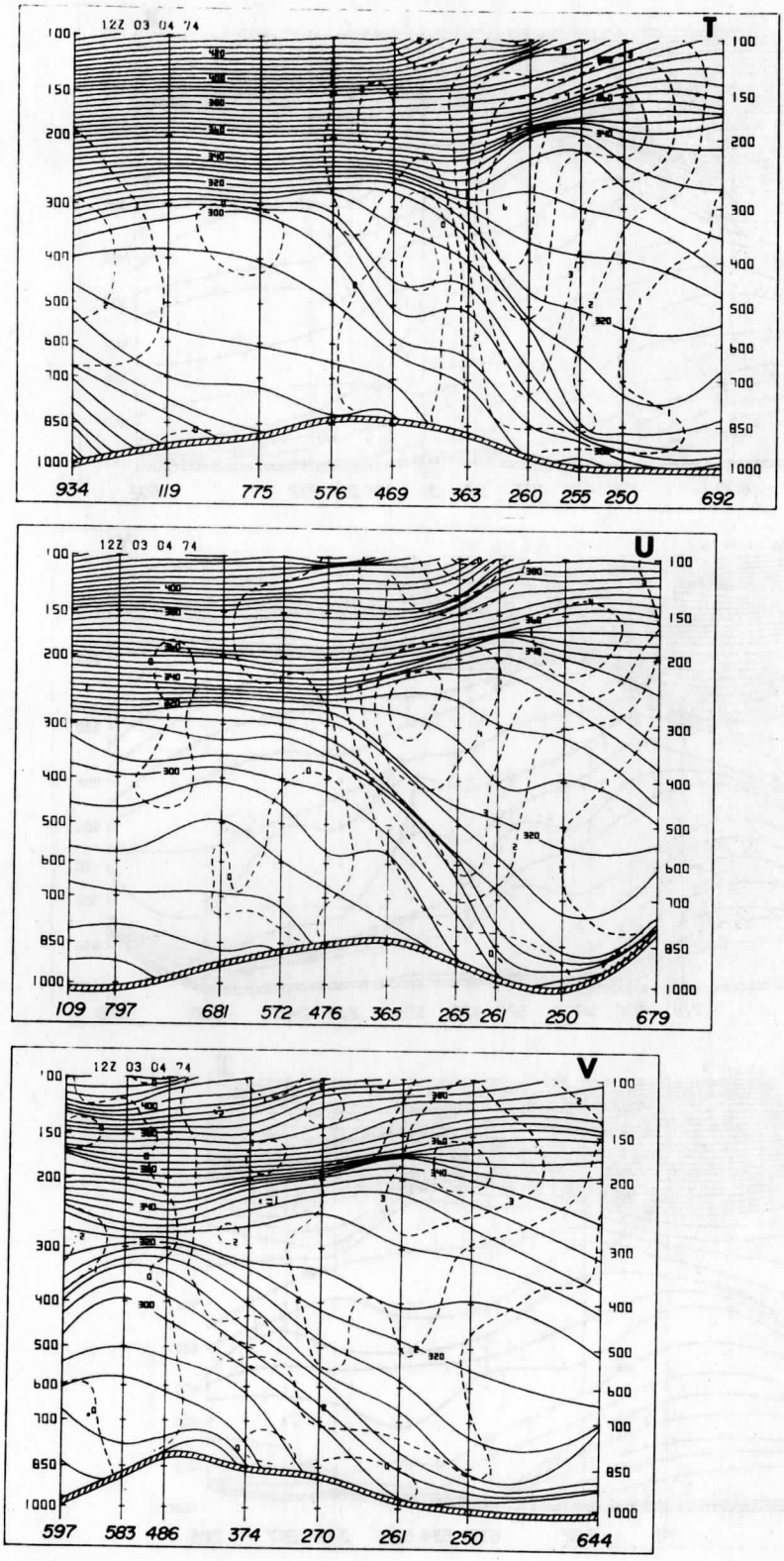
12Z 03 04 74
T
100
150
200
300
400
500
600
700
850
1000
934 119 775 576 469 363 260 255 250 692
12Z 03 04 74
U
109 797 681 572 476 365 265 261 250 679
12Z 03 04 74
V
597 583 486 374 270 261 250 644

FIG. 10

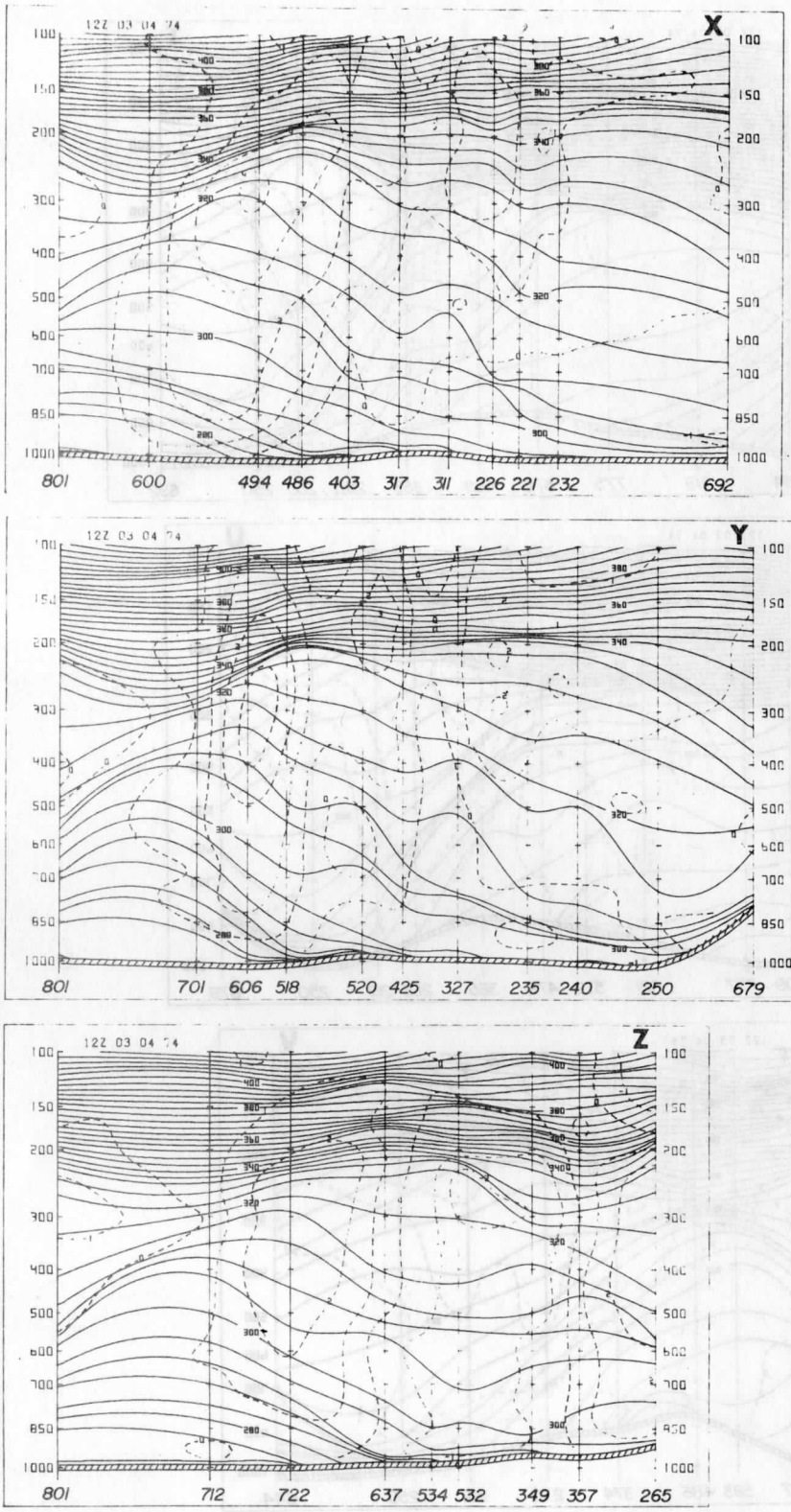
12Z 03 04 74
X
100
150
200
300
400
500
600
700
850
1000
801
600
494 486 403 317 311 226 221 232
692
12Z 03 04 74
Y
801
701 606 518 520 425 327 235 240 250
679
12Z 03 04 74
Z
801
712 722 637 534 532 349 357 265

FIG. 11

Analyses obtained from the cross-sectionally based analysis scheme for 1200 GMT 3 April 1974

Fig. 12. Analyses of surface parameters. Surface height in decameters, pressure in centibars, wind speed in m $s^{-1}$, temperature and potential temperature in °K.

Fig. 13. Isobaric analyses at 900 mb. Temperature and dew point in °K, heights in decameters, geostrophic and observed (final enhanced) wind speeds in m $s^{-1}$.

Fig. 14. Same as Fig. 13 but at 700 mb.

Fig. 15. Same as Fig. 13 but at 500 mb.

Fig. 16. Same as Fig. 13 but at 300 mb.

Fig. 17. Isentropic analyses at 305 K. Pressure in centibars, stream function to be multiplied by $10^6 cm^2 s^{-2}$, mixing ratio in g/kg, geostrophic and observed (final enhanced) wind speeds in m $s^{-1}$.

Fig. 18. Same as Fig. 17 but for 315 K. No mixing ratio analysis shown.

Fig. 19. Same as Fig. 17 but for 325 K. No mixing ratio analysis shown.

Fig. 20. Mass ($\Delta P/10°K$) centered about various isentropic surfaces. Provides an indicator of inverse static stability. Units centibars/10°K.

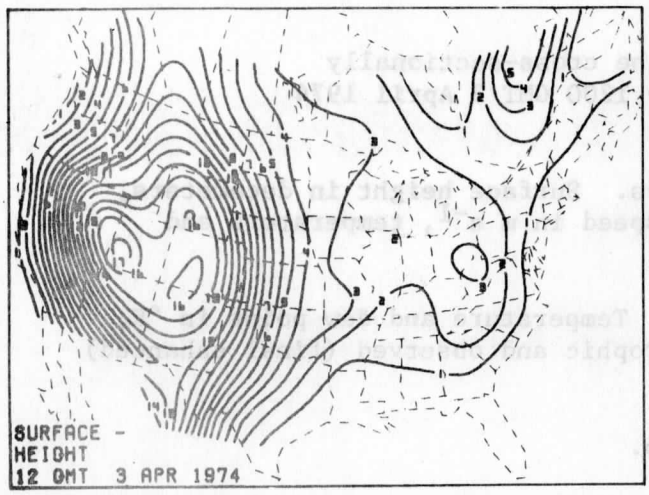
SURFACE -
HEIGHT
12 GMT 3 APR 1974

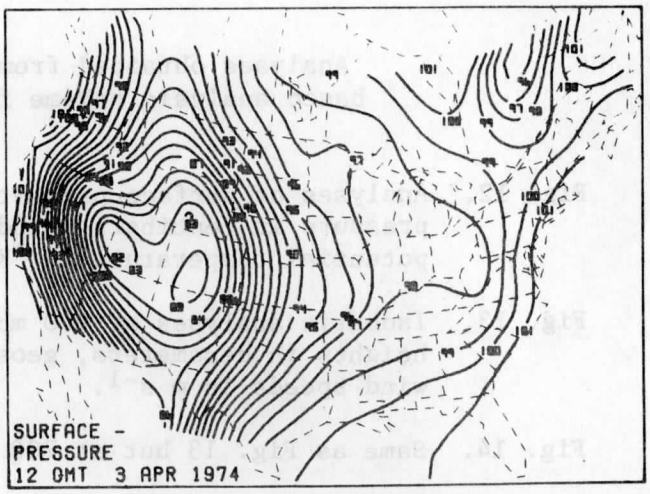
SURFACE -
PRESSURE
12 GMT 3 APR 1974

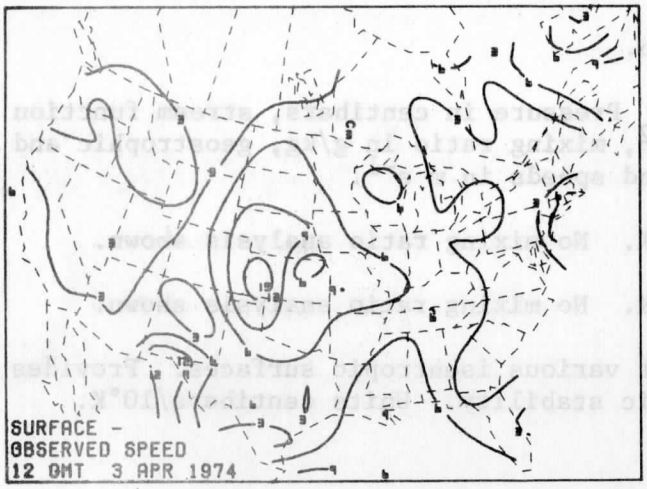
SURFACE -
OBSERVED SPEED
12 GMT 3 APR 1974

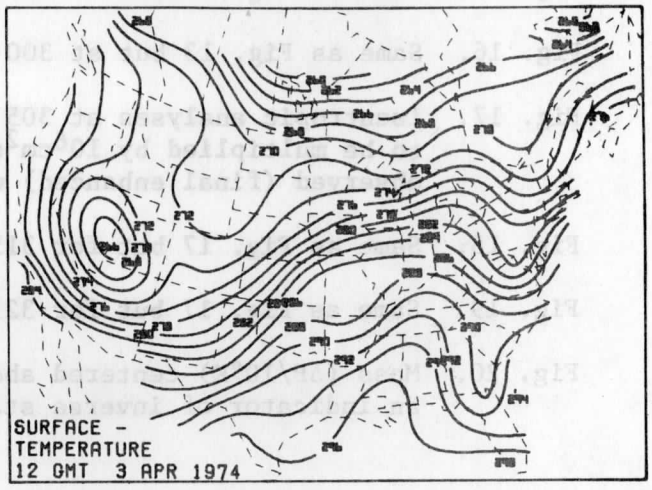
SURFACE -
TEMPERATURE
12 GMT 3 APR 1974

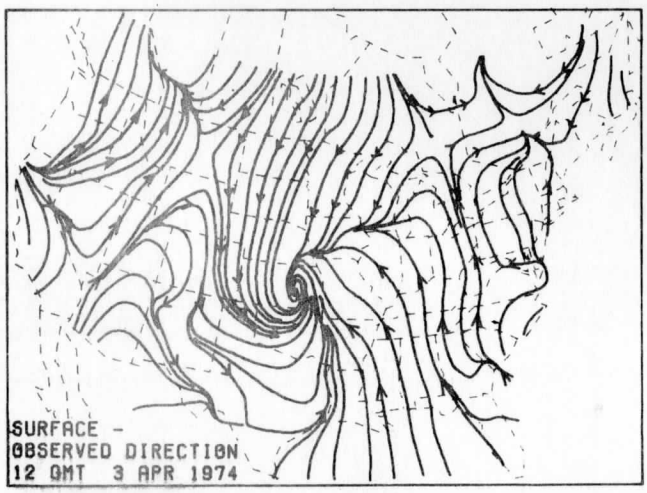
SURFACE -
OBSERVED DIRECTION
12 GMT 3 APR 1974

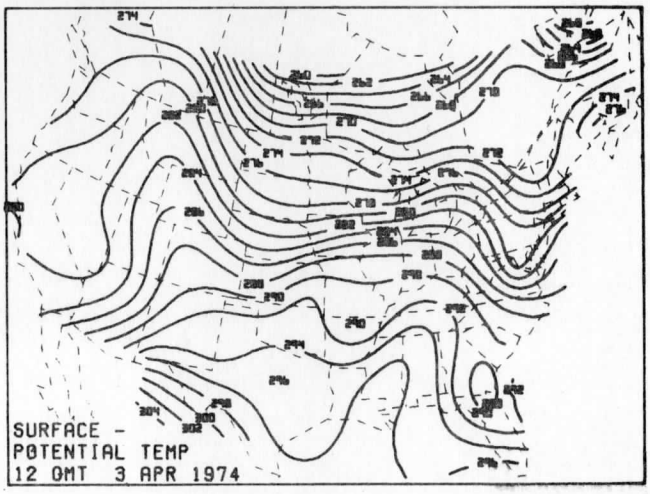
SURFACE -
POTENTIAL TEMP
12 GMT 3 APR 1974

FIG. 12

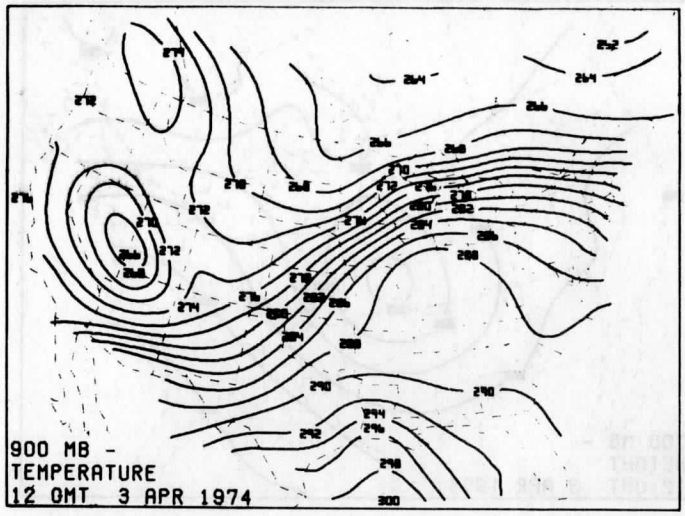
900 MB -
TEMPERATURE
12 GMT 3 APR 1974

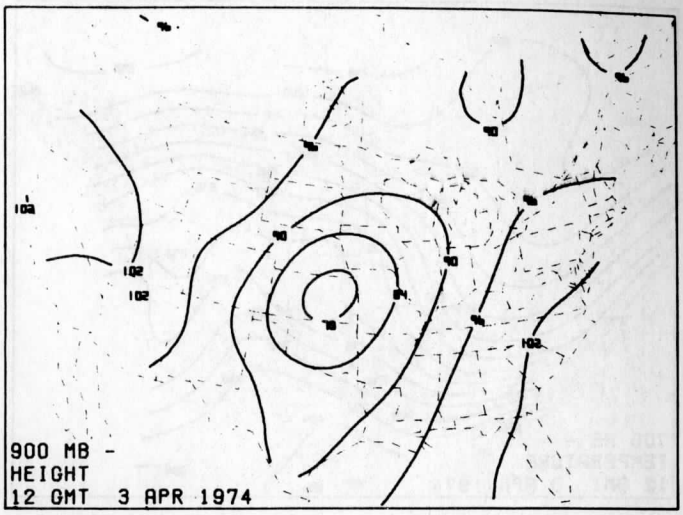
900 MB -
HEIGHT
12 GMT 3 APR 1974

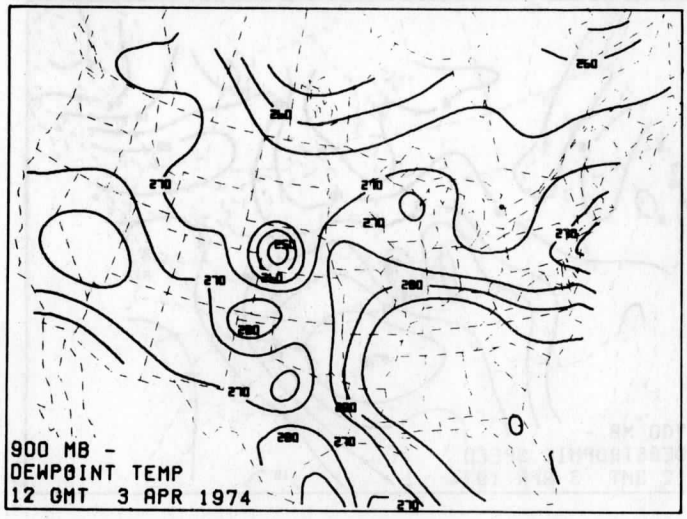
900 MB -
DEWPOINT TEMP
12 GMT 3 APR 1974

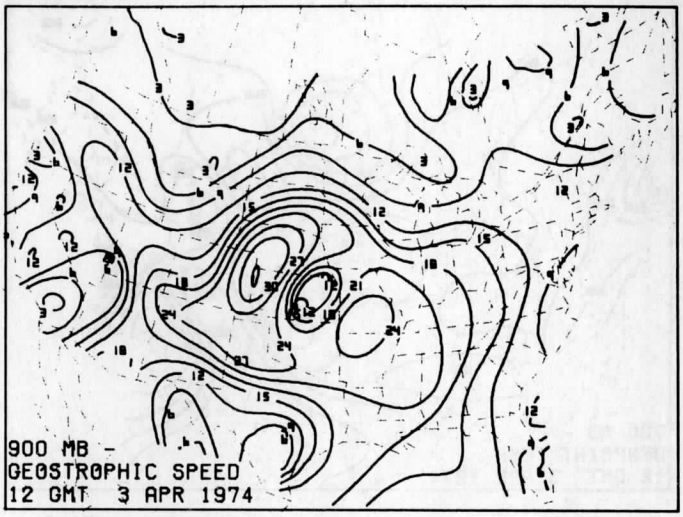
900 MB -
GEOSTROPHIC SPEED
12 GMT 3 APR 1974

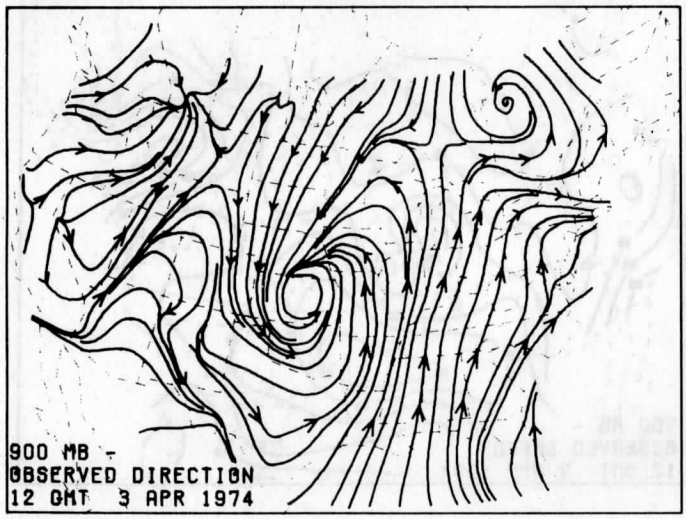
900 MB -
OBSERVED DIRECTION
12 GMT 3 APR 1974

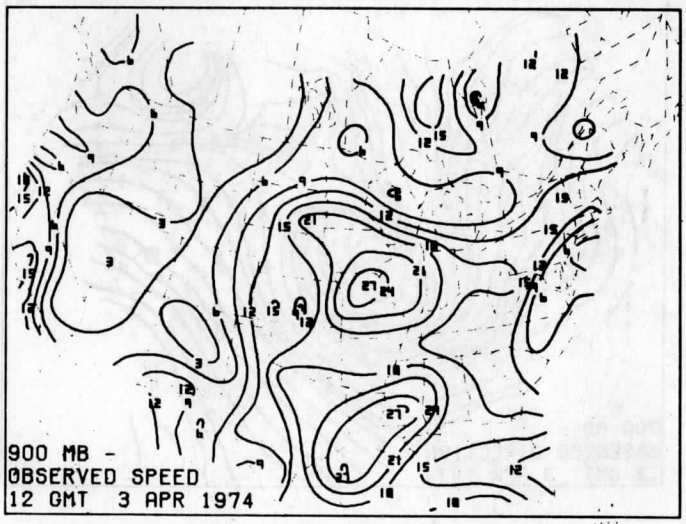
900 MB -
OBSERVED SPEED
12 GMT 3 APR 1974

FIG. 13

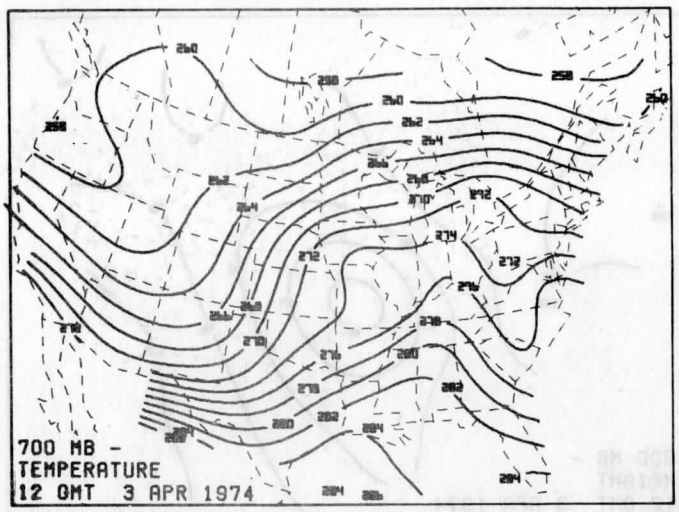
700 MB -
TEMPERATURE
12 GMT 3 APR 1974

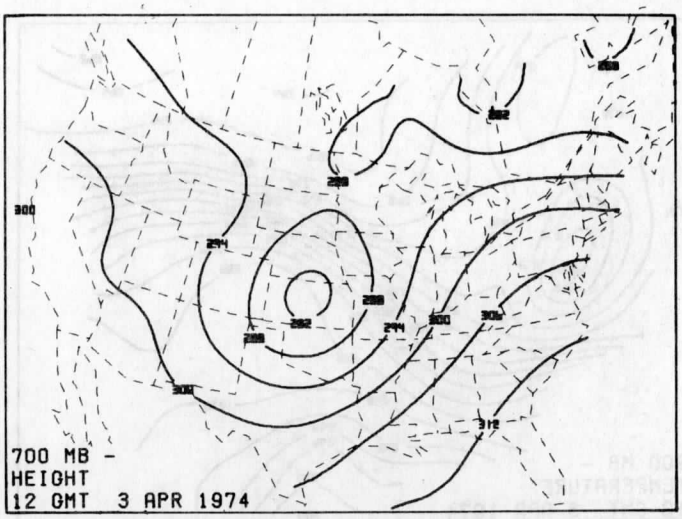
700 MB -
HEIGHT
12 GMT 3 APR 1974

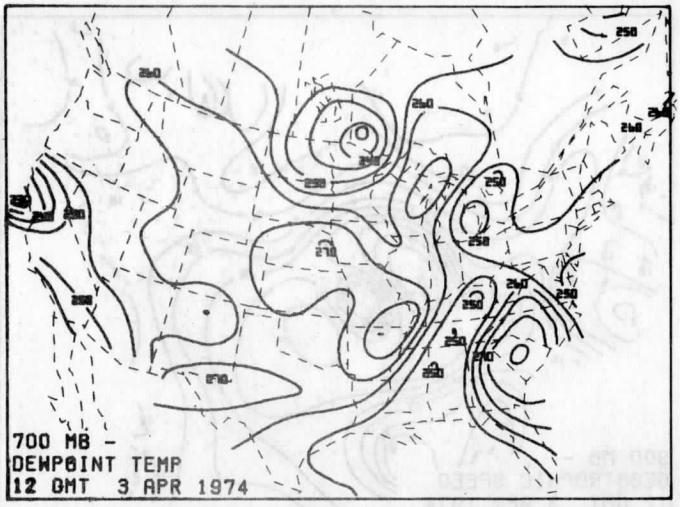
700 MB -
DEWPOINT TEMP
12 GMT 3 APR 1974

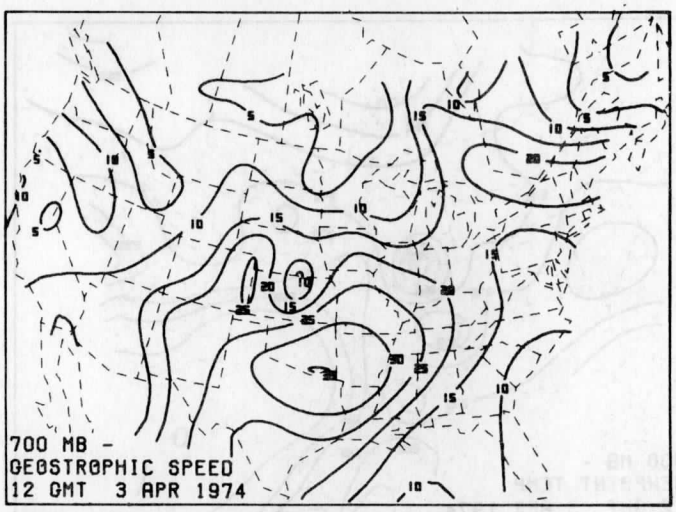
700 MB -
GEOSTROPHIC SPEED
12 GMT 3 APR 1974

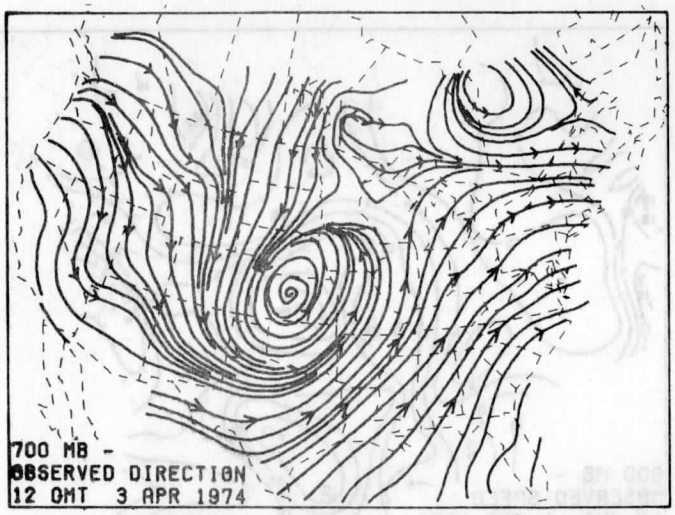
700 MB -
OBSERVED DIRECTION
12 GMT 3 APR 1974

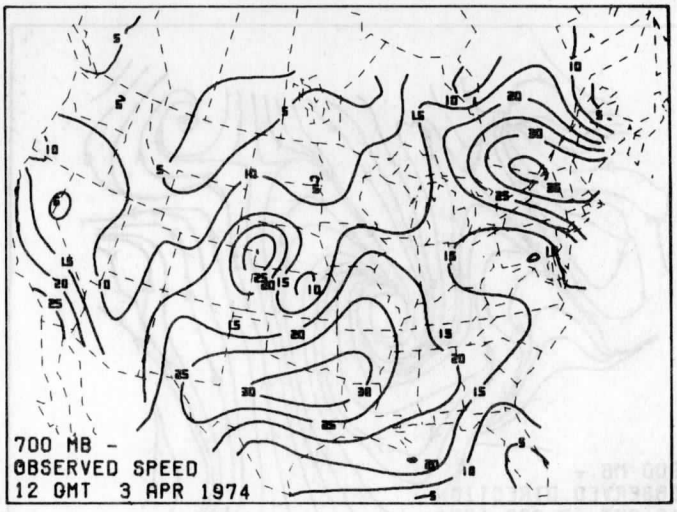
700 MB -
OBSERVED SPEED
12 GMT 3 APR 1974

FIG. 14

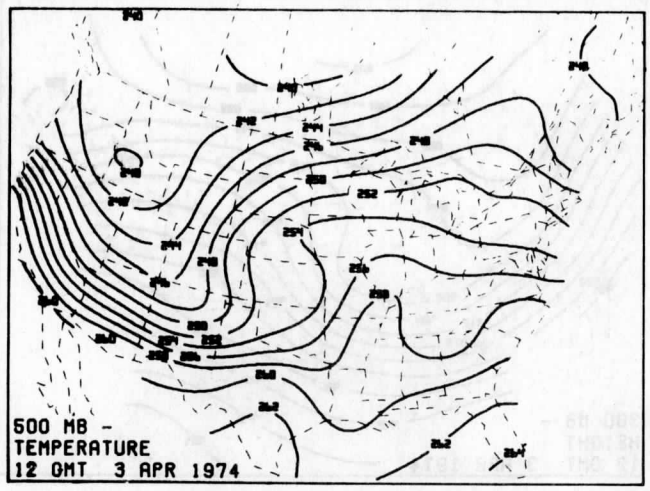
500 MB -
TEMPERATURE
12 GMT 3 APR 1974

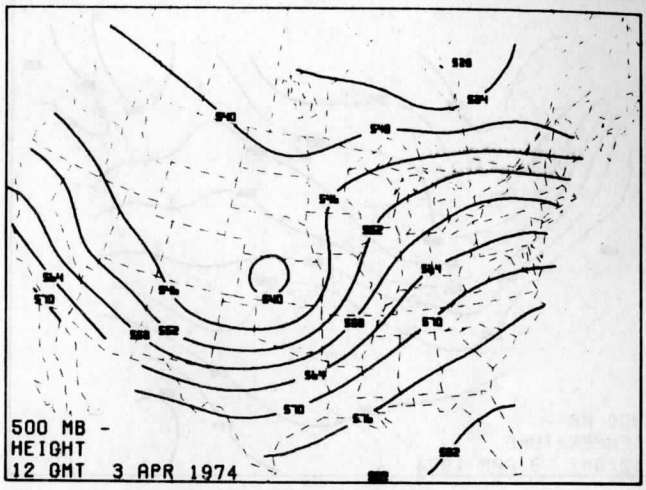
500 MB -
HEIGHT
12 GMT 3 APR 1974

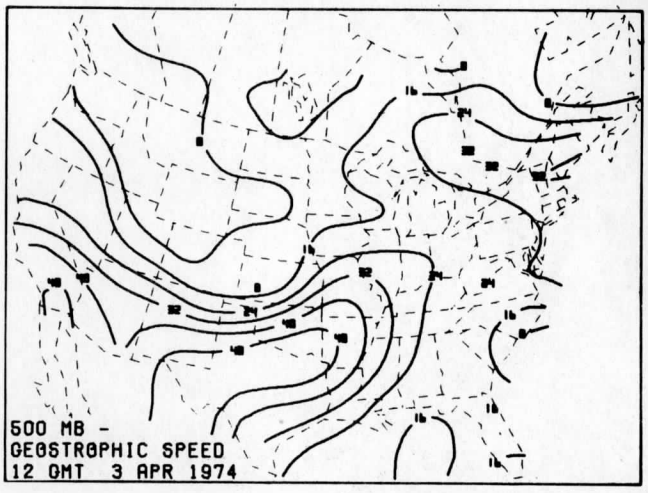
500 MB -
GEOSTROPHIC SPEED
12 GMT 3 APR 1974

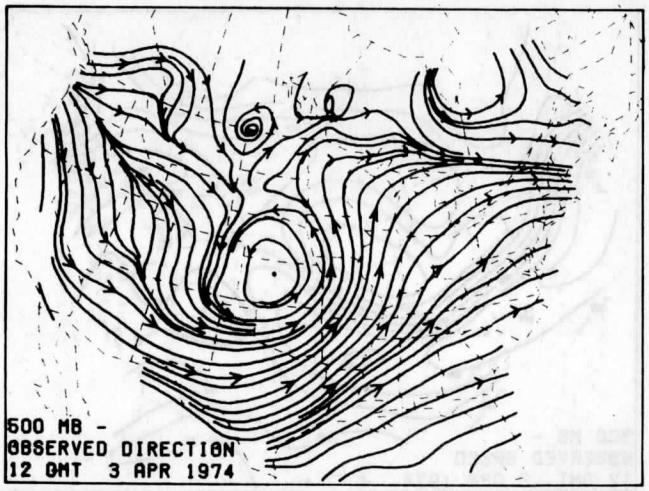
500 MB -
OBSERVED DIRECTION
12 GMT 3 APR 1974

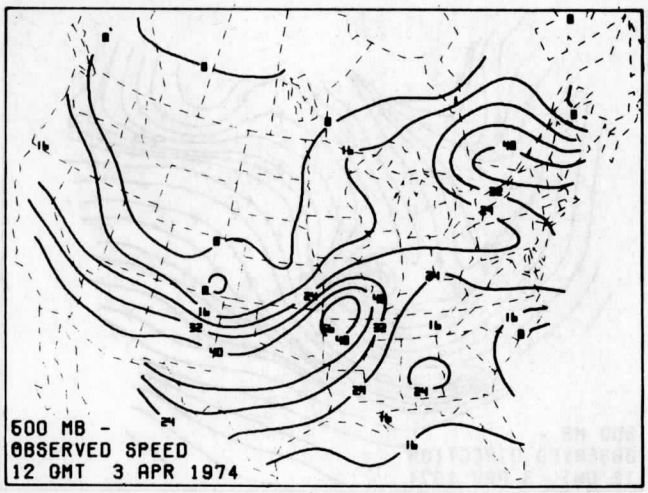
500 MB -
OBSERVED SPEED
12 GMT 3 APR 1974

FIG. 15

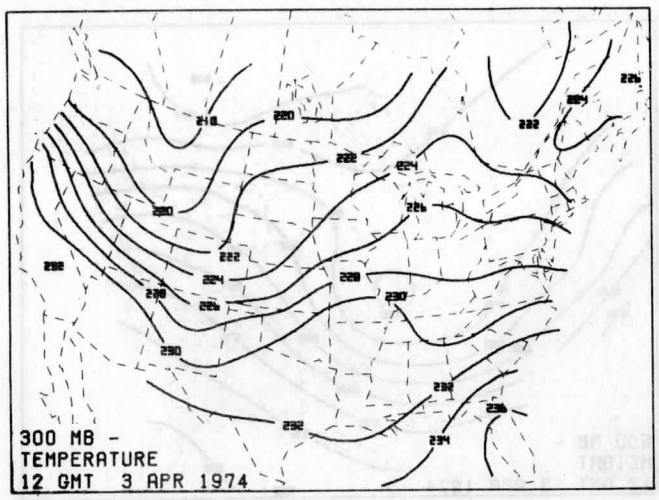
300 MB -
TEMPERATURE
12 GMT 3 APR 1974

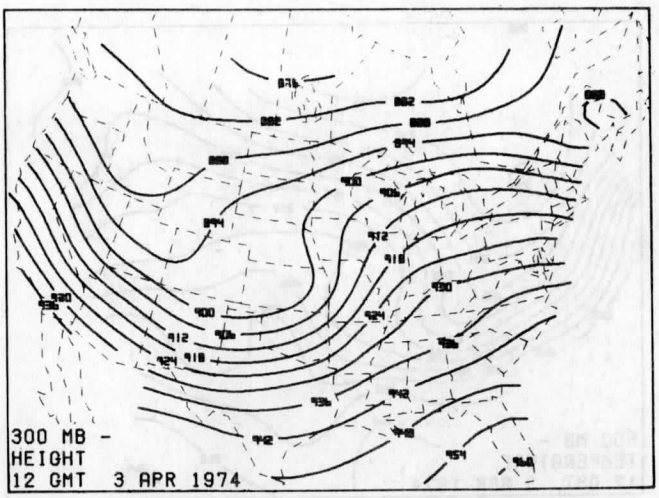
300 MB -
HEIGHT
12 GMT 3 APR 1974

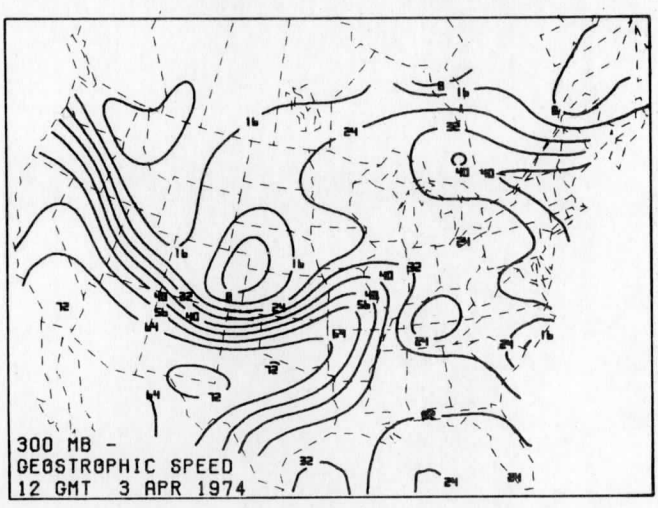
300 MB -
GEOSTROPHIC SPEED
12 GMT 3 APR 1974

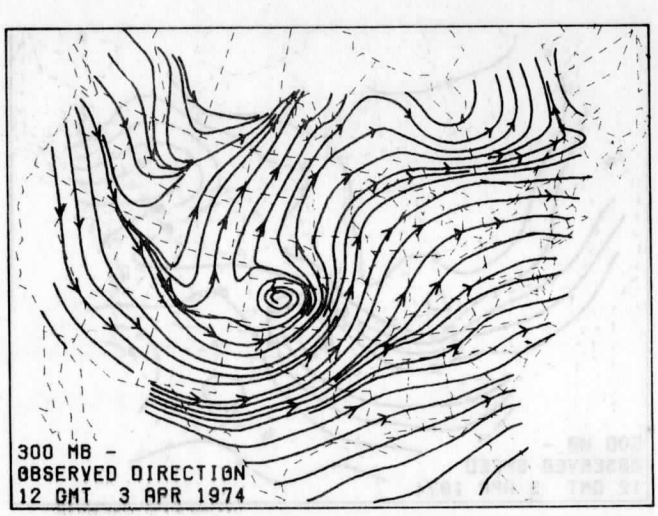
300 MB -
OBSERVED DIRECTION
12 GMT 3 APR 1974

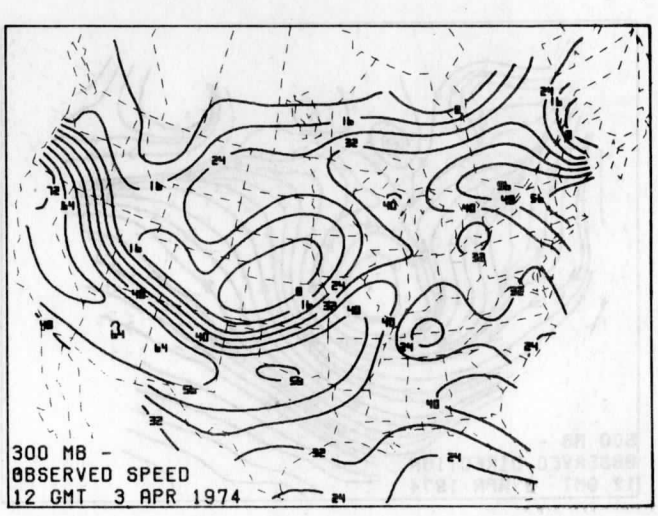
300 MB -
OBSERVED SPEED
12 GMT 3 APR 1974

FIG. 16

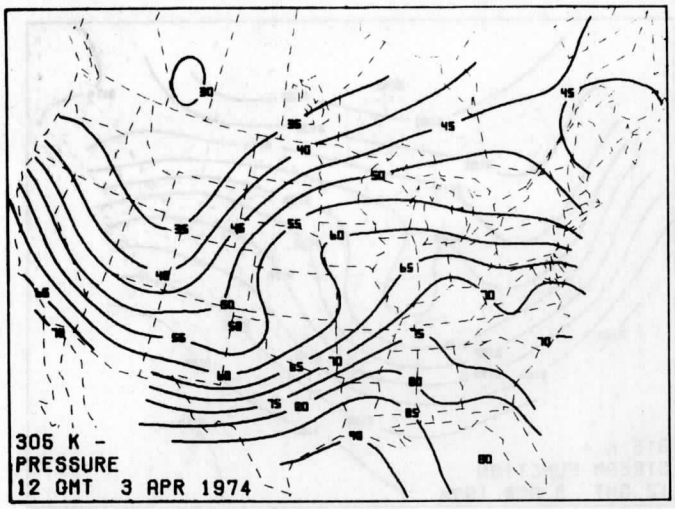
305 K -
PRESSURE
12 GMT 3 APR 1974

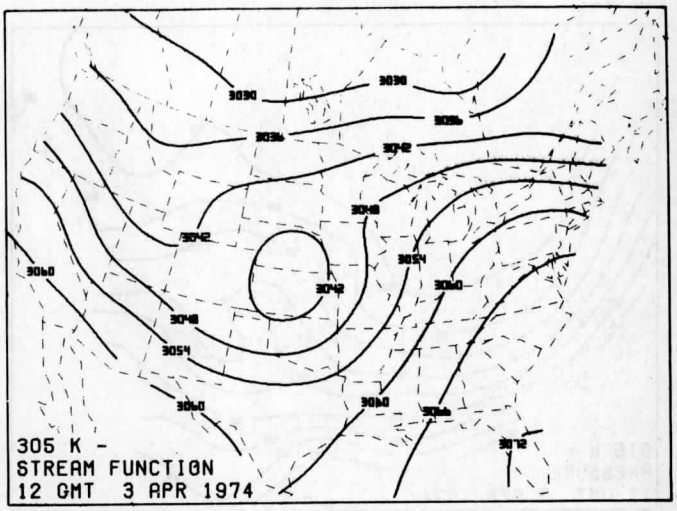
305 K -
STREAM FUNCTION
12 GMT 3 APR 1974

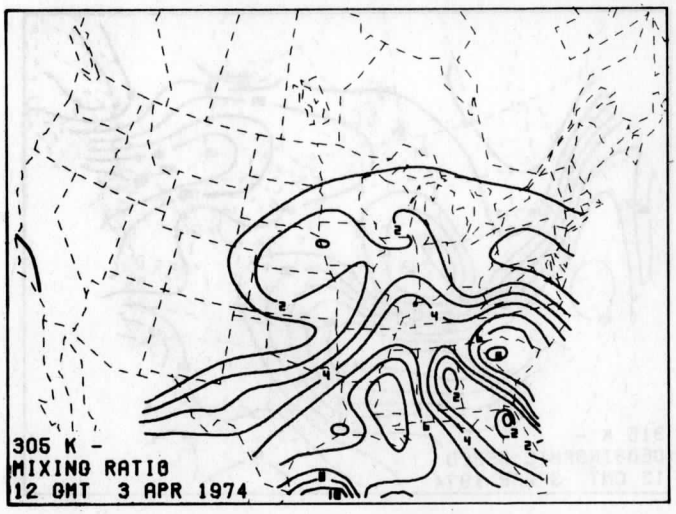
305 K -
MIXING RATIO
12 GMT 3 APR 1974

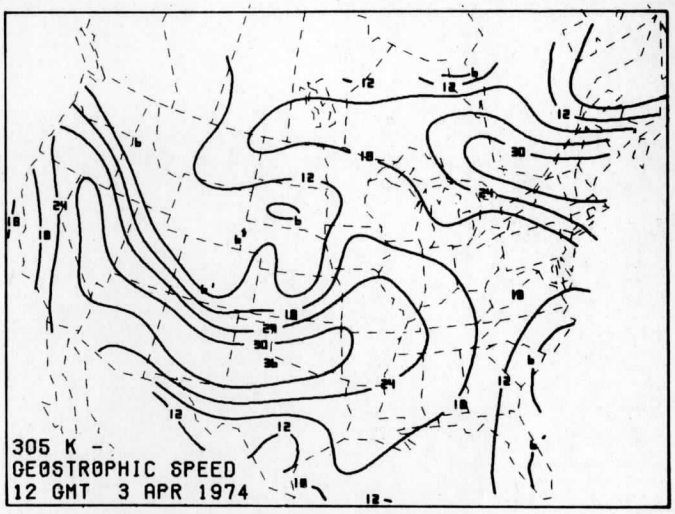
305 K -
GEOSTROPHIC SPEED
12 GMT 3 APR 1974

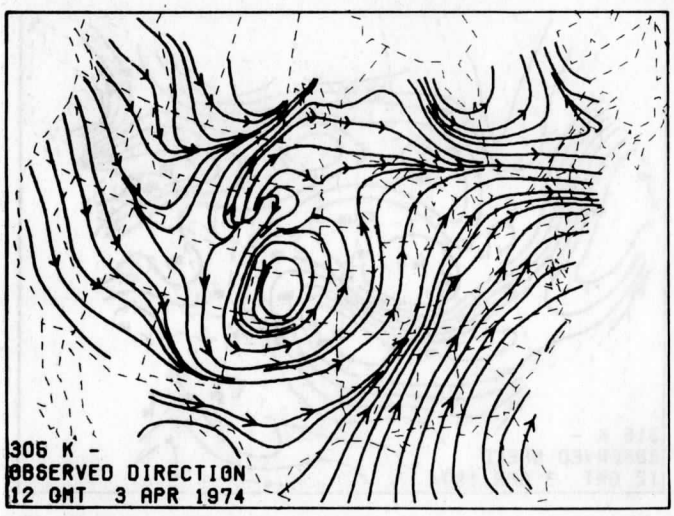
305 K -
OBSERVED DIRECTION
12 GMT 3 APR 1974

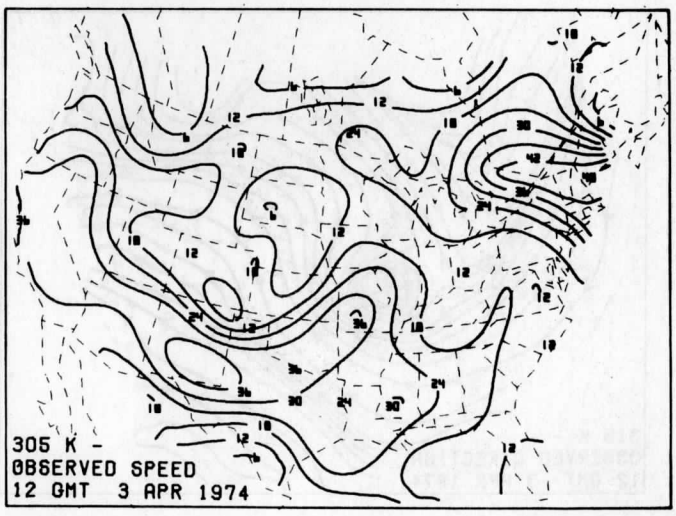
305 K -
OBSERVED SPEED
12 GMT 3 APR 1974

FIG. 17

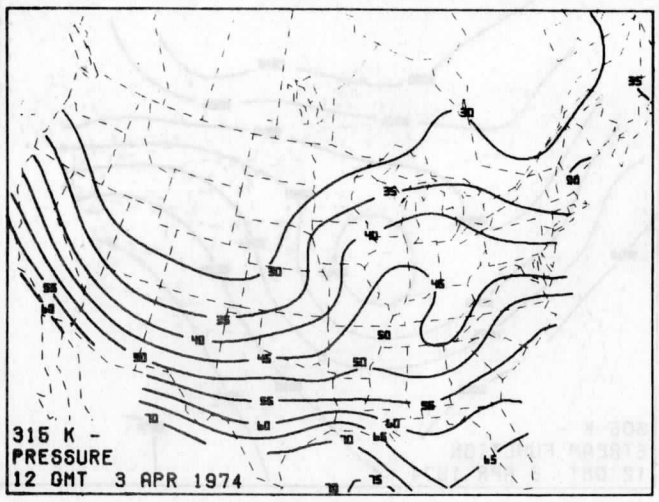
315 K -
PRESSURE
12 GMT 3 APR 1974

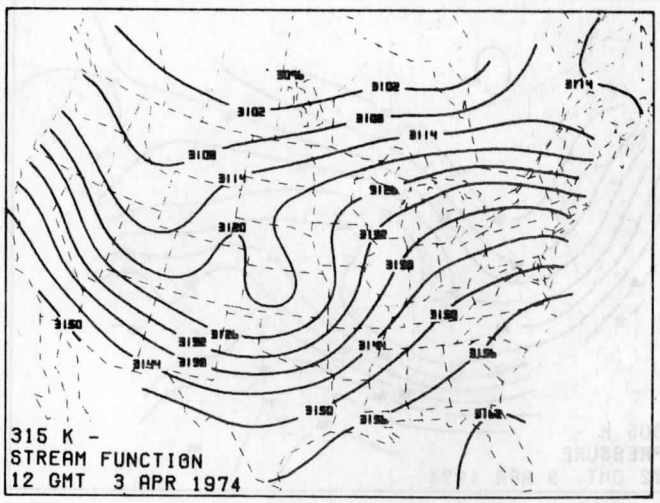
315 K -
STREAM FUNCTION
12 GMT 3 APR 1974

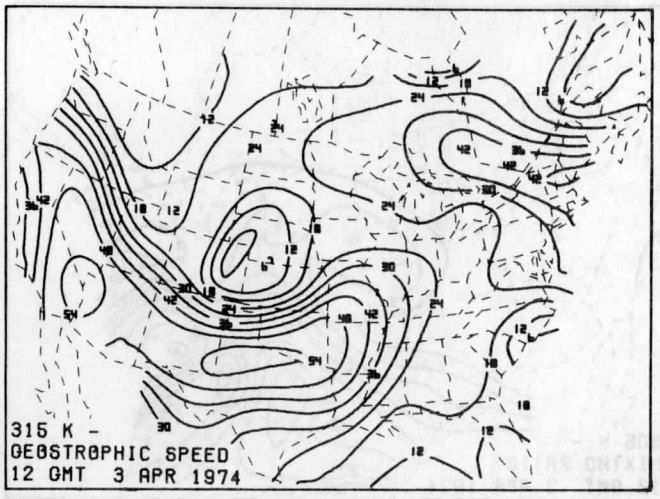
315 K -
GEOSTROPHIC SPEED
12 GMT 3 APR 1974

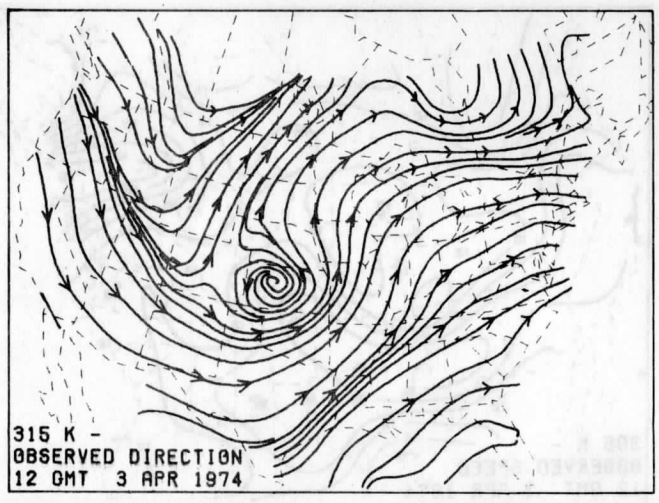
315 K -
OBSERVED DIRECTION
12 GMT 3 APR 1974

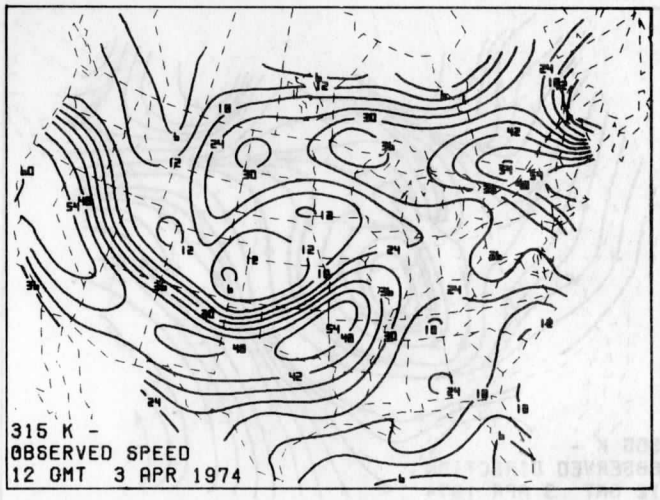
315 K -
OBSERVED SPEED
12 GMT 3 APR 1974

FIG. 18

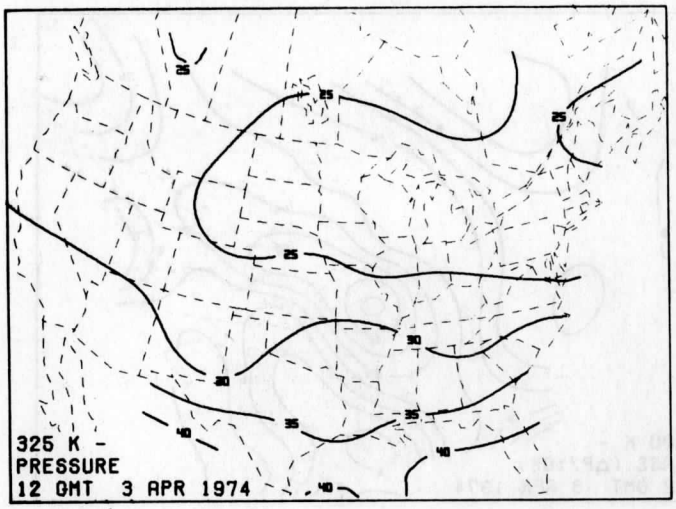
325 K -
PRESSURE
12 GMT 3 APR 1974

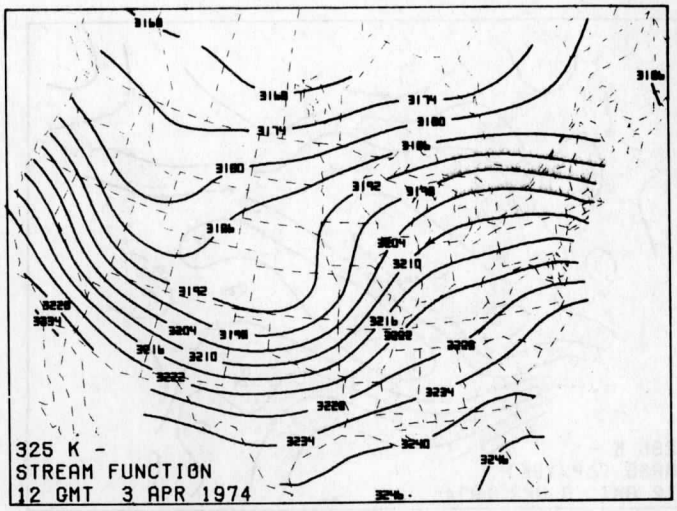
325 K -
STREAM FUNCTION
12 GMT 3 APR 1974

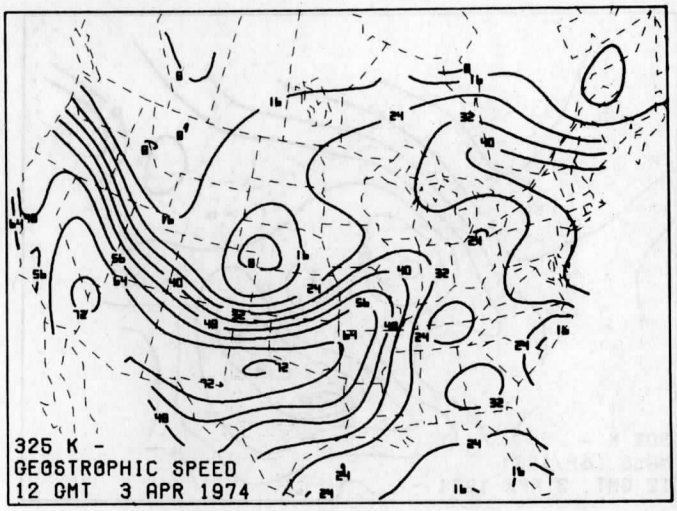
325 K -
GEOSTROPHIC SPEED
12 GMT 3 APR 1974

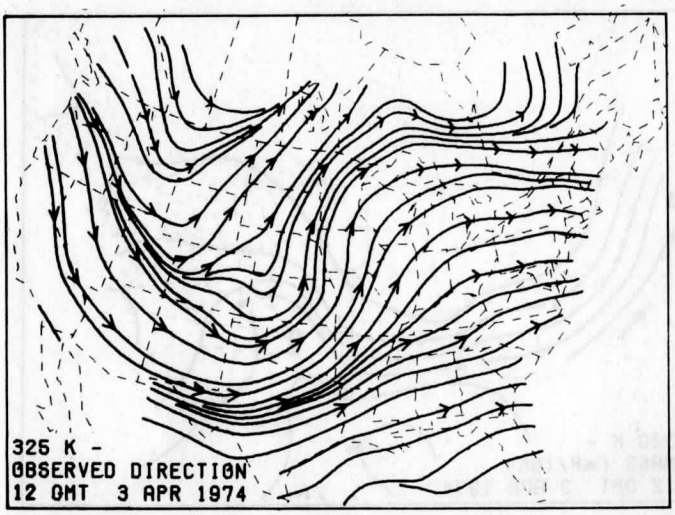
325 K -
OBSERVED DIRECTION
12 GMT 3 APR 1974

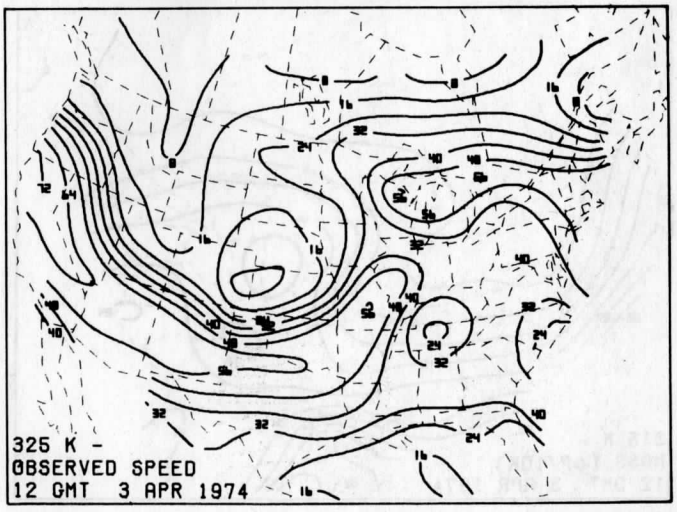
325 K -
OBSERVED SPEED
12 GMT 3 APR 1974

FIG. 19

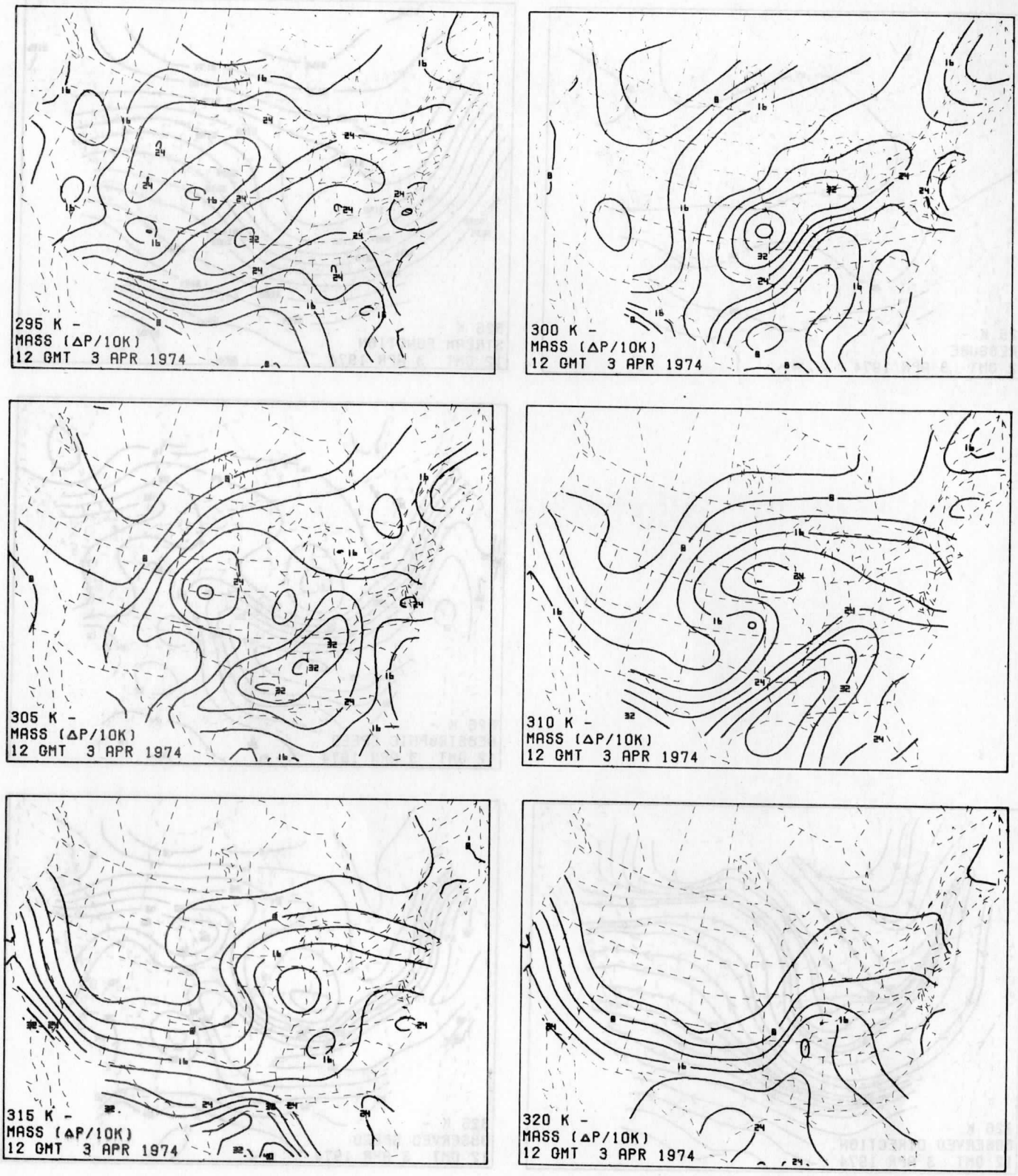
295 K -
MASS (ΔP/10K)
12 GMT 3 APR 1974
300 K -
MASS (ΔP/10K)
12 GMT 3 APR 1974
305 K -
MASS (ΔP/10K)
12 GMT 3 APR 1974
310 K -
MASS (ΔP/10K)
12 GMT 3 APR 1974
315 K -
MASS (ΔP/10K)
12 GMT 3 APR 1974
320 K -
MASS (ΔP/10K)
12 GMT 3 APR 1974

FIG. 20

Analyses obtained from the cross-sectionally based analysis scheme for 0000 GMT 4 April 1974

Fig. 21. Analyses of surface parameters. Surface height in decameters, pressure in centibars, wind speed in m $s^{-1}$, temperature and potential temperature in °K.

Fig. 22. Isobaric analyses at 900 mb. Temperature and dew point in °K, heights in decameters, geostrophic and observed (final enhanced) wind speeds in m $s^{-1}$.

Fig. 23. Same as Fig. 22 but at 700 mb.

Fig. 24. Same as Fig. 22 but at 500 mb.

Fig. 25. Same as Fig. 22 but at 300 mb.

Fig. 26. Isentropic analyses at 305 K. Pressure in centibars, stream function to be multiplied by $10^6 cm^2 s^{-2}$, mixing ratio in g/kg, geostrophic and observed (final enhanced) wind speeds in m $s^{-1}$.

Fig. 27. Same as Fig. 26 but for 315 K. No mixing ratio analysis shown.

Fig. 28. Same as Fig. 26 but for 325 K. No mixing ratio analysis shown.

Fig. 29. Mass ($\Delta P/10°K$) centered about various isentropic surfaces. Provides an indicator of inverse static stability. Units centibars/10°K.

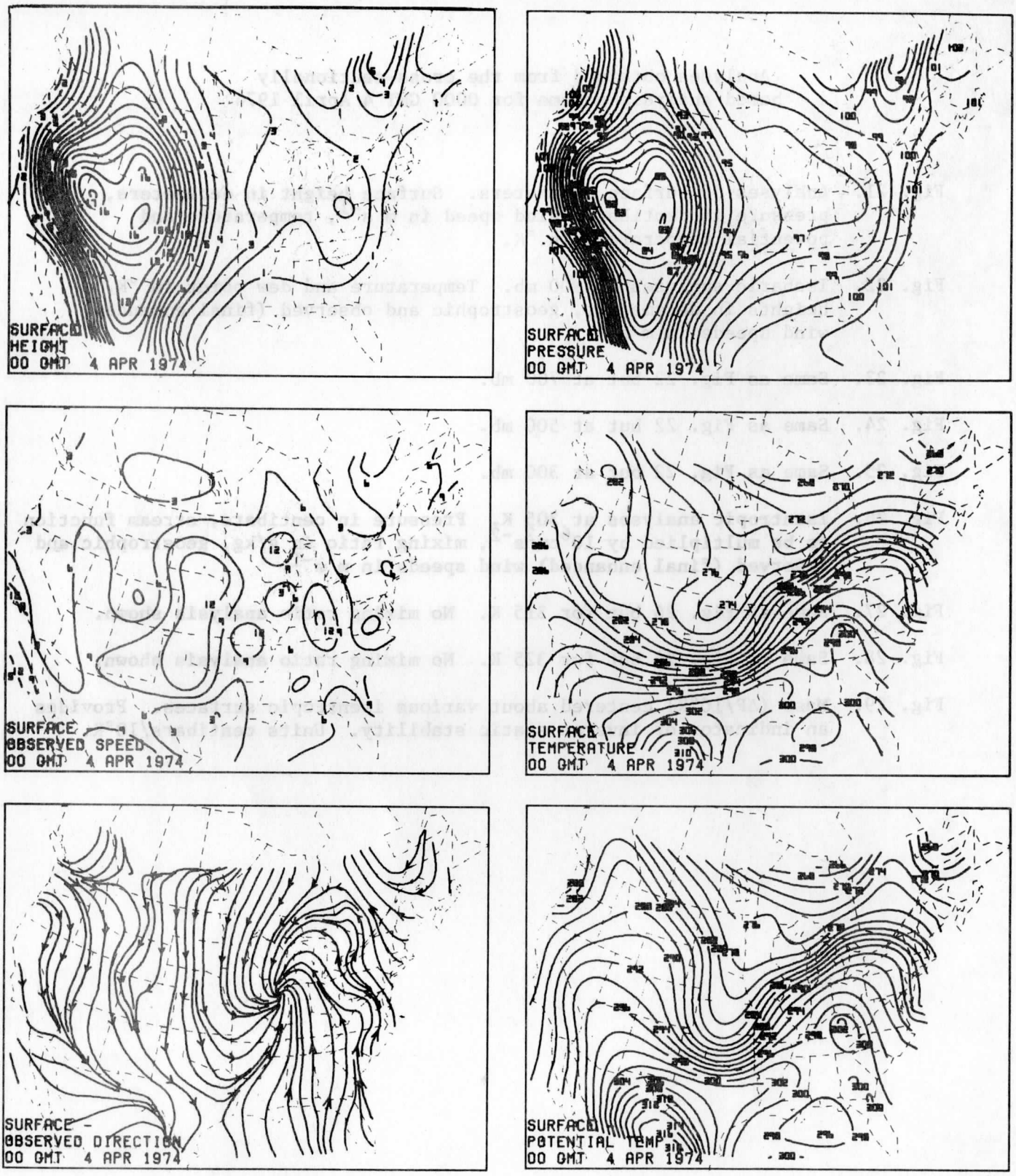
SURFACE
HEIGHT
00 GMT 4 APR 1974
SURFACE
PRESSURE
00 GMT 4 APR 1974
SURFACE
OBSERVED SPEED
00 GMT 4 APR 1974
SURFACE
TEMPERATURE
00 GMT 4 APR 1974
SURFACE
OBSERVED DIRECTION
00 GMT 4 APR 1974
SURFACE
POTENTIAL TEMP
00 GMT 4 APR 1974

FIG. 21

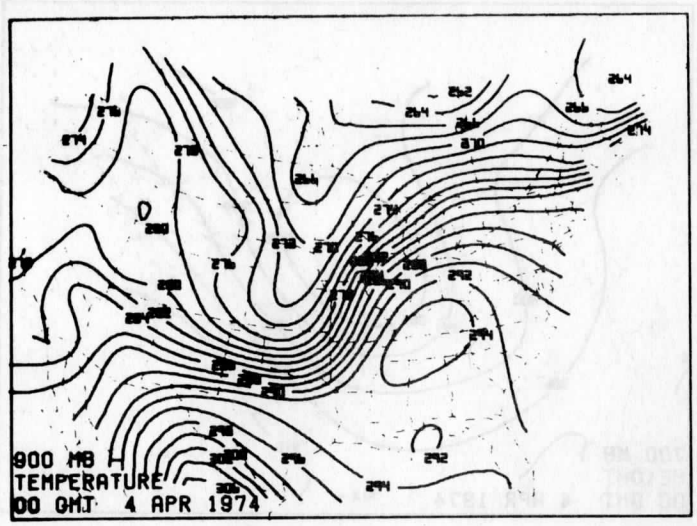
900 MB -
TEMPERATURE
00 GMT 4 APR 1974

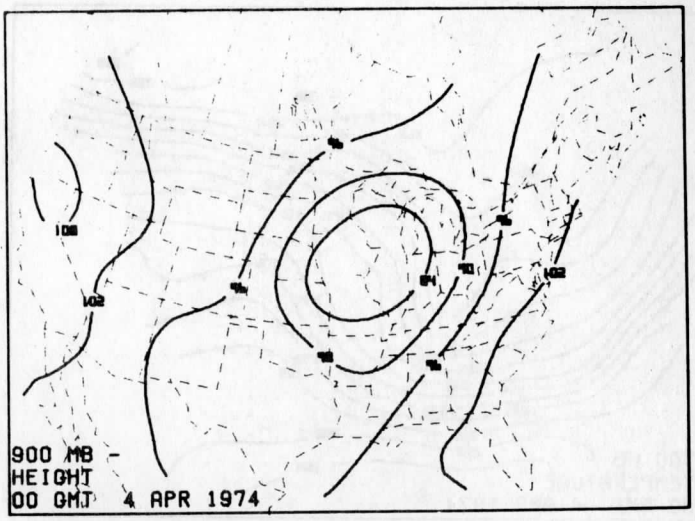
900 MB -
HEIGHT
00 GMT 4 APR 1974

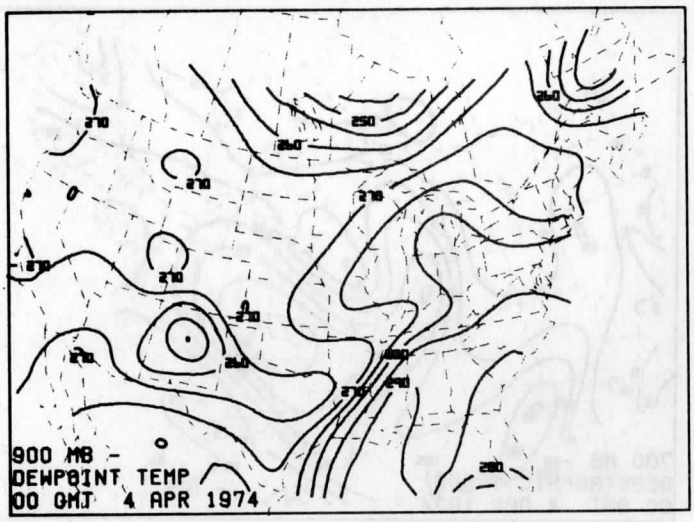
900 MB -
DEWPOINT TEMP
00 GMT 4 APR 1974

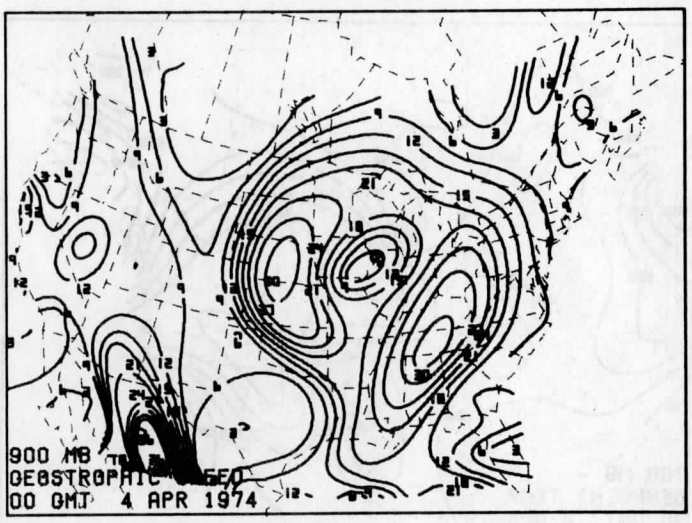
00 GMT 4 APR 1974

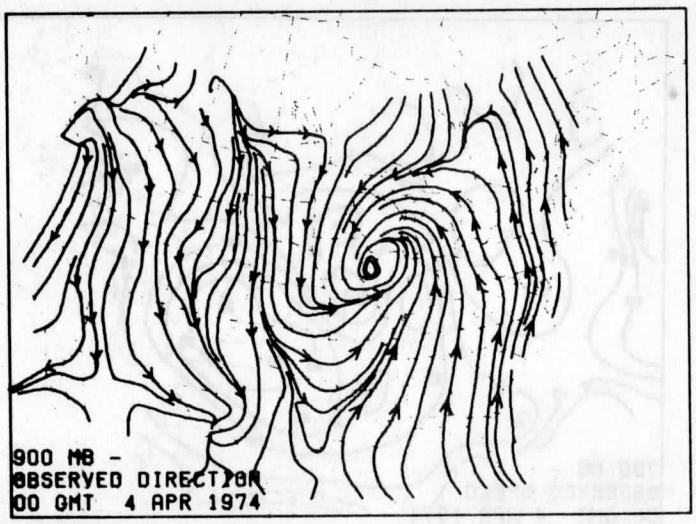
900 MB -
OBSERVED DIRECTION
00 GMT 4 APR 1974

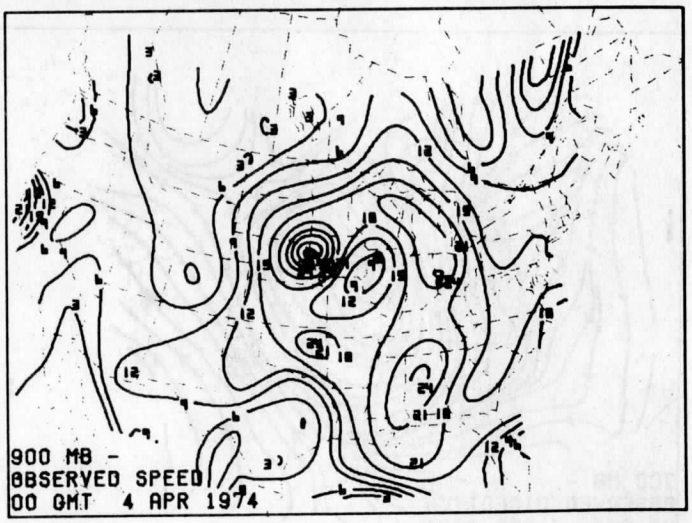
900 MB -
OBSERVED SPEED
00 GMT 4 APR 1974

FIG. 22

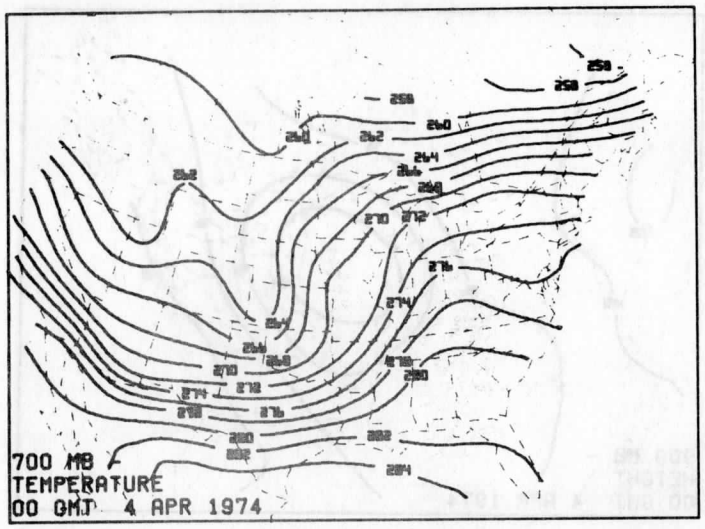
700 MB -
TEMPERATURE
00 GMT 4 APR 1974

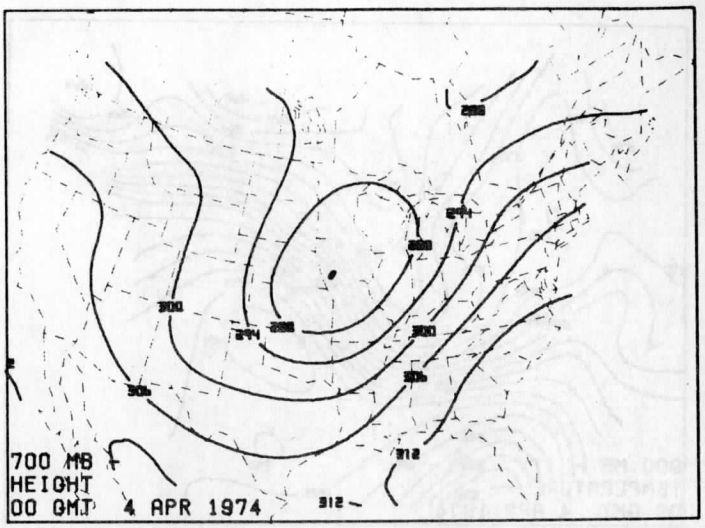
700 MB -
HEIGHT
00 GMT 4 APR 1974

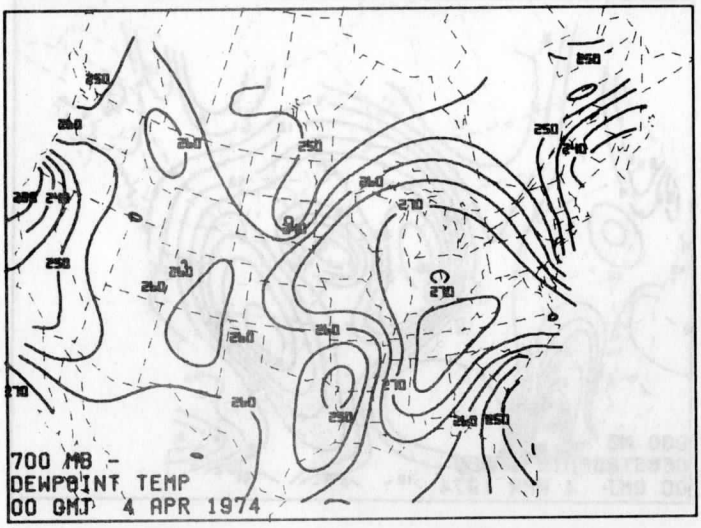
700 MB -
DEWPOINT TEMP
00 GMT 4 APR 1974

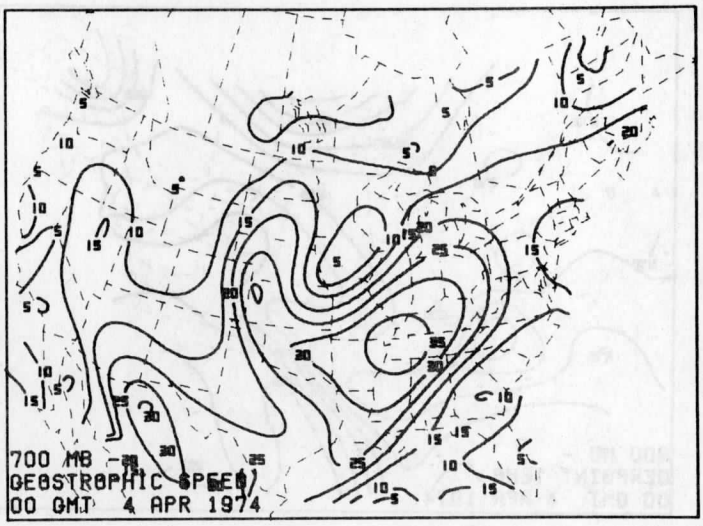
700 MB -
GEOSTROPHIC SPEED
00 GMT 4 APR 1974

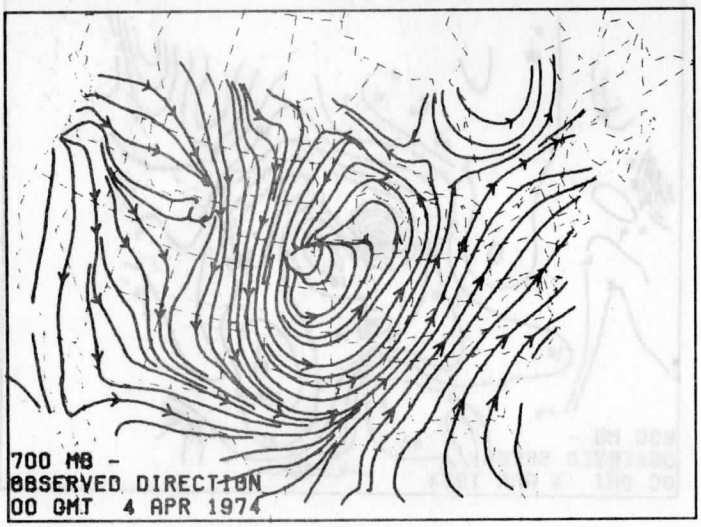
700 MB -
OBSERVED DIRECTION
00 GMT 4 APR 1974

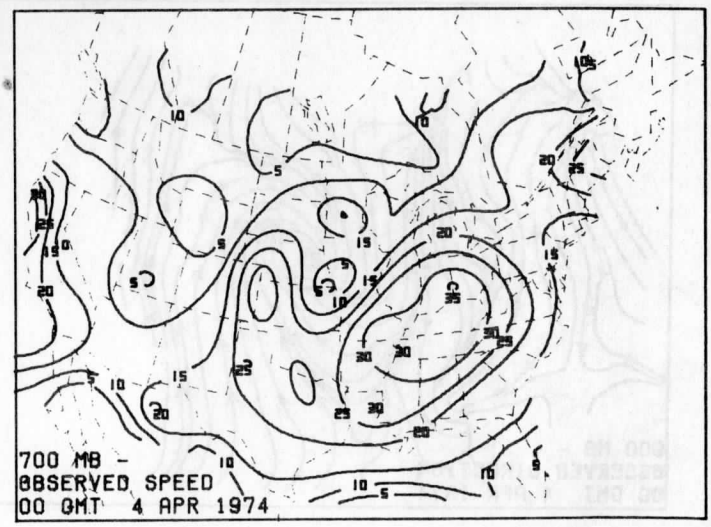
700 MB -
OBSERVED SPEED
00 GMT 4 APR 1974

FIG. 23

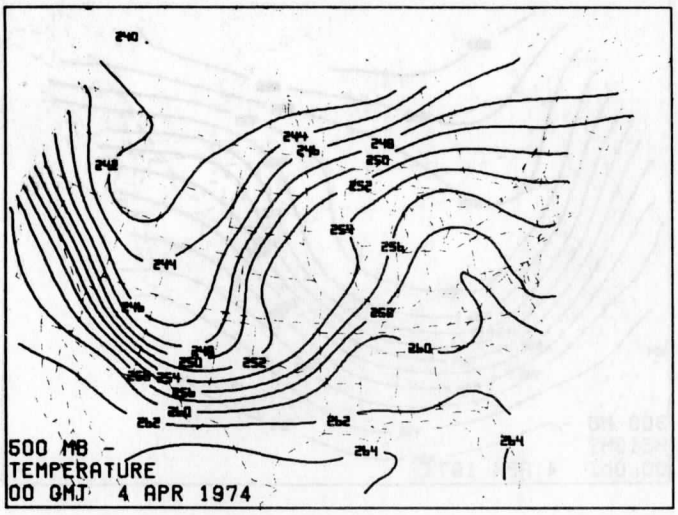
500 MB -
TEMPERATURE
00 GMT 4 APR 1974

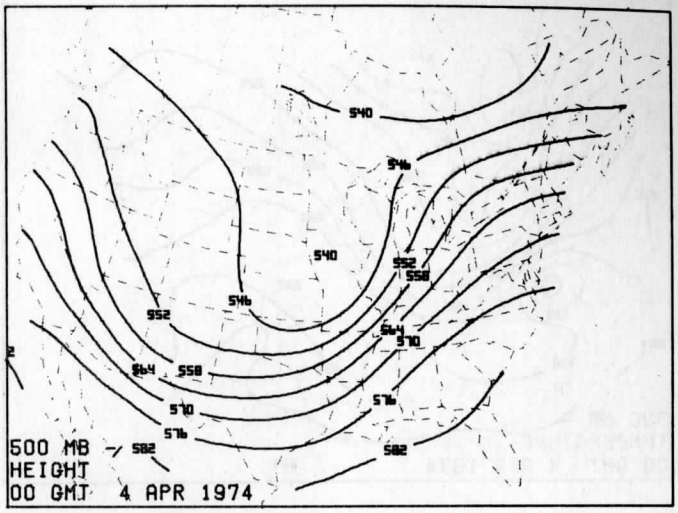
500 MB -
HEIGHT
00 GMT 4 APR 1974

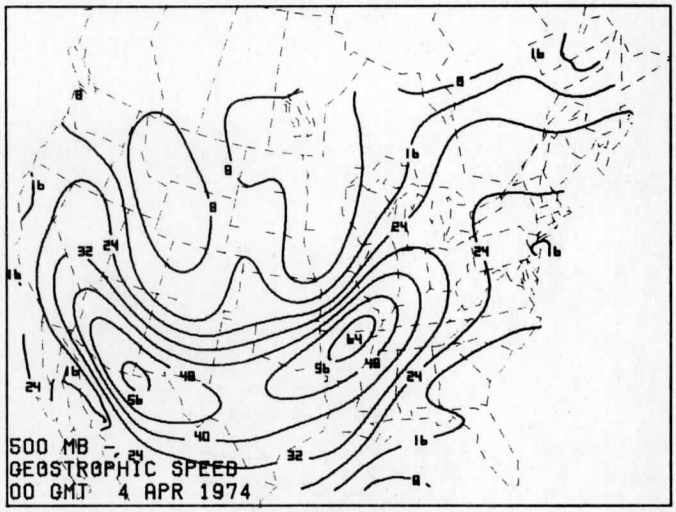
500 MB -
GEOSTROPHIC SPEED
00 GMT 4 APR 1974

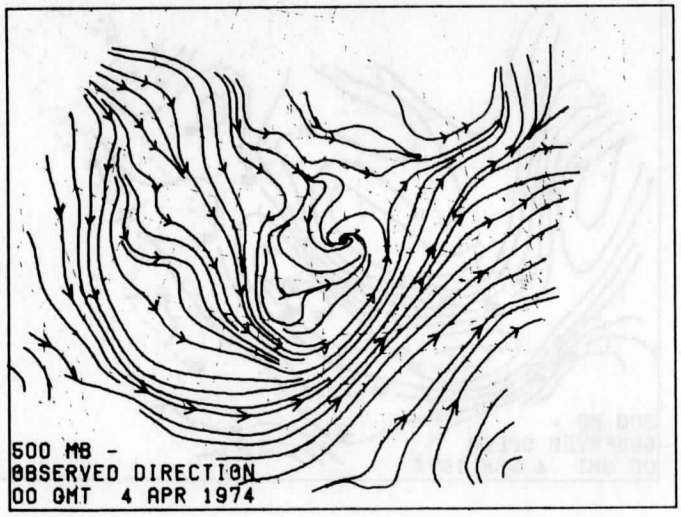
500 MB -
OBSERVED DIRECTION
00 GMT 4 APR 1974

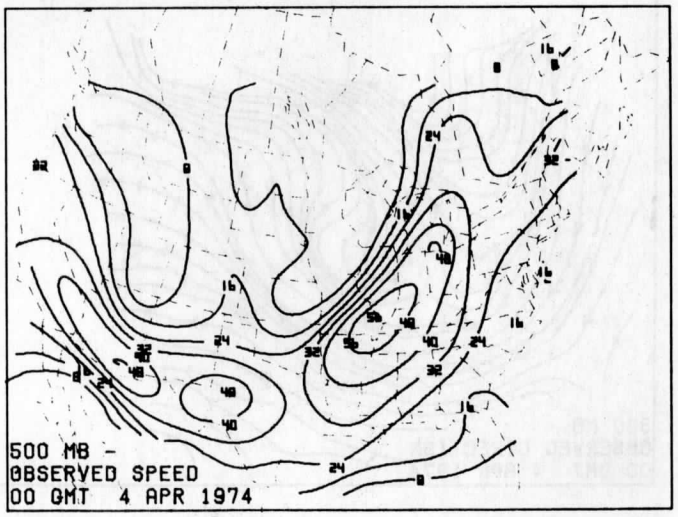
500 MB -
OBSERVED SPEED
00 GMT 4 APR 1974

FIG. 24

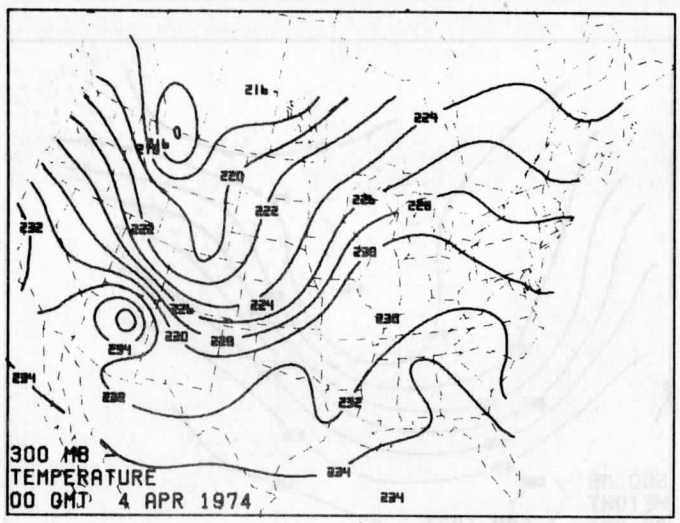
300 MB
TEMPERATURE
00 GMT 4 APR 1974

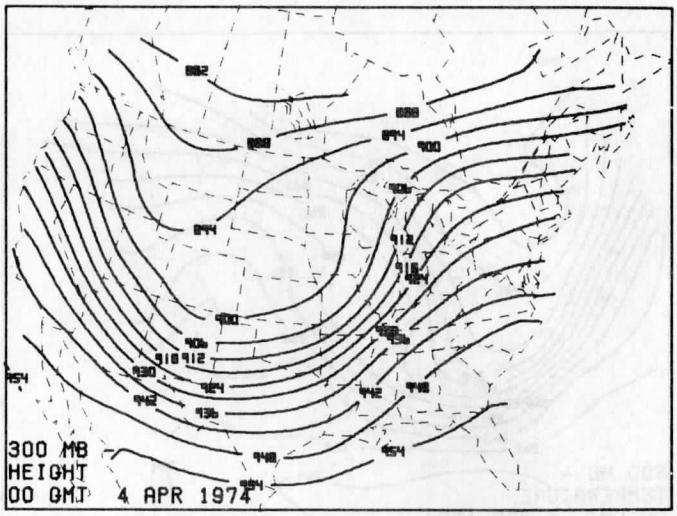
300 MB
HEIGHT
00 GMT 4 APR 1974

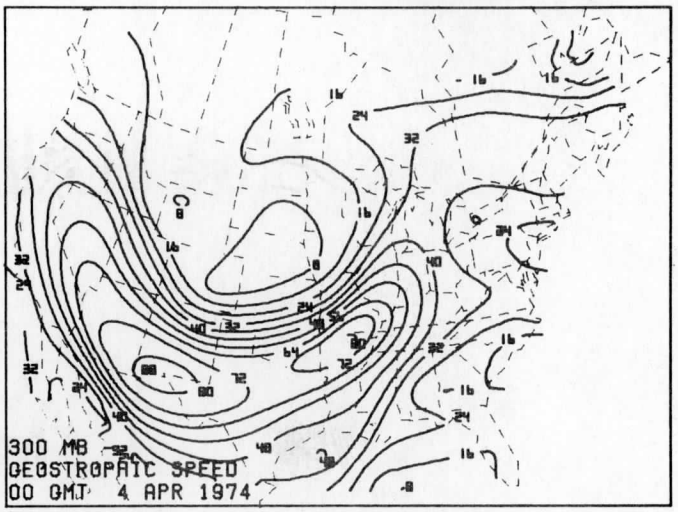
300 MB
GEOSTROPHIC SPEED
00 GMT 4 APR 1974

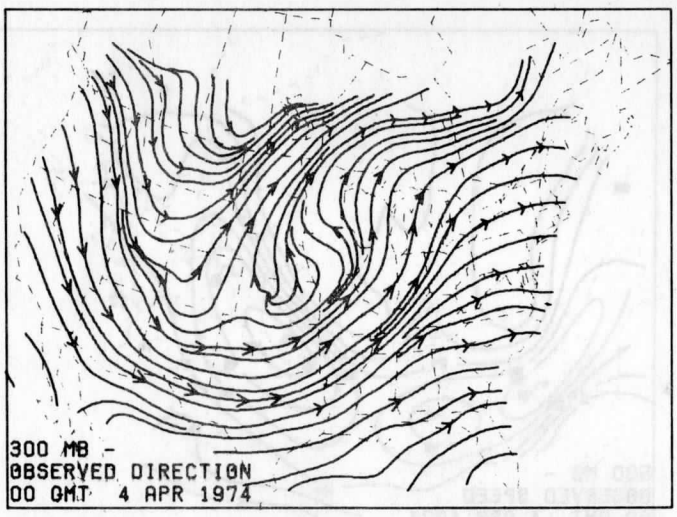
300 MB
OBSERVED DIRECTION
00 GMT 4 APR 1974

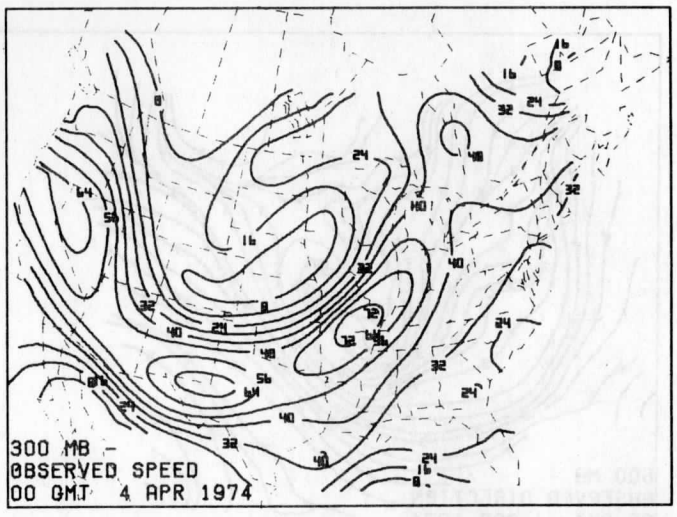
300 MB
OBSERVED SPEED
00 GMT 4 APR 1974

FIG. 25

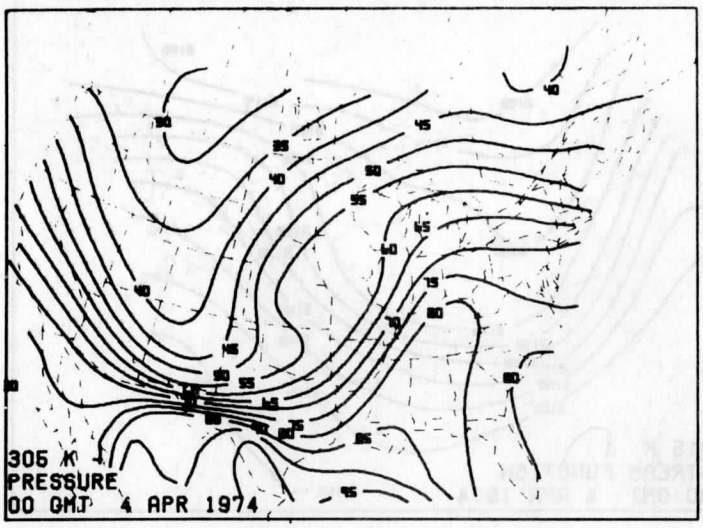
305 K -
PRESSURE
00 GMT 4 APR 1974

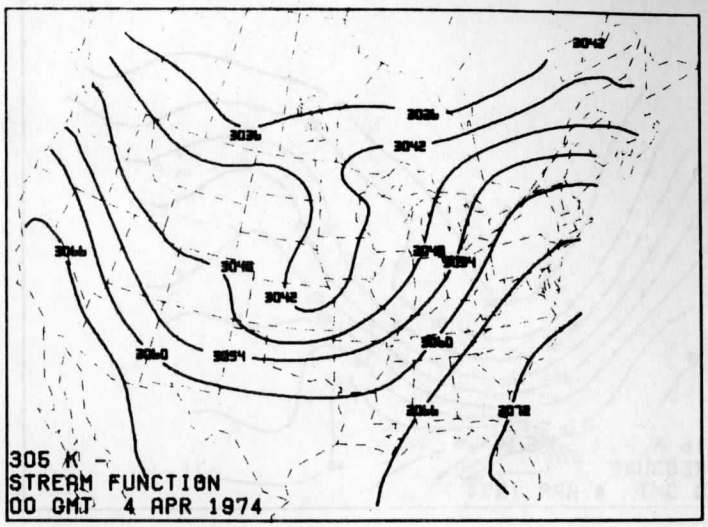
305 K -
STREAM FUNCTION
00 GMT 4 APR 1974

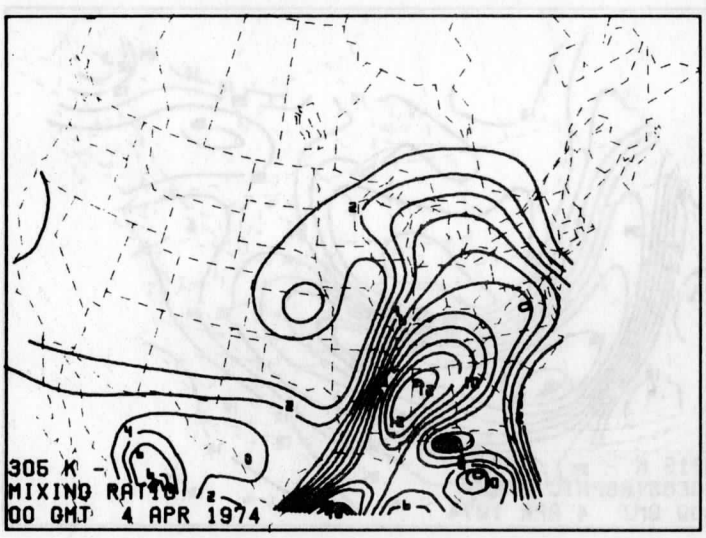
305 K -
MIXING RATIO
00 GMT 4 APR 1974

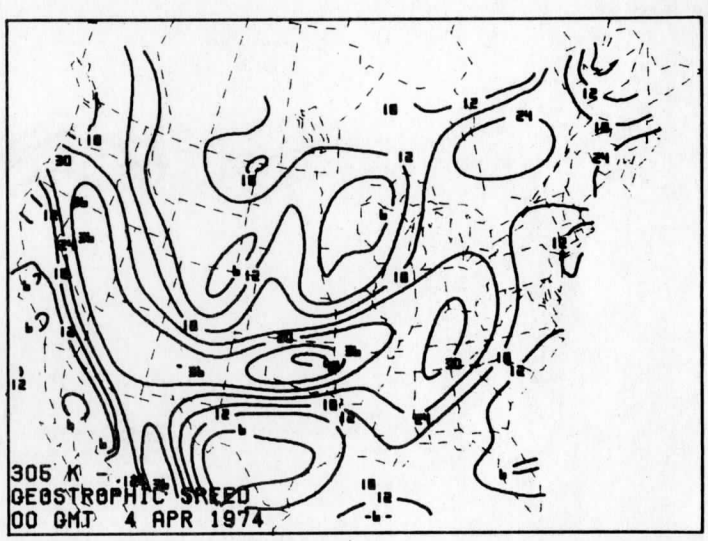
305 K -
GEOSTROPHIC SPEED
00 GMT 4 APR 1974

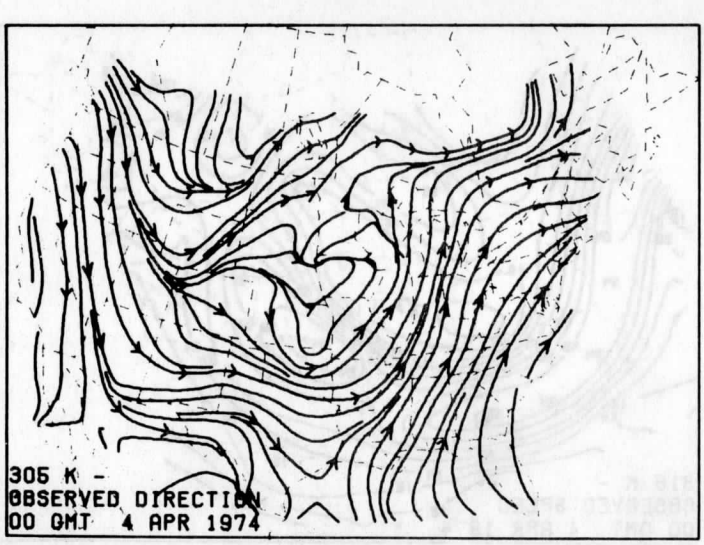
305 K -
OBSERVED DIRECTION
00 GMT 4 APR 1974

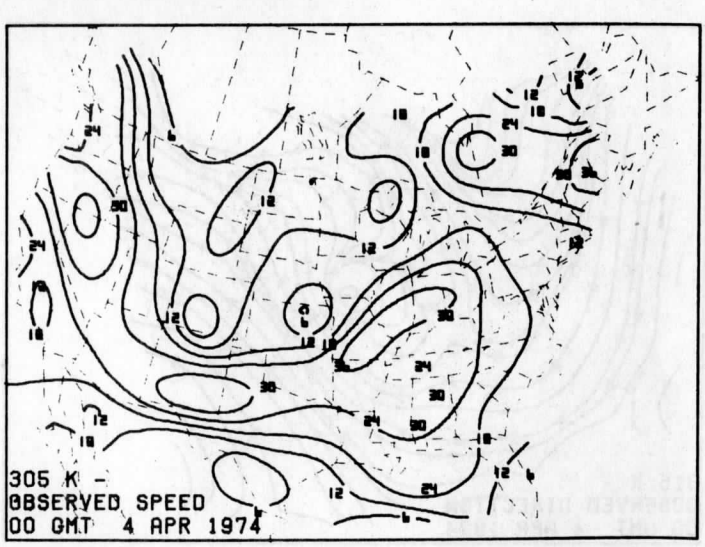
305 K -
OBSERVED SPEED
00 GMT 4 APR 1974

FIG. 26

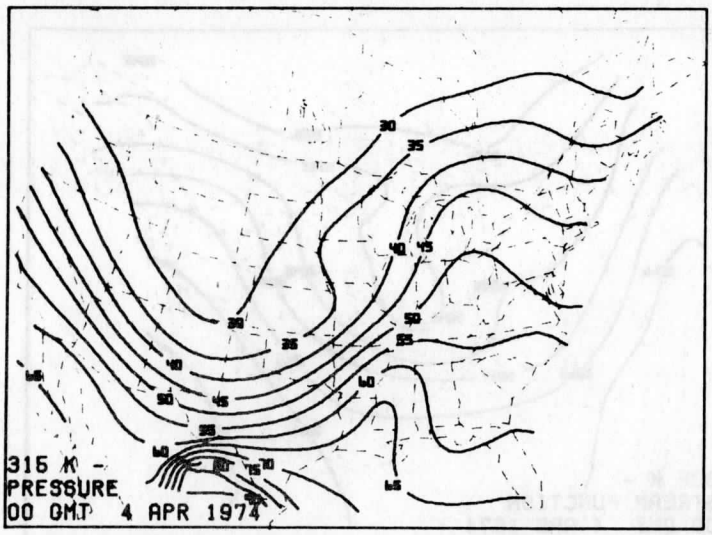
315 K -
PRESSURE
00 GMT 4 APR 1974

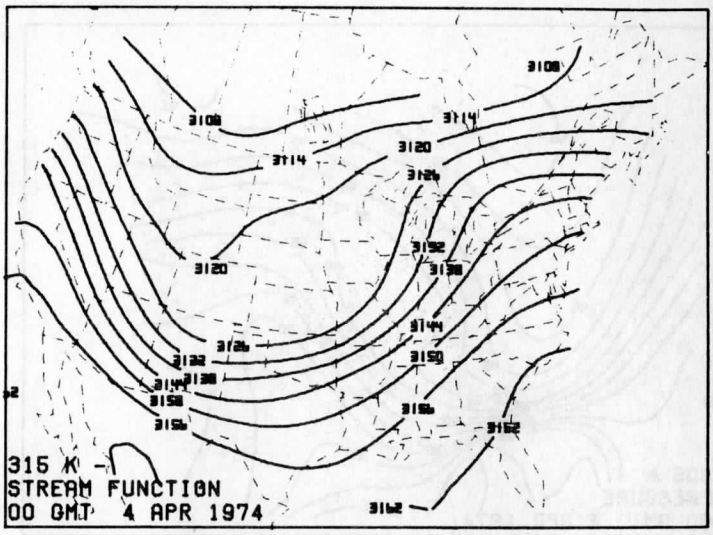
315 K -
STREAM FUNCTION
00 GMT 4 APR 1974

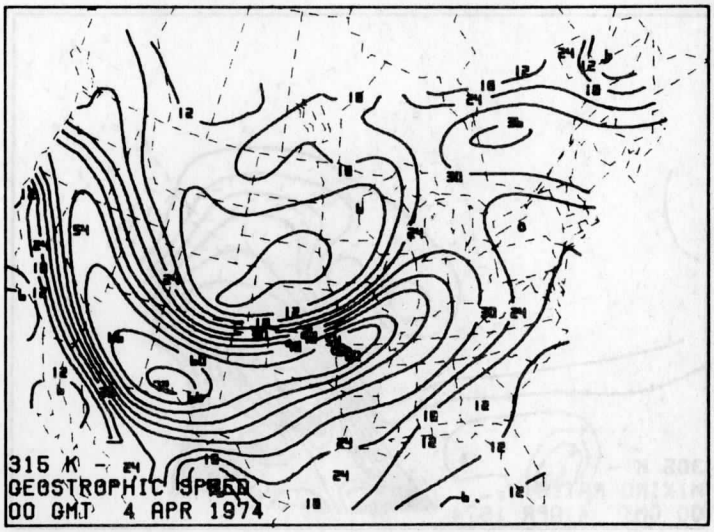
315 K -
GEOSTROPHIC SPEED
00 GMT 4 APR 1974

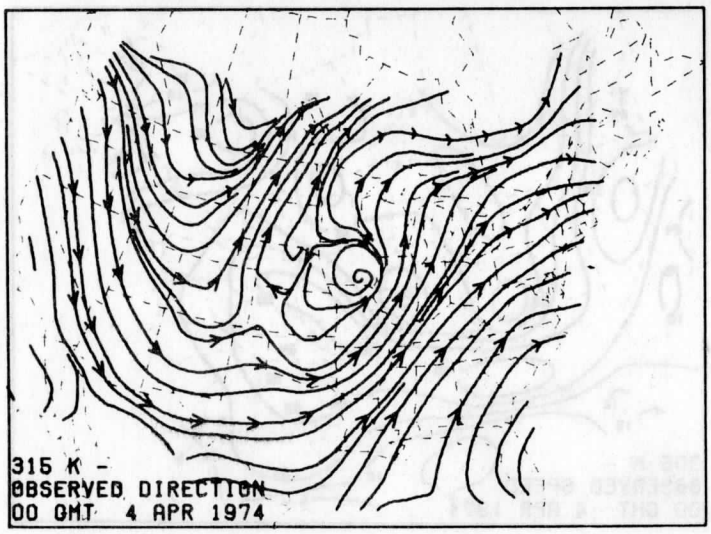
315 K -
OBSERVED DIRECTION
00 GMT 4 APR 1974

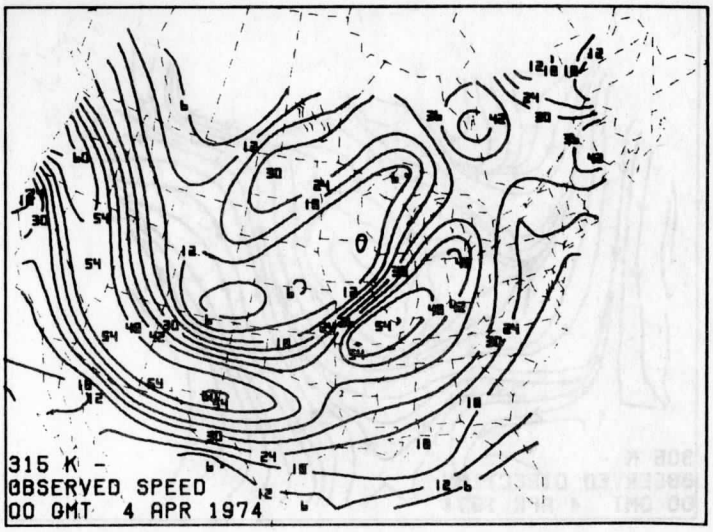
315 K -
OBSERVED SPEED
00 GMT 4 APR 1974

FIG. 27

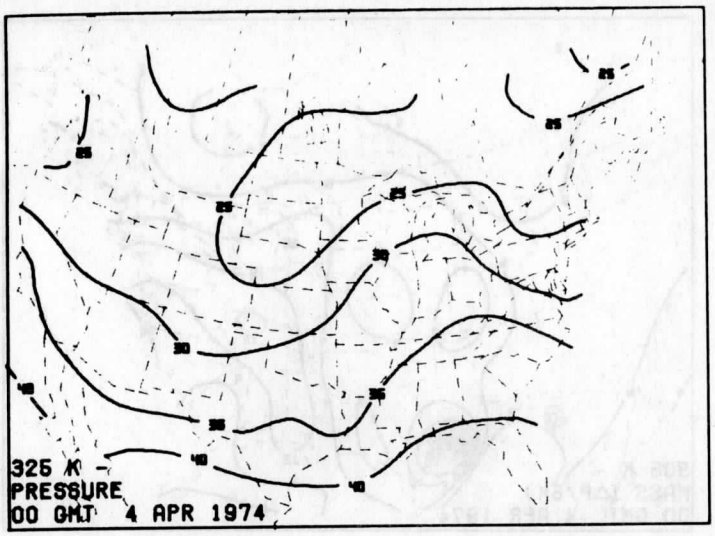
325 K -
PRESSURE
00 GMT 4 APR 1974

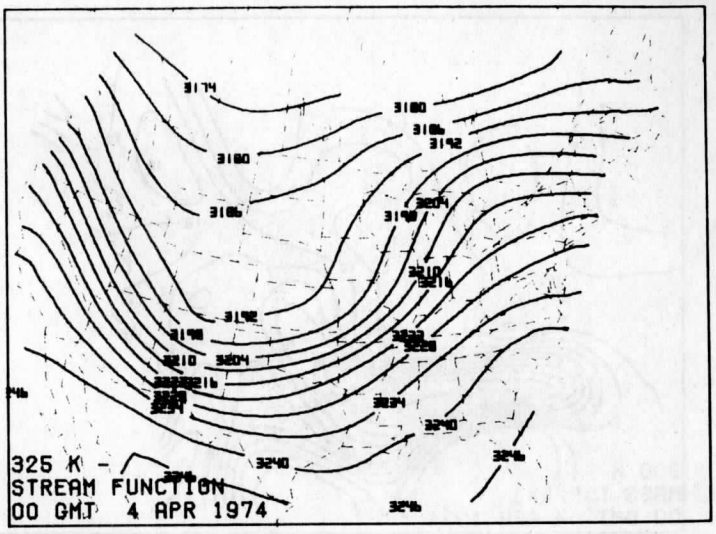
325 K -
STREAM FUNCTION
00 GMT 4 APR 1974

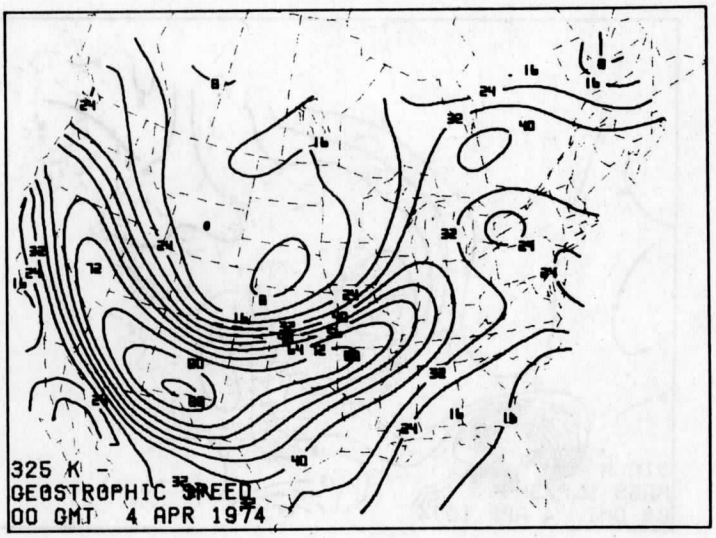
325 K -
GEOSTROPHIC SPEED
00 GMT 4 APR 1974

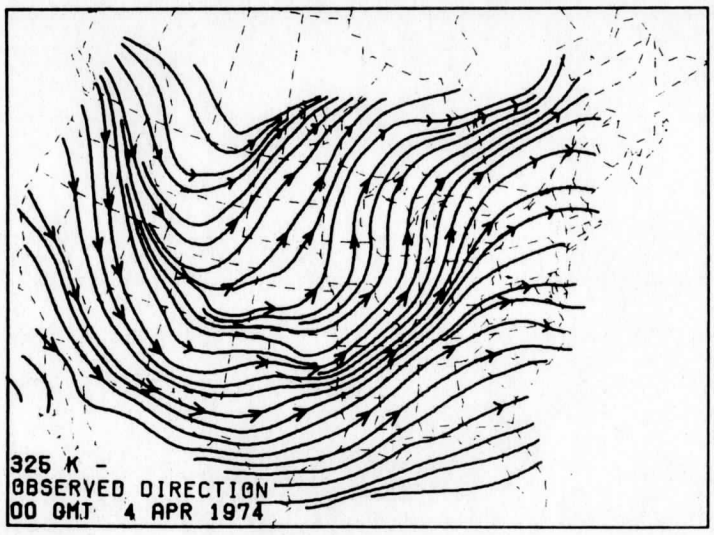
325 K -
OBSERVED DIRECTION
00 GMT 4 APR 1974

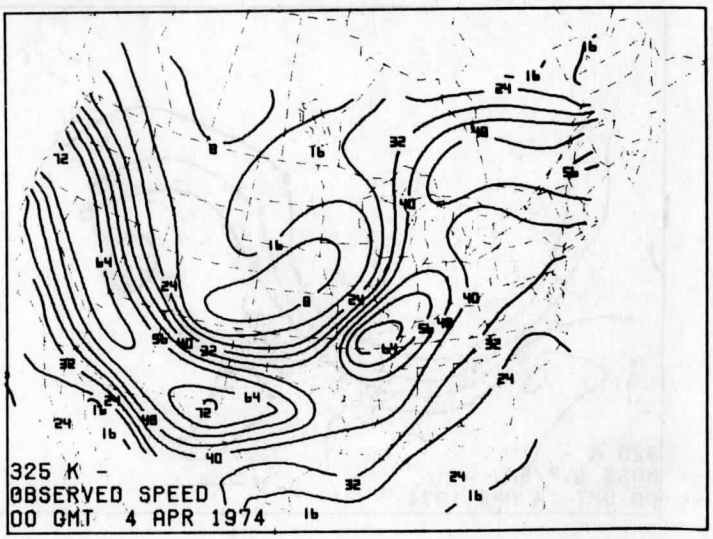
325 K -
OBSERVED SPEED
00 GMT 4 APR 1974

FIG. 28

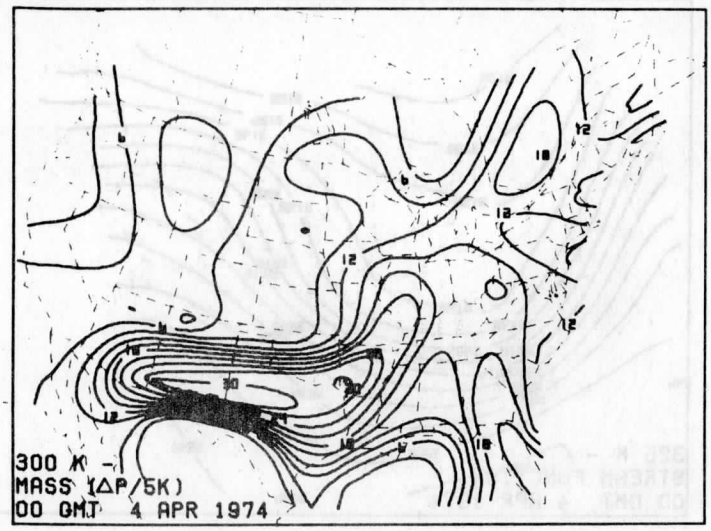
300 K -
MASS (ΔP/5K)
00 GMT 4 APR 1974

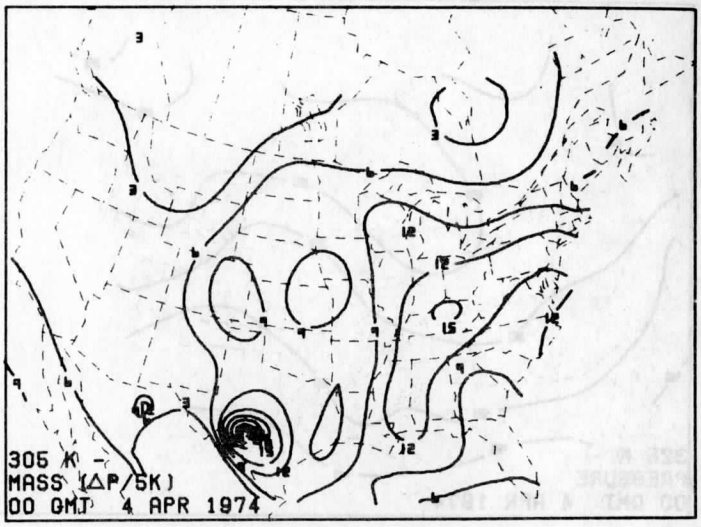
305 K -
MASS (ΔP/5K)
00 GMT 4 APR 1974

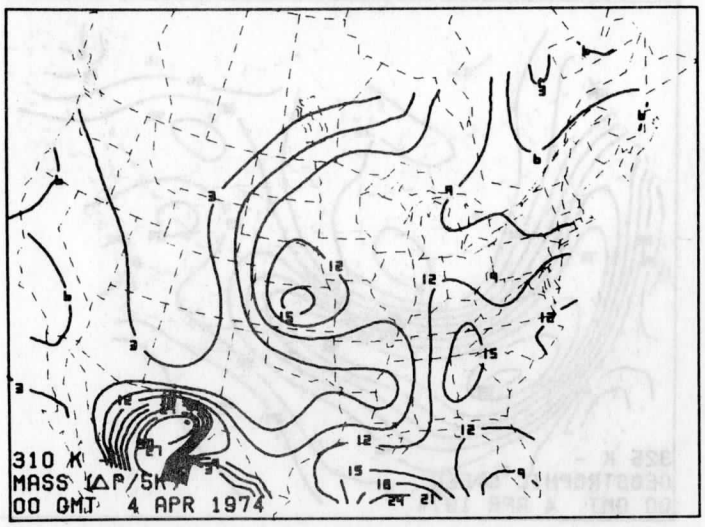
310 K -
MASS (ΔP/5K)
00 GMT 4 APR 1974

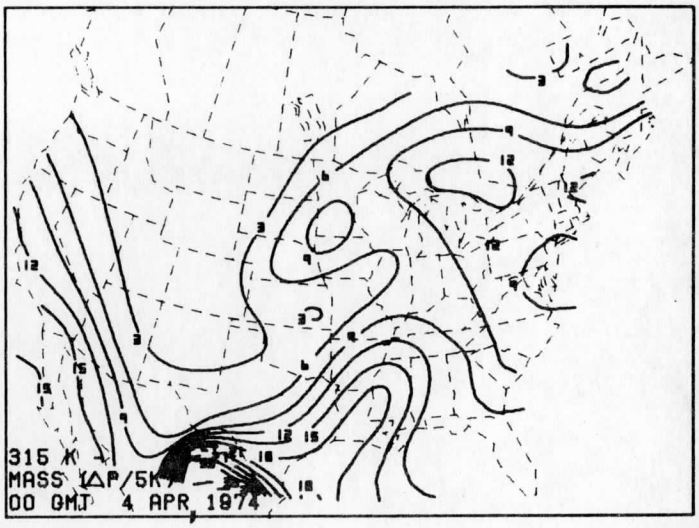
315 K -
MASS (ΔP/5K)
00 GMT 4 APR 1974

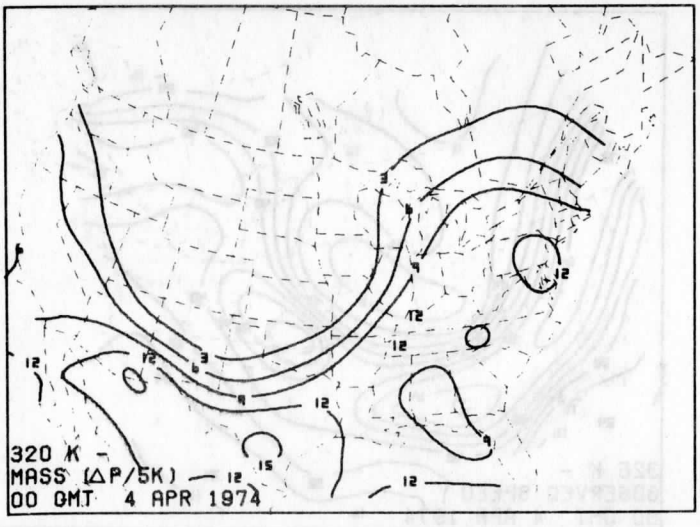
320 K -
MASS (ΔP/5K)
00 GMT 4 APR 1974

FIG. 29

Acknowledgments

A complete list of the many individuals involved in the realization of this effort is too long to compile completely. However, special recognition must be made to Mr. Thomas Whittaker, whose unflagging belief in the procedure has been an inspiration in itself. Prof. Lyle Horn must also be thanked for his unfailing patience and for extending me the freedom to accomplish this work. Dr. Christopher Hayden and Mr. Thomas Koehler must also be recognized for their comments on the text. To the remainder of the people who offered comments and criticisms, I express a sincere "Thank you!". This research was supported by National Oceanic and Atmospheric Administration (Meteorological Satellite Laboratory) Grant 04-4-158-2.

References

Bergthorsson, P. and B.R. Döös, 1955: Numerical weather map analysis. Tellus, 7, 329-340.

Cressman, G.P., 1959: An operational objective analysis scheme. Mon. Wea. Rev., 87, 367-381.

Flattery, T.W., 1970: Spectral models for global analysis and forecasting. Proc. Sixth AWS Tech. Exchange Conf., U.S. Naval Academy 21-24 Sept. 1974, Air Weather Service Tech. Rept. 242, 42-54.

Gandin, L.S., 1963: Objective analysis of meteorological fields. Gidrometeorologicheskoe Izdotel'Stvo, Leningrad. Translated from Russian, Israel Program fro Scientific Translations, Jerusalem, 1965, 242 pp.

Gilchrist, B. and Cressman, G.P., 1954: An experiment in objective analysis. Tellus, 6, 309-318.

Hoxit, L.R. and C.F. Chappell, 1975: Tornado outbreak of April 3-4, 1974; Synoptic analysis, NOAA Technical Report, NOAA TR ERL 338-APCL 37, Boulder, Colorado, 48 pp.

Johnson, D.H., 1957: Preliminary research in objective analysis. Tellus, 9, 316-322.

Johnson, D.R. and W.D. Downey, 1976: The absolute angular momentum budget of an extra-tropical cyclone. Mon. Wea. Rev., 104, 3-14.

McPherson, R.D., 1975: Progress, problems and prospects in meteorological data assimilation. Bull. Amer. Meteor. Soc., 56, 1154-1166.

National Meteorological Center, 1971: Technical Procedures Bulletin #65. New initialization procedure for the 6-layer (PE) numerical prediction model. N.O.A.A., Washington, D.C.

Otto-Bliesner, B., D.P. Baumhefner, T.W. Schlatter and R. Bleck, 1977: A comparison of several meteorological analysis schemes over a data-rich region. Mon. Wea. Rev., 105, 1083-1091.

Panofsky, H.A., 1949: Objective weather map analysis. J. Meteor., 6, 386-392.

Schlatter, T.W., 1975: Some experiments with a multivariate statistical objective analysis scheme. J. Appl. Meteor., 12, 1093-1101.

_____, G.W. Branstator and L.G. Thiel, 1976: Testing a global multivariate statistical objective analysis scheme with observed data. Mon. Wea. Rev., 104, 765-783.

Shapiro, M.A. and J.T. Hastings, 1973: Objective cross-section analysis by Hermite polynomial interpolation of isentropic surfaces. J. Appl. Meteor., 12, 753-762.

Shuman, F.G., 1957: Numerical methods in weather predication: I. The balance equation. Mon. Wea. Rev., 85, 329-332.

Whittaker, T.M. and R.A. Petersen, 1977: Objective cross-sectional analysis incorporating thermal enhancement of the observed winds. Mon. Wea. Rev., 105, 147-153.

# A Test of Seven Methods which Perform Grid to Observation Interpolations

Thomas L. Koehler

Department of Meteorology, University of Wisconsin-Madison, Wisconsin 53706

Abstract

The interpolation of grid point values to observation locations is a necessary step in analysis techniques which interpolate differences between observed and first guess values. Evaluations of seven methods which perform this "inverse" interpolation are presented. Analytic functions provide the data values at both grid points and observation locations, so that interpolation errors may be defined exactly. The results indicate that the overlapping quadratic polynomial method presented by Bleck and Haagenson (1968) yields the best results in terms of accuracy and economy.

## 1. Introduction

Operational objective analysis techniques are designed to interpolate information from unevenly distributed observations to a uniformly distributed set of grid points. More often than not, these schemes interpolate the differences between observed and first guess values rather than observed values directly. First guess values may be obtained from climatology, or a previous analysis or a forecast. In any event, the first guess values are usually available only on a uniform set of grid points, and first guess estimates at the observation points must be obtained to perform the analysis. The impact of the methods used in this "inverse" (grid to observation) interpolation is generally not discussed in objective analysis schemes. Yet large errors in this step will probably degrade the final analysis, so finding a method which provides very small errors in the first guess estimate is important. Tests have been designed with the intention of interpolating first guess data from the grid system of the National Weather Service limited area fine mesh (LFM) model to Nimbus 6 satellite sounding locations. At the time of these tests the LFM grid was polar stereographic with a grid spacing of 190.5 km true at 60°N.

## 2. Interpolation Methods

Seven interpolation methods as listed in Table 1 are tested. A short description of each follows.

TABLE 1. Interpolation Methods

| Label | Method Description |
|---|---|
| D1 | Inverse distance weights. |
| D2 | Inverse squared distance weights. |
| C1 | Modified one pass Cressman technique. |
| B1 | Bilinear. |
| B2 | 2-D overlapping quadratic polynomials. |
| L2 | 2-D least squares quadratic. |
| L3 | 2-D least squares cubic. |

Methods D1, D2 and C1 are distance weighting methods as shown in Figure 1. With these methods, the estimated value of variable Q at the point of observation ($Q_o$) is found by a weighted sum of the grid point values of Q at points 1 thru 4. Thus,

$$Q_o = w_1 Q_1 + w_2 Q_2 + w_3 Q_3 + w_4 Q_4 \tag{1}$$

The three methods differ only in the manner in which the weights are determined.

$$\text{Method D1} : w_i = (1/d_i)/\left(\sum_{j=1}^{4} 1/d_j\right) \; ; \; i=1,4 \tag{2}$$

$$\text{Method D2} : w_i = (1/d_i^2)/\left(\sum_{j=1}^{4} 1/d_j^2\right) \; ; \; i=1,4 \tag{3}$$

$$\text{Method C1} : w_i = \left(\frac{N^2 - d_i^2}{N^2 + d_i^2}\right)/\left(\sum_{j=1}^{4} \frac{N^2 - d_j^2}{N^2 + d_j^2}\right) \; ; \; i=1,4 \tag{4}$$

$$N = 1.5 \text{ grid intervals}$$

C1 is a simplified version of the analysis method presented by Cressman (1959). This method was designed for interpolating from observations to grid points, and may not necessarily perform well as an "inverse" interpolation method. Note that the weights for these schemes have been normalized to sum to unity.

The methods B1 and B2 are data fitting techniques; polynomials of various degrees are fit to the data at surrounding grid points to estimate a value at the observation. The bilinear method, B1, uses only the surrounding 4 grid points as shown in Figure 2. First, estimates at points A and B are found by assuming a linear variation between grid points in the x-direction. Note that A and B are at the same x position as the observation. Thus $Q_o$ is found by assuming a linear variation between points A and

FIGURE 1.

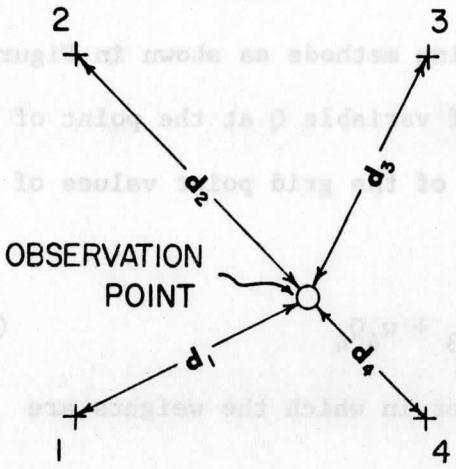


Schematic for methods D1, D2 and C1.

FIGURE 2.

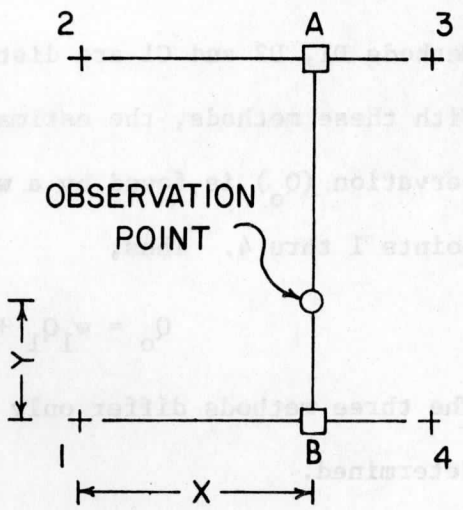


Schematic for method B1

FIGURE 3.

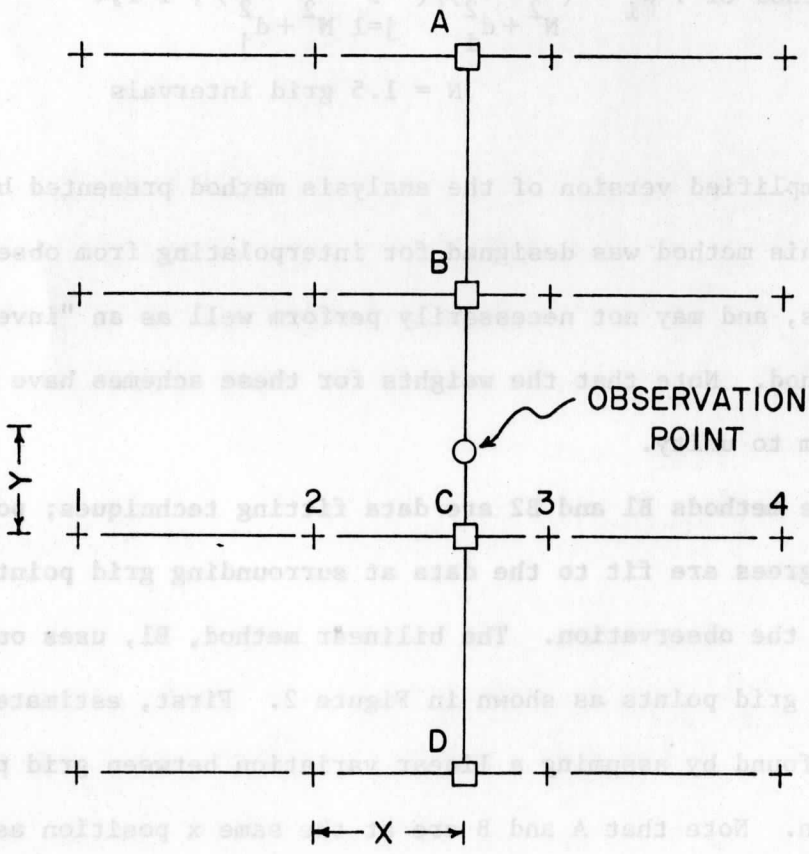


Schematic for method B2.

B. In mathematical terms,

$$Q_o = [(x)Q_3 + (1-x)Q_2](y) + [(x)Q_4 + (1-x)Q_1](1-y) \qquad (5)$$

where x and y are grid interval distances from point 1, both of which lie between 0 and 1 inclusive.

Method B2 is adapted from Bleck and Haagenson (1968). This method uses the 16 grid points surrounding the observation and separates the x and y directional dependence in a manner similar to the bilinear method as shown in Figure 3. Estimates at points A, B, C and D, at the x position of the observation, are found by constructing 4 separate sets of overlapping polynomials. For example,

$$Q_o = x(x-1)/2[(1-x)Q_1 + (x)Q_4] + (x-1)[1.5x^2 - x - 1]Q_2 - (x)[1.5x^2 - 2x - .5]Q_3 \qquad (6)$$

This equation is derived from a linear combination of the quadratic polynomials fitted to the values at points 1-2-3 and 2-3-4 respectively, which yields a cubic polynomial between points 2 and 3. A similar polynomial is then fit to points A, B, C and D in the y-direction to find $Q_o$. Overlapping quadratic interpolation polynomials are also employed by Whittaker and Petersen (1977) for cross-section analysis, and by Petersen (1977) in three-dimensional isentropic analysis. An equivalent method which uses cubic Hermite polynomials in cross-section analysis is presented by Shapiro and Hastings (1973).

The final two methods, L2 and L3, apply a straightforward least squares approach to fitting two-dimensional polynomials to the same 16 points used in method B2. Method L2 fits a 2-dimensional quadratic and method L3 a 2-dimensional cubic.

Method L2 : $$Q_o = a_1x^2 + a_2xy + a_3y^2 + a_4x + a_5y + a_6 \quad (7)$$

Method L3 : $$Q_o = b_1x^3+b_2x^2y+b_3xy^2+b_4y^3+b_5x^2+b_6xy+b_7y^2+b_8x+b_9y+b_{10} \quad (8)$$

The a and b coefficients for these equations are found using normal least squares methods.

## 3. Test Data

Meaningful tests of the methods described above require data sets with known values at both grid and observation points. Three-dimensional analytic functions of height, temperature and wind were chosen to provide such data sets, since values at a point can be determined "exactly" simply by specifying the coordinates. The analytic functions were chosen to be realistic meteorologically with nonlinearity adequate to identify the relative problems and merits of the interpolation methods. The analytic functions are modifications of those presented by Sanders (1971). Fields generated by these functions exhibit a decrease of temperature variance and an increase in height and wind variances with altitude up to the tropopause (realistic midlatitude properties). Height and temperature fields derived at 500mb from these functions are illustrated in Figure 4. The fields are superimposed on the grid mesh used in these experiments.

## 4. Results

Tests were performed for 75 simulated observation points which are shown in Figure 5. The locations for these observations were chosen from a typical set of Nimbus 6 soundings taken during August, 1975. Comparisons of interpolated vs. observed values were made for each interpolation method at the 850, 500 and 300mb levels. The results of these comparisons, which

FIGURE 4.

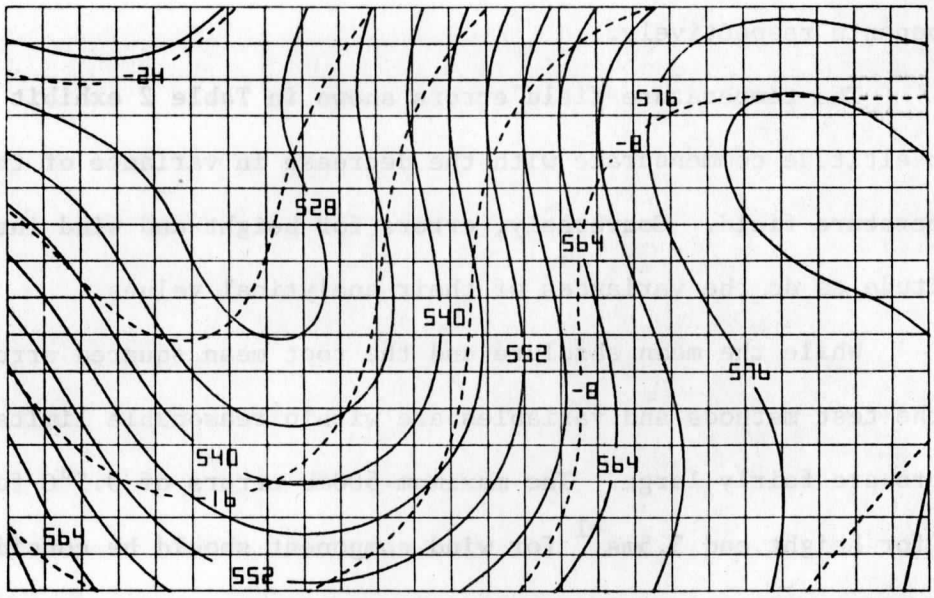


**Sample analytic fields for height (solid:dkm) and temperature (dashed:°C).**

FIGURE 5.

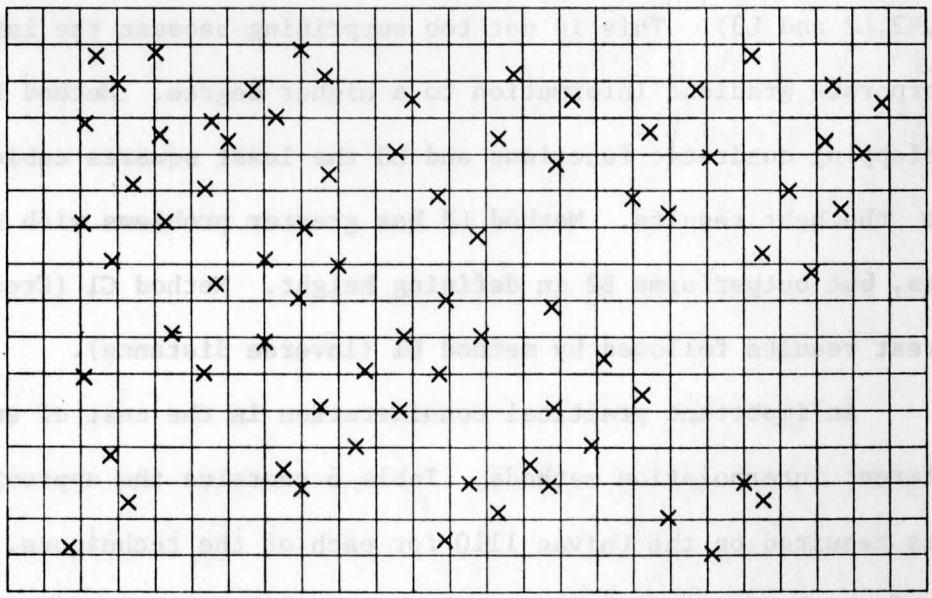

**Observation locations.**

are presented in Tables 2 through 5, for temperature, height, u and v wind components respectively.

The temperature field errors shown in Table 2 exhibit a decrease with altitude commensurate with the decrease in variance of the analytic temperature field. Conversely, errors for height and wind increase with altitude as do the variances of their analytical values.

While the mean absolute and the root mean squared errors for most of the test methods and variables are within reasonable limits, the maximum errors are fairly large. The maximum 500mb errors of 0.5°C for temperature, 15m for height and $3.5ms^{-1}$ for wind component should be considered unacceptable since this interpolation is only the first step in the analysis, and such large errors in this step will probably degrade the final analysis. In almost all cases, the maximum errors are negative, indicating problems in defining maxima.

In general, the errors for the simple distance weighting methods (D1,D2 and C1) are greater than those from the polynomial fitting methods (B1,B2,L2 and L3). This is not too surprising because the latter methods incorporate gradient information to a higher degree. Method B2 which uses overlapping quadratic functions and L3 the least squares cubic method provide the best results. Method L3 has greater problems with the wind variables, but outperforms B2 in defining height. Method C1 (Cressman) gave the poorest results followed by method D1 (inverse distance).

An important practical consideration is the cost of employing the different interpolation methods. Table 6 contains the approximate computing times required on the Univac 1110 for each of the techniques. Note that B2, one of the best two methods, required only 14% more time than the first four

TABLE 2. TEST RESULTS FOR TEMPERATURE (°C)

| | | INTERPOLATION METHODS | | | | | | |
|---|---|---|---|---|---|---|---|---|
| | MB LEVEL | DI | D2 | CI | BI | B2 | L2 | L3 |
| MEAN ABSOLUTE ERRORS | 850 | 0.16 | 0.10 | 0.22 | 0.03 | 0.00 | 0.01 | 0.00 |
| | 500 | 0.10 | 0.06 | 0.14 | 0.02 | 0.00 | 0.01 | 0.00 |
| | 300 | 0.04 | 0.03 | 0.06 | 0.01 | 0.00 | 0.00 | 0.00 |
| ROOT MEAN SQUARED ERRORS | 850 | 0.20 | 0.13 | 0.27 | 0.04 | 0.00 | 0.01 | 0.00 |
| | 500 | 0.13 | 0.08 | 0.17 | 0.02 | 0.00 | 0.01 | 0.00 |
| | 300 | 0.06 | 0.04 | 0.07 | 0.01 | 0.00 | 0.00 | 0.00 |
| MAX. ERRORS | 500 | -0.47 | -0.25 | -0.40 | -0.06 | 0.01 | 0.02 | 0.01 |

TABLE 3. TEST RESULTS FOR HEIGHT (METERS)

| | | INTERPOLATION METHODS | | | | | | |
|---|---|---|---|---|---|---|---|---|
| | MB LEVEL | DI | D2 | CI | BI | B2 | L2 | L3 |
| MEAN ABSOLUTE ERRORS | 850 | 2.2 | 1.4 | 2.8 | 0.6 | 0.3 | 0.4 | 0.3 |
| | 500 | 3.3 | 2.2 | 4.7 | 0.8 | 0.3 | 0.4 | 0.3 |
| | 300 | 4.3 | 2.8 | 6.1 | 1.0 | 0.3 | 0.5 | 0.3 |
| ROOT MEAN SQUARED ERRORS | 850 | 2.8 | 1.7 | 3.6 | 0.7 | 0.5 | 0.5 | 0.4 |
| | 500 | 4.5 | 2.8 | 5.9 | 1.0 | 0.5 | 0.5 | 0.4 |
| | 300 | 5.7 | 3.6 | 7.4 | 1.2 | 0.5 | 0.6 | 0.4 |
| MAX. ERRORS | 500 | -14.9 | -8.3 | -14.3 | -2.5 | -1.4 | 1.4 | 1.1 |

TABLE 4. TEST RESULTS FOR U COMPONENT (M/S)

| | | INTERPOLATION METHODS | | | | | | |
|---|---|---|---|---|---|---|---|---|
| | MB LEVEL | DI | D2 | CI | BI | B2 | L2 | L3 |
| MEAN ABSOLUTE ERRORS | 850 | 0.23 | 0.12 | 0.30 | 0.06 | 0.01 | 0.05 | 0.02 |
| | 500 | 0.41 | 0.27 | 0.52 | 0.15 | 0.07 | 0.16 | 0.11 |
| | 300 | 0.48 | 0.30 | 0.61 | 0.17 | 0.07 | 0.21 | 0.18 |
| ROOT MEAN SQUARED ERRORS | 850 | 0.30 | 0.15 | 0.38 | 0.09 | 0.05 | 0.11 | 0.06 |
| | 500 | 0.56 | 0.44 | 0.74 | 0.28 | 0.21 | 0.35 | 0.25 |
| | 300 | 0.72 | 0.45 | 0.85 | 0.25 | 0.16 | 0.47 | 0.41 |
| MAX. ERRORS | 500 | -1.74 | -1.68 | -3.15 | -1.57 | -1.21 | -2.05 | -1.39 |

TABLE 5. TEST RESULTS FOR V COMPONENT (M/S)

| | | INTERPOLATION METHODS | | | | | | |
|---|---|---|---|---|---|---|---|---|
| | MB LEVEL | DI | D2 | CI | BI | B2 | L2 | L3 |
| MEAN ABSOLUTE ERRORS | 850 | 0.30 | 0.17 | 0.39 | 0.08 | 0.05 | 0.06 | 0.05 |
| | 500 | 0.57 | 0.32 | 0.72 | 0.16 | 0.13 | 0.23 | 0.18 |
| | 300 | 0.66 | 0.36 | 0.84 | 0.17 | 0.12 | 0.33 | 0.26 |
| ROOT MEAN SQUARED ERRORS | 850 | 0.39 | 0.23 | 0.50 | 0.11 | 0.07 | 0.10 | 0.08 |
| | 500 | 0.78 | 0.54 | 0.94 | 0.44 | 0.35 | 0.58 | 0.44 |
| | 300 | 0.84 | 0.50 | 1.06 | 0.39 | 0.26 | 0.73 | 0.61 |
| MAX. ERRORS | 500 | -3.12 | -3.56 | -3.04 | -3.46 | -2.48 | -3.69 | -2.87 |

Table 6

| Method | Time (seconds) |
|---|---|
| D1 | 4.326 |
| D2 | 4.352 |
| C1 | 4.388 |
| B1 | 4.293 |
| B2 | 4.859 |
| L2 | 15.714 |
| L3 | 16.945 |

methods, despite using data from 16 rather than 4 grid points. Both least squares methods require relatively large amounts of time.

In conclusion, B2, the overlapping quadratic polynomial method described by Bleck and Haagenson (1968) appears to be the best method among those considered here for providing grid to observation interpolations. Fitting a least squares cubic gives comparable accuracy, but requires many more computations and thus computer time. It is not unreasonable to assume that these results are applicable to other situations which require the estimation of meteorological variables from a uniform grid to either another uniform grid or to nonuniform locations.

## References

Bleck, R. and P.L. Haagenson, 1968: Objective analysis on isentropic surfaces. NCAR Technical Notes, NCAR-TN-39, Boulder, Colorado, 27 pp.

Cressman, G., 1959: An operation objective analysis system. Mon. Wea. Rev., 87, 367-374.

Petersen, R.A., 1977: Three-dimensional objective analysis based on isentropic cross-sectional techniques. Meteorological Applications of Satellite Indirect Soundings II, Project Report, NOAA Grant 04-4-158-2, Dept. of Meteorology, University of Wisconsin, Madison.

Sanders, F., 1971: Analytic solutions of the nonlinear omega and vorticity equations for a structurally simple model of disturbances in the baroclinic westerlies. Mon. Wea. Rev., 99, 393-407.

Shapiro, M.A. and J.T. Hastings, 1973: Objective cross-section analyses by Hermite polynomial interpolation on isentropic surfaces. J. Appl. Meteor., 12, 753-762.

Whittaker, T.M. and R.A. Petersen, 1977: Objective cross-sectional analyses incorporating thermal enhancement of the observed winds. Mon. Wea. Rev., 105, 147-153.

# EFFECTS OF POST-PROCESSING ON THE NATIONAL METEOROLOGICAL CENTER'S PRIMITIVE EQUATION PREDICTION MODELS

BY

RICHARD ALEXANDER HYDE

## Abstract

A brief review is given of some of the post-processing operations (cf. time-averaging, unstaggering, space filtering, and balancing) used by the National Meteorological Center on the raw numerical forecast fields of its primitive equation prediction models. A theoretical investigation hypothesizes that these operations significantly alter the forecast data so that the model's constraints of a hydrostatic and mass conserving atmosphere may be lost after post-processing occurs. This contention is supported when diagnostic relationships consistent with the model's finite differencing are used to analyze hydrostatic equilibrium and mass continuity in post-processed data from an LFM forecast. The post-processed data set shows a hydrostatic defect of order 1% and a mass defect of much greater relative error; the nature of the error varies between grid points. The defects are greater if the diagnostic scheme (even when of higher order) is not consistent with the numerical scheme in the model. The study also finds that for diagnostics done on the post-processed forecast fields (1) pressure coordinate equations may have nonhydrostatic correction terms of significant magnitude and (2) secondary circulations may be altered in importance with respect to advective processes.

List of Symbols

| | |
|---|---|
| $\alpha$ | polynomial coefficients |
| c | phase speed |
| $C_p$ | specific heat of air at constant pressure |
| $\Delta\pi$ | finite difference for vertical space variable; grid spacing |
| $\Delta t$ | finite difference for time; time step |
| $\Delta x, \Delta y$ | finite difference for horizontal space variables; grid spacings |
| $\Delta z$ | amplitude of synoptic scale disturbance |
| $\Delta z'$ | amplitude of gravity wave |
| $\eta$ | hydrostatic defect |
| $f, f_o$ | coriolis parameter |
| F | arbitrary atmospheric variable |
| g | gravitational acceleration |
| i,j,k | indices for spacial discretization |
| J | Jacobian of coordinate transformation: cartesian to pressure |
| L | wavelength; also wavelength of synoptic scale disturbance |
| L' | wavelength of gravity wave |
| m | map factor |
| $M_d$ | multiplicative factor for desloshing error |
| $M_{fd}$ | multiplicative factor for finite differencing |
| $M_s$ | multiplicative factor for smoothing error |
| $M_t$ | multiplicative factor for time averaging error |
| $M_u$ | multiplicative factor for unstaggering error |
| n | index for time discretization |
| $\omega$ | vertical velocity in pressure coordinates |
| p | pressure; independent vertical coordinate variable |

$\pi$ Exner function; independent vertical coordinate variable

$\phi = gz$ geopotential

$R$ gas constant

$\rho$ density

$\sigma = p/p_{sfc}$ independent vertical coordinate variable

$\hat{\sigma}$ static stability

$\dot{\sigma}$ vertical velocity in $\sigma$ coordinates

$t$ time

$T$ temperature

$T_{pp}$ post-processed temperature

$\theta$ potential temperature

$u$ horizontal velocity, x component

$u_g$ geostrophic wind, x component

$v$ horizontal velocity, y component

$\vec{V}_2$ velocity vector, horizontal component

$\vec{V}_3$ velocity vector

$\vec{V}_g$ geostrophic velocity vector, horizontal component

$w$ vertical velocity in cartesian coordinates

$x,y$ independent horizontal coordinate variables

$z$ independent vertical coordinate variable

$\zeta_g$ geostrophic vorticity, vertical component

Operators

$\vec{\nabla}_{2,\chi}$ horizontal gradient in $\chi$ coordinates

$\vec{\nabla}_{3,\chi}$ gradient operator in $\chi$ coordinates

## 1. Introduction

The primitive equation, limited fine mesh numerical model ("the LFM") of the National Meteorological Center (NMC) has been used extensively in recent years by the National Weather Service as an aid in operational forecasting. As with other numerical models, the LFM also has been used to generate data sets for diagnostic studies of atmospheric processes. Usually the LFM fields studied are not actual output of the model. Instead facsimile maps or data save tapes are used. Such maps and tapes are produced by subjecting the numerical results of the LFM's integrations to a variety of operations in which the output is transformed into a data set which is both more useful for routine analysis (e.g. sigma coordinates are replaced by pressure coordinates) and also more consistent with observed atmospheric behavior (e.g. gravity waves and computational instabilities are removed). Collectively these operations are termed "post-processing". The numerical integrations of the LFM comprise a data set termed "$\sigma$-files"; and the data which result after post-processing occurs are included in the "p-files".

The paper which follows deals with some of the effects of post-processing. In Chapter 2, a brief discussion of some of NMC's post-processing operations is followed by a comparison of several LFM fields before and after post-processing. Chapter 3 invokes basic arguments to explore theoretically the error which may result from various post-processing operations. The effect this error may have upon hydrostatic equilibrium, mass continuity, and secondary circulation compensation is explored to ascertain if a diagnostic study of the physical processes in a post-processed model atmosphere could yield results inconsistent with the physics of the model. With this understanding of post-processing error, an actual LFM forecast is diagnostically examined in Chapter 4.

## 2. NMC's post-processing of the LFM's numerical output

Documents by Stackpole (1968), Stackpole (1969), and Gerrity and Newell (1976) give a fairly complete description of the manner in which NMC transforms numerical, sigma coordinate output (σ-files) into post-processed, pressure coordinate fields (p-files). This chapter will review NMC's post-processing operations (except for the treatment of moisture parameters) and will end with an actual comparison of several σ-file variables and their corresponding p-file variables.

### (a) Computation of the pressure coordinate vertical velocity.

Gerrity and Newell (1976) describe the post-processing computation of $\omega$ (= dp/dt) from the model's vertical velocity $\dot{\sigma}$ (= dσ/dt):

> "...the output code calculates $\omega$ by means of $\omega(x,y,\sigma,t) = \frac{dp}{dt} = \frac{\partial p}{\partial t_\sigma} + \vec{V}_2(x,y,\sigma,t)\cdot\vec{\nabla}p(x,y,\sigma,t) + \dot{\sigma}(x,y,\sigma,t)\,\frac{\partial p}{\partial \sigma}\,(x,y,t)$. The calculation is made for the midpoint of each σ-layer at every second time step during the 2 hours preceding a 6, 12, 18, etc. forecast hour. The average value of this calculation over the 2-hour period is accumulated."*

### (b) Extrapolation and unstaggering of variables from sigma coordinates to pressure coordinates

The model's σ-coordinate computations are interpolated to standard p-coordinate levels during post-processing. This procedure is described by Stackpole (1969):

> [For the variables u,v,θ located at the midpoints of σ-layers, the operation is]"...to assign the layer variables a value of pressure corresponding to the mean value of π [the Exner function, = $(p/1000^{R/C_p}$] for that layer. Then all the variables are assumed to vary linearly

---

*Gerrity and Newell [1976], page 5.

with $\pi$ from the $\sigma$ layers to the desired pressure levels. ...Indeed this is the general rule--interpolation to a particular surface is made linearly in $\pi$ from the centers of the two $\sigma$ layers bracketing the surface. As with all general rules, there is an exception--no interpolation is made across or through the tropopause...[That is], we would not use the [values of a variable] of the layers above and below the tropopause (even though these are the layers bracketing the desired pressure surface) but would [either] extrapolate down from the two stratosphere layers... [or] would extrapolate upward from the two upper troposphere layers [whichever is appropriate]." [For the variables $\phi$ and $\dot{\sigma}$ located at the $\sigma$ levels,] "...the interpolations of this quantity are made directly from the appropriate one-on-each-side $\sigma$ surface to the pressure level."* [$\dot{\sigma}$ is interpolated in the horizontal.]

In the process of interpolation, the staggered relationship of the model's variables is eliminated. Figures 1(a) and 1(b) show respectively the staggered, $\sigma$-coordinate grid array of the model and the unstaggered, p-coordinate grid array of the post-processed data.

(c) Desloshing the height field

Gerrity and Newell (1976) give a rationale and procedure for altering the geopotential height field during post-processing.

"Because of the limited area nature of the LFM, there is a tendency for the numerical solutions to exhibit a trapped, large-scale, predominantly external gravity wave. To eliminate this wave, the raw forecast geopotential is not used directly. The so-called "deslosh" routine involves the calculation of a geopotential which satisfies the inverse-balance equation at 500 mb. The forcing terms of this

---

*Stackpole (1969), page II-18.

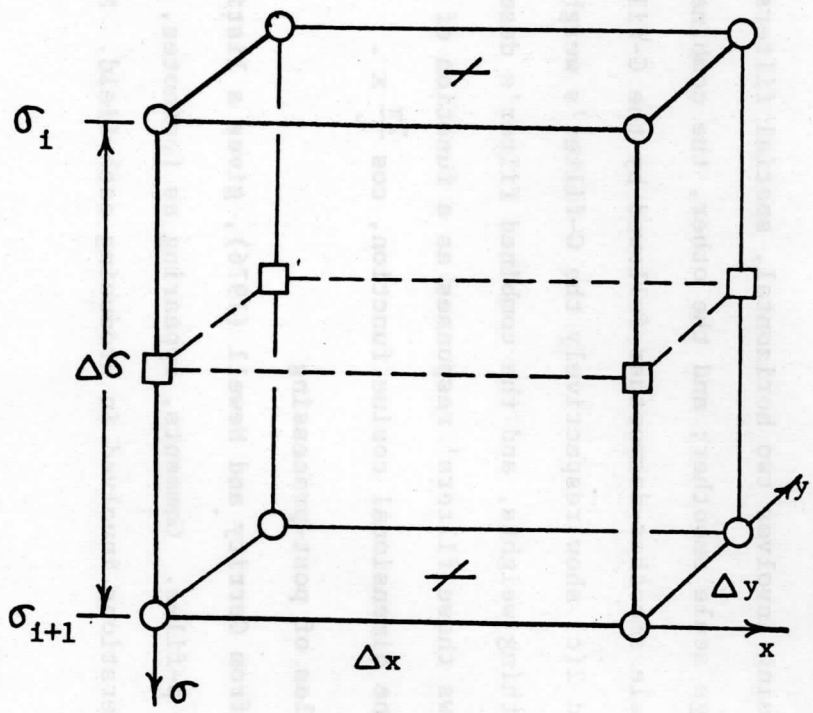


FIGURE 1a
[from Shuman and Hovermale (1968)]

○ = z,π
□ = u,v,θ
\+ = σ̇

LFM σ-coordinate, staggered grid array.

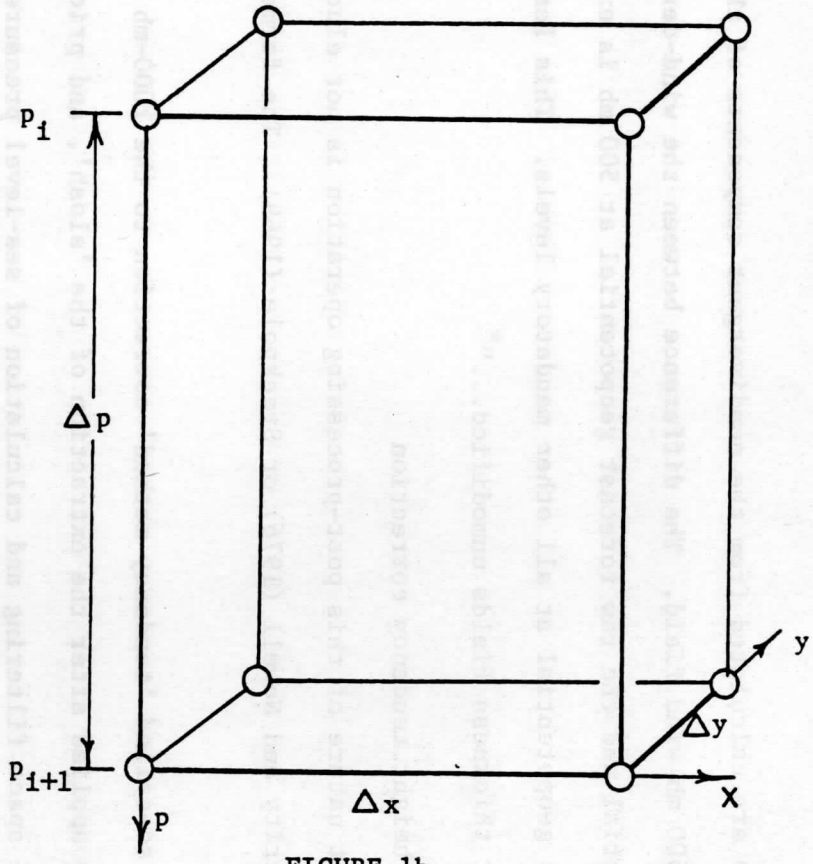


FIGURE 1b

○ = p,ϕ,u,v,θ,ω

Post-processed, p-coordinate, unstaggered grid array.

equation are calculated from the nondivergent components of the predicted 500 mb wind field. The difference between the wind-derived geopotential and the raw forecast geopotential at 500 mb is extracted from the geopotential at all other mandatory levels. This leaves the forecast thickness fields unmodified..."*

(d) 1000 mb height tendency correction

The exact nature of this post-processing operation is not elucidated by either Gerrity and Newell (1976) or Stackpole (1969). The former note only that

"...the so-called 'tendency method' correction to the 1000-mb height field is applied after the extraction of the 'slosh', and prior to both the space filtering and calculation of sea-level pressure."**

(e) Horizontal filtering (smoothing)

NMC's post-processing involves two horizontal, spatial filters. One, the G filter, is a large scale smoother; and the other, the combined filter, consists of a small scale smoother-desmoother followed by the G-filter. Figures 2(a), 2(b), and 2(c) show respectively the G-filter's weights, the combined filter's smoothing weights, and the combined filter's desmoothing weights. Figure 3 shows these filters' responses as a function of wavelength, L, when applied to a one dimensional cosine function, $\cos \frac{2\pi}{L} x$ .

(f) Summary and examples of post-processing

Table 1, adapted from Gerrity and Newell (1976), gives a listing of the fields included in the p-files. Comments, appearing as footnotes, summarize the post-processing operations involved in producing each field. Notice,

---

*Gerrity and Newell (1976), pages 3 and 4.

**Gerrity and Newell (1976), page 5.

| | | | | | | |
|---|---|---|---|---|---|---|
| $\frac{1}{1024}$ | 0 | $\frac{-9}{1024}$ | $\frac{-16}{1024}$ | $\frac{-9}{1024}$ | 0 | $\frac{1}{1024}$ |
| 0 | 0 | 0 | 0 | 0 | 0 | 0 |
| $\frac{-9}{1024}$ | 0 | $\frac{81}{1024}$ | $\frac{144}{1024}$ | $\frac{81}{1024}$ | 0 | $\frac{-9}{1024}$ |
| $\frac{-16}{1024}$ | 0 | $\frac{144}{1024}$ | $\frac{256}{1024}$ | $\frac{144}{1024}$ | 0 | $\frac{-16}{1024}$ |
| $\frac{-9}{1024}$ | 0 | $\frac{81}{1024}$ | $\frac{144}{1024}$ | $\frac{81}{1024}$ | 0 | $\frac{-9}{1024}$ |
| 0 | 0 | 0 | 0 | 0 | 0 | 0 |
| $\frac{1}{1024}$ | 0 | $\frac{-9}{1024}$ | $\frac{-16}{1024}$ | $\frac{-9}{1024}$ | 0 | $\frac{1}{1024}$ |

FIGURE 2(a)

from Gerrity & Newell (1976)

Weights of the 49-point G-filter.

| | | |
|---|---|---|
| $\frac{1}{16}$ | $\frac{1}{8}$ | $\frac{1}{16}$ |
| $\frac{1}{8}$ | $\frac{1}{4}$ | $\frac{1}{8}$ |
| $\frac{1}{16}$ | $\frac{1}{8}$ | $\frac{1}{16}$ |

FIGURE 2(b)

from Gerrity & Newell (1976)

Weights of the 9-point combined filter's smoother.

| | | |
|---|---|---|
| $\frac{1}{16}$ | $\frac{-3}{8}$ | $\frac{1}{16}$ |
| $\frac{-3}{8}$ | $\frac{9}{4}$ | $\frac{-3}{8}$ |
| $\frac{1}{16}$ | $\frac{-3}{8}$ | $\frac{1}{16}$ |

FIGURE 2(c)

from Gerrity & Newell (1976)

Weights of the 9-point combined filter's desmoother.

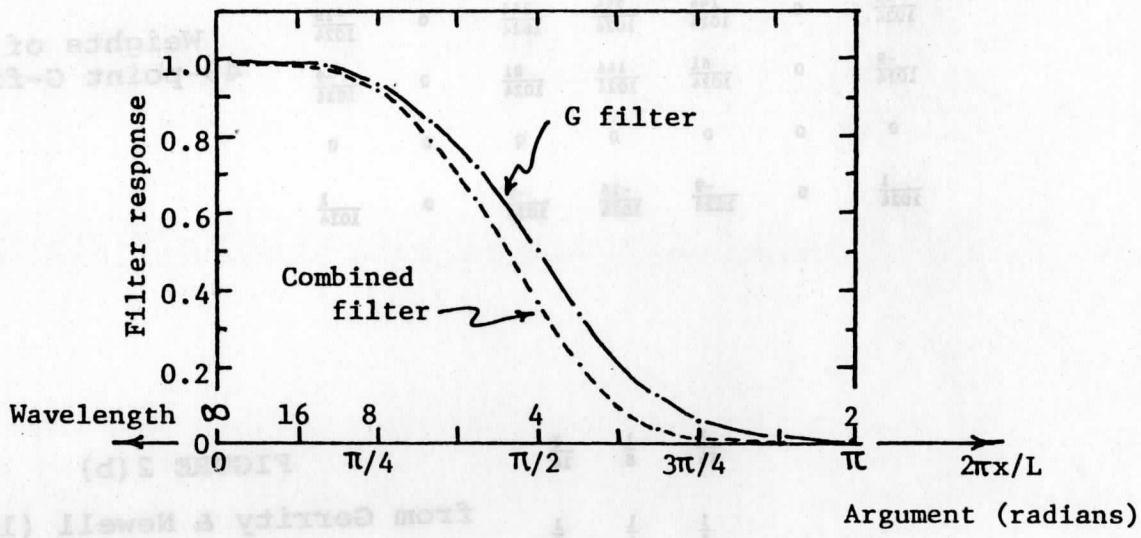


FIGURE 3

[from Stackpole, (1968)]

Response of NMC's filters applied to cos(2πx/L)

TABLE 1 [from Gerrity and Newell (1976)]

| FIELD | LEVEL | UNITS | POST-PROCESSING OPERATIONS |
|---|---|---|---|
| 1. Geopotential height | 850mb-100mb<br>1000mb | m | b,c,e<br>c,d,e |
| 2. Winds (u,v) | 1000mb-100mb | $m\ s^{-1}$ | b,e |
| 3. Air temperature | 1000mb-100mb | °K | b,e |
| 4. Dewpoint temperature | 1000mb-300mb | °K | b,e |
| 5. p-coord. vertical velocity | 1000mb-400mb and 200mb | $\mu b\ s^{-1}$ | a,b,e |
| 6. Tropopause pressure | | mb | h |
| 7. Absolute vorticity | 500mb | $s^{-1}$ | b,e |
| 8. Stream function | 500mb | $m^2 s^{-1}$ | b,e |
| 9. Mean relative humidity | | % | g |
| 10. Sea level pressure | | mb | d,f |
| 11. Lifted index | | °K | g |
| 12. Quantitative precipitation | | m | g |
| 13. Tropopause temperature | | °K | b |
| 14. σ layer relative humidity | 3 trop. layers | % | h |
| 15. Boundary layer θ,u,v | 25mb above ground | various | h |
| 16. Surface level vertical velocity | σ level at ground | $\mu b\ s^{-1}$ | h |
| 17. Surface pressure | σ level at ground | mb | h |

(a) Computed from $\dot{\sigma}$ and time averaged
(b) Interpolated from σ to p (θ,u,v vertically unstaggered; ω horizontally unstaggered.)
(c) Desloshed
(d) Computed by tendency method
(e) Filtered horizontally
(f) "The sea-level pressure is calculated from the resultant 1000mb geopotential [tendency method] and 1000-500mb thickness. The use of the smoothed 1000mb geopotential precludes any requirement for smoothing the calculated sea level pressure." Gerrity and Newell (1976) page 5.
(g) Not considered in this study although post-processing operations may occur.
(h) None; raw model output (σ-files) placed directly into p-files without alteration.

however, that a few of the model's actual, σ-coordinate variables (e.g. 6, 14, 15, 16, 17) are simply incorporated without alteration into the p-files.

That post-processing has a considerable effect can be evidenced by comparing several of the raw, σ-coordinate fields included in the p-files with the corresponding post-processed fields.* Figure 4 shows the model's σ surface pressure (Table 1, item 17) and the post-processed mean sea level pressure (Table 1, item 10). Notice that over the Atlantic Ocean (where the σ surface is at sea level) the post-processed data are missing the severe $2\Delta y$ oscillation observed in the σ data. As a second example, Figure 5 compares the horizontal velocity field in the σ planetary boundary layer (Table 1, item 15) with the post-processed wind field at 1000 mb (Table 1, item 2). Granted, some difference in these wind fields must be expected both because they are at different levels and because the σ and p surfaces may have different slopes. However, this likely does not account for the fact that the extreme convergence and divergence seen in the σ data are absent in the post-processed fields. Together, these two examples provide evidence that the forecast variables of the model suffer substantial alteration during post-processing.

## 3. Theoretical examination of error introduced by post-processing

Chapter 2 indicated that model forecast fields are altered during post-processing. A basic consideration, then, is the quantitative degree to which the atmosphere that is obtained by post-processing is different from its parent atmosphere which was predicted by the model's equations and constraints

---

*For this comparison, data were taken from save-tapes of the 24 hour forecast of the LFM run initialized at 12 GMT on 23 Feb. 1975.

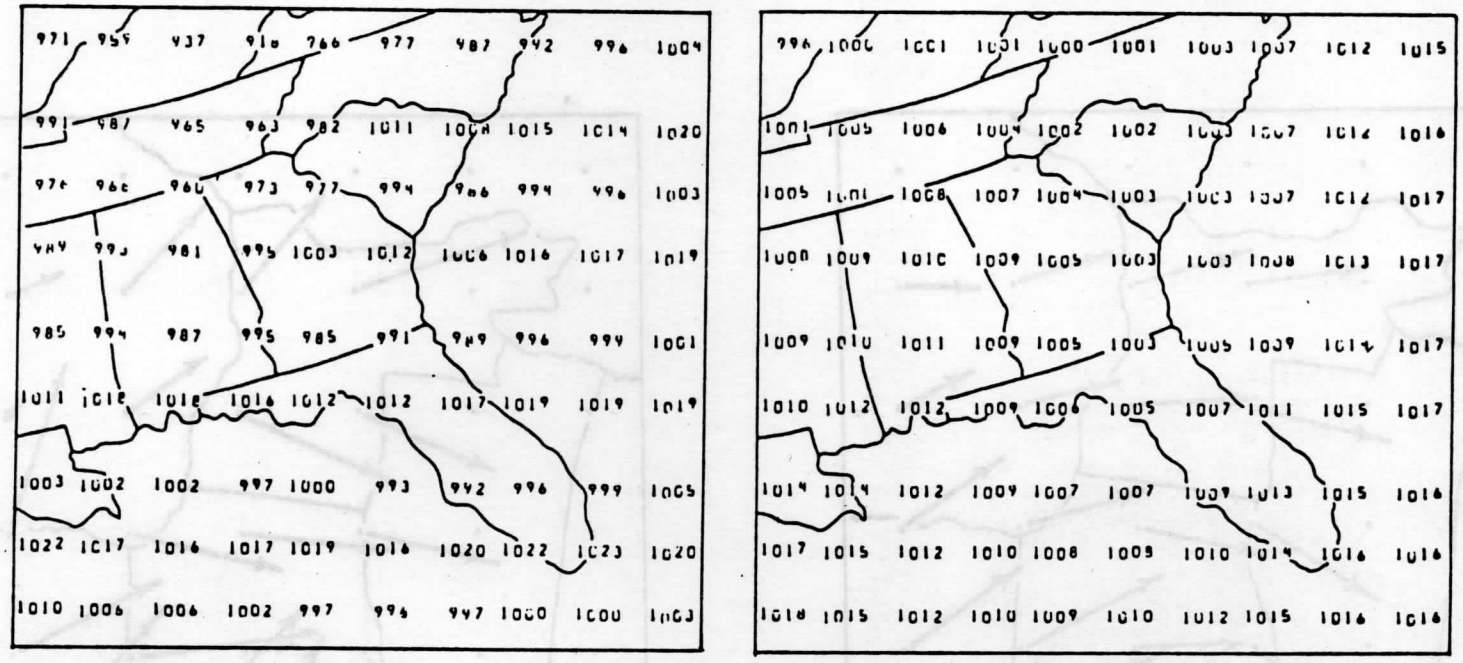

FIGURE 4

LEFT: LFM's raw $\sigma$-coordinate surface pressure.

RIGHT: LFM's post-processed mean sea level pressure.

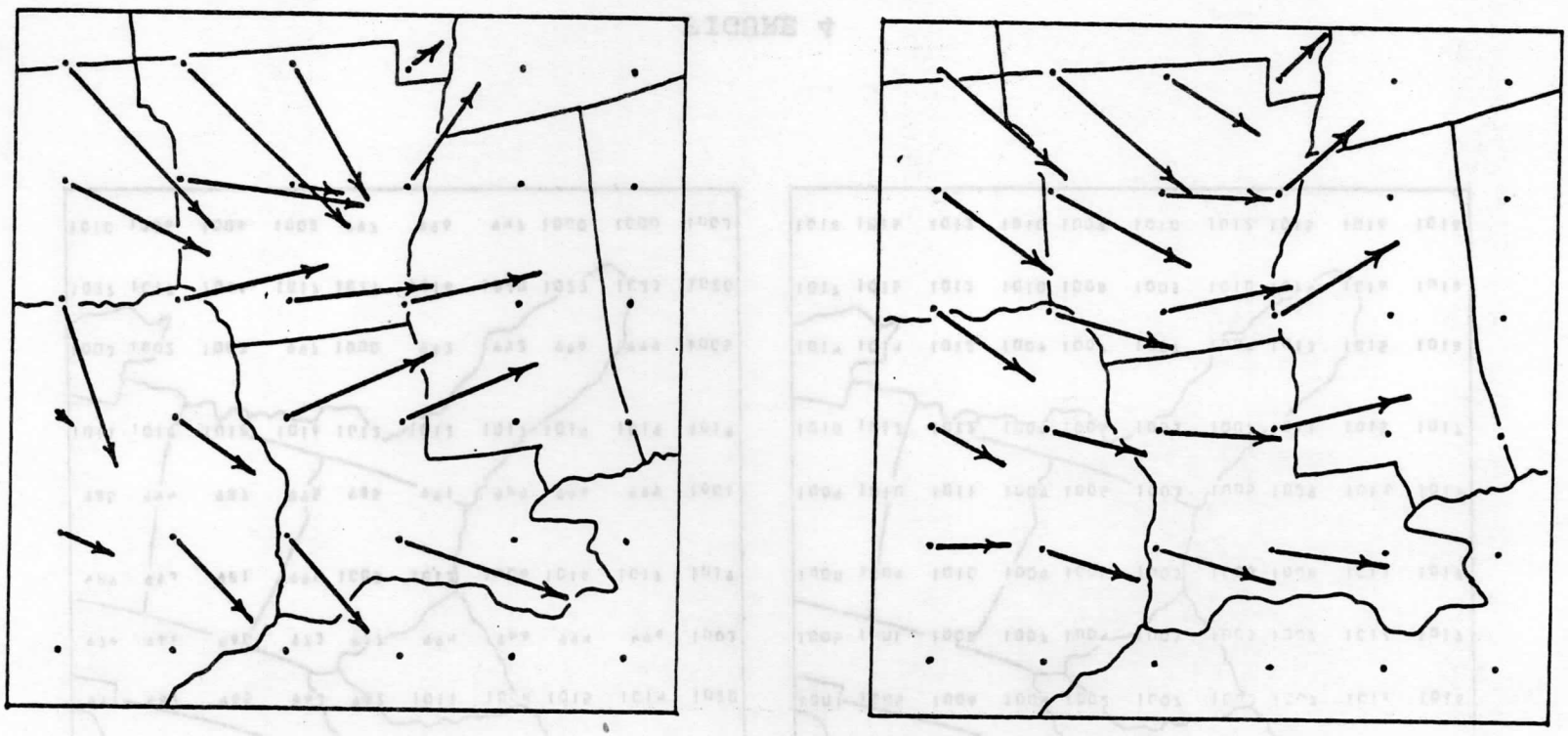

FIGURE 5

LEFT: LFM's raw $\sigma$-coordinate boundary layer winds.

RIGHT: LFM's post-processed p-coordinate 1000mb winds.

(given the initial conditions). For example, if the model is hydrostatic, will the post-processed fields of temperature and geopotential also be in hydrostatic equilibrium?

Some investigation of such questions in related aspects has already appeared in the literature. Mahlman and Moxim (1976), when using a procedure similar to NMC's for computing $\omega$ from $\dot{\sigma}$ in their general circulation/tracer model, found that "...the change of coordinates can lead to serious error"; computational residuals were as large as the net tendency term in their budget analysis. However, by employing an alternative method to obtain $\omega$, they were able to considerably reduce the error. The authors concluded that there was "...substantial improvement ...from avoiding an ambiguous direct calculation of $\omega$ from sigma coordinate information."

Apart from the investigation by Mahlman and Moxim, the literature contains virtually no discussion of the effect of post-processing operations. Unfortunately, a complete, quantitative examination here is prohibited by two factors. First, certain of the post-processing operations are insufficiently described in the literature to allow a reasonable, theoretical investigation of their effect. Second, a complete set of $\sigma$ coordinate data from the model for a diagnostic analysis was not available for this study. Consequently, this chapter will turn to very basic arguments to examine the error introduced by four of the post-processing operations: time-averaging, unstaggering, desloshing, and filtering. These errors will be compared with the truncation error of finite differencing; also they will be examined for their potential effect on hydrostatic equilibrium and mass continuity as well as the quasi-geostrophic vorticity and energy relationships.

(a) The error in time-averaging

The LFM's vertical motion field is subjected to the post-processing

operation of time-averaging (Sec. 2(a)). When applied to a one-dimensional Fourier component* discretized in time, the component suffers both an amplitude reduction and a phase shift.

$$[\cos(\tfrac{2\pi}{L} cn\Delta t)]_{\substack{\text{post-}\\\text{processed}}} = \overline{\cos(\tfrac{2\pi}{L} cn\Delta t)}^{t} = M_t \cos(\tfrac{2\pi}{L} c(n-6)\Delta t),$$

where $M_t = \frac{1}{7}\{1 + 2\cos(\frac{2\pi}{L} c2\Delta t) + 2\cos(\frac{2\pi}{L} c4\Delta t) + 2\cos(\frac{2\pi}{L} c6\Delta t)\}$,

Figure 6 shows the weights at each time step; Figure 7 shows the multiplicative factor, $M_t$, as a function of wavelength, $L = c\Delta t$ (c is the phase speed). Thus, in the LFM, the post-processed vertical velocity not only may be reduced in amplitude but also it is more like the vertical velocity field one hour (6 time steps) prior to the forecast rather than like the velocity field at the forecast time.

(b) The error in unstaggering

During post-processing, certain variables are removed from their staggered positions at the mid-levels of layers (Sec. 2(b)). The error introduced can be seen schematically in Figure 8 and Figure 9. In Figure 8 a variable, say temperature, (T), is represented by the solid circles and solid line. In Figure 9, (T) is again shown along with the unstaggered (post-processed) temperature, ($T_{pp}$), which is represented by the open circles and dashed line.

From Figure 9 the effect of unstaggering (T) to form ($T_{pp}$) becomes immediately obvious; the post-processed temperature, $(T_{pp})_{i+\frac{1}{2}}$, representing a layer say from (i) to (i+1) (obtained from some average of $(T_{pp})_i$ and $(T_{pp})_{i+1}$), may be quite different from the original temperature of the layer,

---

*Only a single Fourier component prior to synthesis need be investigated.

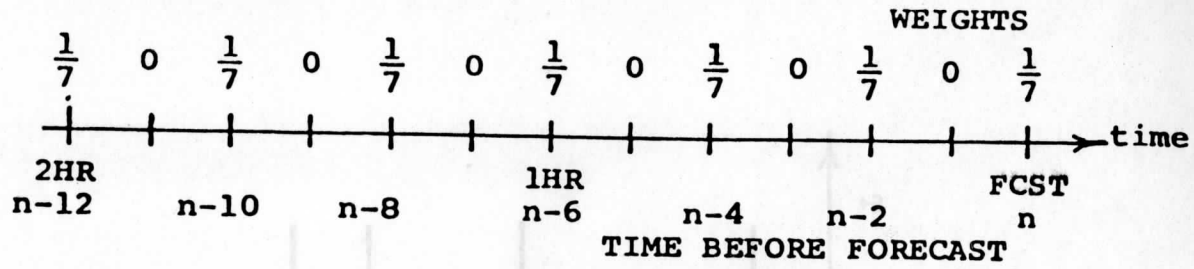


FIGURE 6 (above)

Weights for time-averaging.

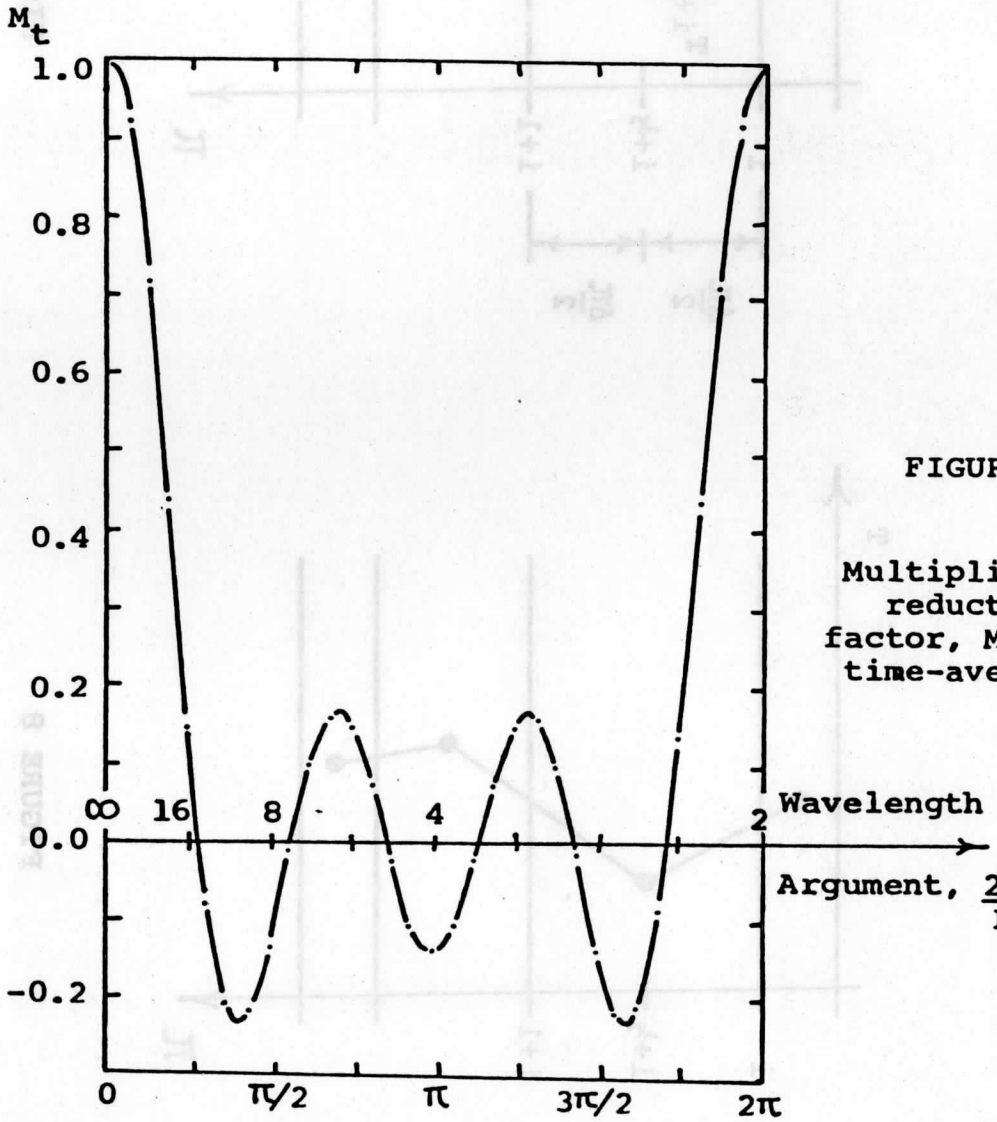


FIGURE 7

Multiplicative reduction factor, $M_t$, for time-averaging.

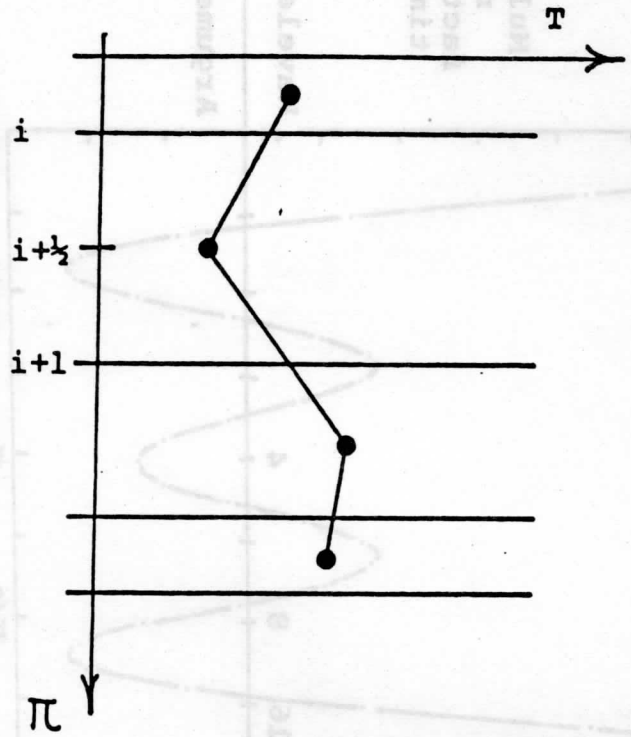


FIGURE 8

Model output, T.
(See text)

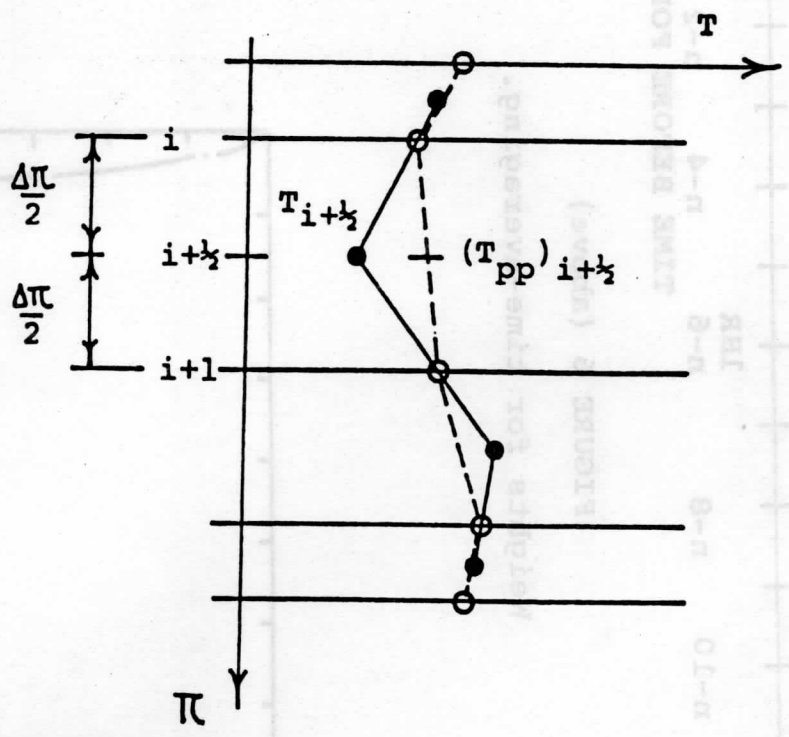


FIGURE 9

Model output, T, with unstaggered (post-processed) profile, $T_{pp}$, derived from it.
(See text)

$(T)_{i+\frac{1}{2}}$ . Quantitatively, if

$$(T_{pp})_{i+\frac{1}{2}} = M_u (T)_{i+\frac{1}{2}} ,$$

where $M_u$ is a multiplicative factor due to unstaggering and $(T_{pp})_{i+\frac{1}{2}}$ is the mean for the layer, then the relative error

$$\frac{(T)_{i+\frac{1}{2}} - (T_{pp})_{i+\frac{1}{2}}}{(T)_{i+\frac{1}{2}}} = 1 - M_u = - \frac{(\Delta\pi)^2}{2} \frac{(\partial^2 T/\partial\pi^2)_{i+\frac{1}{2}}}{(T)_{i+\frac{1}{2}}} .$$

That is, the error is proportional to the curvature of the curvature of the profile of the variable (here, temperature). Similar results would be expected for an analysis of unstaggering in the horizontal.

(c) The error in desloshing

The raw forecast geopotential of the model is desloshed during post-processing (Sec. 2(c)). Figure 10 gives a schematic view of desloshing a predominately external gravity wave (of wavelength L' and amplitude $\Delta z'$) from the synoptic field (of wavelength L and amplitude $\Delta z$). The method preserves thickness. However, any quantity in which horizontal derivatives of the height field must be calculated--geostrophic winds, geostrophic vorticities, etc.--may be affected by the desloshing. For example, consider the geostrophic advection of geostrophic vorticity. Let the geostrophic velocity be scaled as $u_g \sim (\frac{\Delta z}{L} + \frac{\Delta z'}{L'}) = \frac{\Delta z}{L} [1 + (\frac{\Delta z'}{\Delta z})(\frac{L}{L'})]$ and the gradient of geostrophic vorticity as $\frac{\partial \zeta_g}{\partial x} \sim (\frac{\Delta z}{L^3} + \frac{\Delta z'}{L'^3}) = \frac{\Delta z}{L^3} [1 + (\frac{\Delta z'}{\Delta z})(\frac{L}{L'})^3]$, where in both relationships the unprimed term is the synoptic contribution and the primed term is the gravity wave contribution. Further, let the vorticity advection after post-processing be

$$[u_g \frac{\partial \zeta_g}{\partial x}]_{\substack{\text{post-} \\ \text{processed}}} \sim (\frac{\Delta z}{L})(\frac{\Delta z}{L^3}) ,$$ the synoptic contribution only.

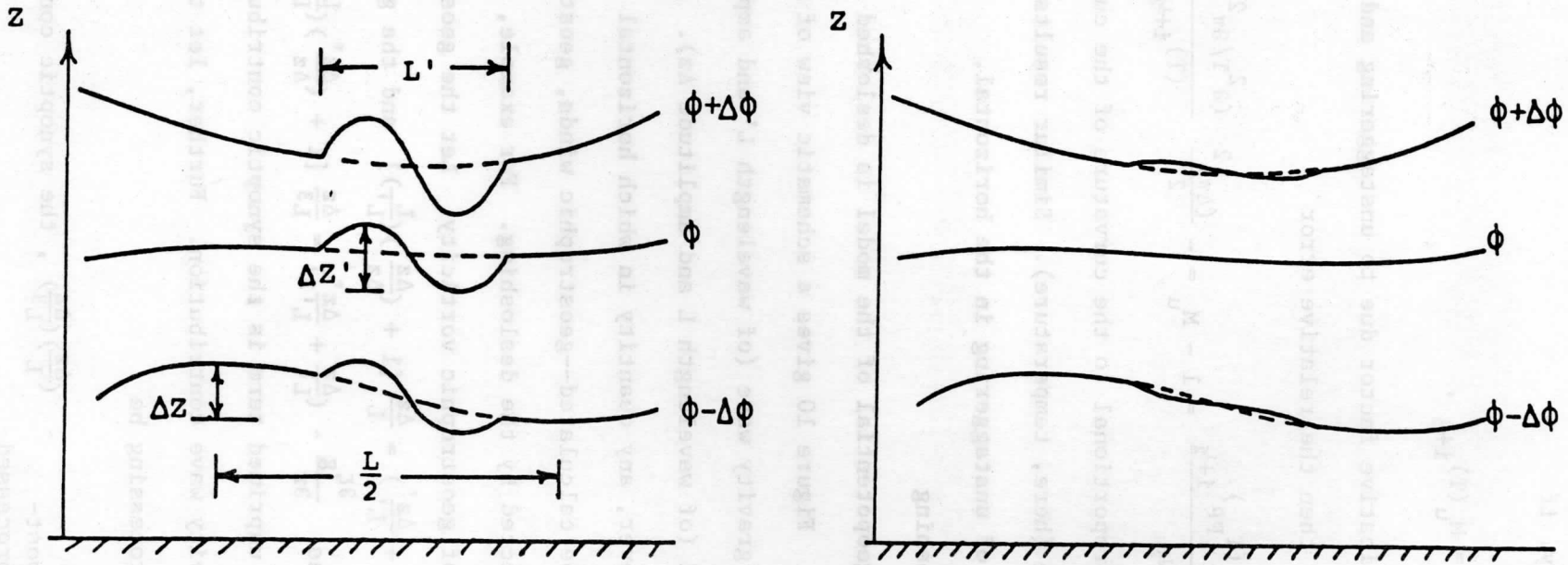


FIGURE 10

Schematic of gravity wave removal from height field during desloshing.
LEFT: Before desloshing. RIGHT: After desloshing.

Then

$$\left[u_g \frac{\partial \zeta_g}{\partial x}\right]_{\substack{\text{post-}\\ \text{processed}}} = M_d \left[u_g \frac{\partial \zeta_g}{\partial x}\right]$$

where the multiplicative factor due to desloshing,

$$M_d \sim \frac{1}{\left[1 + \left(\frac{\Delta z'}{\Delta z}\right)\left(\frac{L}{L'}\right)\right]\left[1 + \left(\frac{\Delta z'}{\Delta z}\right)\left(\frac{L}{L'}\right)^3\right]} ,$$

indicates that error might enter through an amplitude effect $\left(\frac{\Delta z'}{\Delta z}\right)$ or a scale effect $(L/L')$. Figure 11 shows the family $M_d$ = constant for varying scales and amplitudes of the gravity wave. If the typical gravity wave which is desloshed is "trapped, large-scale, predominantly external",* then possibly $0 < \left(\frac{\Delta z'}{\Delta z}\right) < 0.25$ and $0.75 < \left(\frac{L'}{L}\right) < 1$ are reasonable estimates. The result is that $0.5 < M_d < 1$.**

(d) The error in horizontal smoothing

When the post-processing operation of smoothing with NMC's combined filter is applied to a one-dimensional Fourier component,

$$\left[\cos \frac{2\pi}{L} i\Delta x\right]_{\substack{\text{post-}\\ \text{processed}}} = M_s \cos \frac{2\pi}{L} i\Delta x ,$$

where the multiplicative factor, $M_s$, is shown in Figure 12.

(e) Post-processing error vs. finite differencing error

To put the magnitudes of the various post-processing errors into perspective, they can be compared with the truncation error which arises when finite differencing is used in place of the calculus. Finite differencing

---

*Gerrity and Newell (1976) p. 3.

**Since the contribution of the gravity wave to a geostrophically computed variable is generally not desired, the damping effect of $M_d$ may be beneficial in bringing geostrophic computations down to their proper synoptic scale values.

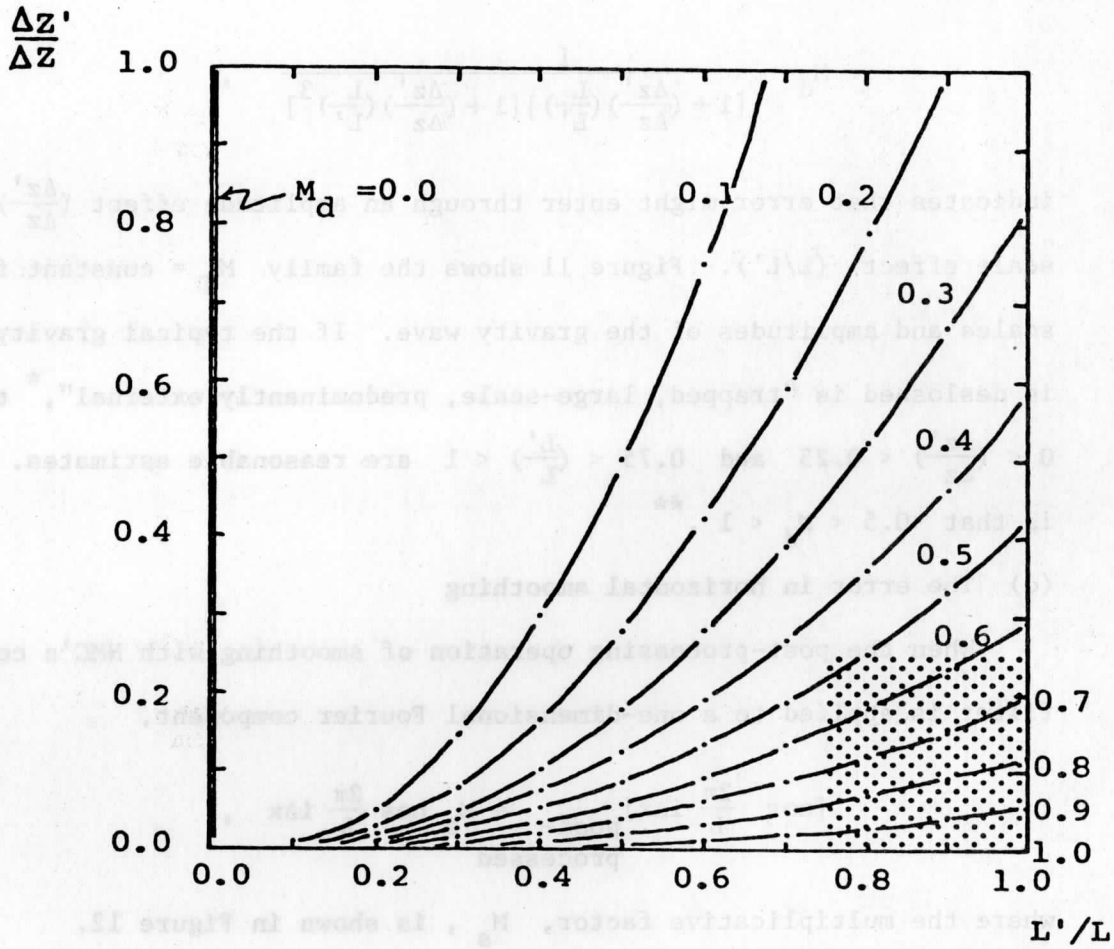


FIGURE 11

Multiplicative factor, $M_d$, for desloshing $U_g \frac{\partial \zeta_g}{\partial x}$.

Reasonable estimates for the gravity wave might be $0<(\Delta z'/\Delta z)<.25$ and $.75<(L'/L)<1$. This region is shaded.

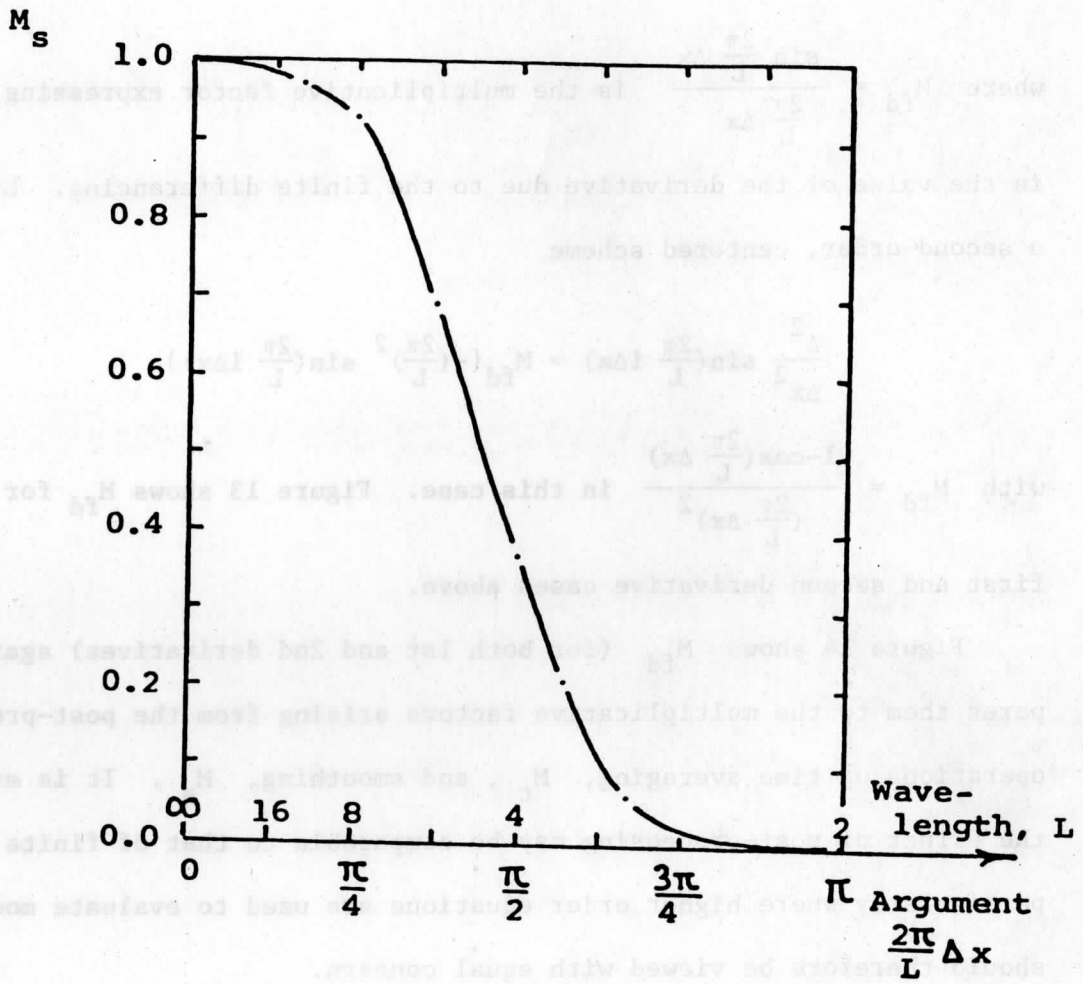


FIGURE 12

Multiplicative reduction factor, $M_s$, for horizontal smoothing.

(from Stackpole, 1968)

error has been well documented [Haltiner, 1971]. For example, applying a first order, centered difference scheme to a Fourier component

$$\frac{\Delta}{\Delta x} \sin(\frac{2\pi}{L} i\Delta x) = M_{fd} \frac{2\pi}{L} \cos(\frac{2\pi}{L} i\Delta x)$$

where $M_{fd} = \dfrac{\sin \frac{2\pi}{L} \Delta x}{\frac{2\pi}{L} \Delta x}$ is the multiplicative factor expressing a reduction in the value of the derivative due to the finite differencing. Likewise, for a second order, centered scheme

$$\frac{\Delta^2}{\Delta x^2} \sin(\frac{2\pi}{L} i\Delta x) = M_{fd}\{-(\frac{2\pi}{L})^2 \sin(\frac{2\pi}{L} i\Delta x)\}$$

with $M_{fd} = \dfrac{1-\cos(\frac{2\pi}{L} \Delta x)}{(\frac{2\pi}{L} \Delta x)^2}$ in this case. Figure 13 shows $M_{fd}$ for both the first and second derivative cases above.

Figure 14 shows $M_{fd}$ (for both 1st and 2nd derivatives) again and compares them to the multiplicative factors arising from the post-processing operations of time averaging, $M_t$, and smoothing, $M_s$. It is evident that the effect of post-processing may be comparable to that of finite differencing--particularly where higher order equations are used to evaluate model output--and should therefore be viewed with equal concern.

(f) The effect of post-processing on various primitive equations

This section concentrates upon the possible effects which may result in using post-processed data (time-averaged, unstaggered, desloshed, smoothed) in the equations of hydrostatic equilibrium and mass continuity; however, any error which may arise from finite-differencing will not be included.

The first primitive equation to be examined here is that of hydrostatic balance. The LFM is constrained to be hydrostatic (i.e. $0 = \frac{\Delta\phi}{\Delta p} + \frac{RT}{p}$, in

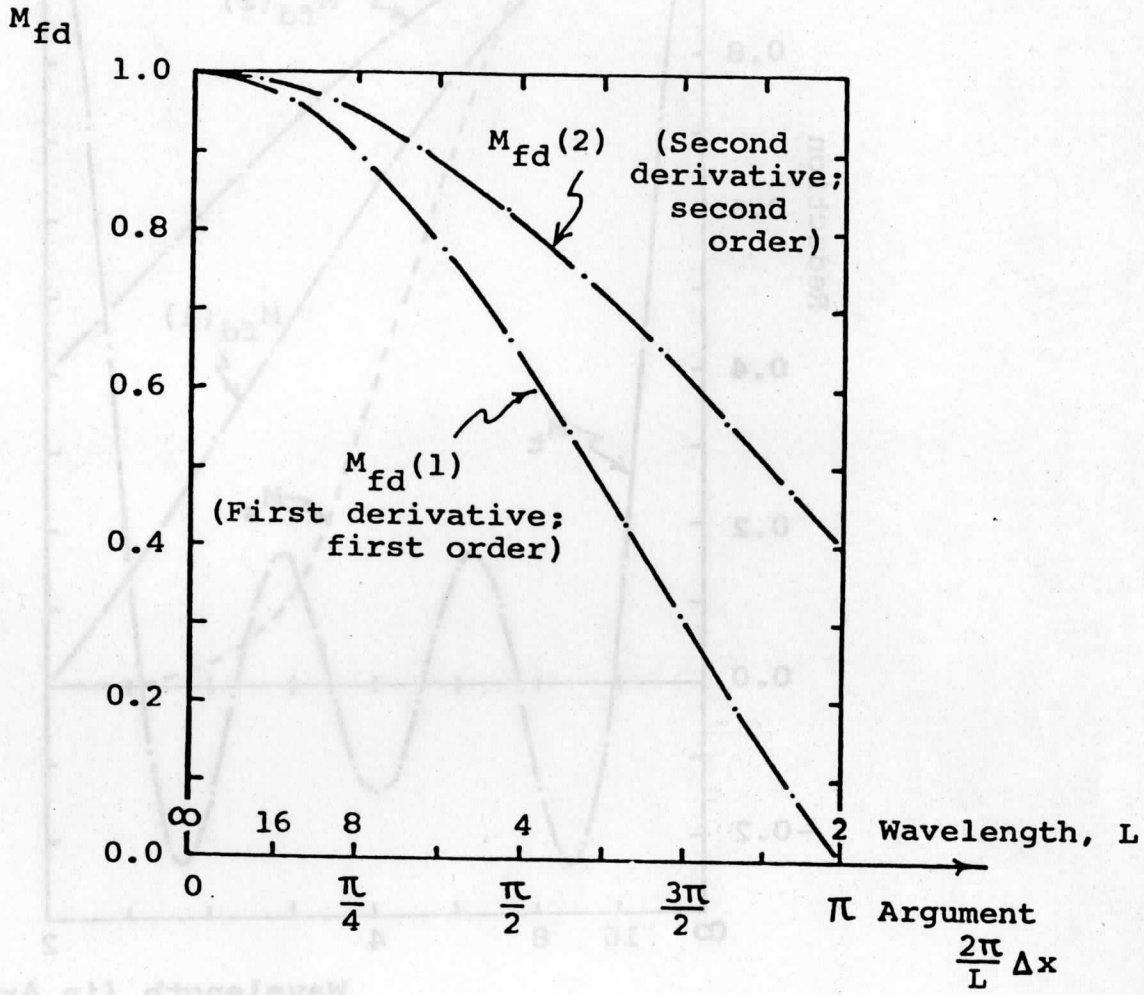


FIGURE 13

Multiplicative reduction factors for finite differencing.

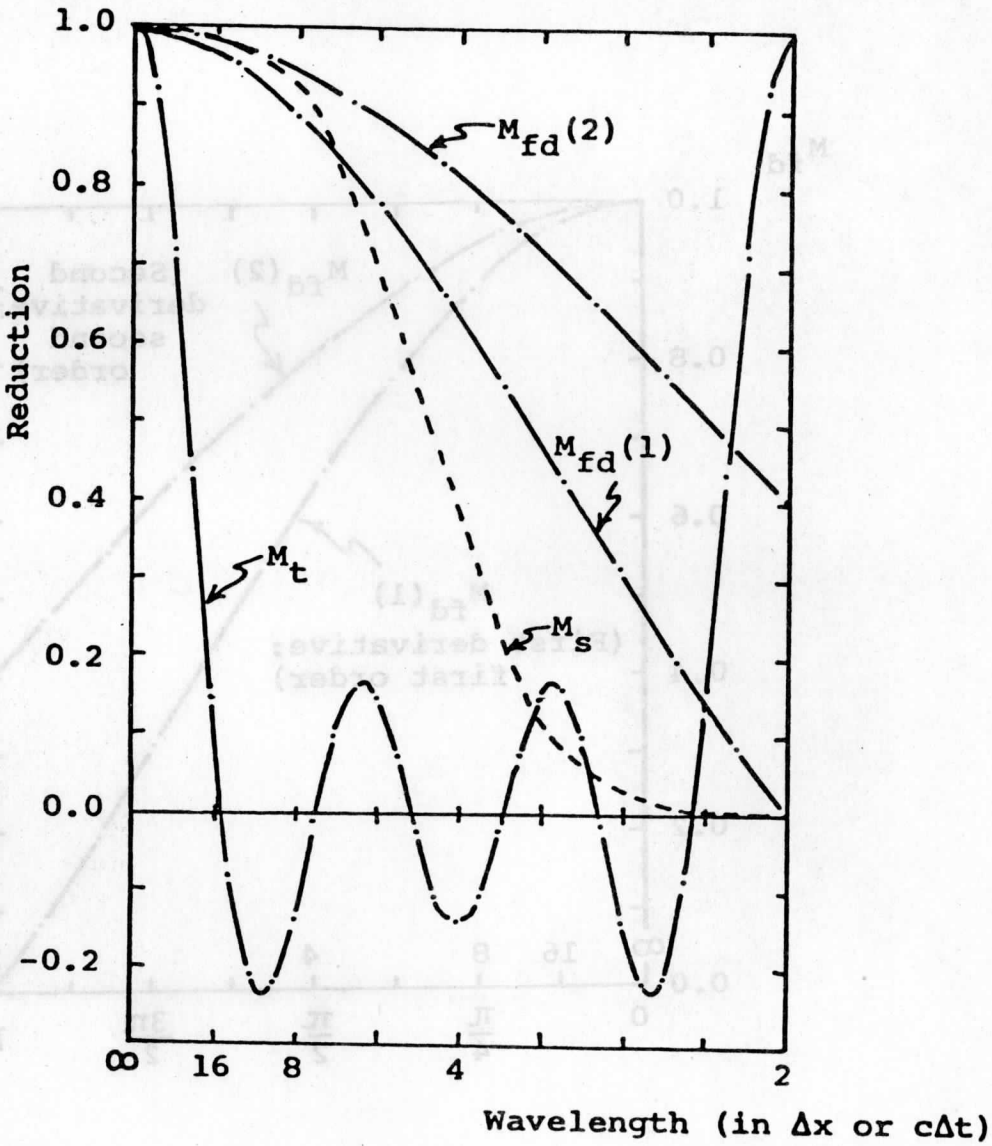


FIGURE 14

Comparison of various reduction factors encountered in post-processing operations or finite differencing.

p-coordinates for simplicity) and so the raw model output of temperature and geopotential should be in hydrostatic equilibrium. But after post-processing has occurred, are the data still hydrostatic? Table 2 summarizes the situation indicating which post-processing operations affect the variables and thereby possibly affect the hydrostatic equilibrium. Since the unstaggering process perturbs the temperature field independently of the height field, the post-processed data may not be hydrostatic even though the LFM itself is hydrostatic.

One immediate consequence of the post-processed data set not being hydrostatic is that the exact, hydrostatic coordinate transformation from cartesian $(x,y,z,t)$ to pressure $(x,y,p,t)$ no longer applies. Consequently, pressure coordinate equations used diagnostically on the post-processed data will have to include correction terms which contain the hydrostatic defect, call it $\eta$. Several places where such correction terms may be important are the following:

(i) The Jacobian, $J$, of the $(x,y,z)$ to $(x,y,p)$ transformation is

$$J = \frac{\partial(x,y,z)}{\partial(x,y,p)} = \left|\frac{\partial z}{\partial p}\right| .$$

If a hydrostatic defect, $\eta$, exists (Dutton and Johnson, 1967),

$$J = \left|\rho(g+\eta)\right|^{-1} = \frac{1}{\rho g}\left|1 - \frac{\eta}{g} + \left(\frac{\eta}{g}\right)^2 - \left(\frac{\eta}{g}\right)^3 + \ldots\right| .$$

And so, for example, integrals of some quantity, $F$, transformed from cartesian to pressure space must have a correction associated with the defect terms:

$$\iiint F\,dxdydz = \iiint F\,J\,dxdydp = \left|1 - \frac{\eta}{g} + \ldots\right| \iiint F\,\frac{1}{\rho g}\,dxdydp .$$

Also, in the continuity equation, (Johnson, 1977),

TABLE 2: Hydrostatic Equilibrium

| Variable \ Post-processing Operation | Time Averaging | Unstaggering | Desloshing | Smoothing |
|---|---|---|---|---|
| $\phi$ | No | No | Yes | Yes |
| T | No | Yes | No | Yes |
| Effect on Hydrostatic Equilibrium? | No(i) | Maybe(ii) | No(iii) | Probably Not(iv) |

(i) Neither $\phi$ nor T are subjected to time-averaging; hence there is no effect on the equation.

(ii) Since T is unstaggered but $\phi$ is not, the dependent variables are subjected to different treatment--T will be reduced by the factor $M_u$. Hence the term $\frac{RT}{p}$ will probably not cancel the term $\Delta\phi/\Delta p$. Physically, the thickness $\Delta\phi/\Delta p$ had a corresponding temperature, T, in the model; but after post-processing the same thickness may have a different, non-hydrostatic temperature, $M_u T$.

(iii) While $\phi$ is desloshed but T is not, the desloshing routine is such that hydrostatic thickness is preserved.

(iv) Both $\phi$ and T are subjected to the same smoothing operation; and so both probably will be reduced by an equal amount, $M_s$, which will cancel from each term leaving no net effect on the equation.

$$\frac{\partial}{\partial t}(\rho J) + \frac{\partial}{\partial x}(\rho J u) + \frac{\partial}{\partial y}(\rho J v) + \frac{\partial}{\partial p}(\rho J \omega) = 0 \quad ,$$

correction terms will appear both as powers of $(\eta/g)$ and as spatial and temporal derivatives of $(\eta/g)$ :

$$(\vec{\nabla}_{2,p} \cdot \vec{V}_2 + \frac{\partial \omega}{\partial p}) \left| 1 - \frac{\eta}{g} + \ldots \right| + (\frac{\partial}{\partial t} + \vec{V}_3 \cdot \vec{\nabla}_{3,p}) \left| 1 - \frac{\eta}{g} + \ldots \right| = 0 \ .$$

(ii) First order, spatial differential operators acting on any variable, F, transform from cartesian to pressure as

$$\vec{\nabla}_{2,z} F = \vec{\nabla}_{2,p} F + \frac{\partial F}{\partial p} \vec{\nabla}_{2,z} p \quad ,$$

and as

$$\frac{\partial F}{\partial z} = \frac{\partial F}{\partial p} \frac{\partial p}{\partial z} \quad .$$

If a hydrostatic defect is present, $\frac{\partial p}{\partial z} = -\rho(g+\eta)$ and so the vertical derivative transformation always will have a correction term. But the transformed horizontal gradient operator will be affected only when $F$ is some function of the height of a pressure surface, $z$ . For example, when $F = z$ , the horizontal pressure force (and consequently the geostrophic wind) transforms with a correction term:

$$\frac{1}{\rho} \vec{\nabla}_{2,z} p = g \vec{\nabla}_{2,p} z + \eta \vec{\nabla}_{2,p} z \ .$$

Higher order derivatives of the height of a pressure surface, $z$ , (e.g. geostrophic vorticity, geostrophic vorticity advection, and thermal wind, $\partial \vec{V}_g / \partial p$) will contain other correction terms, some being spatial gradients of the defect.

Should any of the correction terms (i.e. terms with $\eta/g$ or $\vec{\nabla}_{3,p}(\eta/g)$) be comparable to any term in an equation, then neglect of such correction terms in a $p$ coordinate, diagnostic analysis of the post-processed data

could conceivably lead to erroneous conclusions. Omission of such correction terms at first may not seem serious since the defect is likely small. But consider that often important atmospheric processes are associated with terms which are the small residuals of larger forcing terms; thus a correction term, while small, may be a sizeable fraction of the residual term. For example, suppose that $\eta$ is only a few percent of $g$; then the correction to the pressure force also will be only a few percent. But since accelerations--which are often computed as residuals of the forces in the equation of motion--are only of the order of 10% of the forces, the correction term may be easily 20% or so of the accelerations--a considerable effect. (In Chapter 4, using actual LFM post-processed data, an estimate of the size of some of the correction terms in $(\frac{\eta}{g})$ will be presented.)

The other primitive equation to be examined here is that of continuity of mass. The LFM is also constrained to conserve mass (i.e. $\vec{\nabla}_2 \cdot \vec{\nabla}_2 + \frac{\partial \omega}{\partial p} = 0$, in $p$ coordinates, for simplicity). Again the question arises as to whether or not the post-processed atmosphere also obeys the continuity equation. Table 3 summarizes the situation. Since the time-averaging and unstaggering procedures alter the vertical velocity field differently from the horizontal velocity field, the post-processed velocity fields may not necessarily conserve mass even though the LFM itself is constrained to do so.

(g) The effect of post-processing on the quasi-geostrophic relationships

Higher-order, derived equations are often applied diagnostically to numerical model output to examine the relative importance of various atmospheric processes forcing development. It is therefore crucial to investigate the effect post-processing may have upon the validity of the information obtained in such studies. Consider, for example, the quasi-geostrophic equations of vorticity and thermodynamics-energy [Holton, 1972]:

TABLE 3: Mass Continuity

| Variable \ Post-processing Operation | Time Averaging | Unstaggering | Desloshing | Smoothing |
|---|---|---|---|---|
| $\vec{V}_2$ | No | No (horizontally)<br>Yes (vertically) | No | Yes |
| $\omega$ | Yes | Yes (horizontally)<br>No (vertically) | No | Yes |
| Effect on Mass Conservation | Likely(i) | Maybe(ii) | No(iii) | Probably Not(iv) |

(i) $\omega$ , which is subjected to a time-averaging operation during post-processing is reduced (by $M_t$) and phase-shifted while $\vec{V}_2$ is neither. Thus $(\partial\omega/\partial p)$ may not cancel $\vec{V}_2 \cdot \vec{V}_2$ .

(ii) $\omega$ and $\vec{V}_2$ are not unstaggered identically likely resulting in the 2 terms not canceling one another.

(iii) Neither $\omega$ nor $\vec{V}_2$ is desloshed; hence there is no effect on the equation.

(iv) $\omega$ and $\vec{V}_2$ are smoothed identically meaning that the smoothing factor, $M_s$ for each will probably cancel from both terms leaving the equation largely unaffected.

vorticity $$\frac{\partial \zeta_g}{\partial t} = -\vec{V}_g \cdot \vec{\nabla}_{2,p} (\zeta_g + f) - f_0 \vec{\nabla}_{2,p} \cdot \vec{V}_2$$

thermodynamics-energy $$\frac{\partial}{\partial t} \left(-\frac{\partial \Phi}{\partial p}\right) = -\vec{V}_g \cdot \vec{\nabla}_{2,p} \left(-\frac{\partial \Phi}{\partial p}\right) + \hat{\sigma}\omega$$

where $V_g$ is the geostrophic wind;

$\zeta_g$ is the geostrophic vorticity $\left(= \frac{1}{f} \nabla^2_{2,p} \phi\right)$;

$f_0$ is the local value of the coriolis parameter = constant;

$\hat{\sigma}$ is the stability $\left(= -\frac{1}{\rho\theta} \frac{\partial \theta}{\partial p}\right)$;

Each of these equations neglects various processes which are considered to be an order of magnitude less than the main terms of the equations.

As Holton (1972) discusses, the secondary circulations ($\vec{\nabla}_2 \cdot \vec{V}_2$ and $\omega$) generally compensate for the advection (vorticity and thickness, respectively) to keep the atmosphere geostrophic and hydrostatic. It is worthwhile, then, to know if this compensation in the post-processed atmosphere is different from that in the original model atmosphere. Consider a ratio of the compensation in the vorticity equation in these 2 cases. Recall that post-processing may affect the vorticity advection by desloshing ($M_d$) and smoothing ($M_s$) the height field (twice) ($= M_d M_s^2$); the divergence by unstaggering ($M_u$) and smoothing ($M_s$) the velocity field ($= M_u M_s$). Hence

$$\frac{\left[\vec{V}_g \cdot \vec{\nabla}_{2,p} (\zeta_g + f)/f_0 \vec{\nabla}_{2,p} \cdot \vec{V}\right]_{\substack{\text{post-processed} \\ \text{atm.}}}}{\left[\vec{V}_g \cdot \vec{\nabla}_{2,p} (\zeta_g + f)/f_0 \vec{\nabla}_{2,p} \cdot \vec{V}\right]_{\substack{\text{model} \\ \text{atm.}}}} \sim \frac{M_d M_s^2}{M_u M_s} = \frac{M_d M_s}{M_u}$$

From the estimates of Section 3, this ratio is likely <1 implying that the divergence (the horizontal part of the secondary circulation) in the post-processed atmosphere is more important than in the raw model output. That is, the compensation for the vorticity advection may appear greater in the post-processed atmosphere than in the original atmosphere of the model.

A similar investigation may be done for the thermodynamics-energy equation. Post-processing may alter thickness advection by smoothing ($M_s$) and unstaggering ($M_u$) the horizontal velocity field, and by smoothing ($M_s$) the height field ($= M_s^2 M_u$), and alter the $\hat{\sigma}\omega$ compensation by time-averaging ($M_t$), smoothing ($M_s$), and unstaggering ($M_u$) the vertical velocity field, and by smoothing ($M_s$) and unstaggering ($M_u$) the temperature field ($= M_t M_s^2 M_u^2$). It follows that

$$\frac{[-\vec{V}_g \cdot \vec{\nabla}_{2,p}(-\frac{\partial\phi}{\partial p})/\hat{\sigma}\omega]_{\substack{\text{post-processed} \\ \text{atm.}}}}{[-\vec{V}_g \cdot \vec{\nabla}_{2,p}(-\frac{\partial\phi}{\partial p})/\hat{\sigma}\omega]_{\substack{\text{model} \\ \text{atm.}}}} \sim \frac{M_s^2 M_u}{M_t M_s^2 M_u^2} = \frac{1}{M_t M_u} .$$

Previous estimates show this ratio is probably > 1. Thus the effect of post-processing here is opposite that in the vorticity equation. Here the vertical motion (part of the secondary circulation) does not compensate for the advection of thickness as much in the post-processed data as in the original model data; the vertical secondary circulation appears weaker after post-processing.

The relative error incurred in these equations by post-processing may be considered, for example, by the ratios

$$\frac{[\vec{V}\cdot\vec{\nabla}_{2,p}(\zeta_g+f)]_{\text{model}} - [\vec{V}\cdot\vec{\nabla}_{2,p}(\zeta_g+f)]_{\substack{\text{post-} \\ \text{processed}}}}{[\vec{V}\cdot\vec{\nabla}_{2,p}(\zeta_g+f)]_{\text{model}}} \sim 1 - M_d M_s^2 \sim \text{Order}[10^{-1}]$$

and

$$\frac{[\hat{\sigma}\omega]_{\text{model}} - [\hat{\sigma}\omega]_{\substack{\text{post-} \\ \text{processed}}}}{[\hat{\sigma}\omega]_{\text{model}}} \sim 1 - M_t M_u M_s^2 \sim \text{Order}[10^{-1}].$$

Thus the error due to post-processing may be of the same order as the terms which are neglected in the quasi-geostrophic approximation. The implication

follows immediately that the neglected terms in the equations probably cannot be computed from the post-processed fields as residuals of the main terms.

To conclude, the analysis of this chapter, while unsophisticated, indicates that post-processing may alter the original model atmosphere significantly; the resulting, post-processed atmosphere may be considerably different from the original in a quantitative sense.

## 4. Diagnostic analysis of hydrostatic equilibrium and mass conservation in LFM post-processed output.

The quantitative effects of post-processing will be dealt with further in this chapter by diagnostically examining actual LFM post-processed data. The data will be investigated as to its degree of hydrostatic balance and mass conservatism. Diagnostic, finite differencing equations as closely parallel as possible to those of the model will be employed so that the truncation error of the finite differencing schemes will be minimized between model and diagnostics; then the discrepancies observed should be primarily due to post-processing.

For this investigation, the p-files for the 24 HR forecast fields of the LFM run initialized at 12 GMT 23 Feb 1975 were chosen from data save-tapes from NMC. Fig. 15 presents a synoptic analysis at 12 GMT 23 Feb 1975 prepared from conventional (RAOB and surface) data. Fig. 16 shows 12 grid points at which the post-processed LFM data are analyzed.

### (a) Hydrostatic equilibrium

Hydrostatic equilibrium is examined here through

$$g + \frac{RT}{p}\frac{\Delta p}{\Delta z} = \eta \stackrel{?}{=} 0$$

where $\eta$ is the hydrostatic defect, if any. Appendix A gives the details of

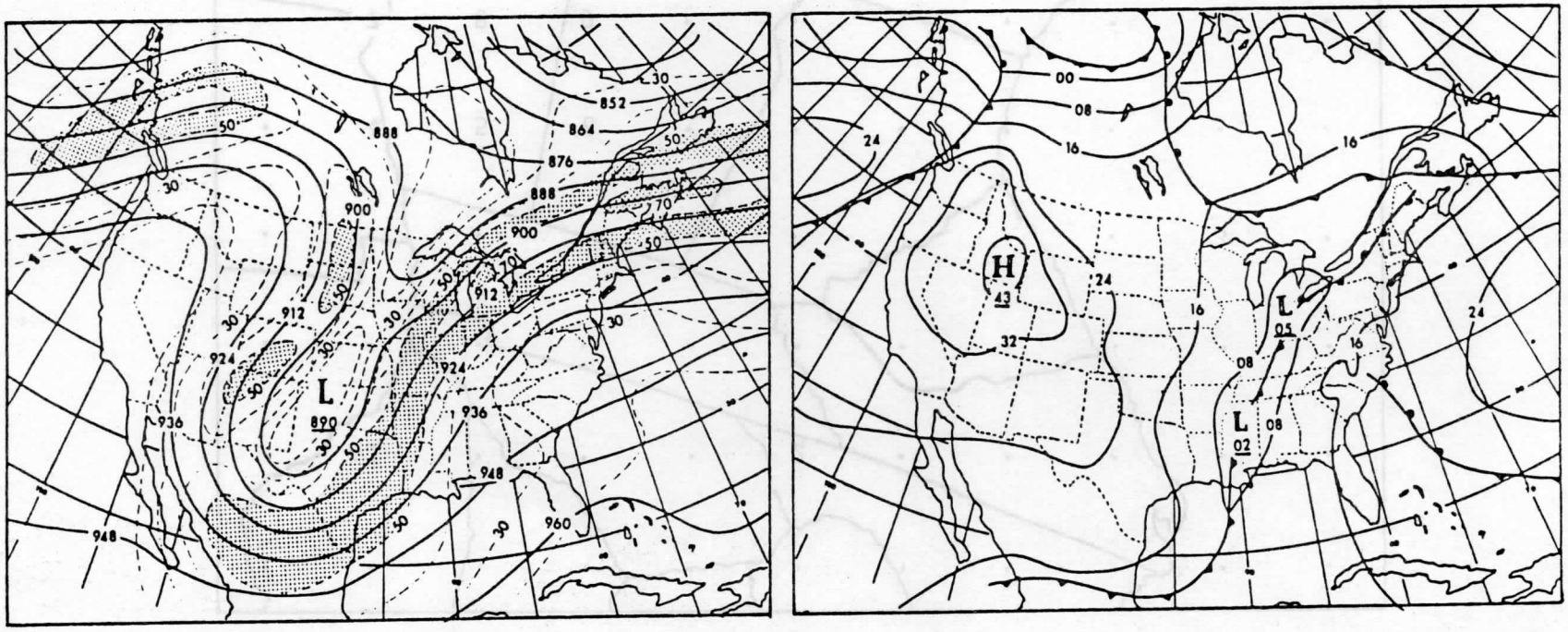


FIGURE 15

NMC analysis (conventional data) 12GMT 23 Feb 1975.
LEFT: 300mb contours & isotachs ($ms^{-1}$); RIGHT: surface.

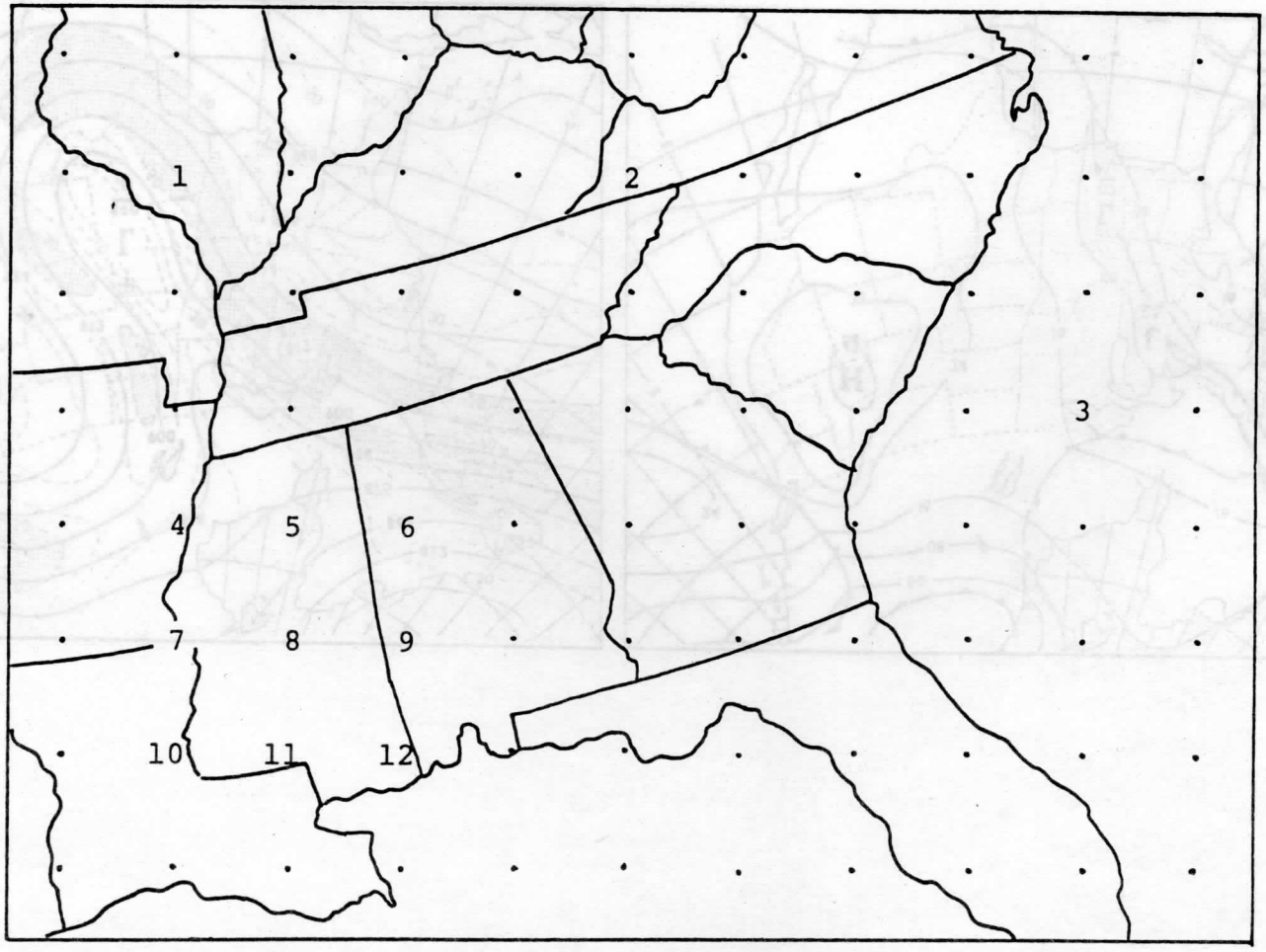


FIGURE 16

LFM grid points chosen for diagnostic study
of post-processed data.

the calculation of the term $\frac{RT}{p}(\Delta p/\Delta z)$ in a manner consistent with the LFM's finite differencing. (Appendix B presents the computation of $\frac{RT}{p}(\Delta p/\Delta z)$ using other finite difference schemes or numerical approximations; in general, these seem less satisfactory.)

Figure 17 shows $\frac{RT}{p}(\Delta p/\Delta z)$ for points 1,2,3, and 8; Figure 18 for points 4 through 12. These two figures indicate that the post-processed fields are generally non-hydrostatic with a maximum relative defect of roughly 2%. It is also apparent from Figure 18 that the defect may have considerable horizontal variation over a short distance--e.g. at 925 mb between points 6 and 12 or at 350 mb between points 5 and 11.

The error analysis of Section 3(f), Table 2, indicated (i) that unstaggering $\theta$ with respect to $\Phi$ is one possible component of a hydrostatic defect and (ii) that the component of error due to unstaggering is related to the curvature in a variable's profile. The analysis presented in this section will attempt to support this theoretical contention by demonstrating that where there is curvature in the profile of $\theta$ there is a contribution to the hydrostatic defect. However, as will be seen, there may be a hydrostatic defect even when there is no curvature in $\theta$ ; hence, other sources of error must exist in addition to the unstaggering contribution. For the component of the hydrostatic defect due to unstaggering, note the following:

(i) Figure 19 shows the post-processed potential temperature profile, $\theta(\pi)$ , for points 1,2,3, and 8. Assuming that the curvature displayed by these post-processed fields is like that found in the model's $\sigma$-file fields, then the relative error due to curvature (Sec. 3(b)) is of the order of 2%. (The maximum absolute error is roughly 5°K.)

(ii) Next, notice in Figure 19 that points 1 and 8 (both located in the frontal zone) have inversions--strong negative $\theta$ curvature--at 850 mb;

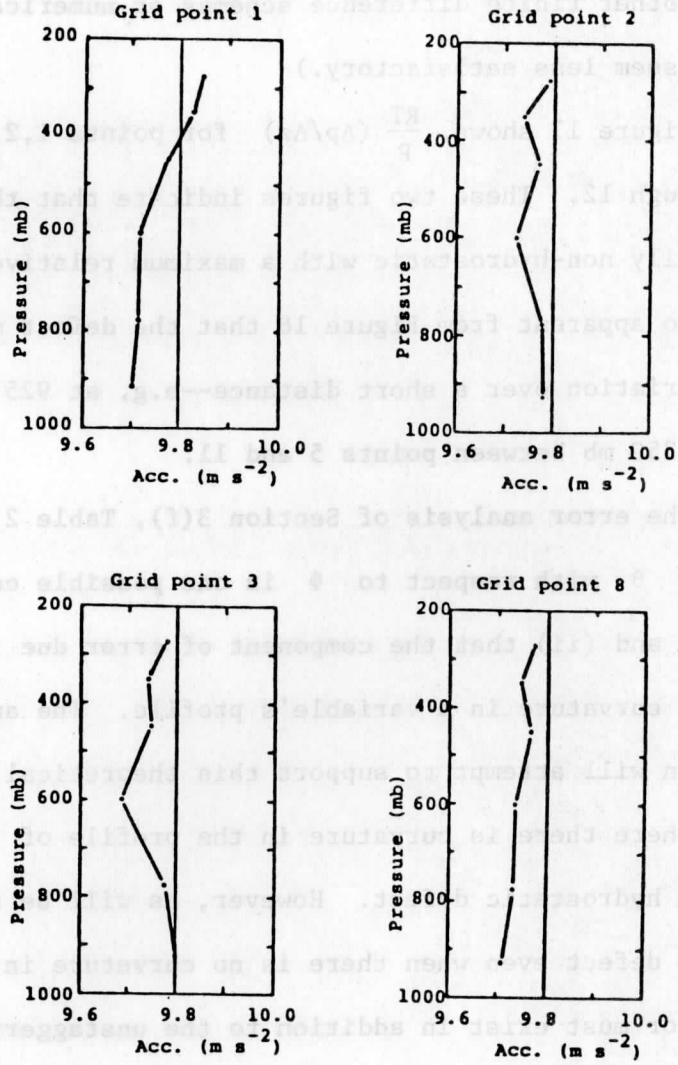


FIGURE 17

Vertical pressure gradient acceleration, $\left|\frac{RT}{p}\frac{\Delta p}{\Delta z}\right|$,
computed by method in Appendix A,
compared with gravity, g=9.8 m/s$^2$.

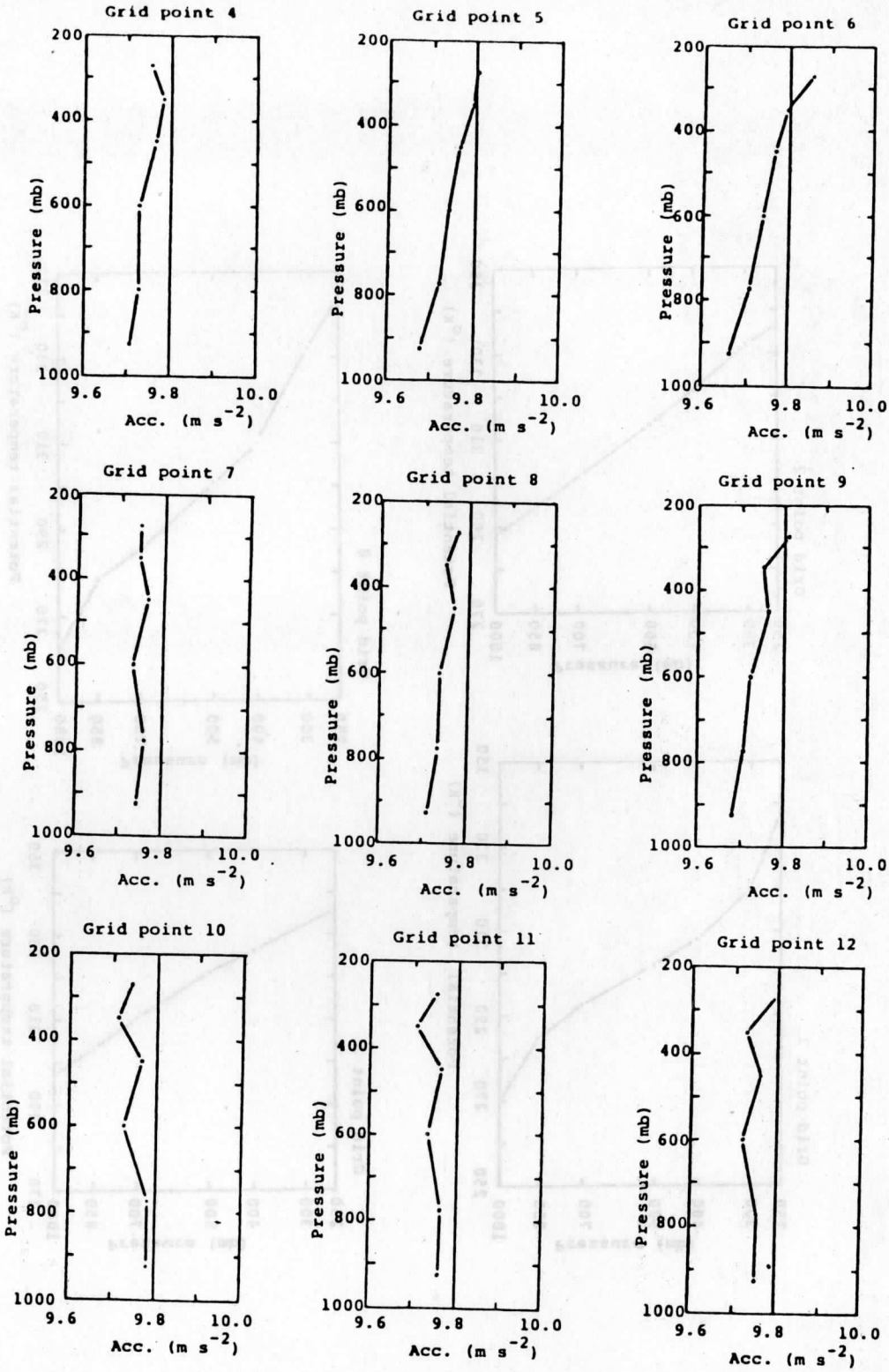


FIGURE 18

Vertical pressure gradient acceleration, $\left|\frac{RT}{p}\frac{\Delta p}{\Delta z}\right|$, computed by method in Appendix A, compared with gravity, g=9.8 m/s$^2$.

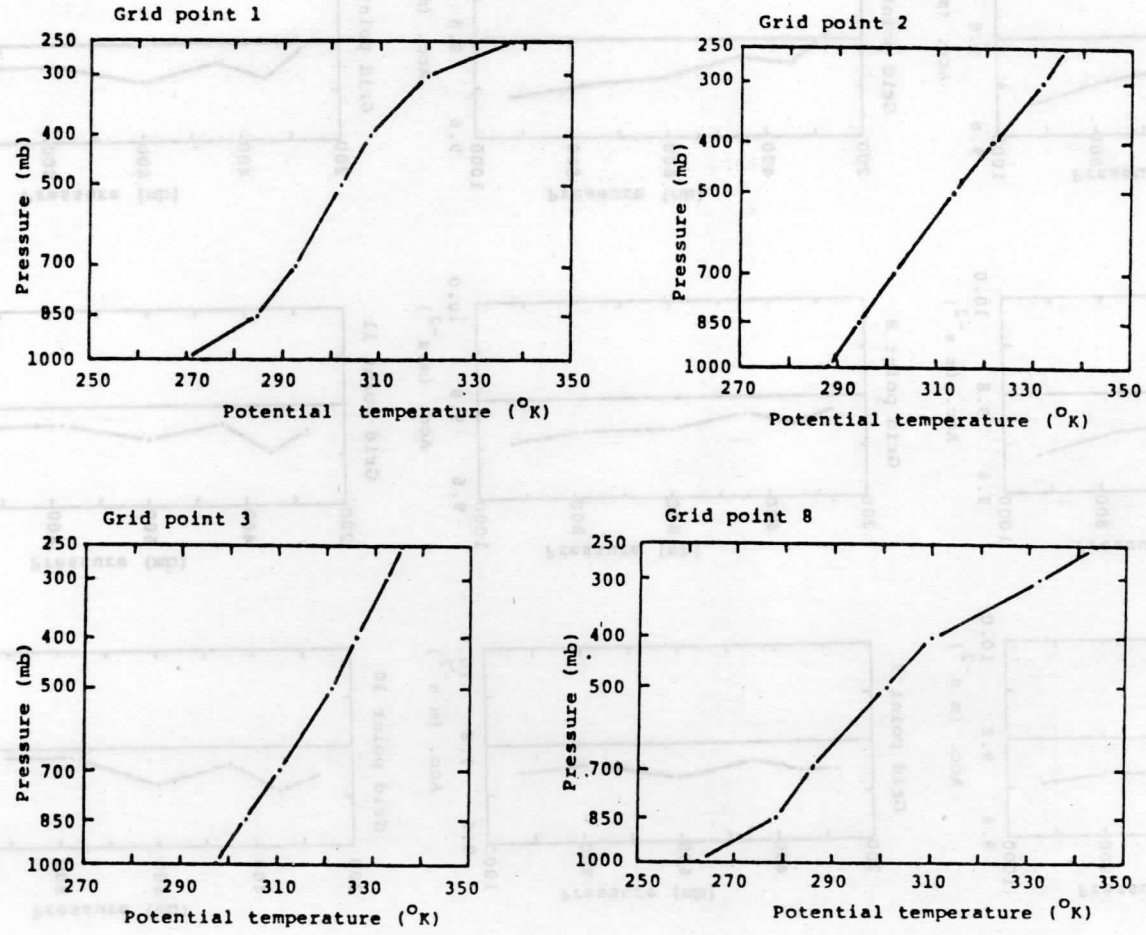


FIGURE 19

Vertical profiles of potential temperature as a function of $\pi = (\frac{p}{1000})^{\frac{R}{c_p}}$.

points 2 and 3 (both located in the warm sector), do not. Correspondingly, notice in Figure 17 that $\eta$ at 850 mb is large for points 1 and 8 while it is small at that same level for points 2 and 3. That is, the defect is large where the curvature is large. This same pattern is again indicated at 275 mb. There is strong curvature in $\theta$ ---the tropopause--at point 1 but not at points 2,3, or 8; and correspondingly, the defect has a different character at point 1 than it has at points 2,3, and 8.

Together the above observations seem to indicate that at levels where the curvature in $\theta$ is strong, the process of unstaggering $\theta$ not only contributes to the hydrostatic defect found in the post-processed fields, but also accounts for the magnitude of the defect.

Section 3(f) indicated that in the presence of a hydrostatic defect correction terms accounting for the defect should not be neglected when using pressure coordinate, diagnostic equations. The analysis just presented shows a 2% defect to be common in the post-processed data. Hence, pressure forces and geostrophic winds, for example, will be in error by about 2% if the correction terms are omitted. Such an omission, however, corresponds to roughly a 20% error in inertial accelerations and ageostrophic winds, respectively. It was seen that there is also a strong spatial variation of $\eta$ in certain regions. Hence correction terms containing the gradient of the defect may be important in relations involving higher order derivatives of the height field and in the continuity equation. This will be examined for the latter in the next section.

(b) Mass conservation

Mass conservation is examined in this section with the continuity equation

$$\overline{\left(\frac{\Delta\omega}{\Delta p}\right)}^{xy} + \overline{\left(\frac{\Delta u}{\Delta x}^{y} + \frac{\Delta v}{\Delta y}^{xy}\right)}^{xy} = \varepsilon \stackrel{?}{=} 0$$

where $\varepsilon$ is the mass defect, if any. Appendix C gives the details of calculating the terms on the left-hand side of the equation in a manner consistent with the LFM's finite differencing. (Appendix D presents alternative schemes for computing the left-hand side; in general, they seem less satisfactory.)

In Figure 20, $-\overline{\left(\frac{\Delta\omega}{\Delta p}\right)}^{xy}$ is compared with $\overline{\left(\frac{\Delta\bar{u}^{y}}{\Delta x}+\frac{\Delta\bar{v}^{x}}{\Delta y}\right)}^{xy}$ at grid points 4 through 12. The difference of the two curves is the mass defect, $\varepsilon$. It is immediately apparent from Figure 20 that, at least in regions of the post-processed atmosphere, there exist considerable violations of mass conservation. It also appears that $\left|\overline{\left(\frac{\Delta\omega}{\Delta p}\right)}^{xy}\right|$ is generally less than $\left|\overline{\left(\frac{\Delta\bar{u}^{y}}{\Delta x}+\frac{\Delta\bar{v}^{x}}{\Delta y}\right)}^{xy}\right|$ and that the profiles of these quantities may change significantly over relatively short distances.

The theoretical investigation of Section 3(f) indicated that a mass defect might potentially arise from the following three sources of error:

(i) The time-averaging of $\omega$ (Table 3). Section 3(a) showed that $\omega$ would be damped and phase-shifted with respect to $\vec{V}_2$ as a result of NMC's time-averaging scheme. A plausible indication of the damping may be the observed suppression in Figure 20 of the vertical velocity divergence compared to the horizontal velocity divergence.

(ii) The unstaggering of $\vec{V}_2$ in the vertical and $\omega$ in the horizontal (Table 3). The unstaggering error in $\vec{V}_2$ and $\omega$ is proportional to the curvature of their profiles (Sec. 3(b)). Figure 21 shows u(p) and v(p) at grid point 8 and $\omega(x)$ and $\omega(y)$ at 700 mb in the vicinity of point 8. The curvature displayed introduces roughly a 20% relative error in the variables (although in locations it may be much greater). But since these variables are differentiated in the continuity equation, their error enters in a complicated way depending upon the spatial randomness of that error. As

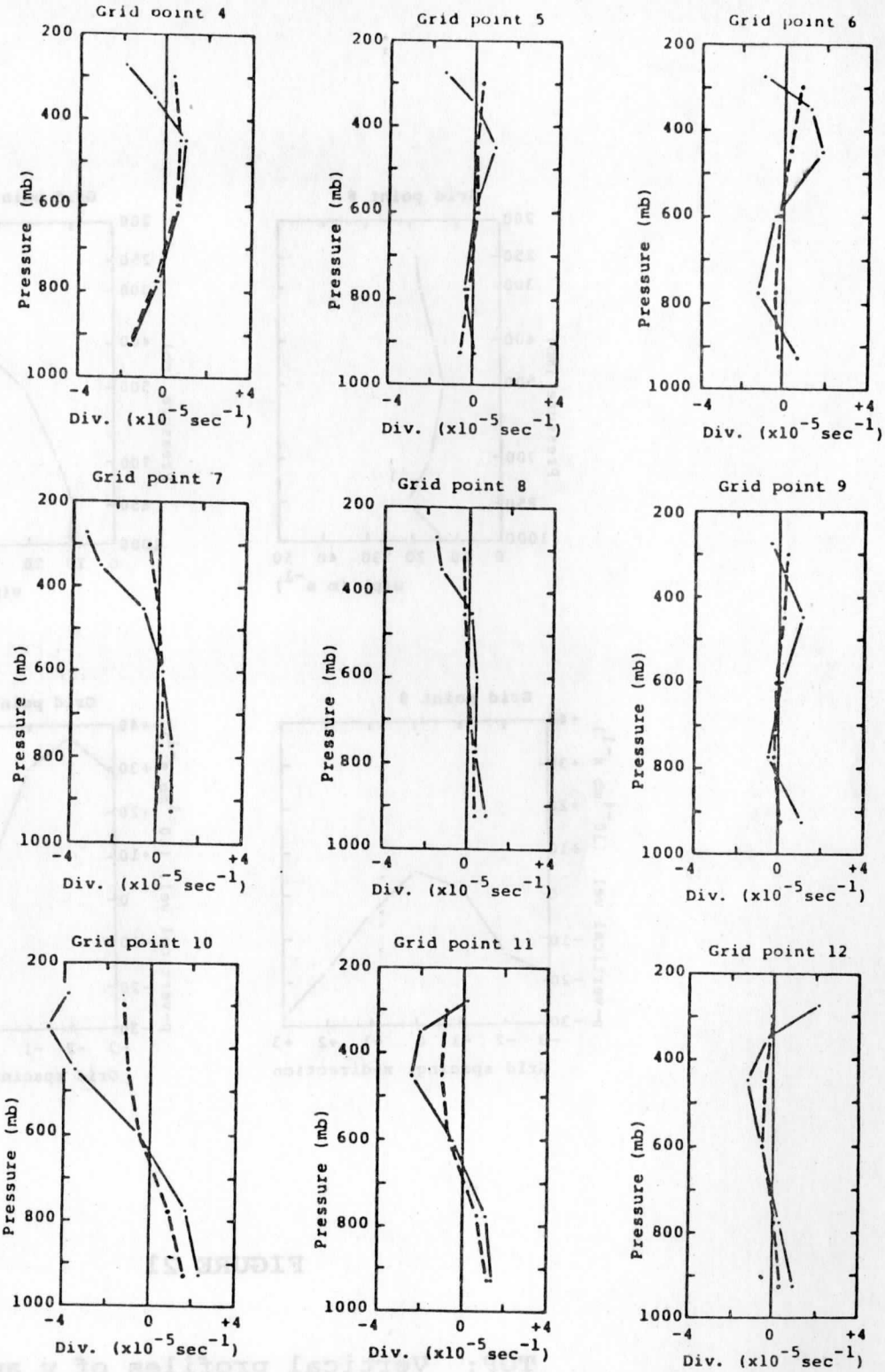


FIGURE 20

Velocity divergences computed by method of Appendix C.
$\vec{\nabla}_p \cdot \vec{v}$ in solid; $-\frac{\partial \omega}{\partial p}$ in dashed.

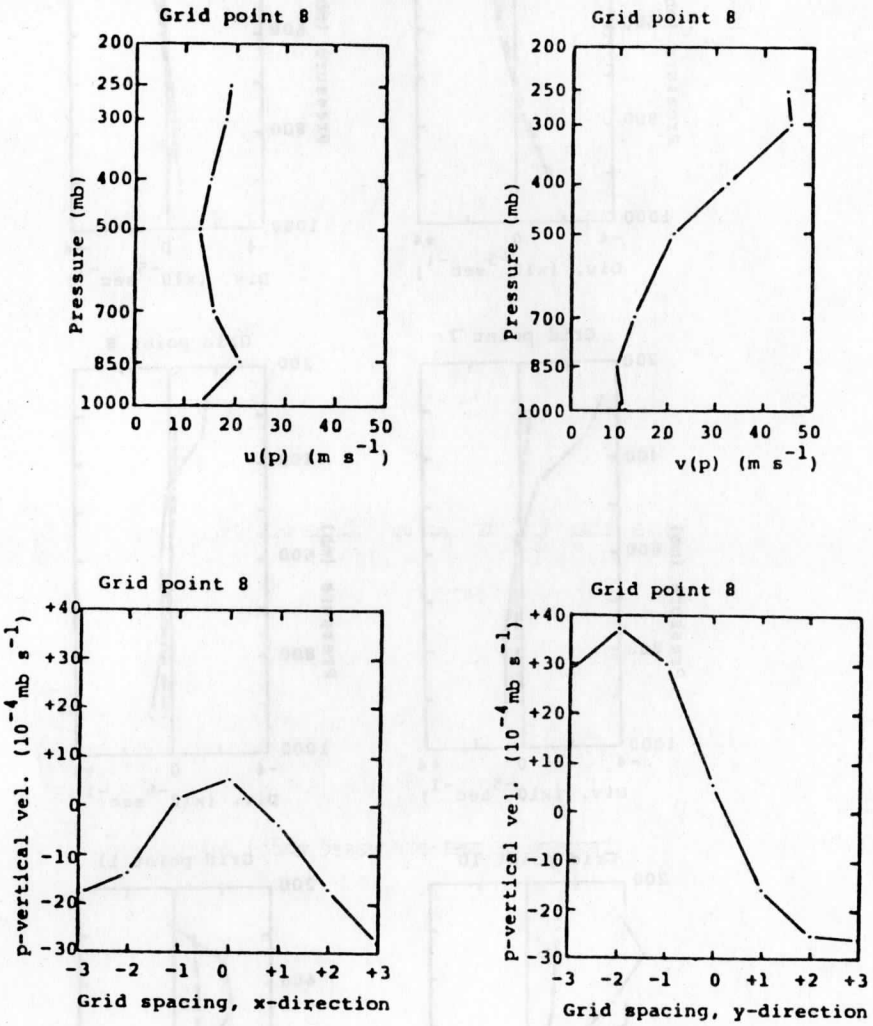


FIGURE 21

TOP: Vertical profiles of u and v.

BOTTOM: Horizontal profiles of $\omega$ at 700mb.

a result, the error in mass conservation due to unstaggering is difficult to estimate.

(iii) The non-hydrostatic nature of the post-processed data. Since the post-processed data appears to have a hydrostatic defect, $\eta$, (Section 4(a)), correction terms in the non-hydrostatic continuity equation (Sec. 3(f)),

$$(\vec{\nabla}_{2,p}\cdot\vec{\nabla}_2 + \frac{\partial\omega}{\partial p})\left|1 - \frac{\eta}{g} + \ldots\right| + (\frac{\partial}{\partial t} + \vec{\nabla}_3\cdot\vec{\nabla}_{3,p})\left|1 - \frac{\eta}{g} + \ldots\right| = 0 \quad ,$$

containing $\eta$ may be important if mass continuity is being analyzed diagnostically. Such terms were calculated from the post-processed data in the vicinity of grid point 8, 400 mb. $\vec{\nabla}_2\cdot\nabla_2(\frac{\eta}{g})$ was found to be only an order of magnitude less than $\vec{\nabla}_2\cdot\vec{\nabla}_2$ or $\partial\omega/\partial p$ while all the other terms in $(\eta/g)$* were at least several orders of magnitude less. Thus roughly 10% error may be introduced into the mass defect by using only the hydrostatic continuity equation, $\vec{\nabla}_3\cdot\vec{\nabla}_3 = 0$, when the post-processed data are not hydrostatic.

It appears that all three error sources just discussed could play an important part in rendering the post-processed model output seriously non-conserving of mass.

---

* $\frac{\partial}{\partial t}(\frac{\eta}{g})$ was estimated from a scaling argument.

## 5. Conclusions

This study did not concern itself with the qualitative, descriptive use of the LFM's post-processed fields for operational forecasting. However, this study has raised a number of important problems regarding the use of the post-processed forecast fields for quantitative, diagnostic studies. To recapitulate, a cursory comparison of actual LFM output and post-processed data for a single case showed that dramatic alterations were made. (See Figs. 4 and 5.) Further, a theoretical examination concerning itself with only a limited number of post-processing operations--some of which could only qualitatively be argued and some of which could only quantitatively be approximated--supports the comparison by indicating that physical constraints imposed upon the model (e.g. mass conservation and hydrostatic balance) may be lost in post-processing manipulations. This conjecture was borne out in an actual, numerical examination of a post-processed LFM forecast. It was also found theoretically that a higher-order, diagnostic (cf. quasi-geostrophic) view of the atmosphere gained from the post-processed data gave a quite erroneous depiction of the actual atmosphere of the model. And so, serious concern must be expressed when fields generated by the LFM and subjected to the NMC post-processing routine are used for any quantitative, diagnostic study of atmospheric processes.

This study was seriously limited by the lack of a complete set of $\sigma$ coordinate output from the model. It is suggested, therefore, that such data be obtained and that a rigorous, numerical study be performed to explicitly document the sources and magnitudes of post-processing error. Such a study would hopefully determine the randomness of the error and indicate whether spatial and temporal averaging or large volume budget techniques would reduce post-processing error to an insignificant level. Until such a time, the LFM post-processed data should probably be used very cautiously in quantitative, diagnostic studies.

## Appendix A: Formulation of a diagnostic equation for hydrostatic equilibrium

Hydrostatic balance in the LFM (Shuman & Hovermale, 1968) is achieved through the constraint

$$gz_{\sigma} + C_p \theta \pi_{\sigma} = 0 \ ,$$

where the subscript denoting differentiation has the meaning $f = (f_{m+\frac{1}{2}} - f_{m-\frac{1}{2}})/(\sigma_{m+\frac{1}{2}} - \sigma_{m-\frac{1}{2}})$. The variables have the vertical configuration of Figure 1(a), $\theta$ being staggered with respect to $z$ and $\pi$.

To diagnose the post-processed data, an analogous scheme must be employed to reduce truncation error. If $p$ replaces $\sigma$ as the vertical coordinate, then one form this equation takes is

$$g + \frac{RT}{p} \frac{\Delta p}{\Delta z} = 0 \ .$$

Since the post-processed data is unstaggered, Figure 22, a suitable approximation for this equation for the layer (m) to (m+1) might be

$$g + \frac{R[\frac{1}{2}(T_m + T_{m+1})]}{[\frac{1}{2}(p_m + p_{m+1})]} \left[\frac{(p_{m+1} - p_m)}{(z_{m+1} - z_m)}\right] = 0 \ .$$

That is, simple arithmetic means are used to represent the temperature and pressure of the layer, and simple differencing across the layer represents the derivative.

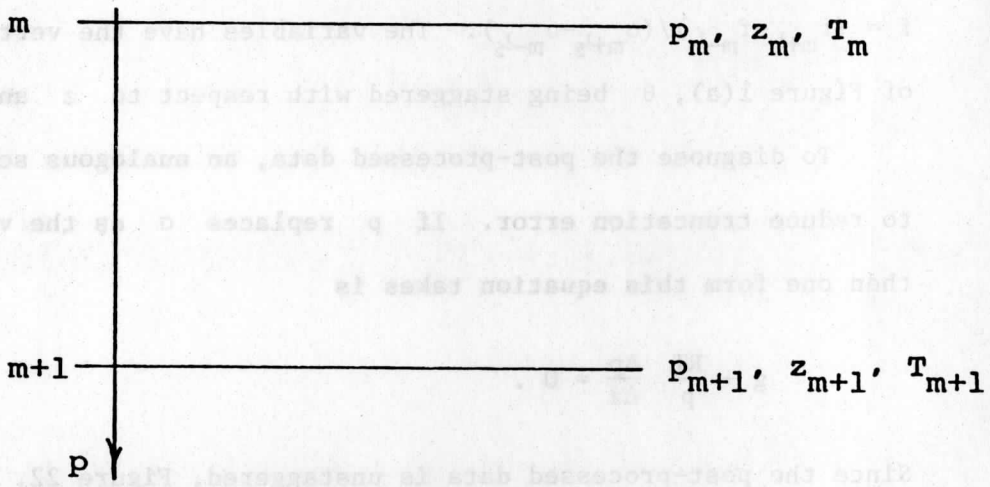


FIGURE 22

Vertical arrangement of
unstaggered, post-processed data.

## Appendix B: Computation of hydrostatic equilibrium by other finite-difference or numerical schemes

Appendix A presented the numerical scheme used in the text for diagnosing hydrostatic equilibrium in the post-processed data. That scheme employed finite-differencing which paralleled as closely as possible the finite-differencing used in the LFM. This appendix presents some other methods--some of them of higher order than the model's--which were tried in the diagnostic analysis of hydrostatic balance. The results shown below indicate that these other methods, even the higher-order ones, generally are worse than the lower order finite-differencing which is compatible with the model; this is probably due to the differences in the truncation error inherent in the model's differencing scheme. Hence, truncation considerations seem crucial in model diagnostics.

For the hydrostatic equation in the form

$$g + \frac{RT}{p}\frac{\partial p}{\partial z} = 0 \ ,$$

the various methods for computing $\frac{RT}{p}\,\partial p/\partial z$ are presented below along with graphs of the results.

Method I. Since $z$ is given at each of $n$ standard pressure levels, a polynomial of order $(n-1)$ is constructed to fit $z$. That is $z(p) = \alpha_0 + \alpha_1 p + \alpha_2 p^2 + \ldots + \alpha_{n-1} p^{n-1}$. The polynomial is differentiated to give $\partial z/\partial p = \alpha_1 + 2\alpha_2 p + \ldots + (n-1)\alpha_{n-1} p^{n-2}$. Then $\frac{RT}{p}\,\partial p/\partial z$ is calculated for every standard pressure level where $p$ and $T$ are given and $\frac{\partial p}{\partial z} = (\frac{\partial z}{\partial p})^{-1}$ is obtained by evaluating the differentiated polynomial. Figure 24 shows the results for points 1,2,3, and 8 .

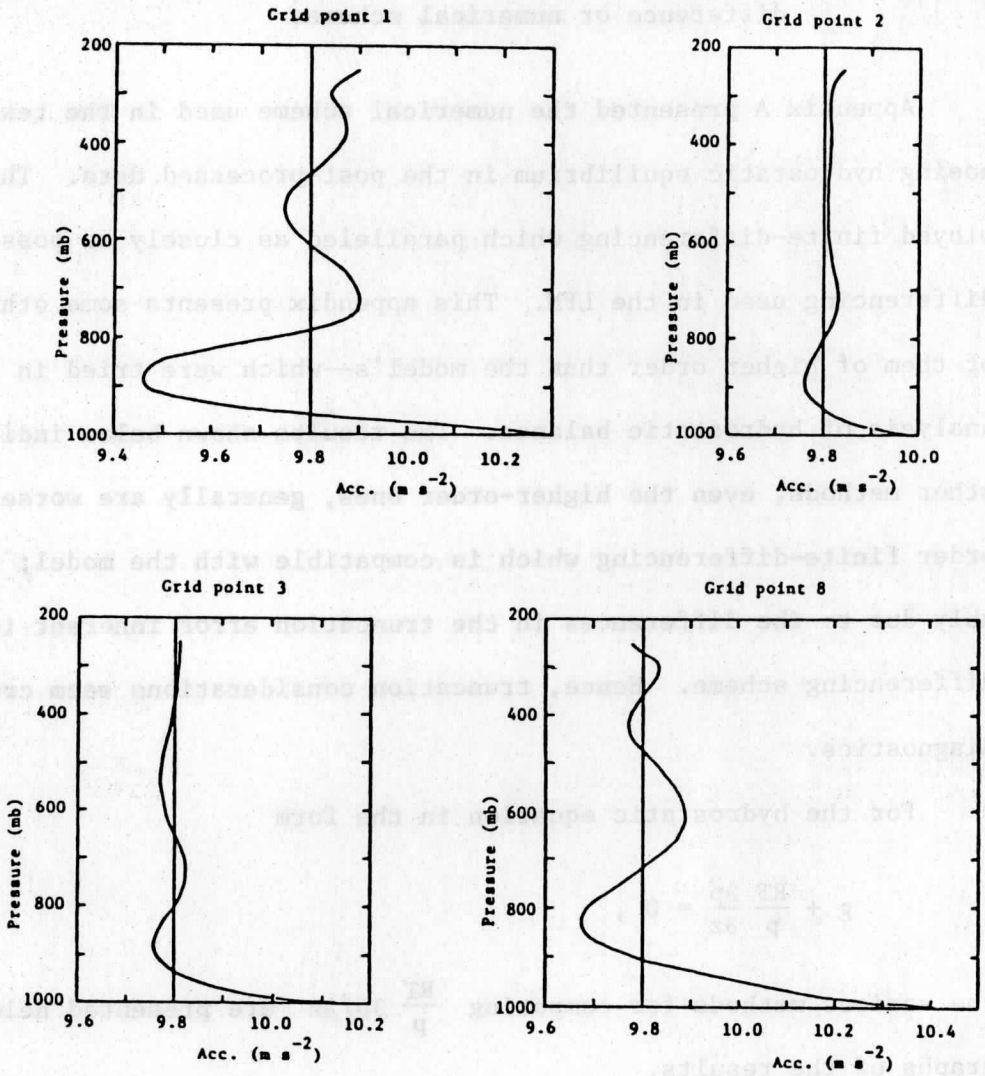


FIGURE 24

Vertical pressure gradient acceleration, $\left|\frac{RT}{p}\frac{\Delta p}{\Delta z}\right|$, computed by Method I, Appendix B, compared with gravity, g=9.8 m/s$^2$.

Method II. Three standard pressure levels, Figure 23, are used to compute $\frac{RT}{p}\left(\frac{\Delta z}{\Delta p}\right)^{-1}$. $p$ and $T$ are taken from the central level (m), $p_m$ and $T_m$. $\left(\frac{\Delta z}{\Delta p}\right)_m$ is approximated by a weighted finite difference derived from a Taylor series expansion of $z$ about $p_m$, (Greenspan, 1974),

$$\left(\frac{\Delta z}{\Delta p}\right)_m \simeq \frac{-(\Delta p_{m+1})^2 z_{m-1} + [(\Delta p_{m+1})^2 - (\Delta p_{m-1})^2] z_m + (\Delta p_{m+1})^2 z_{m+1}}{(\Delta p_{m-1})(\Delta p_{m+1})[(\Delta p_{m+1}) + (\Delta p_{m-1})]} ,$$

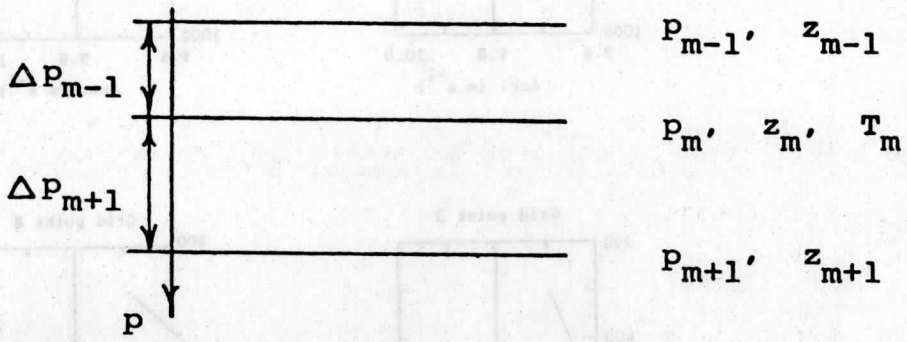


FIGURE 23

**Vertical arrangement of variables used in computations of Methods II and III.**

which is accurate to Order 2 in $(\Delta p_{m-1}, \Delta p_{m+1})$. Figure 25 shows the results for points 1,2,3, and 8.

Method III. Again, 3 standard pressure levels, Figure 23, are used to compute $\frac{RT}{p}\left(\frac{\Delta z}{\Delta p}\right)^{-1}$. Values for $p$ and $T$ are $p_m$ and $T_m$. $\left(\frac{\Delta z}{\Delta p}\right)$ is approximated by the simple difference which excludes the central level:

$$\left(\frac{\Delta z}{\Delta p}\right)_m \simeq \frac{z_{m+1} - z_{m-1}}{p_{m+1} - p_{m-1}} .$$

This approximation has only first order accuracy. Figure 26 shows the calculation for points 1 and 2 only; points 3 and 8 display a nearly identical character to 1 and 2.

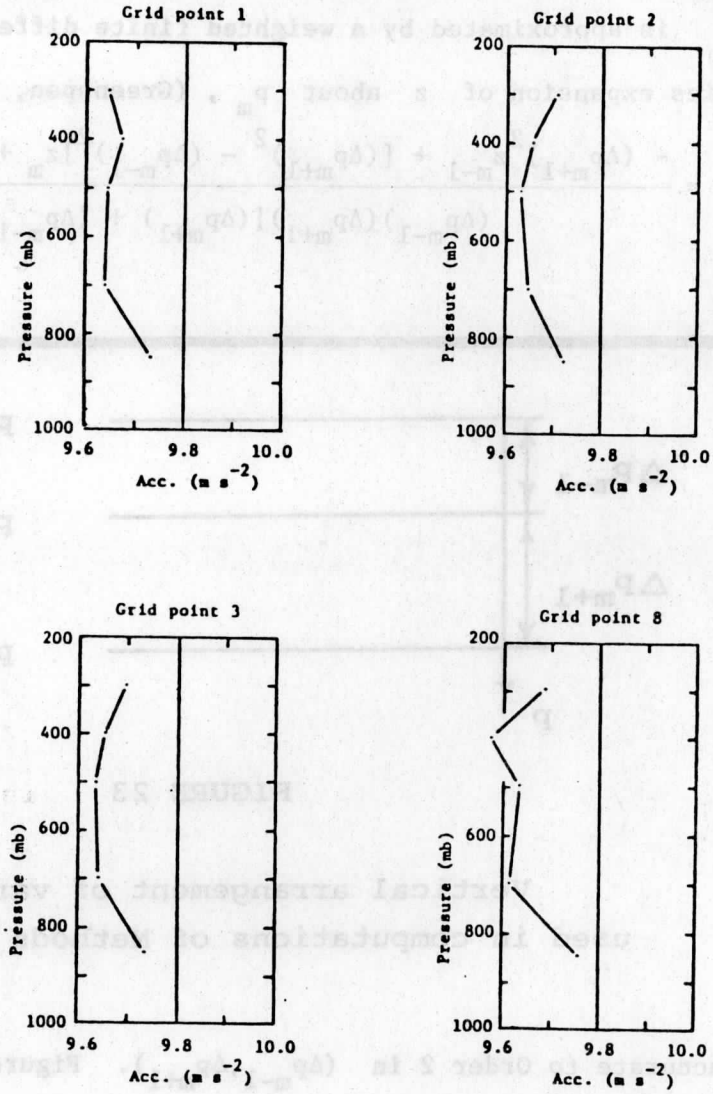


FIGURE 25

Vertical pressure gradient acceleration, $\left|\frac{RT}{p}\frac{\Delta p}{\Delta z}\right|$, computed by Method II, Appendix B, compared with gravity, g=9.8 m/s$^2$.

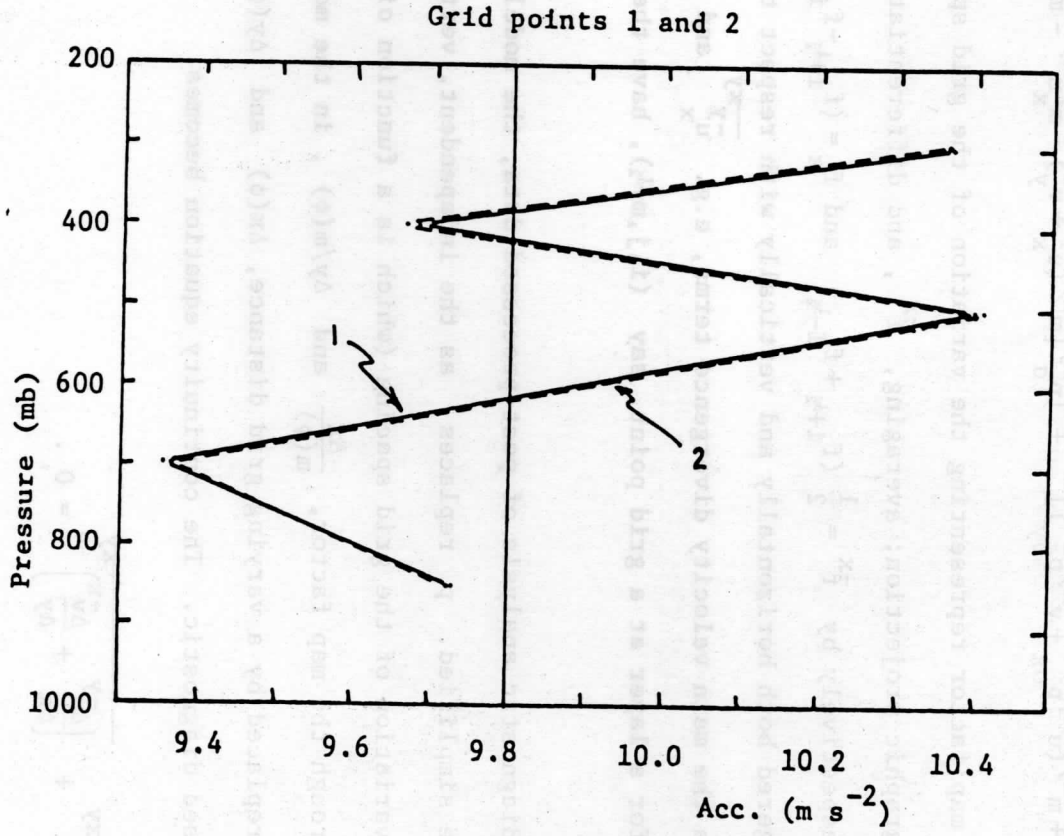


FIGURE 26

Vertical pressure gradient acceleration, $\left|\frac{RT}{p}\frac{\Delta p}{\Delta z}\right|$, computed by Method III, Appendix B, compared with gravity, g=9.8 m/s$^2$.

Appendix C: Formulation of a diagnostic equation for mass continuity

The $\sigma$ coordinate, LFM equation for conservation of mass (Shuman & Hovermale, 1968) is given by

$$\bar{p}^{t}_{\sigma t} + \overline{[\bar{p}^{xy}_{\sigma}\dot{\sigma}_{\sigma} + \bar{m}^{xy}(\bar{u}^{xy}\bar{p}^{y}_{\sigma x} + \bar{v}^{xy}\bar{p}^{x}_{\sigma y})]}^{xy} + \overline{\{\bar{p}^{xy}_{\sigma}[\bar{m}^{xy}(\bar{u}^{y}_{x} + \bar{v}^{x}_{y}) - \bar{m}^{y-xy}_{x}u^{xy} - \bar{m}^{x-xy}_{y}v^{xy}]\}}^{xy} = 0 ;$$

(m) is the map factor representing the variation of the grid spacing on the polar sterographic projection; averaging, $\bar{f}^{x}$, and differentiation, $f_x$, are given respectively by $\bar{f}^{x} = \frac{1}{2}(f_{i+\frac{1}{2}} + f_{i-\frac{1}{2}})$ and $f_x = (f_{i+\frac{1}{2}} - f_{i-\frac{1}{2}})/(x_{i+\frac{1}{2}} - x_{i-\frac{1}{2}})$. $\vec{V}_2$ is staggered both horizontally and vertically with respect to $\dot{\sigma}$. (Figure 1(a)) Thus the main velocity divergence terms, e.g. $\overline{u^{y}_{x}}^{xy}$ and $\overline{\dot{\sigma}_{\sigma}}^{xy}$, calculated for a layer at a grid point, say $(i,j,m+\frac{1}{2})$, have the weights in Figure 27.

For a diagnostic analysis of post-processed data, the model equation above may be simplified. p replaces as the independent, vertical coordinate. The variation of the grid spacing (which is a function of latitude, $\phi$) is given through the map factor, $\frac{\Delta x}{m(\phi)}$ and $\Delta y/m(\phi)$, in the model but can be explicitly replaced by a varying grid distance, $\Delta x(\phi)$ and $\Delta y(\phi)$, in the post-processed diagnostic. The continuity equation becomes

$$\overline{\frac{\Delta\omega}{\Delta p}}^{xy} + \overline{\left(\frac{\Delta\bar{u}^{y}}{\Delta x} + \frac{\Delta\bar{v}^{x}}{\Delta y}\right)}^{xy} = 0 .$$

To compute these velocity divergence terms from the post-processed data in a fashion analogous to the model's computation, the following scheme was used:

(i) At each grid point $(i,j)$, the value of $(\Delta x)_{i,j}$ and $(\Delta y)_{i,j}$ was computed from the value of $\Delta x$ and $\Delta y$ at neighboring grid points by the weights shown in Figure 28.

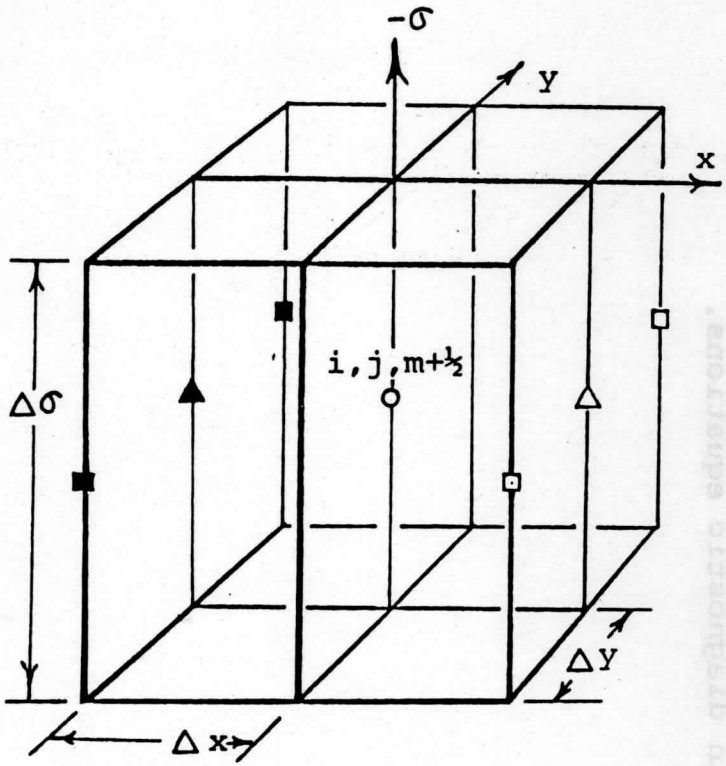


△ =+1/4 □ =+1/8

▲ =-1/4 ■ =-1/8

Weights for u in term $\overline{\bar{p}^{xy}\bar{m}^{xy}\bar{u}^{y}_{x}}^{xy}$ of model at (i,j,m+½).

Rotate -π/2 about axis for v term.

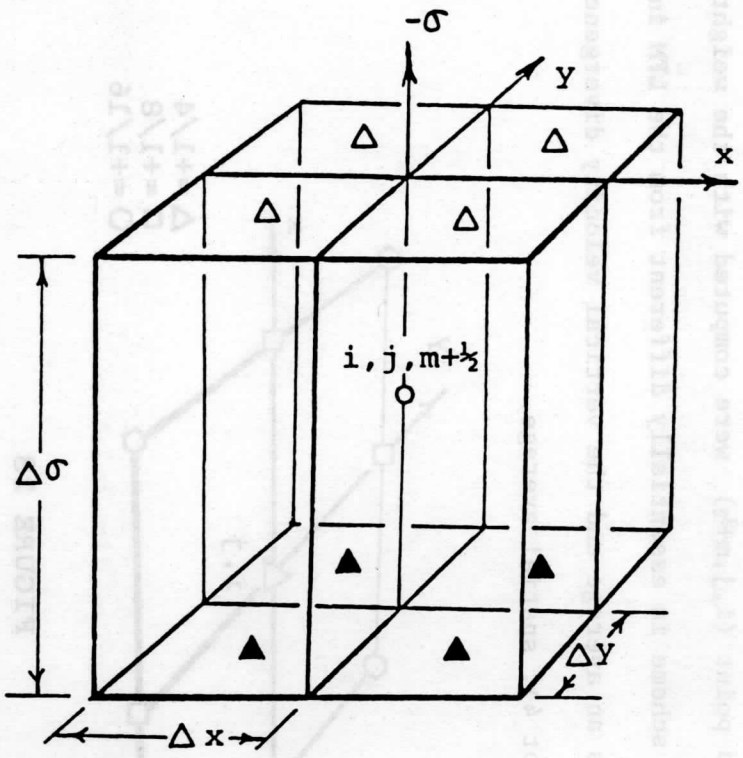


△ =+1/4

▲ =-1/4

Weights for $\dot{\sigma}$ in term $\overline{\bar{p}^{xy}\dot{\sigma}_{\sigma}}^{xy}$ of model at (i,j,m+½).

FIGURE 27

(ii) For a layer--i.e. between standard pressure levels, the velocity divergence terms at a grid point $(i,j,m+\frac{1}{2})$ were computed with the weights shown in Figure 29. This scheme is essentially different from the LFM in that $\vec{V}_2$ for the layer is an average and the vertical velocity divergence is a broader (9 points, not 4), spatial average.

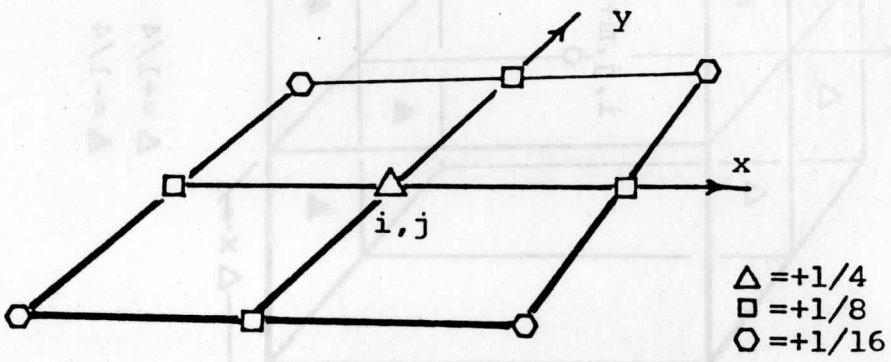


FIGURE 28

Weights for computing $(\Delta x)_{i,j}$ and $(\Delta y)_{i,j}$ in diagnostic equations.

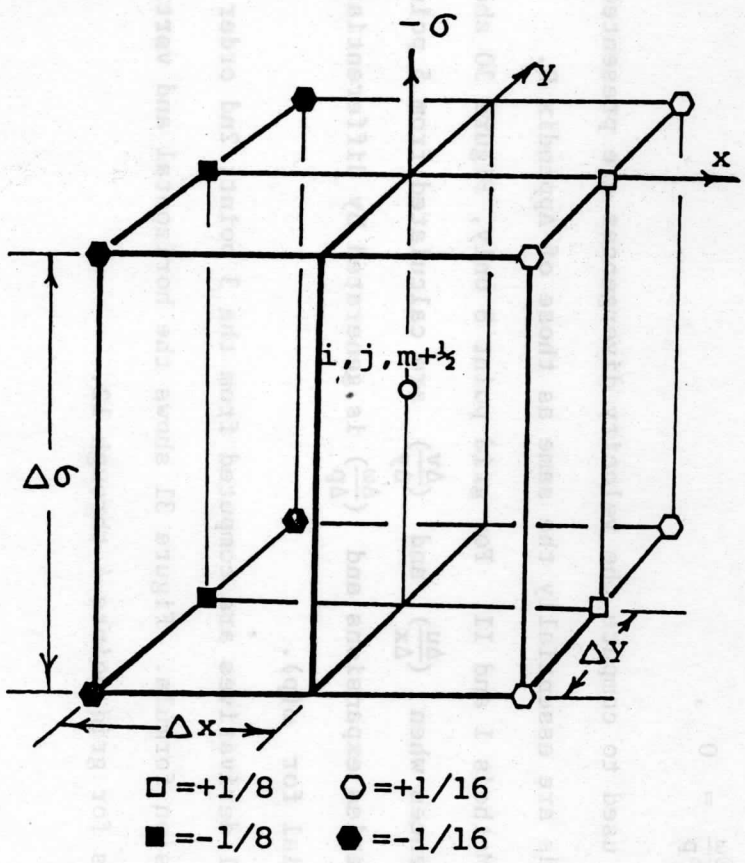


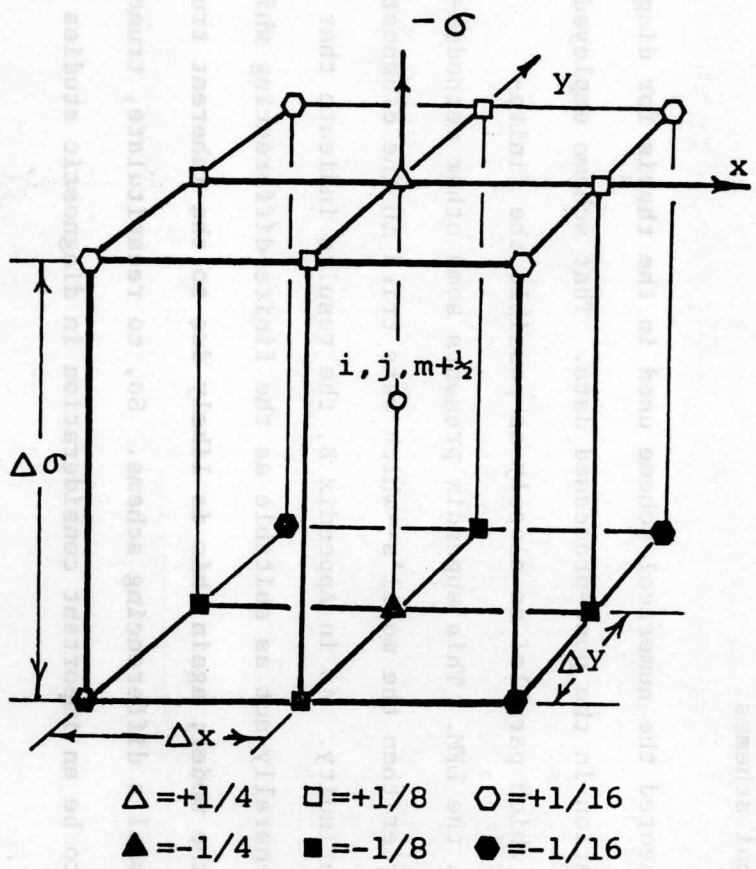


FIGURE 29

Weights for u in term $\overline{\overline{u}^{y}_{x}}^{xy}$ of diagnostic equation.
Rotate $-\pi/2$ about p-axis for v term.

Weights for $\omega$ in term $\overline{\overline{\omega_p}}^{xy}$ of diagnostic equation.

## Appendix D: Computation of mass continuity by other finite-difference or numerical schemes

Appendix C presented the numerical scheme used in the thesis for diagnosing mass conservation in the post-processed data. That scheme employed finite-differencing which parallel as closely as possible the finite-differencing used in the LFM. This appendix presents some other methods--some of them of higher order than the model's--which were tried in the diagnostic analysis of mass continuity. As in Appendix B, the results indicate that these methods are generally not as suitable as the finite-differencing which is compatible with the model; again this is likely due to the inherent truncation error of the model's differencing scheme. So, to recapitulate, truncation error appears to be an important consideration in diagnostic studies of model output.

For the mass conservation equation in the form

$$\frac{\partial u}{\partial x} + \frac{\partial v}{\partial y} + \frac{\partial \omega}{\partial p} = 0 \quad ,$$

the various methods used to compute the velocity divergences are presented below. These methods are essentially the same as those of Appendix B.

Combination: Methods I and II. For grid point 8 only, Figure 30 shows the velocity divergences when $(\frac{\Delta u}{\Delta x})$ and $(\frac{\Delta v}{\Delta y})$ are calculated from 5 point, 4th order, Taylor series expansions and $(\frac{\Delta \omega}{\Delta p})$ is generated by differentiating a 5th order polynomial for $\omega(p)$.

Method II. All derivatives are computed from the 3 point, 2nd order Taylor series expansion formula. Figure 31 shows the horizontal and vertical velocity divergences for grid points 4 through 12.

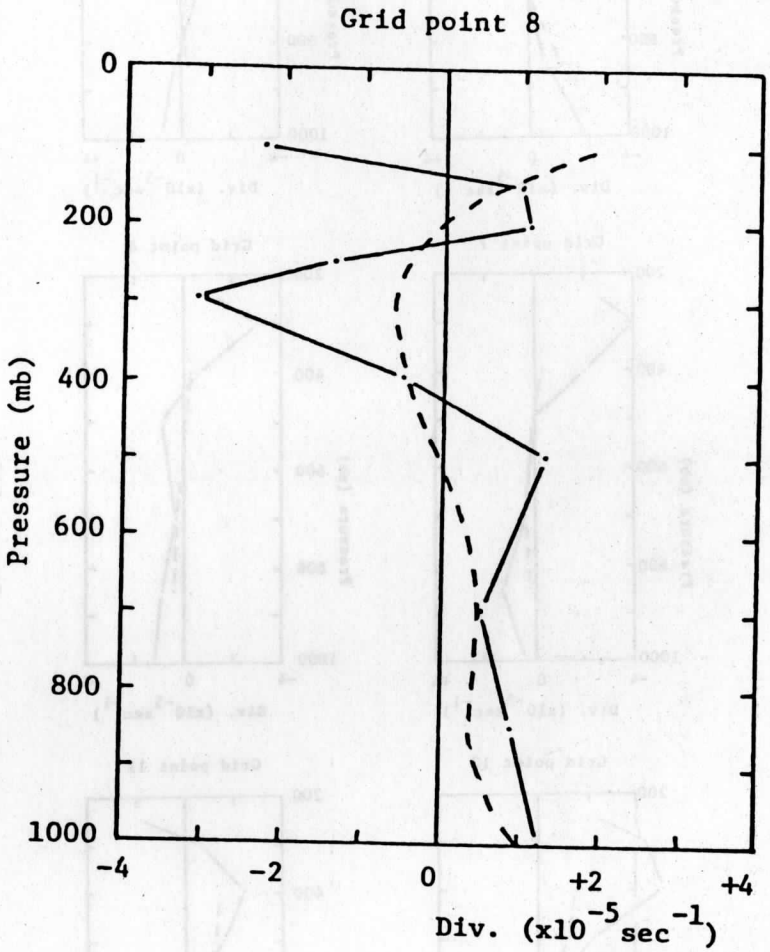


FIGURE 30

Velocity divergences computed by a combination of Methods I and II, Appendix B. $\vec{V}_p \cdot \vec{V}$ in solid; $-\frac{\partial \omega}{\partial p}$ in dashed.

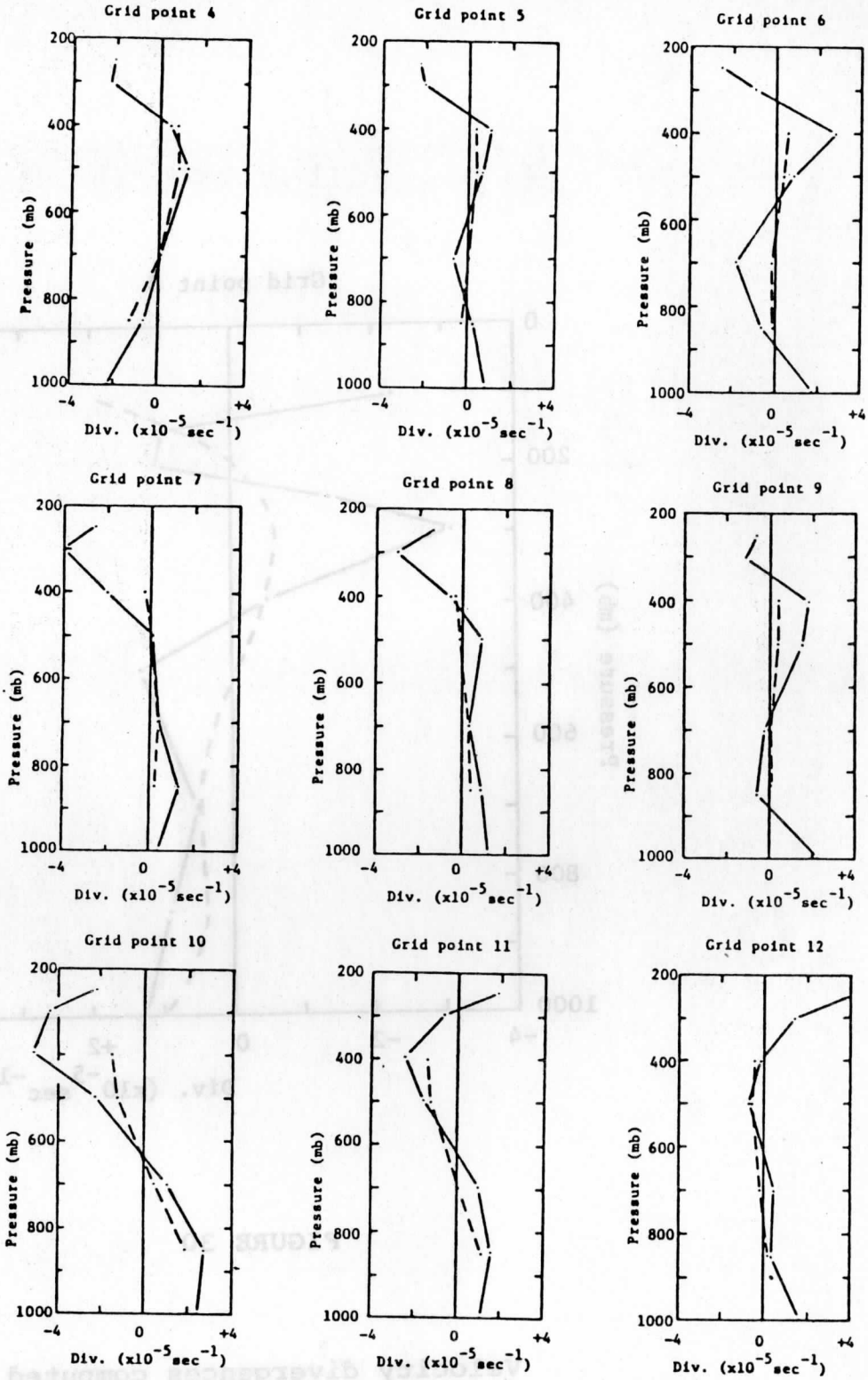


FIGURE 31

Velocity divergences computed by Method II, Appendix B.
$\vec{\nabla}_p \cdot \vec{V}$ in solid; $-\frac{\partial \omega}{\partial p}$ in dashed.

Acknowledgments

This article was originally presented as a University of Wisconsin-Madison, Department of Meteorology Master's thesis. The author extends his thanks to Lyle H. Horn, thesis advisor; David D. Houghton, thesis reader; Thomas M. Whittaker, computing specialist; and also to Thomas L. Koehler and Christopher M. Hayden who added constructive comments.

References

Dutton, J.A. and Johnson, D.R. (1967). The theory of available potential energy and a variational approach to atmospheric energetics; Advances in Geophysics, Vol. 12, pp. 333-436.

Gerrity, Jr., Joseph P. and Newell, John (1976). "Post-processing the LFM Forecasts"; Technical Procedures Bulletin No. 174, October 7, 1976 NOAA; U.S. Dept. of Commerce.

Greenspan, Donald (1974). Discrete Numerical Methods in Physics and Engineering, Academic Press, Inc., New York, N.Y. 1974.

Haltiner, George J. (1971). Numerical Weather Prediction, John Wiley and Sons, Inc., New York, N.Y., 1971.

Holton, James, R. (1972). An Introduction to Dynamic Meteorology, Academic Press, Inc., New York, N.Y., 1972.

Johnson, Donald R., (1977). "Isentropic Numerical Models: Results on model development for zonally averaged and secondary circulations"; Scientific Report to the National Science Foundation; Department of Meteorology and Space Science and Engineering Center, Univ. of Wisconsin, Madison, WI, November 1977.

Mahlman, J.D. and Moxim, W.J. (1976). "A Method for Calculating More Accurate Budget Analyses of 'Sigma' Coordinate Model Results"; Monthly Weather Review, Vol. 104, No. 9, September 1976, pp. 1102-1106.

Shuman, Frederick G. and Hovermale, John B. (1968). "An Operational Six-Layer Primitive Equation Model"; J. Applied Meteorology, Vol. 7, No. 4, August 1968, pp. 525-547.

Stackpole, John D. (1968). "Smoothing in the 6-layer (PE) Numerical Prediction Model"; Technical Procedures Bulletin No. 10; February 8, 1968, NOAA; U.S. Dept. of Commerce.

Stackpole, John D. (1969). "Operational Prediction Models at the National Meteorological Center"; Environmental Science Services Administration--Weather Bureau; U.S. Dept. of Commerce; November 1969.

# The Computation of Isentropic Atmospheric Trajectories Using a "Discrete Model" Formulation

Ralph A. Petersen
Geography Department, Northern Illinois University, DeKalb, Illinois 60115

Louis W. Uccellini
Space Science and Engineering Center, University of Wisconsin-Madison 53706

## Abstract

An explicit technique for computing atmospheric trajectories, based on Greenspan's discrete model formulation, is presented as an alternative to the commonly used implicit scheme developed by Danielsen. The method provides an economical means of objectively obtaining computer generated trajectories and accounts for variable acceleration along the entire trajectory paths. The initial results presented show that the explicit computations are stable and very nearly energy conservative. An application of the discrete model approach to a real data base and comparisons with trajectories determined by the implicit method yielded favorable results, illustrating the utility of the explicit technique as a diagnostic tool.

## 1. Introduction

The construction of three-dimensional atmospheric trajectories provides a valuable diagnostic tool for illustrating and understanding three-dimensional transport and exchange processes associated with extratropical weather disturbances. The trajectory approach has been successfully applied to studies including the stratospheric and tropospheric air mass exchanges associated with a jet streak (Danielsen, 1964; Reiter, 1972), the dispersal of upper atmospheric pollutants and possible nuclear contamination (Reiter, 1972), the three-dimensional structure and moisture transport within extratropical cyclones (Danielsen, 1966, 1967; Buzzi and Rizzi, 1975), and the kinetic energy budget for an extratropical cyclone (Sechrist and Dutton, 1970). Trajectory models which use wind forecasts from operational primitive equation models at the National Meteorological Center (Reap, 1972) have also been developed to improve temperature and cloud forecasts.

The purpose of this paper is to present a new technique for constructing computer generated trajectories as an alternative to the widely used implicit scheme developed by Danielson (1961) and discussed in Section 2. Using this new approach, trajectories are computed by applying an explicit system of equations based on a "discrete model" theory developed by Greenspan (1972, 1973) to the atmospheric equations of motion (Section 3). The method provides for objective, rapid and economical computations of trajectories; is stable for cyclonic and anticyclonic curvature; and explicitly accounts for the impact that spatial variations in the $\psi$ tendency will have upon the parcel accelerations. The stability and accuracy of the method are tested by applying the explicit technique to test cases (Section 4). A diagnostic study utilizing standard rawinsonde upper air data is then presented to test the applicability of the explicit technique to a real atmospheric data base (Section 5). Comparisons of selected trajectories computed by the explicit and implicit techniques are also shown.

2. The implicit technique for constructing atmospheric trajectories

The most widely used method to compute atmospheric trajectories for diagnostic studies which rely on the standard 12 h radiosonde upper atmospheric data base was developed by Danielsen (1961). Trajectories are constructed on isentropic surfaces by simultaneously solving for energy and total displacement formulas:

$$\frac{d}{dt}\left(\frac{U^2}{2}\right) + \frac{d}{dt}\psi = \frac{\partial}{\partial t}\psi \quad , \tag{1}$$

$$D = \left(\frac{U_1 + U_2}{2}\right) dT \quad , \tag{2}$$

where $U_1$ and $U_2$ are the wind speeds at the initial and final times, respectively and $\psi$ is the Montgomery stream function.

Danielsen advocated the isentropic framework for constructing trajectories.In the absence of latent heating, the potential temperature tends to be conserved for 12 h periods, and parcels are therefore likely to remain on isentropic surfaces. Also, trajectories can be computed more accurately in the isentropic framework since two dimensional flow implicitly includes vertical motions which would have to be calculated separately in Cartesian or isobaric coordinates. Danielsen's original method has been advanced by automating the technique and by including the effects of latent heat release on the trajectories (Danielsen, 1967; Bleck, 1967).

Danielsen's trajectory technique, however, has several drawbacks. The implicit nature of the scheme requires iteration for the simultaneous solution of (1) and (2). The construction of final trajectories by the iteration procedure is an intricate process and, for anticyclonic trajectories, the iteration does not always converge to a unique solution (Danielsen, 1961). Another difficulty involves estimating $\partial\psi/\partial t$ when the time step of the

implicit scheme is too large (a 12 h time step is normally imposed by the availability of upper atmospheric data). The large time step and implicit nature of this method also make it difficult to explicitly account for variable parcel accelerations which occur along the trajectory path. Reiter (1972) attempted to include significant changes in the parcel accelerations by incorporating geostrophic departures within the iteration procedure. But, Reiter's modification involves considerable subjectivity in estimating geostrophic departures at the beginning and end of the 12 h period that are subsequently applied along a significant portion of the trajectory path.

3. An explicit method for computing atmospheric trajectories

The explicit method, based on the "discrete model" formulation of Greenspan (1972, 1973), calculates parcel acceleration, velocity and distance at successive time steps. The system of equations as applied to constructing adiabatic, atmospheric trajectories is based on first determining the acceleration using the inviscid equations of motion

$$a_x^{(t)} = -\frac{\Delta\psi^{(t)}}{\Delta x} + f^{(t)}v^{(t)} \quad , \tag{3}$$

$$a_y^{(t)} = -\frac{\Delta\psi^{(t)}}{\Delta y} - f^{(t)}u^{(t)} \quad . \tag{4}$$

In the discrete formulation $a_x$,u and $a_y$,v are the accelerations and velocity components in the x and y directions, respectively, f is the coriolis parameter and superscripts refer to time step number. The new velocity and distance components are then calculated by Greenspan's discrete formulation:

$$u^{(t+1)} = u^{(t)} + \Delta t(3/2\ a_x^{(t)} - 1/2\ a_x^{(t-1)}) \quad , \tag{5}$$

$$v^{(t+1)} = v^{(t)} + \Delta t(3/2\ a_y^{(t)} - 1/2\ a_y^{(t-1)}) \quad , \tag{6}$$

$$x^{(t+1)} = x^{(t)} + \frac{\Delta t}{2}(u^{(t+1)} + u^{(t)}) \quad , \tag{7}$$

$$y^{(t+1)} = y^{(t)} + \frac{\Delta t}{2}(v^{(t+1)} + v^{(t)}) \quad . \tag{8}$$

A special "starter" formula is used for the first time increment

$$u^{(1)} = u^{(o)} + \Delta t\, a_x^{(o)} \quad , \tag{9}$$

$$v^{(1)} = v^{(o)} + \Delta t\, a_y^{(o)} \quad . \tag{10}$$

Readers may recognize the similarity of the (3/2a - 1/2a) term in (5) and (6) to the Adams-Bashforth scheme which was found to be quite stable (Lilly, 1965), but for small $\Delta t$ only (Young, 1968). Greenspan (1972), however, found that in discretized applications the above explicit system conserves energy and is stable and accurate for a wide range of $\Delta t$.

To close the system of equations, new $\psi$ values must be available at every time step to calculate the spatial derivatives in (3) and (4). For diagnostic studies where $\psi$ is available at 12 h intervals, $\psi^{(t)}$ is specified on a latitude-longitude grid by using the initial and final $\psi$ values, and by assuming $(\partial\psi/\partial t)_{i,j}$ varies linearly at each grid point so that at time step n,

$$\psi_{i,j}^{(t)} = \psi_{i,j}^{(o)} + \left[\frac{\psi^{(f)} - \psi^{(o)}}{t_f - t_o}\right]_{i,j} n\Delta t \quad . \tag{11}$$

When $\psi$ values are available 12 h before and after the time interval for which trajectories are constructed, a nonlinear approximation for $(\partial\psi/\partial t)_{i,j}$ is calculated using overlapping quadratic Lagrangian polynomials. This procedure, as presented by Bleck and Haagenson (1968) and expanded upon by Whittaker and Petersen (1976),has the advantage that the derivatives of the resulting third order polynomial are continuous and implicitly equivalent

to second-order Taylor series approximations at the beginning and end of the period for which the trajectories are computed. Once $\psi_{i,j}^{(t)}$ is specified, $\frac{\Delta\psi}{\Delta x}_{i,j}^{(t)}$ and $\frac{\Delta\psi}{\Delta y}_{i,j}^{(t)}$ are calculated at grid points using standard centered differences over a $2\Delta x$ and $2\Delta y$ interval. The gradients are then interpolated from the grid point location to the parcel position using the overlapping polynomial technique. With the gradients of $\psi$ specified at the parcel position, the acceleration, new velocity and new position can be determined.

A summary of the technique as applied to the standard radiosonde data base is listed below:

1) Specify $\psi^{(o)}$ and $\psi^{(f)}$ at each grid point and $u^{(o)}$ and $v^{(o)}$ either at each grid point or at each station location,
2) Using $\psi^{(o)}$, calculate $\frac{\Delta\psi}{\Delta x}^{(o)}$, $\frac{\Delta\psi}{\Delta y}^{(o)}$ and then with $u^{(o)}$, $v^{(o)}$ calculate $a_x^{(o)}$, $a_y^{(o)}$ using (3) and (4),
3) Calculate $u^{(1)}$, $v^{(1)}$ with (9) and (10),
4) Calculate new positions $x^{(t+1)}$, $y^{(t+1)}$ with (7) and (8),
5) Determine $\psi^{(t+1)}$ using either the linear or nonlinear approach; calculate gradients of $\psi$ at the grid points and interpolate them to the parcel position,
6) Calculate $a_x^{(t+1)}$, $a_y^{(t+1)}$ with (3) and (4),
7) Calculate $u^{(t+1)}$, $v^{(t+1)}$ using (5) and (6),
8) Go back to step 4 until $n\Delta t$ = 12 hours.

## 4. Initial experiments

Although the discrete model formulation conserves total energy for closed systems (Greenspan, 1972), the application of the technique to an open system, in which the accelerations are approximated by the inviscid, adiabatic equations of motion, and the interpolation of $\psi$ gradients from grid points to

parcel positions can introduce spurious energy sources. The initial experiments were designed to determine the magnitude of this spurious energy generation for a simplified, steady state flow. With steady state assumptions, (1) reduces to

$$\frac{d}{dt}\left(\frac{U^2}{2} + \psi\right) = \frac{d}{dt}(T) = 0 \quad , \tag{12}$$

so that the total energy (T) for a parcel remains constant. Any deviations from the initial total energy for a parcel represents a spurious energy source related to the discrete methodology and to the numerical interpolation technique needed for specifying $\psi$ gradients at parcel positions.

For the initial experiments, a zonal $\psi$ field and constant f were specified so that $d\underset{\sim}{U}_g/dt = 0$. Five parcels were chosen with parcels 1 and 2 initialized with a subgeostrophic u component of 15.0 and 20.0 m $s^{-1}$, respectively. Parcel 3 was initialized with a geostrophic u component of 25.0 m $s^{-1}$ and parcels 4 and 5 were initialized with supergeostrophic u components of 30.0 and 35.0 m $s^{-1}$. The initial v component was set equal to zero for all 5 parcels. With the $\psi$ gradients kept constant in time, the parcel trajectories initialized with an ageostrophic wind should undergo an inertial oscillation (Newton, 1959) and therefore return to their respective original latitudinal position with a period equal to one half pendulum day and with a wind speed equal to the original speed assigned to each parcel. The parcel initialized with a geostrophic wind speed should maintain a constant zonal component with v remaining equal to zero. The experiments were repeated with $\Delta t$ set equal to 300, 600, 900, 1200 and 1800 seconds.

Figure 1 illustrates the response of the 5 trajectories with $\Delta t$ set at 900 sec. The subgeostrophic parcels (1 and 2) initially turned to the left and accelerated, passed the equilibrium at which the u component is in

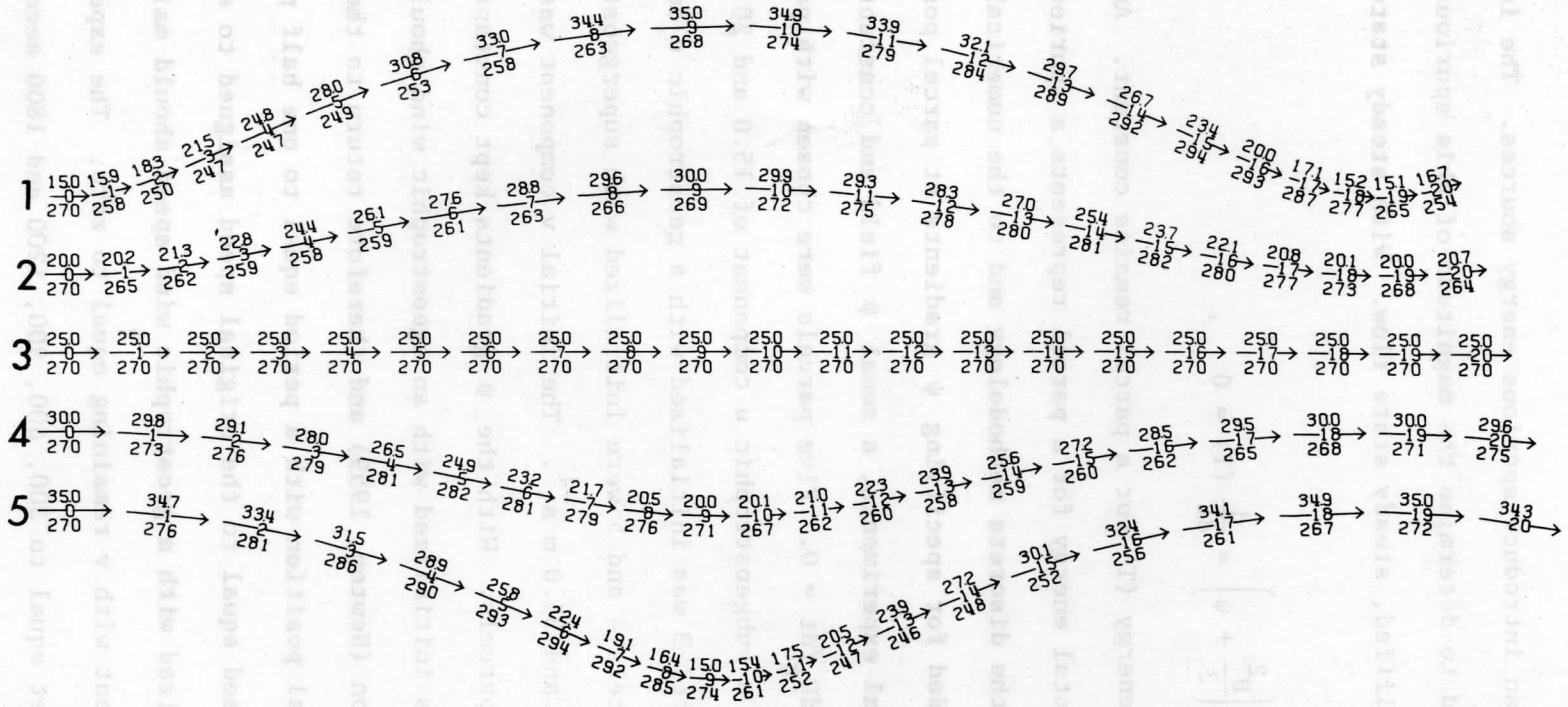


Fig. 1. Trajectories for various initial wind speeds with initial $\psi$ field held constant. Trajectories 1 and 2 are initialized with a subgeostrophic wind, trajectory 3 is in geostrophic balance; trajectories 4 and 5 are initialized with a supergeostrophic wind. Trajectories are calculated with $\Delta t$ = 15 min.

geostrophic balance, and began turning to the right while still accelerating. After 9 h, these parcels decelerated while continuing a turn to the right, as the v component became negative. The parcels then slowly turned to the left (after 15 h), completing the inertial oscillation by 19 h. The sequence of parcel accelerations was reversed for the supergeostrophic parcels (4 and 5). These initially ageostrophic parcels all displayed a period of oscillation equal to one half pendulum day as expected. After one full oscillation and a return to within 50 m of their initial latitudinal position, parcels had velocities within .04 m $s^{-1}$ of their original values. The trajectory for Parcel 3, initialized with a geostrophic wind speed, remained zonal throughout the 24 h period.

Figure 1 also illustrates that the supergeostrophic, subgeostrophic and geostrophic parcels were located at an equal distance from the starting position after the period of oscillation. The more supergeostrophic or subgeostrophic a parcel was initially, the greater the respective, subsequent decelerations or accelerations were in the x direction, thus neutralizing the different initial wind speeds. Applying the implicit technique (1 and 2) over the period of the inertial oscillation with an equal initial and final wind speed and without accounting for the ageostrophic departures yields a distance which varies for the different parcels, being greater for the supergeostrophic than for the subgeostrophic parcels. This example demonstrates the importance of objectively accounting for the geostrophic departures along the entire trajectory.

Energy diagnostics for parcels 1, 2, 4 and 5 are presented in Tables I and II. The accumulated change in total energy (T) over the first half of the inertial oscillation are given for various $\Delta t$ (Table I). The magnitudes of the accumulated changes in T were found to be a maximum at this time;

| Parcel | 1 | 2 | 4 | 5 |
|---|---|---|---|---|
| Initial Velocity | 0.6 $U_g$ | 0.8 $U_g$ | 1.2 $U_g$ | 1.4 $U_g$ |
| 1800 s | +5.46 | +2.28 | -1.32 | -1.74 |
| 1200 s | +2.35 | +1.01 | -0.57 | -0.83 |
| 900 s | +1.32 | +0.57 | -0.30 | -0.48 |
| 600 s | +0.62 | +0.29 | -0.10 | -0.22 |
| 300 s | +0.24 | +0.16 | +0.07 | -0.07 |

$\Delta t$

Table I: Accumulated total energy changes ($*10^4$ ergs $g^{-1}$) from 0 to 9 hours for parcels 1, 2, 4 and 5 and $\Delta t$ of 300 to 1800 s, with a geostrophic wind ($U_g$) of 25 m $s^{-1}$.

| Parcel | 1 | 2 | 4 | 5 |
|---|---|---|---|---|
| Initial Velocity | 0.6 $U_g$ | 0.8 $U_g$ | 1.2 $U_g$ | 1.4 $U_g$ |
| 1800 s | - 2.10 | - 1.39 | + 2.15 | + 5.05 |
| 1200 s | - 0.88 | - 0.60 | + 0.92 | + 2.18 |
| 900 s | - 0.49 | - 0.33 | + 0.52 | + 1.21 |
| 600 s | - 0.21 | - 0.14 | + 0.23 | + 0.53 |
| 300 s | - 0.04 | - 0.03 | + 0.07 | + 0.13 |

$\Delta t$

Table II: Accumulated total energy changes ($*10^4$ ergs $g^{-1}$) from 0 to 1 hour for parcels 1, 2, 4 and 5 and $\Delta t$ of 300 to 1800 s, with a geostrophic wind ($U_g$) of 25 m $s^{-1}$.

whereas by (12), dT/dt should have been zero. Supergeostrophic parcels which are decelerating during this period experienced a decrease in the total energy, while subgeostrophic parcels experienced an increase in the total energy. In general, successive reductions in the $\Delta t$ by 300 second increments for the trajectory computation reduced the magnitude of the spurious energy changes by nearly a half. But for all cases, the important factor is that the maximum accumulated changes in T were 2 to 3 orders of magnitude less than the individual changes in the kinetic and potential energies for the same time period. Through a full inertial oscillation, however, parcels experienced a reversal in the sign of the acceleration/deceleration. The net changes in T therefore approached zero over the 19 hour period.

The magnitudes of the changes in T during the first hour reveal the influence of the special "starting formulas" (9 and 10) that are needed for the first time step (Table II). The magnitudes of dT/dt during the first hour were of opposite sign and nearly two thirds the magnitude of the accumulated change in T during the next 8 h period. The large errors are due to the nature of the starting formula and to the initial conditions. With v initially set equal to zero, the u wind component is kept constant during the first time increment when it should be either increasing or decreasing as the ageostrophic parcels are subjected to latitudinal displacement. This error could be minimized by using a smaller initial time step which would then be expanded in subsequent iterations until the standard time interval is achieved.

This initial experiment demonstrates the stability of the discrete formulation and the accuracy of the interpolation scheme in maintaining zonal geostrophic trajectories while also accounting for accelerations which result from initially unbalanced flow. Since the changes in the total energy which accumulated during successive iterations were at least 2 to 3 orders of magnitude

less than changes in the kinetic and potential energies, the amount of error introduced to the trajectory paths by the discrete model approach should be minimal.

5. Application of explicit method to a diagnostic study

The explicit trajectory method was applied to an atmospheric data base to test the applicability of the discrete model formulation in diagnostic studies which rely upon the rawinsonde network.

Nearly 100 trajectories were computed on the 330 K isentropic surface for the 12 h period 1200 GMT 10 May through 0000 GMT 11 May 1973. The trajectories were initialized on a 2° latitude by 2° longitude grid within a domain bounded by 123°W 51 N, 83°W 51 N, 123°W 35°N and 83°W 35°N. The $\psi$ gradients were specified utilizing the subjective $\psi$ analyses shown in Figure 2 and by assuming a 12 h linear $\psi$ tendency at each grid point. The winds were initialized from subjective isotach and isogon analyses from 1200 GMT 10 May. The subjective isentropic analyses in this study were cross checked with 15 vertical cross sections to incorporate the detailed vertical resolution of individual rawinsonde ascents within the horizontal wind analyses on isentropic surfaces (see Shapiro, 1970). An 1800 s time step was used to calculate the trajectories.

At 1200 GMT 10 May 1973, three jet streaks on the 330 K surface (Fig. 2) were embedded within a general westerly flow stretching from the West Coast to the Great Lakes region. A deepening trough over the Great Lakes region yielded more cyclonic curvature to the flow field in the eastern third of the United States. By 0000 GMT 11 May, the two western jet streaks intensified slightly and propagated eastward while the eastern streak propagated northeastward and weakened (Fig. 2). The trough over the Great Lakes deepened slightly and was better defined by 0000 GMT.

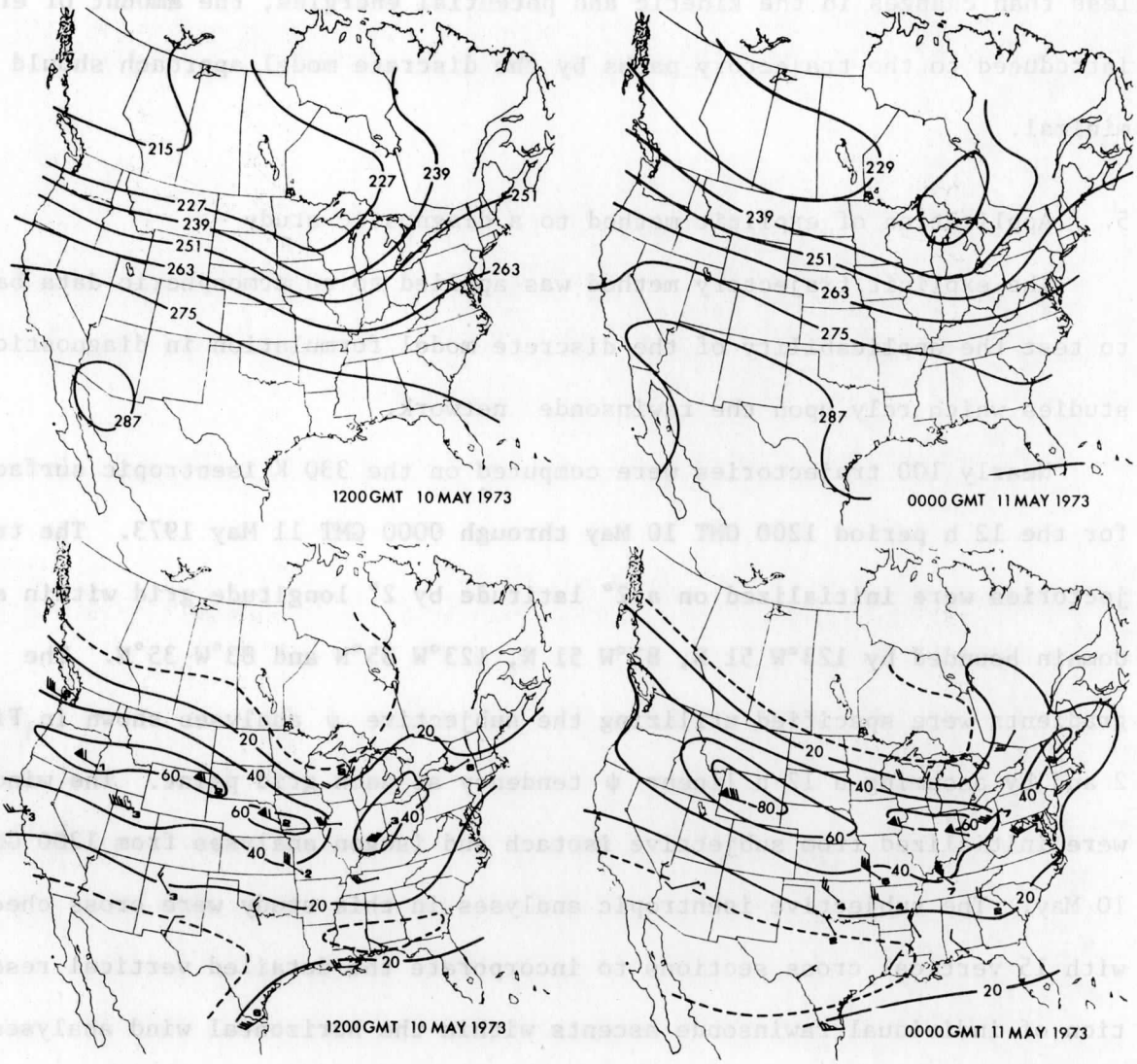


Fig. 2. 330 K isentropic analyses for 1200 GMT 10 May and 0000 GMT 11 May 1973; $\psi$ analysis on top ($275 = 3.275 * 10^5 m^2 s^{-2}$), isotach analysis on bottom ($m\ s^{-1}$). Wind barbs represent selected station wind reports rounded off to nearest 5 $m\ s^{-1}$; solid barb = 50 $m\ s^{-1}$, long barb = 10 $m\ s^{-1}$, short barb = 5 $m\ s^{-1}$. The number at station is actual last digit of wind report.

Figure 3 illustrates 20 trajectories which represent the larger sample of the trajectories computed. In general, the final wind speed of the parcels were within 5 to 10 m $s^{-1}$ and 20° of the observed wind speed and direction, respectively. The final trajectory wind speeds were usually greater than the observed winds which should be expected since frictional effects related to strong horizontal and vertical wind shears are not included in the scheme.

The trajectories initialized within the jet streak over the western United States moved rapidly eastward while accelerating slightly, then turned to the right and began decelerating by 0000 GMT 11 May. Trajectories E and P, initially located to the south of the western jet streak, accelerated toward the region of strong $\psi$ gradients and maximum winds. Upon approaching the deepening trough over the Great Lakes region, G and H turned cyclonically and accelerated in response to the increasing $\psi$ gradient.

Trajectories L and Q are included to illustrate the ability of the explicit technique to compute trajectories within weaker and more variable flow regimes which could result in more erratic parcel movement. Trajectories M, N, O and R, S, T depict the parcel responses upon exiting the jet streaks originally extending into the Great Plains (Fig. 2). These parcels turned to the right and decelerated upon exiting the streak. Several of the parcels (R and M) then turned to the left and accelerated later in the 12 h period upon approaching the trough line which extended from the Great Lakes region to the southeast United States. Trajectories R and S depict how critical the initial wind speed and the magnitude of the ageostrophic component were to the trajectories originating in the exit region of the jet streak. Trajectories R and S were originally only 222 km apart, yet ended up nearly 1000 km apart 12 h later. Both trajectories appear to be reasonable in that the final wind

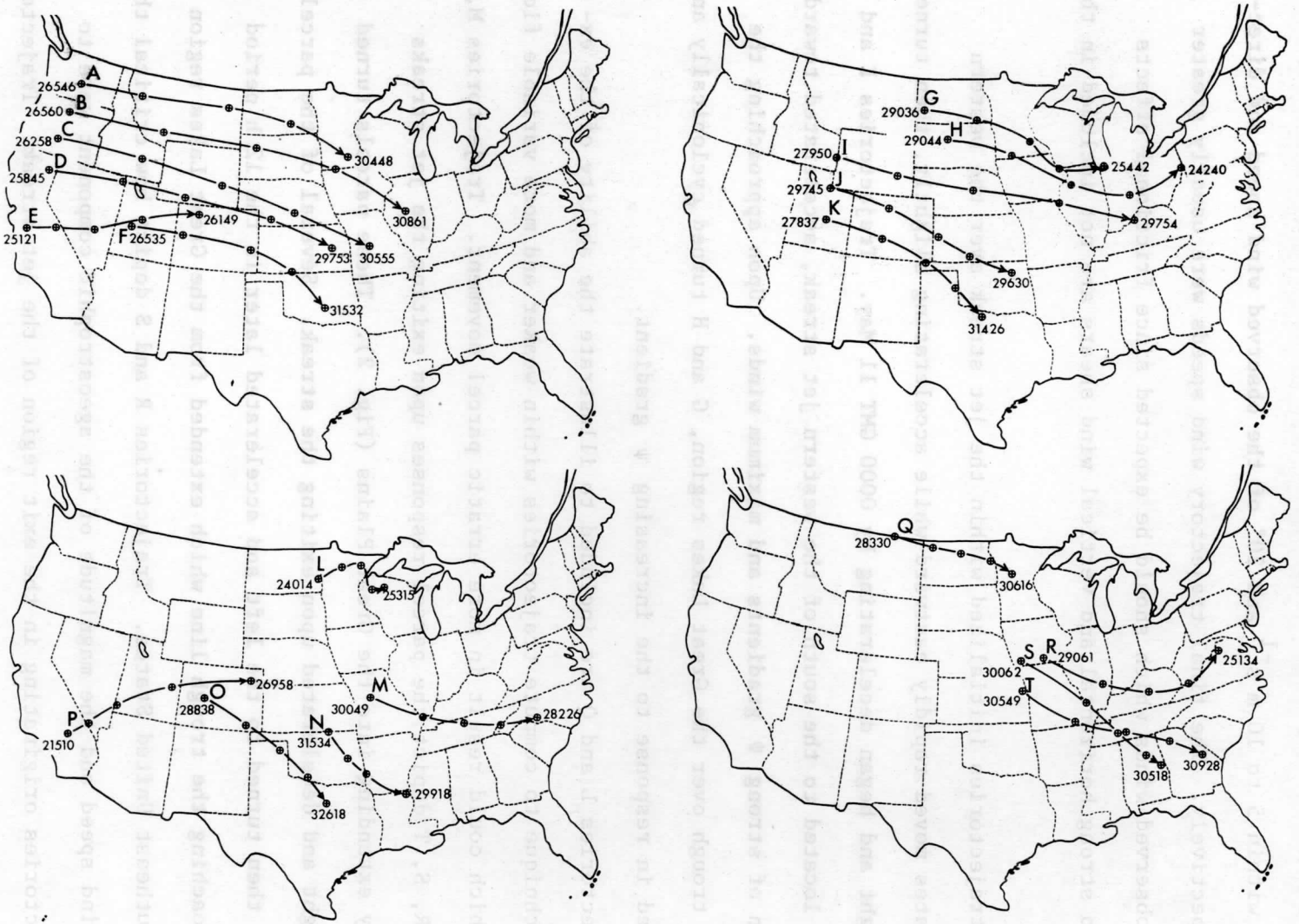


Fig. 3. Trajectories computed for 1200 GMT 10 May through 0000 GMT 11 May 1973 on 330 K isentropic surface utilizing discrete model technique, 3 h positions indicated by ⊕ , initial and final wind direction and speed indicated (31426 = 314° 26 m $s^{-1}$).

speeds were within 2 m $s^{-1}$ of the observed wind speeds and 10° of the observed directions at 0000 GMT 11 May.

Figure 4 illustrates selected comparisons made between trajectories computed with the explicit discrete model formulation, for which the final computed velocities were in close agreement with 0000 GMT observations, and Danielsen's implicit scheme (1 and 2). In general, the discrepancies were minor as the difference in the 12 h position generated by the two methods fell well within the error range expected from data acquisition and analysis errors (Reiter, 1972). However, the two schemes did yield significantly different paths for the parcels (R and S) originating in the exit region of the jet streak (Fig. 4C). In the first case, the explicit trajectory (R, dashed) originated in southeast Iowa, decelerated and turned to the right upon exiting the streak and later accelerated ending near Washington, D.C. with a wind speed and direction nearly equal to the wind observation near that location (Fig. 2). The implicit scheme can not objectively incorporate these variable accelerations along the path of the trajectory since only the average wind speed based on initial and final values are used to determine the distance traveled (2). The implicit scheme therefore yielded an energy consistent trajectory which extended 330 km beyond the endpoint of the trajectory computed with the explicit technique. In the second case, the trajectories originating in southwest Iowa (S) show even more of a discrepancy. The explicit trajectory decelerated rapidly from an initial 64 m $s^{-1}$ wind speed and turned to the right, ending in Alabama. The final wind speed of 18 m $s^{-1}$ and wind direction of 305° were within 2 m $s^{-1}$ and 10°, respectively, of the observed wind near that location. The implicit scheme, using 12 h wind averages did not give this trajectory but yielded an energy consistent trajectory ending near Cape Hatteras, North Carolina, 1000 km from the termination

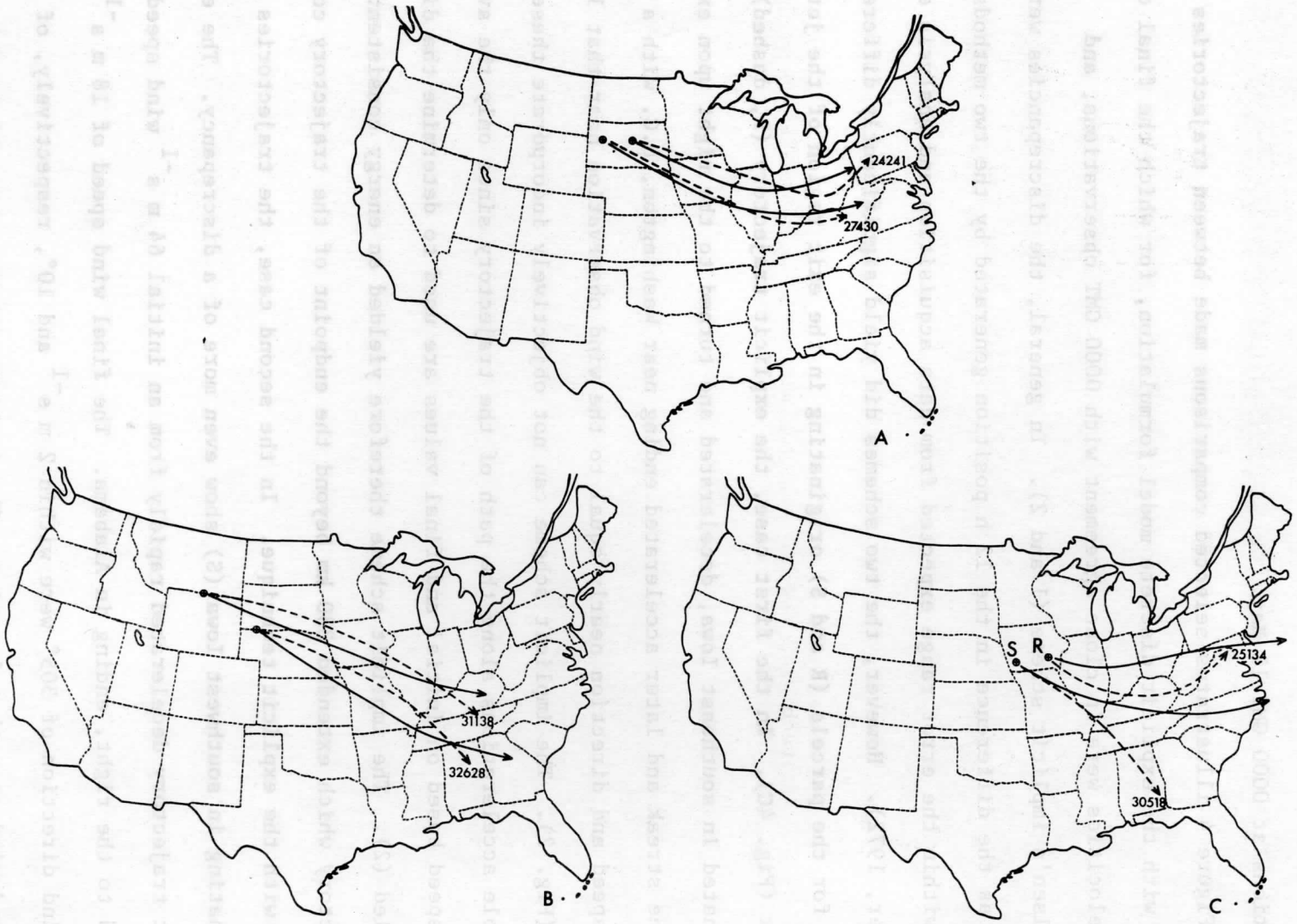


Fig. 4. Trajectories calculated using Danielsen's implicit scheme (solid) and using discrete model formulation (dashed) for period from 1200 GMT 10 May through 0000 GMT 11 May 1973. Final wind direction and speed indicated for trajectories computed using discrete model formulation (27430 = 274° 30 m $s^{-1}$).

of the explicitly computed trajectory.

These two examples again illustrate the ability of the explicit scheme to objectively account for the effect that the $\psi$ tendencies and the initialized and subsequent geostrophic departures along the parcel path have on the calculated trajectory. This sensitivity of trajectories which originate within regions of strong winds and large wind shears also illustrates the importance of careful $\psi$ and wind analyses for computing trajectories with either the explicit or the implicit technique.

## 6. Summary

An explicit technique for calculating atmospheric trajectories is presented in this paper as an alternative method to the standard implicit scheme derived by Danielsen (1961). The technique uses the inviscid equations of motion and the discrete model formulation derived by Greenspan (1972, 1973) to compute trajectories on isentropic surfaces, assuming adiabatic flow. The discrete model formulation is designed specifically for a Lagrangian system and objectively accounts for the geostrophic departures and subsequent accelerations along the entire length of the trajectory.

The initial test of the explicit technique used a simplified steady state $\psi$ distribution and various initial wind speeds to determine the magnitude of the errors introduced by the discretization of the equations of motion and by the grid point to parcel interpolations of the $\psi$ gradient necessary to determine new accelerations at each time step. The discrete model approach yielded trajectories for which the change of total energy was 2 to 3 orders of magnitude less than the individual changes in either the kinetic or potential energies. The computed trajectories accurately simulated the parcel undergoing an inertial oscillation in response to the initial ageostrophic component, since parcels tested were within 50 m of their

initial longitudinal position and .04 m $s^{-1}$ of their initial wind speed after one full period of oscillation. The initial experiment demonstrated the stability of the discrete formulation and the accuracy of the interpolation scheme in maintaining zonal geostrophic trajectories and in accurately accounting for the accelerations resulting from the initially unbalanced flow.

The application of the discrete formulation to a diagnostic case study yielded favorable results. The trajectories ended with computed velocities very close to the observed winds at the 12 h mark. Comparisons with trajectories determined using Danielsen's implicit technique were also generally good. Individual trajectories computed with either technique ended within the error bounds expected from observation and analysis errors. Significant differences, however, occurred for trajectories initialized within the exit region of jet streaks where the influence of the geostrophic departures and subsequent decelerations are very important. In these cases, the implicit scheme was not capable of objectively accounting for the ageostrophic winds along the entire parcel paths and thus yielded significantly different results.

The application of the discrete model approach and the implicit scheme also revealed the sensitivity of the trajectories to the initial and final $\psi$ fields and the initial wind analysis. Great care must be taken in the diagnostic analyses to achieve representative trajectories with either scheme. The use of the trajectories from case studies should also be tempered by recognizing that the inviscid, adiabatic and linear $\psi$ tendency assumptions are made for both the explicit and implicit schemes.

In future experiments, the discrete model approach will be used to study parcel reaction during inertial instability. The effect of nonlinear $\psi$ tendencies on 12 h trajectories will be tested using the AVE data sets (Scoggins and Turner, 1974) in which the soundings are taken every 3 h. The explicit

technique will also be tested in diagnostic case studies in which the wind and $\psi$ fields are objectively analyzed using a thermal enhancement technique (Petersen, 1977).

## 7. Acknowledgments

We wish to thank Dr. Donald F. Greenspan for his inspiration and encouragement during this study, and Dr. Christopher Hayden and Mr. Tom Koehler for their critical review of the manuscript. We also express our appreciation to Mr. Gregory Krause for providing an independent, implicitly determined set of trajectories for the case study, Mr. John Stremikis for drafting the figures and Mrs. Eva Singer for typing the final manuscript.

This research was sponsored in part by the National Oceanic and Atmospheric Administration (Meteorological Satellite Laboratory) grant number 04-4-158-2 and the National Science Foundation, grant ATM75-23223.

References

Bleck, Rainer, 1967: Numerical methods for computing moist isentropic trajectories. Air Force Cambridge Res. Lab., Dept. 67-0617, Bedford, Mass., 35-96.

_____, and P. L. Haagenson, 1968: Objective analysis on isentropic surfaces. NCAR Tech. Note NCAR-TN-39, Boulder, Colo., 27 pp.

Buzzi, A., and R. Rizzi, 1975: Isentropic analyses of cyclogenesis in the lee of the Alps. Riv. Ital. Geofis., Atti del XIII Cong. Intern. Meteor., Alpina, 1, 7-14.

Danielsen, E.F., 1961: Trajectories: isobaric, isentropic and actual. J. Meteor., 18, 470-486.

_____, 1964: Project Springfield Report. Defense Atomic Support Agency, Washington, D.C., 97 pp.

_____, 1966: Research in four-dimensional diagnosis of cyclonic storm cloud systems. Air Force Cambridge Res. Lab., Dept. 66-30, Bedford, Mass., 53 pp.

_____, 1967: Moist isentropic flow and trajectories in a developing wave cyclone. Air Force Cambridge Res. Lab., Dept. 67-0617, Bedford, Mass., 1-34.

Greenspan, D., 1972: A new explicit discrete mechanics with applications. J. Franklin Inst., 294, 231-240.

_____, 1973: Discrete Models, Addison-Wesley Publishing Company, Reading, Mass., 165 pp.

Lilly, D.K., 1965: On the computational stability of numerical solutions of time-dependent non-linear geophysical fluid dynamics problems. Mon. Wea. Rev., 93, 11-26.

Newton, C.W., 1959: Axial velocity streaks in the jet stream: ageostrophic "inertial" oscillations. J. Meteor., 16, 638-645.

Petersen, R.A., 1977: Three-dimensional objective analysis based on isentropic cross-sectional techniques. Meteorological Applications of Satellite Indirect Soundings II, Project Report, NOAA Grant 04-4-158-2, Dept. of Meteorology, University of Wisconsin-Madison, 8-54.

Reap, R.M., 1972: An operational three-dimensional trajectory model. J. Applied Meteor., 11, 1193-1202.

Reiter, E.R., 1972: Atmospheric Transport Processes. Part 3: Hydrodynamic Tracers, AEC Critical Review Series, U.S. AEC., 206 pp.

Scoggins, J.R., and R.E. Turner, 1974: Data for NASA's AVE II pilot experiment, part I: 25-mb sounding data and synoptic charts. NASA Tech. Memo., NASA TMX-64877, Marshall Space Flight Center, Ala., 3-50.

Sechrist, F.S., and J.A. Dutton, 1970: Energy conversions in a developing cyclone. Mon. Wea. Rev., 98, 354-362.

Shapiro, M.A., 1970: On the applicability of the geostrophic approximation to upper-level frontal-scale motions. J. Atmos. Sci., 27, 408-420.

Young, J.A., 1968: Comparative properties of some time differencing schemes for linear and nonlinear oscillations. Mon. Wea. Rev., 96, 357-364.

Whittaker, T.M., and R.A. Petersen, 1977: Objective cross-sectional analyses incorporating thermal enhancement of the observed winds. Mon. Wea. Rev., 105, 147-153.